RHODES UNIVERSITY

Where Leaders Learn

Sulphur isotope study of pyrite from the Twangiza-Namoya Gold Belt, (South Kivu, DRC): a proxy of gold provenance

A thesis submitted in fulfilment of the requirements of the degree of

Master of Science

At

Rhodes University
By

Thapelo Refiloe Patience Moloto

Submitted in January 2018

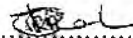Department of Geology, Rhodes University
South Africa

Supervisor: Prof. Steffen H. Büttner

DECLARATION

I declare that this thesis is my own work, and information from other publications is adequately referenced. It is being submitted in fulfilment for the Master of Sciences degree in the Department of Geology, Rhodes University.

THAPELO R.P. MOLOTO

Name of Candidate   Signature

. Signed on the 19th day of January 2018

ACKNOWLEDMENTS

Abstract

Gold in the highly prospective Twangiza-Namoya Gold Belt (TNGB) in the eastern Democratic Republic of Congo (DRC), with its four main deposits at Twangiza, Kamituga, Lugushwa and Namoya, appears to be correlated with the presence of sulphide minerals. Sulphur isotopic compositions of pyrite in the metasedimentary host rocks and in hydrothermal veins are used to identify the possible primary sources of hydrothermal sulphur and, by proxy, hydrothermal gold.

The sulphur isotope signatures of the pyrites from the TNGB deposits show an overall range from -18.4‰ to +22.6‰. δ^{34} values in host rock pyrite are: -2.2‰ to +3.0‰ (Twangiza deposit), -4.2‰ to -0.6‰ (Kamituga deposit), -18.4‰ to -12.7‰ (Lugushwa deposit), and +12.4‰ to +22.6‰ (Namoya deposit). The sulphur isotopic signature of vein pyrite is -5.2‰ to +3.0‰ (Twangiza deposit), -9.1‰ to -7.4‰ (Kamituga deposit), -0.3‰ to +3.2‰ (Lugushwa deposit) and +1.3‰ to +20.4‰ (Namoya deposit). The isotopic data indicate a primary sedimentary to evaporitic source of sulphur in the host rock pyrite. Pyrite from metadiorites shows magmatic S isotope compositions.

Native gold was found in both sedimentary host rock and vein samples. This indicates that native gold was present in the primary metasedimentary sequence of the TNGB. Some vein pyrites in the TNGB have isotopic signatures that are similar to that of the host rock pyrite. These veins have formed from fluids extracted from the hosting metasedimentary sequence. Conversely, other vein pyrite shows different δ^{34}S values compared to the host rock pyrite, suggesting a fluid source that is different from the sedimentary source. Possibly, particularly in the Lugushwa deposit, an igneous source may have released sulphur and possibly gold bearing fluids in addition to those extracted from the sedimentary sequences in the TNGB. However, there is abundant evidence for sulphur and gold mobilised in the sedimentary host rocks and precipitated in the hydrothermal system of the TNGB.

Table of Contents

List of Figures

List of Tables

1. Introduction

1.1. Background

The 2600 km² large Twangiza-Namoya Gold Belt (TNGB) is situated in the South Kivu and Maniema Provinces of eastern Democratic Republic of Congo (DRC), within the southwest of the Kibara belt (Fall, 2008). The TNGB is approximately 210 km long along a northeast-southwest trend and about 60 km wide in the east west direction (Fall, 2008). The gold belt consists of four gold mineralised deposits that formed by the precipitation of gold from hydrothermal fluids in quartz-sulphide veins: Twangiza, Kamituga, Lugushwa and Namoya (Figure 1.1). The TNGB properties are owned by Banro Corporation, which owns the exploration and mining rights in the region.

The Twangiza property, in the northeastern part of the TNGB, is situated 45 kilometres south-southwest of the town of Bukavu in the South Kivu Province. The property covers 1 164 km² and consists of six exploration permits (Banro, 2017). The Kamituga property, which covers an area of 649 km², is also situated in the South Kivu Province but is located 100 km southwest of Bukavu (Banro, 2017). Banro Corporation owns three exploration permits for this area. Also situated in the South Kivu Province, the Lugushwa property covers an area of 641 km² and is located 150 km southwest of Bukavu (Banro, 2017). Banro Corporation also owns three exploration permits for this property. Finally, the Namoya property has one exploration permit that covers 174 km² and is situated in the Maniema Province, approximately 225 km southwest of Bukavu (Banro, 2017).

The TNGB, with more than 12 million ounces of gold (reserves, measured, indicated and inferred resources; Banro, 2017), has the potential to become an important gold province in central East Africa. The resources were estimated using a cut-off grade of 0.4 g/t Au for the Twangiza and Namoya deposits and 1 g/t Au for the Lugushwa and Kamituga deposits (www.BANRO.com). A total of 6.31 Moz in measured and indicated gold resource comes from Twangiza and Namoya. In addition, a combined 4.77 Moz of gold inferred is from the four deposits. Table 1.1.1 below summarizes the gold resources in the TNGB.

Table 1.1.1: BANRO Corporation's gold resources in the TNGB as of 31 December 2015 (www. BANRO.com).

Property	Measured and Indicated			Inferred		
	Tonnes (Mt)	Grade (g/t Au)	Gold (Moz)	Tonnes (Mt)	Grade (g/t Au)	Gold (Moz)
Twangiza	99.36	1.47	4.69	9.83	1.17	0.37
Kamituga	-	-	-	7.26	3.9	0.92
Lugushwa	-	-	-	65.01	1.54	3.22
Namoya	25.68	1.96	1.62	5.03	1.63	0.26
TOTAL	-	-	6.31	-	-	4.77
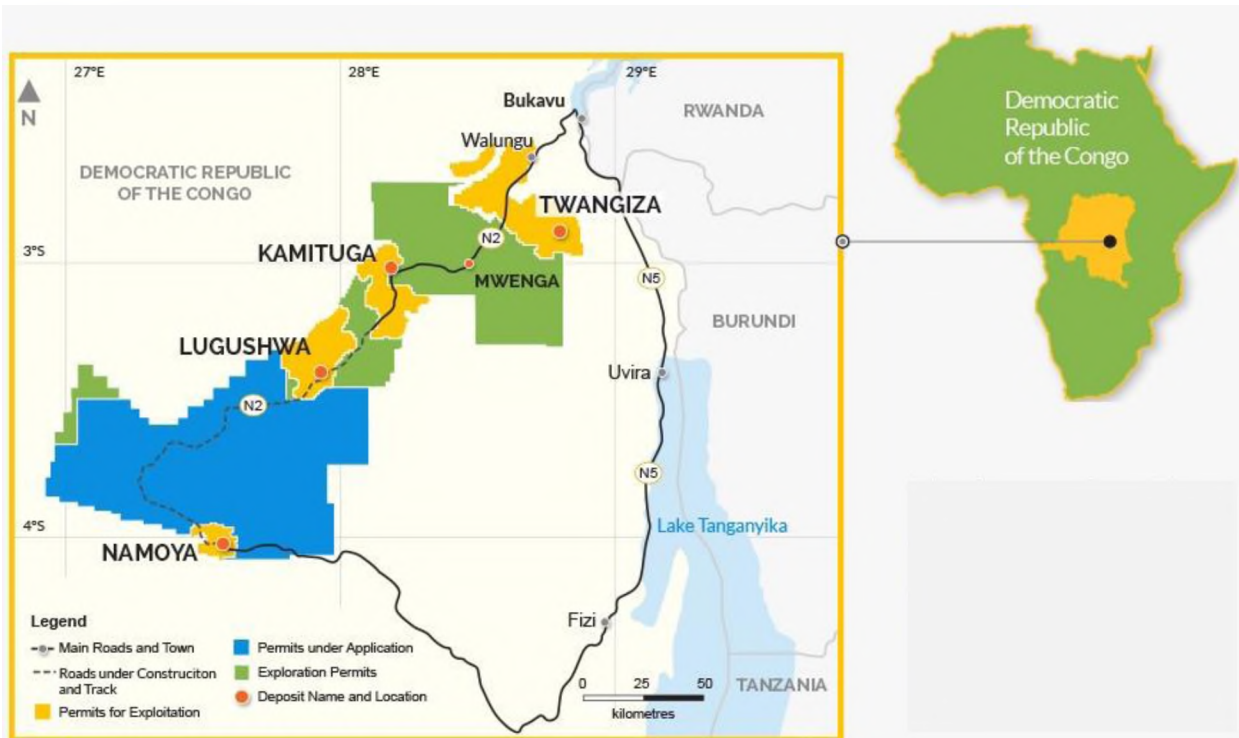
Figure 1.1: Location of the TNGB deposits in the Democratic Republic of Congo showing their positions and exploration permits (modified from www.BANRO.com).

The TNGB deposits were formed by the precipitation of gold from hydrothermal fluids in quartz-sulphide veins. In addition, gold mineralisation also occurs in quartz veins and stockworks and in wall rocks that are associated with veins (Chuwa, 2011). Fall (2008) suggested an association of the Neoproterozoic, possibly Pan African regional compressive stress regime, with the hydrothermal activity in the TNGB. In the hydrothermal system of the TNGB, gold is almost always associated with sulphide minerals (pyrite, arsenopyrite, and minor chalcopyrite and pyrrhotite: Chuwa, 2011). Accordingly, the central hypothesis, and to a large extent, a premise, for this study is that the provenance of sulphur in the hydrothermal vein system may be used as a proxy for gold provenance in the TNGB.

The provenance of hydrothermal fluids is currently investigated in two projects, one of which has been completed. Mr Wesson Reid studies fluid inclusion systematics in his MSc research. Büttner et al. (2016) have used boron isotope signatures and some preliminary results of Reid's work, in order to identify the source of boron in tourmaline bearing veins. However, their study only focused on hydrothermal fluids from the Kamituga and Lugushwa deposits. The boron and fluid sources of which fluid inclusions and tourmaline formed in hydrothermal veins is most likely the sedimentary sequence that hosts the TNGB hydrothermal system. Granitic sources of fluids and boron are unlikely for the analysed veins in Kamituga and Lugushwa (Büttner et al., 2016)

In the current study, the sulphur isotopic signature of pyrite that formed in the metasedimentary host rock sequence will be compared with the isotopic signature of pyrite from the hydrothermal veins nearby. A comparison of the isotopic signatures in veins and host rock may point to sulphur in hydrothermal vein pyrite either extracted from the hosting sequence or from other, possibly granitic sources. Since sulphides are commonly enriched where also the Au grade of the veins is higher, the results will have implications for the provenance of gold. Previous studies that have used sulphur isotope signatures to infer sulphur origin can be found in Strauss and Schieber (1989), Yan et el. (2014), and Noku et al. (2015). However, only Yan et al. (2014) uses pyrite isotopic signatures to infer the source of gold.

1.2. Aims, objectives, and principal research approach

The background of this study is to evaluate the possible primary gold provenance of the hydrothermal vein system in the TNGB by using sulphur isotopes from pyrite as a proxy. Sulphur isotopes will deliver the spectrum of possible sulphur sources in the TNGB. In addition, local and regional variations, and different sources in different parts of the TNGB might be identifiable. In correlation with assayed gold grades and the presence of native gold seen in petrographic studies, it will be possible to associate specific sulphur isotope signatures and sulphur sources with the presence or absence of gold.

Pyrite is analysed through petrography, energy dispersive spectrometry (EDS) and electron probe micro-analysis (EPMA) in order to obtain the pyrite chemistry, texture and mineral assemblages

of the rocks. Sulphur isotopes in pyrites from selected samples are analysed via secondary ion mass spectrometry (SIMS), which were executed at the Geoforschungszentrum (GFZ) at Potsdam (Germany). Pyrite is the sulphide of choice as the SIMS laboratory at the GFZ does not have standard material for other sulphides available. SIMS data will then be used to compare sulphur isotope data of pyrite in host rocks with that of hydrothermal vein pyrite. The data will then be compared with $\delta^{34}S$ data of various geologic reservoirs in order to determine the source of the sulphur in the TNGB host rocks and veins.

1.3. Structure of this study

This thesis is subdivided into 8 major chapters. Chapter 1 provides a brief introduction of the TNGB as well as the aims, objectives, and research approach of this study. Chapter 2 covers the general geology of the TNGB and its deposits. Sampling and analytical methods used in this study are explained in Chapter 3. Chapter 4 and Chapter 5 provide mesoscopic and microscopic observations, respectively. EDS and EPMA results are discussed in Chapter 6. Chapter 7 comprises a brief introduction on sulphur isotope geochemistry, and the sulphur isotope results. These results are discussed in Chapter 8. Chapter 9 presents conclusions as well as recommendations. Appendices have also been included in this study, in which analytical data are presented.

2. Geological background

2.1. The Twangiza-Namoya Gold Belt (TNGB)

The TNGB is situated within the southwest of the Kibara Belt (Fall, 2008). The Kibara Belt is an intra-continental mobile belt that formed between 1400 Ma and 900 Ma (Pohl, 1994) and stretches from Uganda through Rwanda, Burundi and eastern DRC (Figure 2.1). The Kibara Belt is separated into the Karagwe-Ankole Belt (KAB) in the eastern DRC, Rwanda, Burundi, Western Tanzania and South Western Uganda and the Kibara Belt in southwest DRC (Tack et al., 2010; Fernandez-Alonso et al., 2012). Fernandez-Alonso et al. (2012) suggested that the Kibara and Karagwe-Ankole Belts are a product of an intracontinental fold belt. However, Kokonyangi et al. (2004, 2007) and De Bruyne et al. (2015) suggest that these belts may have been a result of an ocean closure that was followed by subduction and collision. The Kivu-Maniema region, where the TNGB is located, is however excluded from the classification due to lack of evidence in the area. A further subdivision by Tack et al. (2010) separates the northeast Kibara Belt into the Western and Eastern Domain based on Rb/Sr age data. Palaeoproterozoic schists and gneisses of Ubendian-Rusizian form the oldest heritage in the region and may underlie the Mesoproterozoic in large parts of central East Africa. The Ubendian-Rusizian outcrops in antiforms and uplifted

blocks within the Kibara Belt but the precise boundaries between Palaeo- and Mesoproterozoic rocks are unclear. This particularly applies to the basement in the eastern DRC (Tack et al., 2010; Fernandez-Alonso et al., 2012) and the TNGB.

The Kibara Belt, the Irumide Belt in Zambia and the Lurio Belt in Mozambique formed in the Mesoproterozoic and cover large areas in Central and Eastern Africa (Pohl, 1994, and references therein). The Kibara Belt is bound by the Congo Craton in the west and by the Tanzania Craton in the east (Pohl, 1994). Contacts are commonly covered by post-Kibara sediments (Pohl, 1994). The Kibara Belt consists mainly of Mesoproterozoic metasedimentary rocks and minor metavolcanic supracrustal units that were intruded by S-type granitiod massifs and sub-ordinate mafic bodies of the same age (Cahen et al., 1984).

The Neoproterozoic Itombwe Supergroup unconformably overlies the Kibara Belt and consists of sedimentary units that are exposed in a large-scale synclinal structure (Cahen et al. 1984; Walemba and Master, 2005). The supergroup is divided into the Upper and Lower Kadubu Groups and are separated by a faulted tectonic contact (Walemba, 2001; Walemba and Master, 2005). The groups contain three stratigraphic levels composed of diamictite and lonestone-bearing iron rich sedimentary rocks (Walemba and Master, 2005). The deposition of the Itombwe Supergroup was followed by the Pan-African orogeny resulting in folding and low-grade metamorphism affecting the supergroup and its older basement (Walemba and Master, 2005).

Pohl (1994) identified three deformational events that affected the northeast part of the Kibara Belt; the first event, D1, is characterised by intense ductile deformation and relatively high-grade metamorphism. The D2 event is characterised by folding, which is accompanied by the formation of axial planar cleavage across the belt. The last event, D3, is characterised by extensional tectonics and rifting with subsequent E-W compression tectonics.

The TNGB succession within the Kibara Belt consists of rocks probably ranging from Palaeoproterozoic to Neoproterozoic ages (Chuwa, 2011 and references therein). The Twangiza deposit lies in the N-S to NNW-SSE trending Neoproterozoic terrain, Kamituga and Lugushwa lie in the NE-SW trending Mesoproterozoic terrain, and Namoya is situated in the NW-SE trending Palaeoproterozoic terrain (Chuwa, 2011), based on large-scale geological maps. However, the entire TNGB lies in poorly exposed regions with thick weathering profiles, is poorly mapped, and in large regions covered by tropical rain forests. Decades of civil unrest in the eastern DRC have posed an additional obstacle to geological research. Hence there has been neither any solid ground check of the inferred geological boundaries, usually proposed based on remote sensing, or sufficient smaller-scale field mapping and reliable analysis of protolith ages. Accordingly, any time estimates of protolith ages of the metasedimentary rocks in the TNGB are hardly supported by hard geochronological evidence.
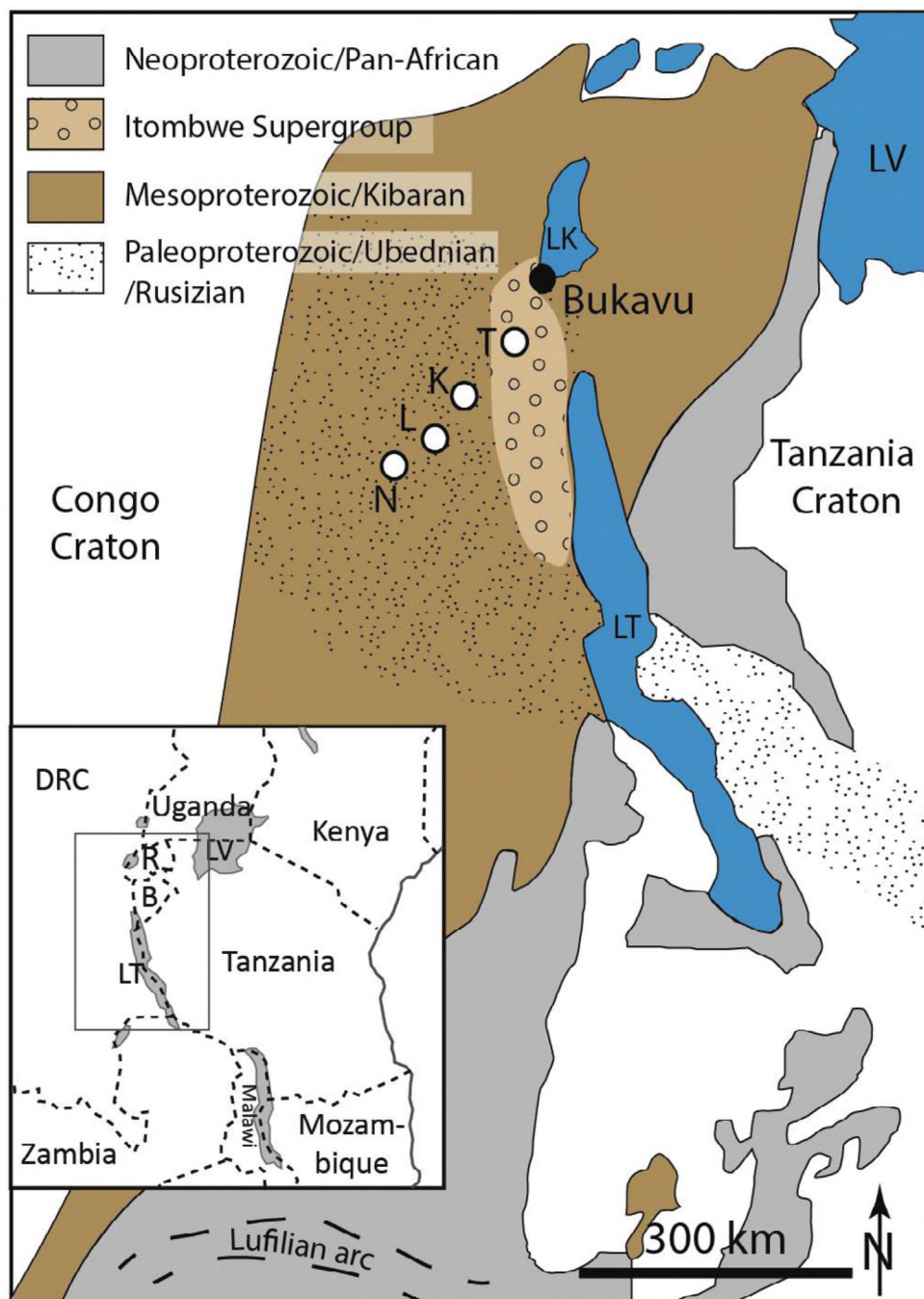
Figure 2.1: Geological map of the TNGB depicting the location of the Banro concessions. T = Twangiza; K = Kamituga; L = Lugushwa; N = Namoya; LK = Lake Kivu; LT = Lake Tanganyika; LV = Lake Victoria; R = Rwanda; B = Burundi (modified after Brinckmann et al., 2001; Walemba and Master, 2005; Tack et al., 2010).

2.2. Twangiza deposit

The eastern terrain of the Twangiza deposit is situated in the north-south trending, Neoproterozoic Itombwe Synclinorium (Cahen et al., 1984; Walemba and Master, 2005). The Itombwe Supergoup,is contained within the synclinorium and unconformably overlies the Kibara Belt (Walemba, 2001). The Itombwe Supergroup has been subdivided into the Lower and Upper Kadubu Groups which are separated by a faulted contact (Walemba, 2001; Walemba and Master, 2005). The Lower Kadubu Group unconformably overlies the Kibara Belt and consists of the Kigogo Formation at the basement as well as the Kalama and Madubwe Formations (Walemba, 2001)). The > 3500m thick Upper Kadubu Group consists of the Nya-Kasiba and Tsibangu Formations where arkosic sandtone outcrops have been found near Twangiza (Walemba, 2001; Walemba and Master, 2005).

The synclinorium extends for approximately 150 km southwards of Twangiza and comprises a sequence of sediments that are marked by upper diamictites and intruded by alkaline intrusive rocks of Pan-African age (Cahen et al., 1984; Walemba and Master, 2005). The rocks in the Twangiza deposit are very weakly metamorphosed and show well-preserved sedimentary features. Macroscopic evidence of metamorphism is absent (Chuwa, 2011). This regional setting sets apart the Twangiza deposits from the other deposits in the TNGB in terms of age of the host rocks, deformation history and preservation.

A study by Rusill et al. (2009) identified three litho-structural terrains from aeromagnetic and radiometric data: A N-S to NNW-SSE trending eastern terrain, A NW-SE trending terrain in the southwest, and a NE-SW trending terrain (Figure 2.2). The N-S to NNW-SSE trending terrain forms part of the Neoproterozoic Itombwe Synclinorium (Cahen et al., 1984, Walemba and Master, 2005). The NW-SE trending terrain is Palaeoproterozoic of age and extends to the west of the Twangiza deposit (Chuwa, 2011). Lastly, the NE-SW trending terrain is Mesoproterozoic in age and forms part of the Kibaran structural grain (Chuwa, 2011). The Twangiza deposit is situated along the interpreted terrain boundary between the NW-SE terrain and the N-S terrain (Walemba and Master, 2005).

In his study, Naas (1998) used surface mapping and geophysical data interpretations to identify the Twangiza anticline, the Gakero syncline and the Mwana anticline near the Twangiza deposit. The Twangiza anticline has a fractured hinge zone which is characterised by axial planar cleavage, radial fractures and micro-shears. Chuwa (2011) believes that these features were instrumental in the concentration and deposition of hydrothermal fluids. The Twangiza deposit is hosted by a doubly plunging anticline which appears to be underlain by an oval shaped deep seated intrusion which is magnetically low (Rusill et al., 2009).

The Twangiza deposit itself is hosted by a sequence of fine-grained clastic sediments that are folded and weakly metamorphosed (Bawah et al., 2008). The clastic sediments are intruded by sills that are 2 – 50 m thick. The sills are separated into feldspar porphyry and mafic porphyry

(Fall, 2008). Their age is unknown but most likely belong to the "G4" granitic phase that took place in the earliest Neoproterozoic (~980 - 1000 Ma; Brinckmann et al., 1994, Tack et al., 2010; Pohl et al., 2013; Melcher et al., 2015). If that was a correct time estimate it also would constrain the minimum depositional age for the hosting sedimentary rocks. These depositional ages are not quite clear but Walemba and Master (2005) deem 1020 ± 50 Ma a possible time when the deposition of Itombwe sediments may have begun. Fernandez-Alonso et al. (2012) however estimate ~710 Ma as the maximum depositional age which would be in conflict with a G4 association of the granitiod rocks at Twangiza. Or, alternatively, if the granitoids were G4, the hosting sediments would be of Mesoproterozoic/Kibaran age and not part of the Itombwe Supergroup.

The sedimentary sequence from bottom up is as follows: black shales, mudstones, siltstones and sandstones, intra-formational conglomerates and conglomerate cover (Naas, 1998). The shale-mudstone-siltstone sequence measures up to 1000 m thick. Intra-formational conglomerates are between 80 – 175 m thick. The conglomerate cover, identified to be Neoproterozoic diamictites, measures from 600 – 1000 m thick (Walemba and Master, 2005).

The Twangiza deposit is mainly hosted by a sedimentary sequence that was intruded by sills which were later affected by alteration within the main deposit (Bawah et al., 2008). The intrusive sills are mafic porphyry and feldspar porphyry (Fall, 2008). Mudstones with high carbonaceous material are the dominant lithology in Twangiza (Chuwa, 2011). These mudstones have a dark grey colour and contain high contents of argillaceous material (Naas, 1998; Bawah et al., 2008). Chuwa (2011) described the mudstones to range from thin interbeds to uniform beds that are up to 80 m thick with subordinate siltstone units commonly interbedded within the mudstone.

Siltstones are light to medium grey in colour and have a slightly coarser texture and more siliceous content than the mudstone (Bawah et al., 2008). The siltstone display an upward fining sequence made up of a sandy basal section to an increasingly clay rich upper section (Chuwa, 2011). Sulphides are usually contained in medium grey to light greywackes and range from 2 – 5 vol% (Naas, 1998). The conglomerate cover is made up of sub-angular to angular clasts of granite, mudstone and siltstone supported by a matrix of dark grey silty mud (Naas, 1998; Bawah et al., 2008).

Sulphides in the main Twangiza orebody occur in veins and as disseminations in the host rocks. Pyrite and arsenopyrite are the main sulphides found in Twangiza. A 12 – 45 m wide porphyry sill is associated with mineralisation in the Twangiza North orebody (Chuwa, 2011). The sill is located on the western limb of the Twangiza anticline. Mineralisation occurs in sediments towards the south of Twangiza (Chuwa, 2011). Bawah et al., (2008) attributed gold mineralisation in Twangiza to an entirely hydrothermal origin and say that there is a generally positive correlation between gold grade and sulphide content.

Furthermore, evidence of hydrothermal activity in the Twangiza deposit related to deep seated alkalic or carbonatitic intrusion was described by Walemba (2001). He suggested mean $^{39}Ar/^{40}Ar$ ages of 529 ± 5 Ma and 436 ± 8 Ma and Rb/Sr ages of 703 ± 14 Ma for granites that formed as a result of magmatism in the Neoproterozoic.
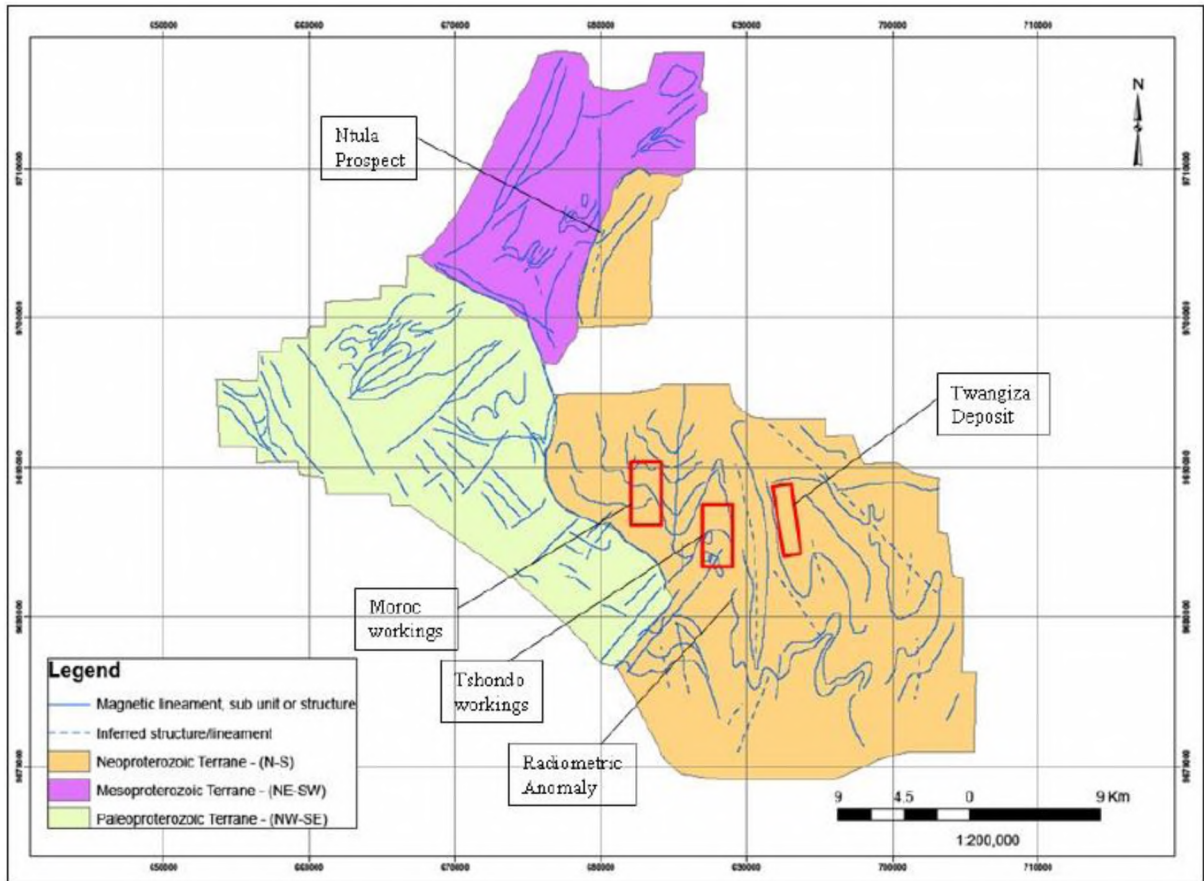
Figure 2.2: Interpreted structures from aeromagnetic map of Twangiza. The Twangiza deposit and other key prospects and workings are indicated (Chuwa, 2011).

2.3. Kamituga deposit

A study by Rusill et al. (2009) inferred two litho-structural terrains in the Kamituga property from aeromagnetic and magnetic data: a NNE-SSW terrain in the southwest and an E-W to NW-SE terrain in the north. The NNE-SSW terrain extends from the Lugushwa property while the E-W to NW-SE terrain occurs in the northern part of the Kamituga property. A domal feature, surrounded by prominent E-W lineaments, occurs in the E-W to NW-SE terrain (Rusill et al., 2009). Chuwa (2011) identified NE-SW trending regional fold structures that are common in the southern part of Kamituga.

Unlike the Twangiza deposit, the Kamituga deposit is generally weakly metamorphosed to lower greenschist facies and the rocks show distinct metamorphic textures (Chuwa, 2011). The weakly metamorphosed rocks in the Kamituga deposit show the development of foliation and schistosity. These rocks are very similar to those in the Lugushwa deposit (Chuwa, 2011). O'Donovan et al. (2005) attributed the local development of actinolite-hornblende-staurolite-garnet (grossular)-biotite-muscovite in Kamituga to amphibolite facies contact metamorphism associated with felsic and mafic intrusive bodies.

The Mobale underground mine which commenced operations in 1937, is the main gold deposit in Kamituga (O'Donovan et al., 2005). Mining mainly occurs in the Mobale orebody. O'Donovan et al. (1999) described eight old mining areas in the Kamituga deposit, namely: the Tshanda deposit, Kahushimira, G15, G22 Grande Mobale, Kalingi, Flat Mero and G1 Kamisumbi.

Primary gold mineralisation in the main Mobale orebody is hosted in quartz veins and schists, which are the main lithological units (O'Donovan et al., 2005). Quartz veins and stockwork systems are sources for high grade gold (Chuwa, 2011). O'Donovan et al. (2005) identified schists, quartzite, quartz phyllite, amphibolite, pegmatite and tourmalinite as the main lithological units in the Mobale orebody (Figure 2.3). The schists are characterised by mica schist and siliceous schist. The mica schist have a beige to dark grey colour and comprise mainly of biotite with accessory muscovite and staurolite (Chuwa, 2011). The siliceous schist is associated with intense quartz veining and contain more quartz than the mica schist.

Chuwa (2011) describe quartz phyllite as a finely laminated to sub-massive unit that is characterised by regular banding of iron oxides, fine quartz, sericite and occasional kaolin and graphite. Amphibolite is massive to schistose and, due to low aluminium content in amphiboles, is inferred to be of an igneous origin (Chuwa, 2011). The amphibolite is made up of hornblende, actinolite, quartz, biotite and muscovite with accessory plagioclase, sphene, ilmenite and base metal sulphides such as pyrite, pyrrhotite, marcasite, chalcopyrite and arsenopyrite (Chuwa, 2011).

Pegmatites, ranging in thickness from a few centimetres to several metres, are mainly composed of quartz, feldspar and muscovite with minor additional microcline and/or orthoclase. Accessory minerals include tourmaline, spessartine, apatite, sulphides and occasionally gold (Chuwa, 2011).

Tourmaline is closely associated with pegmatites within the wall rock and are composed of acicular tourmaline and quartz. Biotite, orthoclase and sulphides (arsenopyrite) occur as secondary minerals (Chuwa, 2011). One tourmaline bearing pegmatite has been dated as 981±15 Ma, which falls into the regional G4 pegmatite/granite emplacement phase (Büttner et al., 2016).

O'Donovan et al. (2005) associated mineralisation at the Mobale orebody with high grade quartz veins. Substantial wall rock mineralisation is attributed to the quartz veins. The veins are associated with sulphides such as pyrite, arsenopyrite, pyrrhotite, galena, stibnite and minor sphalerite (Chuwa, 2011). Furthermore, arsenopyrite is associated with mineralisation in schists along with micro-veinlets of quartz (O'Donovan et al., 2005).
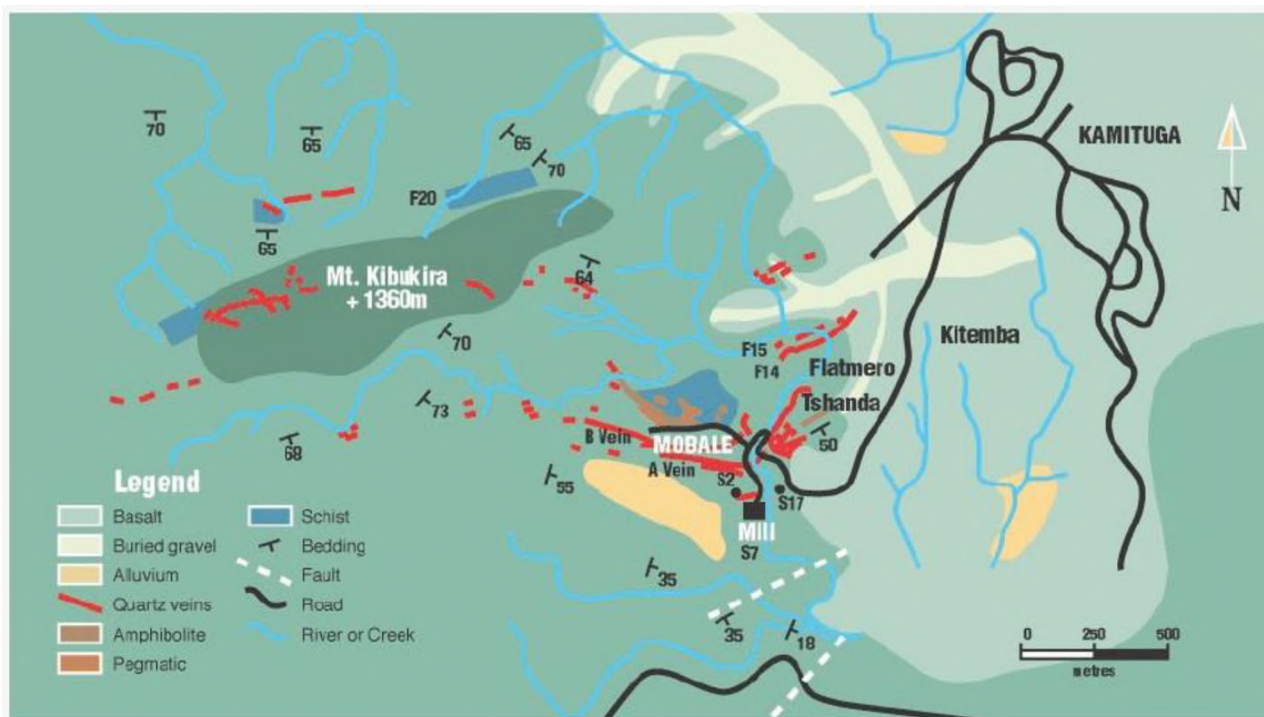
Figure 2.3: Geology plan map of the Kamituga deposit. Note the location of Mobale. Surrounding prospects are also indicated (source: www.BANRO.com/operations/kamituga-project).

2.4. Lugushwa deposit

The Lugushwa deposit, situated approximately 50 km south of Kamituga, is hosted in a northeast-plunging, 200-300 m wide anticlinal structure (Fall and Chuwa, 2007; Chuwa, 2011). The regional geology is dominated by a NE-SW litho-structural terrain which is crosscut by an ENE-WSW structure (Chuwa, 2011). Rocks in the north-western part of Lugushwa appear to be folded with dominant northeast axial trends (Chuwa, 2011).

The host rocks in the Lugushwa deposit are generally weakly metamorphosed up to lower greenschist facies, although the metamorphic grade is slightly lower than that in Kamituga (Chuwa, 2011). The weakly metamorphosed rocks in the Lugushwa deposit show a weak to moderate foliation, with the development of a schistose texture being rare (O'Donovan et al., 2005; Skead, 2007). Fall and Chuwa (2007) described two orebodies in the Lugushwa deposit; the D18-19 orebody and the G20-21 orebody. These orebodies are separated by an E-W trending shear/fault zone. The D18-19 orebody occurs in the hanging wall, whereas the G20-21 orebody occurs in the footwall of the fault (O'Donovan et al., 2005). The Mapale G7, Simali, and 'Filon de Luxe,' are also listed as deposits within the Lugushwa property (www.BANRO.com; Figure 2.4).

Fall and Chuwa (2007) identified metasedimentary rocks, quartzite, and metadiorites as the main lithological units in the Lugushwa deposit. The metasedimentary rocks are metasiltstone, graphitic metapelite and metapelites which are further distinguished into; porphyroblastic metapelite, interbedded metapelite and calcareous metapelite (Chuwa, 2011). Fresh metapelite is fine-grained, even-textured and medium to dark grey in colour (Fall and Chuwa, 2007). The metapelites are intercalated with metasiltstone and quartzite units up to 10 m thick (Chuwa, 2011). Metasiltstones are relatively more quartz-rich than metapelites with up to 55% quartz and up to 45% sericite/muscovite. Graphitic metapelite is dark grey in colour and contains carbonaceous material some of which has been changed to graphite during metamorphism (Chuwa, 2011). Graphitic metapelite is composed of amorphous carbon and graphite, sericite, tourmaline and quartz (Fall, 2006b).

Quartzite has a pale brownish-grey colour and is mainly composed of 85% quartz, 1-5% feldspar and less than 10% muscovite/sericite (Fall, 2006b). The quartzite is mainly massive, has no bedding or foliation, and is commonly interbedded with metapelites. (Chuwa, 2011). Metadiorite is fine-grained and dark grey in colour and comprises hornblende, biotite, chlorite, quartz and feldspar (Fall, 2006b). Chuwa (2011) described the metadiorite to occur as narrow, undulating sills within metasediments.

Sulphides occur in both metadiorite and metasediments with arsenopyrite being the most abundant sulphide. Pyrite, pyrrhotite, with minor chalcopyrite and sphalerite also occur in Lugushwa (Fall, 2007b). Chuwa (2011) associated gold mineralisation in the Lugushwa deposit with interbedded metapelite and metasiltstone lithologies. Mineralisation is most concentrated where the

interbedded metapelite and metasiltstone occur in hinges of plunging folds (Fall and Chuwa, 2007).
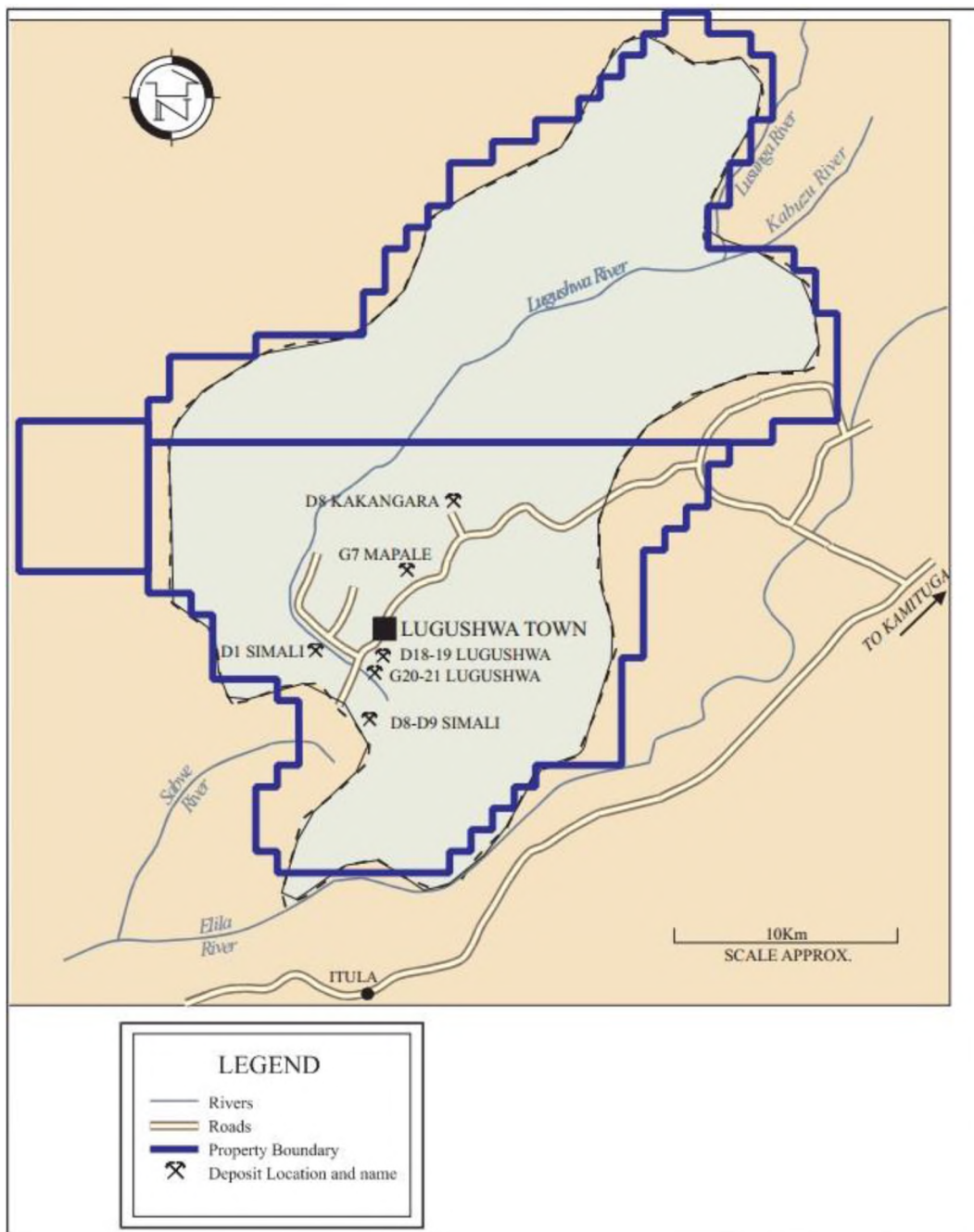
Figure 2.4: Plan of Lugushwa concessions showing ore deposits in the Lugushwa area (O'Donovan et al., 2005).

2.5. Namoya deposit

The Namoya deposit, situated approximately 210 km southwest of Twangiza, is hosted in a NW-SE trending Palaeoproterozoic terrain with Karoo aged sedimentary rocks in the southern part of Namoya (Fall, 2007c). A study by Rusill et al. (2009) inferred a NW-SE structural trend, with an oval-shaped feature in the centre, from aeromagnetic and magnetic data in the north-eastern part of the Namoya property.

The host rocks in the Namoya deposit were metamorphosed into lower to mid greenschist facies (Chuwa, 2011). The rocks depict a well-developed foliation compared to the other deposits in the TNGB and have a developed schistosed fabric (Fall, 2007c). O'Donovan et al. (2005) described four orebodies in the Namoya deposit; Namoya Summit in the south-east, Kakula in the middle, Mwendamboko in the northwestern end and Muviringu near Mwendamboko (Figure 2.5). Mwendamboko is the largest of all these orebodies with a strike length of about 600 m NW-SE (Mbuya et al. 2008). These orebodies are aligned along a NW-SE trending shear zone (O'Donovan et al., 2005). An additional orebody, the Filon B, was mined out in 1955 and is located to the southwest of the Namoya Summit orebody (O'Donovan et al., 2005).

Fall (2008) identified metasedimentary and intrusive rocks as the main lithological units in the Namoya deposit. The metasedimentary rocks are; sericite schist, silicified schist and graphitic schist. Sericite schist is fine-grained and is distinguished into greenish sericite schist and sericite schist based on the presence of chlorite and carbonate in the matrix (Fall, 2007c; Mbuya et al. 2008). Graphitic schist is dark grey in colour and is rich in graphite. It is highly schistosed and probably originates from a carbonaceous mudstone or pelitic protolith (Fall, 2007c; Mbuya et al. 2008). Silicified schist is interpreted to have originated from a shaly siltstone protolith and appear to be a product of hydrothermal alteration (Fall, 2007c; Mbuya et al. 2008).

Quartz porphyry and dolerite are the two main types of igneous rocks in Namoya (Fall, 2007c). Quartz porphyry is fine-grained and is composed of anhedral quartz, opaque leucoxene in a fine-grained groundmass of sericite and calcite (Chuwa, 2011). Dolerite is coarse-grained and is composed of plagioclase, chlorite, calcite, quartz, talc, amphibole, epidote, and leucoxene (Chuwa, 2011). Dolerite varies from being a massive equigranular rock to being a highly foliated rock where the primary texture is not preserved (Chuwa, 2011).

Sulphides rarely exceed 5% by volume in host rocks and are mostly associated with quartz veins (Chuwa, 2011). Arsenopyrite and pyrite are the main sulphide phases in the Namoya deposit (Chuwa, 2011). Minor pyrrhotite also occurs in Namoya. Fall (2007c) associated gold mineralisation in the Namoya deposit with quartz veining that occurs as either irregular stockwork veins, foliation parallel veins or irregular cross-cutting vein sets. Gold is generally associated with arsenic, tin, barium, lead and copper (Fall, 2007c). Furthermore, the Namoya deposit forms prominent hills and is thought to be relatively preserved from erosion due to the abundance of quartz in the mineralised zones (Fall, 2007c). Quartz rich sectors within the mineralised zones

contain brittle fractures which display deeper levels of oxidation due to the percolation of ground water (Fall, 2007c).

Chuwa (2011) described arsenopyrite and pyrite as irregular intergrowths, or as scattered anhedral to subhedral crystals which rarely exceed 1% vol. total sulphides. Furthermore, he observed distinct textural variations in arsenopyrite, pyrite and minor pyrrhotite, which either occurred as: euhedral crystals of arsenopyrite and pyrite, disseminated medium- to fine-grained pyrite and arsenopyrite, or as massively remobilized blebs of sulphide phases made up of pyrite, arsenopyrite and minor pyrrhotite.
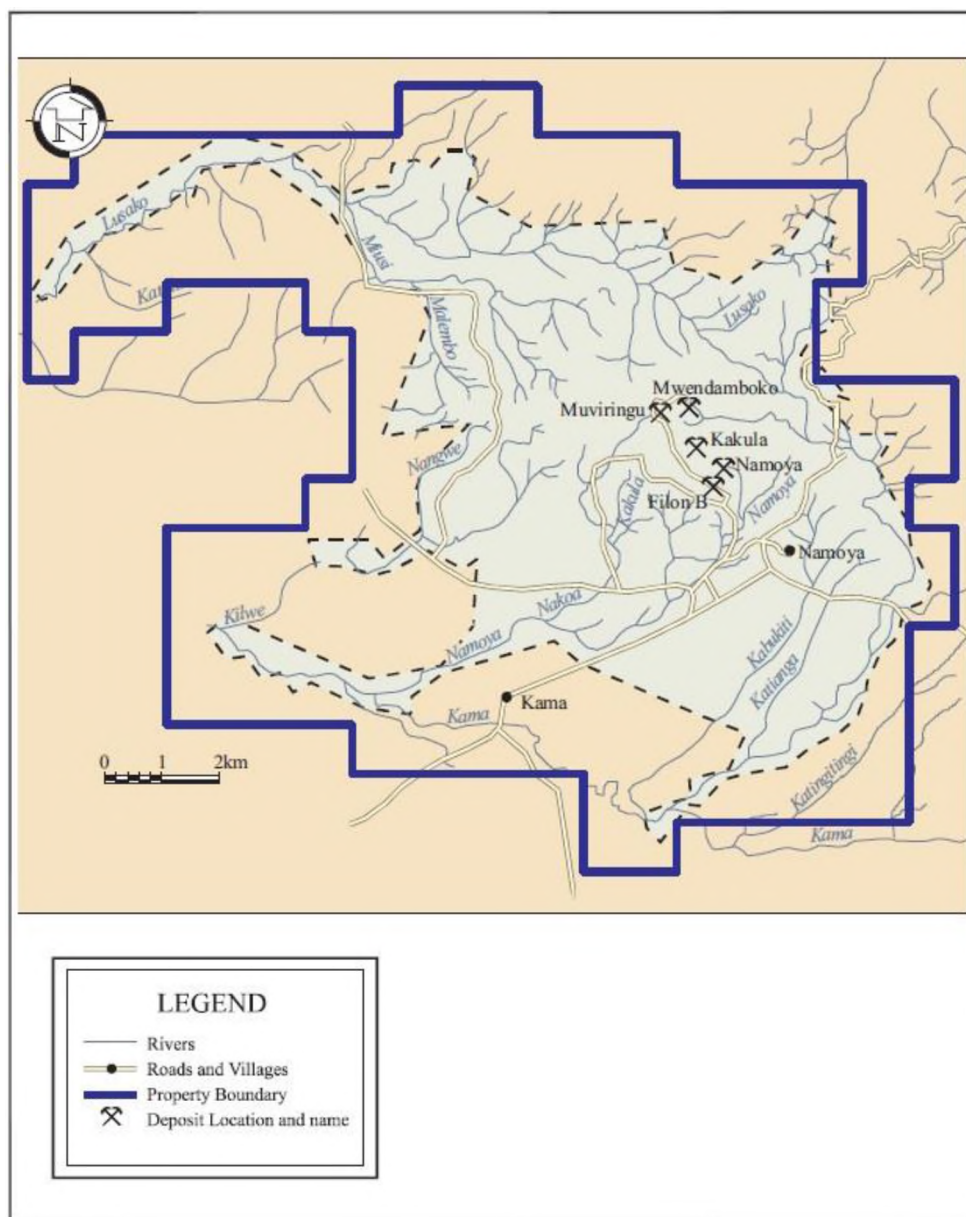
Figure 2.5: Plan of Namoya concessions showing ore deposits in the Namoya area (O'Donovan et al., 2005).

3. Sampling and Methodology

3.1. Sampling

Fieldwork as well as the sampling of drill cores in the Twangiza Namoya Gold Belt (TNGB) was kindly performed by Mr Wesson Reid for his MSc research. A total of 7 samples and 1 polished thin section were taken from Mr Reid`s samples. Mr Gerald Chuwa of Banro Corporation provided an additional 21 samples. The samples were collected from different boreholes at various stratigraphic heights in the four TNGB deposits, namely; Twangiza, Kamituga, Lugushwa and Namoya. Table 3.3.1 gives details of samples collected from the four deposit areas including textural pyrite varieties, gold grade, borehole codes and sample depths. Furthermore, details of the type of host rock and whether the sample is a host rock or vein, and the numbers of the samples are listed.

Only samples that contain sulphides were selected for petrographic and mineral chemical analysis. Furthermore, the samples were selected in order to best represent sulphide occurrence in the host rock and hydrothermal veins. This allows for the comparison of the sulphur isotopic signatures of the host rock and vein pyrites, which in turn allows to discuss the host rocks as potential source of sulphur and possibly gold in the hydrothermal vein system. In total, 39 samples were collected for this study.

3.2. Pyrite classification and nomenclature

Pyrite investigated in this thesis can be associated with four genetic types:

1) Samples from the host rock that contain authigenic or metamorphic pyrite that has grown at the place where it is found, from the sulphur of the hosting metasedimentary rock. The symbol used for such pyrite and the sample that contains such pyrite is HR. HR pyrite does not show any spatial association with hydrothermal veins nearby, such as dissemination halos along veins, or any other phases that suggest precipitation from fluid phases. Typically such pyrite is randomly distributed and may show inclusions of matrix phases. The isotopic signature of such pyrite should reflect the local sulphur source.

2) Pyrite that is found in host rocks (usually metapelitic rocks) but shows some association with hydrothermal activity, such as rims or lenses with quartz or carbonate that are coarser-grained than these phases in the host rock matrix. Pyrite in such textural positions is usually coarse-grained and may be present as clusters of several grains. These domains are interpreted as local hydrothermal segregations. They do not show any connection to a vein network. Accordingly, the pyrite is interpreted to have grown from sulphur from the host rock in which the segregated lens is found. AM HR ("auto-metasomatic growth in the host rock") is used for such pyrite. Isotopically AM HR pyrite should reflect the local sulphur source.

3) Pyrite disseminated from hydrothermal veins into the host rock (VD HR) is found in the host rock nearby hydrothermal veins, within a dissemination halo. Here the spatial relationship between presence of pyrite and the proximity of a hydrothermal vein is evident. Usually, the vein shows hydrothermal pyrite, often with clusters along the vein boundary. Some pyrite crystals may protrude from the host rock into the vein. Within usually a few centimetres, or in places up to a decimetre away from the vein boundary, pyrite becomes less abundant or is absent. Primary pyrite that may have been present in the host rock prior to hydrothermal fluid influx (i.e. HR or AM HR pyrite), is texturally distinct, shows different distribution patterns, and/or grain sizes and shapes. VD HR pyrite should mainly reflect the S-isotopic signature of the hydrothermal fluid from which the vein formed.

4) Pyrite that has grown in hydrothermal veins (V) is located within the veins and texturally part of the vein assemblage. Usually such pyrite is coarse-grained and euhedral. The fluid, and the sulphur dissolved therein, from which V or VD HR pyrite has grown, may have been sourced locally or may derive from unrelated distal sources. Also a mix of local and distal fluids may have been possible, resulting in variable or mixed S-isotopic signatures in pyrite.

3.3. Sample Preparation

Sample selection and macroscopic and mesoscopic descriptions were executed visually and using a hand lens. This level of observation allowed the identification of main sample types (host rock, hydrothermal vein) in which pyrite may occur, and whether or not pyrite may be present. More detailed identification of the often fine-grained assemblages was done microscopically (see Chapter 5). Forty polished thin sections were prepared for mineral identification, petrography, and major and trace elemental analysis (microscopy, EDS and EPMA). Twenty seven samples were then selected for sulphur isotope analyses (SIMS) using EDS and EPMA data and were prepared into 25 mm round polished blocks. On each block, material from two or three samples was fitted in order to reduce time loss related to sample change and standard analysis during SIMS analysis. Sulphides on the blocks were analysed using EDS in order to verify pyrite identity and to obtain backscattered images which aided in the location of pyrite during SIMS analyses.

Table 3.3.1: Samples taken from the TNGB for thin section preparation and EDS and EPMA analyses. The borehole code, sampling depth, gold grade, pyrite genetic type, host rock type and deposit area are also given. Abbreviations are as follows: HR= host rock pyrite; AM HR = pyrite from auto-metasomatic growth in host rock; VD HR = pyrite disseminated from hydrothermal veins into the host rock; V = hydrothermal vein pyrite; B.C.: below cut-off of assaying (<0.2 g/t); N.A.: not analysed.

Sample name	Borehole code	Sampling depth	Au grade (g/t) and association	Pyrite genetic type	Host rock type	Deposit area
TW-FS-03	TDD040	161.00m	9.85	HR	Mudstone	Twangiza
TW-FS-05	TDD300	190.17m	7.12	HR	Mudstone	Twangiza
TW-FS-06	TDD023	142.20 – 142.30m	0.7	No pyrite	Metapelite	Twangiza
TW-FS-07	TDD023	189.20 – 189.29m	0.57	HR, AM HR and V	Carbonaceous mudstone	Twangiza
T3	TDD023	123m	9.19	V	Carbonaceous mudstone	Twangiza
T9	TDD023	176.7m	<0.1	VD HR and V	Carbonaceous mudstone	Twangiza
T12	TDD023	206.3m	<0.1	V	Carbonaceous mudstone	Twangiza
T25	TDD040	152m	63.6	V	Carbonaceous mudstone	Twangiza
T27	TDD300	182m	2.99	V	Carbonaceous mudstone	Twangiza
KG-FS-1	KDD015	46.40m	0.1	HR	Metapelite	Kamituga
KG-FS-2	KDD001	82.50m	0.13	HR	Metapelite (schist)	Kamituga
KG-SIS-1	KDD01	116.65 – 116.75m	3.13	No pyrite	Metapelite	Kamituga
KG-SIS-2	KDD09	141.30 – 141.40m	0.41	V and VD HR	Metapelite	Kamituga
KG-SIS-3	KDD09	142.25 – 142.35m	<0.1	HR and V	Metapelite	Kamituga
KG-SIS-4	KDD014	96.40 – 96.50m	0.04	No pyrite	Metapelite	Kamituga
KG-SIS-5	KDD038	109.20 – 109.30m	1.9	HR	Metadiorite	Kamituga
KG-SIS-6	KDD038	148.50 – 148.60m	0.2	HR	Metadiorite	Kamituga
KG-SIS-7	KDD041	85.05 – 85.10m	0.07	HR, VD HR and V	Metapelite	Kamituga
K17	KDD015	51.8m	1.23	No pyrite	Dark metapelite	Kamituga
LG-FS-1	LDD162	88.10m	<0.01	No pyrite	Metapelite	Lugushwa
LG-FS-4	LDD088	126.10m	0.03	No pyrite	Metapelite	Lugushwa
LG-SI-01	LDD063	182.65 – 182.70m	0.95	No pyrite	Metapelite	Lugushwa

Table 3.3.1: (continued)

Sample name	Borehole code	Sampling depth	Au grade (g/t) and association	Pyrite genetic type	Host rock type	Deposit area
LG-SI-02	LDD063	334.25 – 334.30m	<0.1	HR and AM HR	Metapelite	Lugushwa
LG-SI-03	LDD057	197.98 – 198.03m	0.78	No pyrite	Metapelite	Lugushwa
LG-SI-04	LDD057	350.15 – 350.20m	<0.1	No pyrite	Metapelite	Lugushwa
LG-SI-05	LDD083	123.55 – 123.60m	0.63	V and VD HR	Metapelite	Lugushwa
LG-SI-06	LDD073	200.64 – 200.70m	<0.1	AM HR	Metapelite	Lugushwa
L4	LDD162	84.5m	<0.01	No pyrite	Metapelite	Lugushwa
L4 (Wes)	LDD162	84.5m	<0.01	No pyrite	Metapelite	Lugushwa
NM-FS-1	NDD180	97.62-97.70m	<0.01	HR	Schist	Namoya
NM-FS-2	NDD180	97.98m	<0.01	HR	Schist	Namoya
NM-SI-1	Grab sample	Seketi pit	From mineral. zone	HR, VD HR and V	Altered dolerite	Namoya
NM-SI-2	Grab sample	Seketi pit	N.A., but from mineral. zone	HR and V	Sheared dolerite	Namoya
NM-SI-3	NDD077 (Seketi pit)	36.30 – 37.03m	1.32	HR, VD HR and V	Dolerite	Namoya
NM-SI-4	NDD018	144.05 – 144.15m	0.01	HR	Schist	Namoya
NM-SI-5	NDD018	145.00 – 145.10m	173	HR and V	Schist	Namoya
NM-SI-6	NDD018	142.00 – 142.10m	0.01	HR	Schist	Namoya
NM-SI-7	NDD223	146.70 – 146.80m	0.44	VD HR	Schist	Namoya
NM-SI-8	NDD223	144.24 – 144.40m	0.09	HR	Schist	Namoya

3.4. Analytical Methods

3.4.1. Microscopic petrography

Forty polished thin sections were examined for textural features, mineral identification, and sulphide identification. An Olympus BX60 microscope was used to examine the thin sections under both transmitted and reflected light and photomicrographs were captured using a PAXcam digital camera attached to the microscope.

3.4.2. Energy dispersive spectrometry (EDS)

Energy Dispersive Spectrometry (EDS) studies were conducted at the Rhodes Electron Microscope Unit. An Oxford Instruments INCAEnergy 350 microanalysis system Si-Li detector attached to a TESCAN Vega TS 5136LM SEM was used for spot analyses performed at 20 kV. Each spot analysis was analysed with a time constant of 30 seconds per spot. A cobalt standard was used for peak calibration. The analyses were used to identify mineral phases, particularly pyrite, and to establish the mineral assemblage of the thin sections.

3.4.3. Electron probe micro-analysis (EPMA)

Forty thin sections were analysed for pyrite mineral chemistry and composition in order to determine if the pyrite grains had uniform composition and/or trace elements in its matrix. Pyrite chemistry was acquired using a JEOL JXA 8230 Superprobe at the EPMA laboratory in the Geology Department, Rhodes University. The Superprobe is equipped with four wavelength (WD) spectrometers used to measure major and trace elements as well as produce elemental maps. Major element analysis included S, Fe, Co, Ni, Cu, Zn, As, and Au. Analytical conditions were: 15 kV acceleration voltage; 20 nA probe current; beam size of ~1 μm; and count times of 10 s (peak) and 5 s (upper and lower backgrounds). Co, As, Ni, Ag, Te, Cu, Au, and Bi were analysed as trace elements in separate sessions with instrument calibration designed for trace elemental analysis. Accordingly, there are two data sets for Co, Ni, Cu and Zn, which have been measured as in the major and the trace element EPMA sessions. For trace element analysis, the accelerating voltage employed was 25 kV and 150 nA for the probe current. Counting times were 100 seconds (peak) and 50 seconds (upper and lower backgrounds) with the exception of S and Fe which had lower counting times of 5 seconds (peak) and 2.5 seconds (upper and lower backgrounds) Large crystals (PETL, TAPL, LIFL) were used to analyse Ni, Ag, Te, Cu, Au and Bi. The standards used for quantification of pyrites, characteristic X-rays measured, spectrometer crystals, overlap corrections and detection limits (DL) are detailed in Appendix 1. ZAF correction was used for quantification of major and trace elements. Wavelength dispersive (WDS) elemental maps were acquired using stage scan mode with 15 kV acceleration voltage, 150 nA probe current, ~<1 μm probe diameter and 10 seconds dwell time. The maps were produced for the following elements:

Si, Fe, Ca, P, S, Co, Ni, Cu, Zn, As, Ag, Au. Large crystals were used to analyse Ca (PETL), P (PETL), Ni (LIFL) and Cu (TAPL).

3.4.4. Secondary ion mass spectrometry (SIMS)

This paragraph has been kindly provided by the SIMS laboratory manager Dr Michael Wiedenbeck from the GFZ in Potsdam, Germany. A CAMECA 1280 HR SIMS instrument has been used to determine the $\delta^{34}S$ values on pyrite from the host rocks and from hydrothermal veins. Twenty seven samples were prepared in ten 25 mm diameter epoxy mounts. Two to three samples were fitted on each block in order to maximise lab time. An additional mount containing both the Balmat and Isua 248474 pyrite $\delta^{34}S$ reference materials was used for calibration; these two materials have $\delta^{34}S_{CDT}$ values of 15.1‰ (Crowe and Vaughan, 1996) and 1.99‰ (Whitehouse, 2013), respectively.

The samples were cleaned in high-purity ethanol using an ultrasonic bath prior to being argon sputter coated with a 35 nm thick, high-purity gold coating needed to assure ion conductivity. The actual SIMS analyses employed a $^{133}Cs^+$ ion beam with a total impact energy of 20 keV at the sample surface. An initial 2 nA beam focused to a 10 μm diameter scanned the selected location using a 15 x 15 μm raster for 60 seconds in order to remove locally the gold coat and to establish equilibrium sputtering conditions. Each analysis included an automated centring of the secondary beam on the instrument's field aperture in both X and Y. Data were collected using a 1 nA $^{133}Cs^+$ ion beam focused to a ~5 μm diameter and to which a 10 x 10 μm raster was applied in conjunction with the dynamic transfer capability of the instrument. This assured a flat-bottomed sputtering crater providing for improved within-run stability of the instrument. Low energy, normal incidence electron flooding with a current of <2 μA was used for charge compensation. The vacuum quality in the analysis chamber was between 3e-6 Pa and 1e-6 Pa during data acquisition.

The mass spectrometer was operated at a mass resolution of $M/\Delta M \approx 3500$ for the ^{34}S mass station; this is sufficient to eliminate all significant hydride and oxide isobaric interferences. A 50 eV wide energy window was centred 5 V below peak transmission of our instrument. The instrument was operated in static multi-collection mode with the ^{32}S being detected on the instrument's central Faraday Cup and the ^{34}S being assigned to the H2' FC, to which 10^{10} Ω and 10^{11} Ω resistors were used in the amplifier circuitry, respectively. A single analysis involved 20x 4 second integrations, and these were filtered at the 3σ level. In total, a single analysis including presputtering, automated centring and data collections took around 150 seconds. The count rate on the ^{32}S mass station was typically around $1.2 * 10^9$ counts per second. No drift was detected during the analysis.

Using a zero-point of $^{34}S/^{32}S = 0.044162$ for the CDT isotope scale (Ding et al., 2001), the data from the Balmat reference material indicate a total instrumental mass fractionation of 4.9‰ favouring the ^{34}S isotope. The obtained data is reliable at the ± 1‰ level with respect to all sources of analytical uncertainty. This data has been used to determine the possible provenance of sulphur.

4. Mesoscopic Observations

Mesoscopic observations are discussed for 29 samples as 10 of the 39 samples did not contain any visible sulphides. Tabulated observations can be found in Appendix 2.

4.1. Twangiza deposit

From the Twangiza deposit the sample material includes three metapelitic host rocks and four hydrothermal veins containing pyrite. The metapelites forming the host of the hydrothermal ore body are mesoscopically light grey to dark grey in colour and range from fine- to very fine-grained (Figure 4.1A-C). The samples are more or less carbonaceous mudstones. Individual mineral grains cannot be identified macroscopically and are therefore discussed in Chapter 5.1 as microscopic observations. In the metapelitic host, sulphide crystals typically are randomly distributed.

Sample TW-FS-03 in particular displays light grey and brown weathering on the surface. It contains arsenopyrite and randomly distributed euhedral pyrites, which measure up to 2 mm in size (Figure 4.1A). TW-FS-05 is dark grey in colour and contains pyrite lenses up to 5 mm wide (Figure 4.1B). Theses lenses are surrounded by quartz and appear to be stretched (Figure 4.1B). In addition, shiny, black mica grains are interpreted as detrital material. The peak metamorphic conditions in the Twangiza area are unlikely to have exceeded the biotite minimum growth conditions (Chuwa, 2011). Sample TW-FS-07 has a 6 mm thick vein (Figure 4.1C) composed of pyrite which is associated with a thicker carbonate-rich (mainly siderite) part of that vein. The vein changes orientation in an intertwined or anastomosing geometry. The pyrite is most abundant in a massive sulphide zone that is approximately 6 mm thick.

Vein samples are found in mesoscopically fine-grained, dark grey to medium grey host rocks of carbonaceous mudstone. Sample T3 consists of a >2 cm thick quartz-pyrite vein with sulphide rich off-shoots which can be up to approximately 2 mm thick. In addition, a large, 9 mm wide arsenopyrite grain is found in the quartz-pyrite vein (Figure 4.2A). Sample T9 consists of a quartz-pyrite vein that is up to 8 mm thick. The vein has a zig-zagging pattern intersecting the foliation at high angle (Figure 4.2B). About 1 mm thick off-shoots crosscut the foliation of the host rock at acute angles. The host rock contains pyrite aggregates in about 1 cm long foliation-parallel lenses.

Sample T12 has a narrowly spaced slaty cleavage and brownish weathering on the surface of the quartz-pyrite vein. The vein is up to up to 19 mm thick and displays angular host rock fragments indicating hydraulic brecciation during vein emplacement (Figure 4.2C). Sample T25 is a massive quartz-sulphide vein consisting of arsenopyrite and euhedral pyrite grains (Figure 4.2D). The sulphide size is in the millimetre range and does not exceed 4 mm. Carbonates display a brownish weathering on the surface. Sample T27 is a quartz-sulphide vein with brecciated mudstone fragments. Arsenopyrite grains are 1 mm or smaller and pyrites are not visible in the hand specimen.
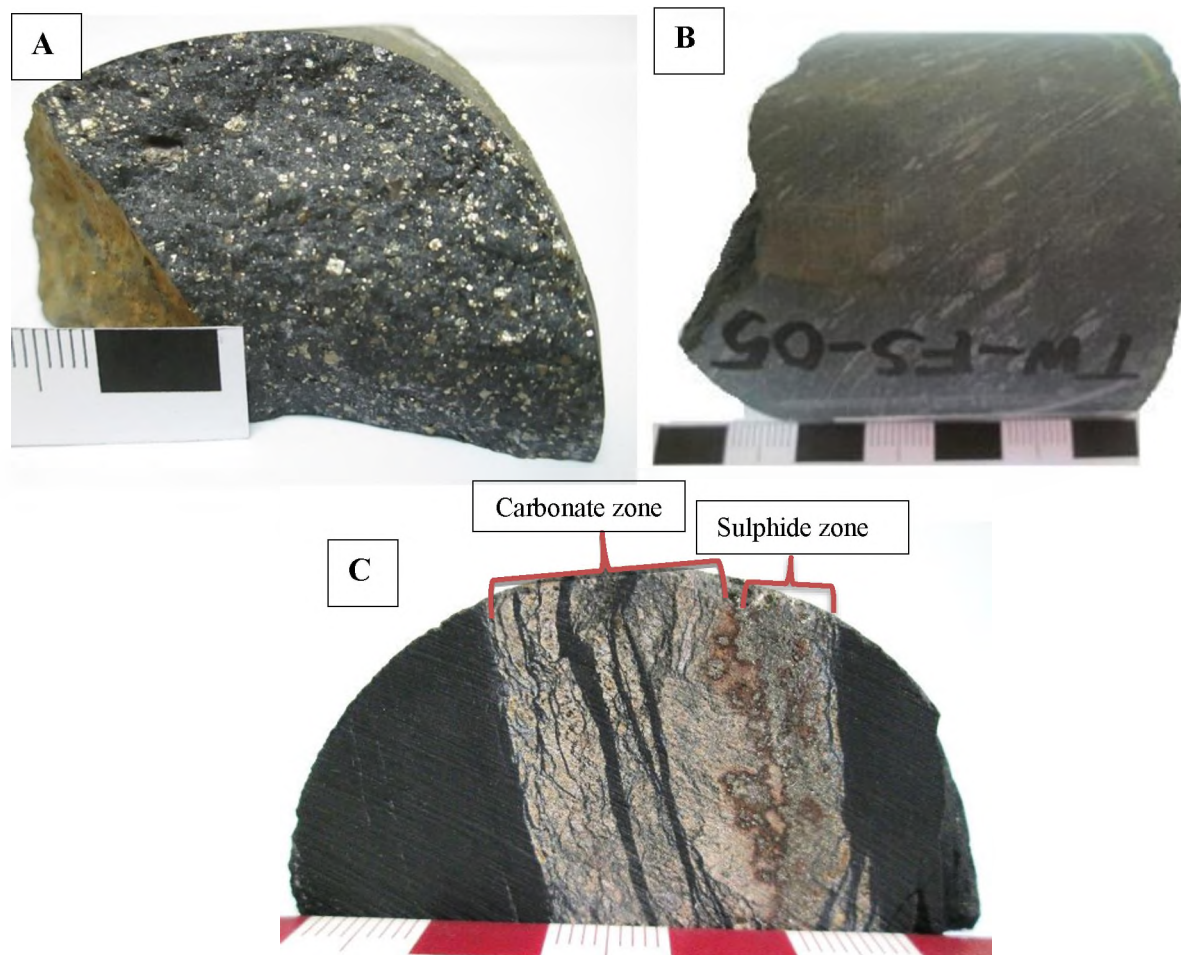
Figure 4.1: Hand specimen photographs of host rock samples from Twangiza. **A)** Sample TW-FS-03 showing euhedral pyrite grains. **B)** TW-FS-05 displaying stretched pyrite lenses. **C)** Anastomosing pyrite-carbonate vein in TW-FS-07. Note massive pyrite zone on the right-hand edge of the vein. The left part of the vein contains essentially siderite carbonate. Scale is segmented into 1 cm units.
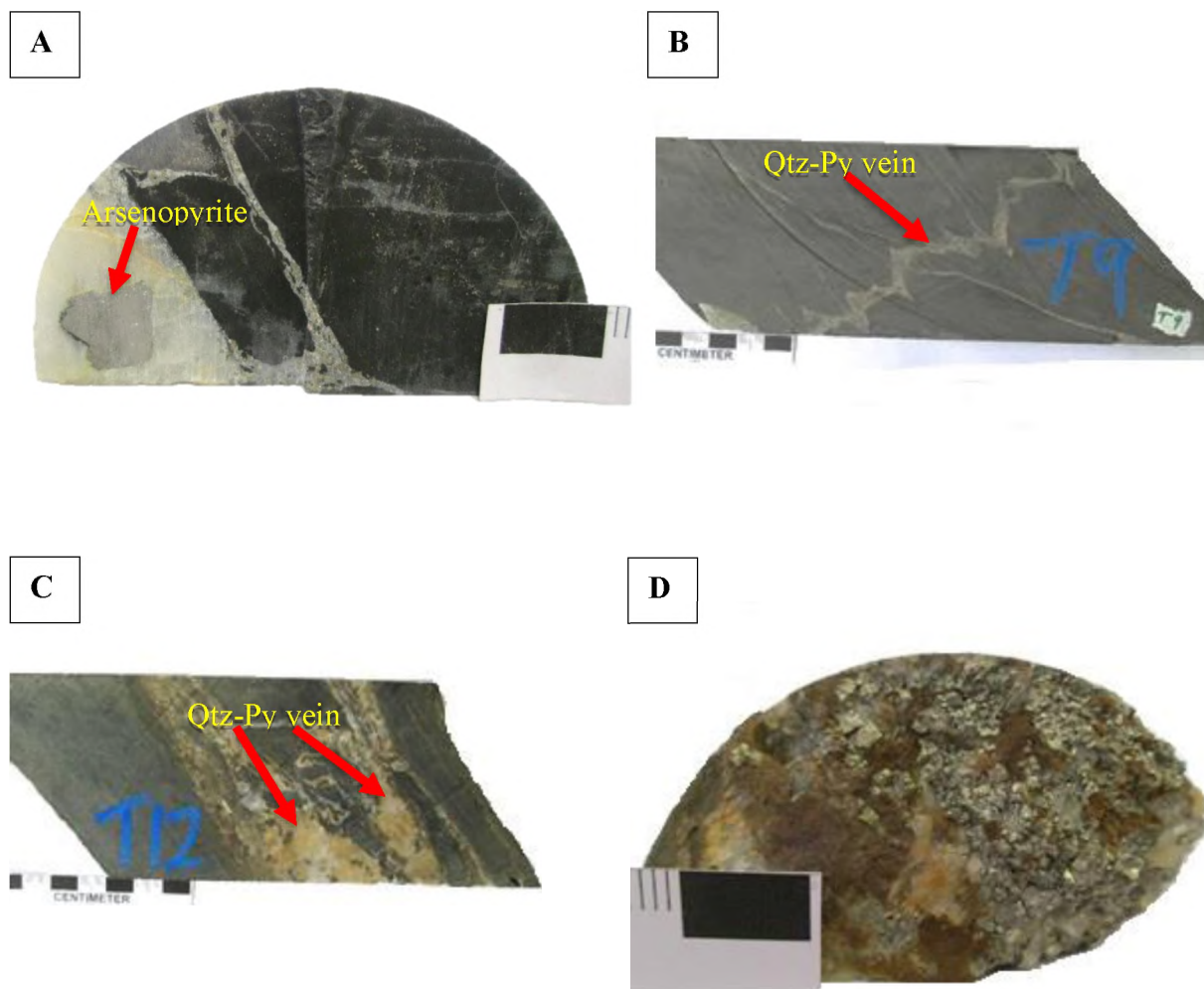
Figure 4.2: Hand specimen photographs of vein samples from Twangiza. **A)** Sample T3 showing an arsenopyrite grain in a quartz-pyrite vein. **B)** An off-shoot cross-cutting a zig-zagging quartz-pyrite (Qtz-Py) vein in sample T9. **C)** Sample T12 showing a quartz-pyrite (Qtz-Py) vein with brownish weathering on the surface. **D)** Sample T25: Cube-shaped pyrite and arsenopyrite grains in a quartz-sulphide vein. Scale is segmented in 1 cm units.

4.2. Kamituga deposit

Sample material from the Kamituga deposit includes three metapelitic host rocks, two metadioritc host rocks and two hydrothermal veins. The metapelites forming the host of the hydrothermal ore body are mesoscopically light grey to dark grey in colour and range from fine-grained to coarse-grained. The metadiorites are grey to dark grey and are coarser-grained than the metapelites. Individual mineral grains cannot be identified macroscopically and are therefore discussed in microscopic observation (see Chapter 5.2). In the host rocks, sulphide crystals are typically randomly distributed.

Three metapelitic host rock samples do not have mesoscopically visible sulphides and will therefore not be discussed in this section. They will, however, be discussed in microscope observation Chapter 5.2 as they contain sulphides that are visible under the microscope.

Sample KG-SIS-2 displays light grey and brown weathering on the surface. It contains chalcopyrite and randomly distributed pyrite grains which measure up to 3mm in size (Figure 4.3A). A weathered quartz vein (up to 1 cm wide) is mostly associated with micas that form a margin around it. It contains an aggregate of massive pyrite along the interface of a 15 mm thick quartz vein. KG-SIS-4 is fine-grained with pyrrhotite and arsenopyrite grains that are 1 mm or smaller. Samples in the Kamituga area are normally unfoliated but shiny biotite grains in KG-SIS-4 display a continuous cleavage (Figure 4.3B). Sample KG-SIS-5 is a metadiorite with brown weathering on the surface (Figure 4.3C). It contains randomly distributed euhedral pyrite grains that are smaller than 1 mm and anhedral pyrite grains that are up to 2 mm in size. KG-SIS-6 is also a metadiorite but is finer-grained and contains less quartz than sample KG-SIS-5 (Figure 4.3D). It contains randomly distributed pyrite which measures up to 2 mm in size. Sample KG-SIS-7 is dark grey in colour and contains quartz lenses up to 1.5 cm wide (Figure 4.3E). Pyrite either is randomly distributed or occurs as < 1 mm stringers.

Vein sample K17 is found in a fine-grained, medium grey metapelite host rock. It contains a quartz vein that measures up to 2.5 cm wide (Figure 4.4A). The vein has a biotite margin. Arsenopyrite and pyrrhotite grains are 1 mm or smaller and appear in both the host rock material and in the vein. Sample KG-SIS-1 is a massive quartz vein (~6 mm long) within the metapelitic host rock (Figure 4.4B). Arsenopyrite, pyrrhotite and chalcopyrite grains are 1 mm or smaller in size, and were observed in the vein as well as the host rock. Pyrites are not visible in the hand specimen of the vein samples.
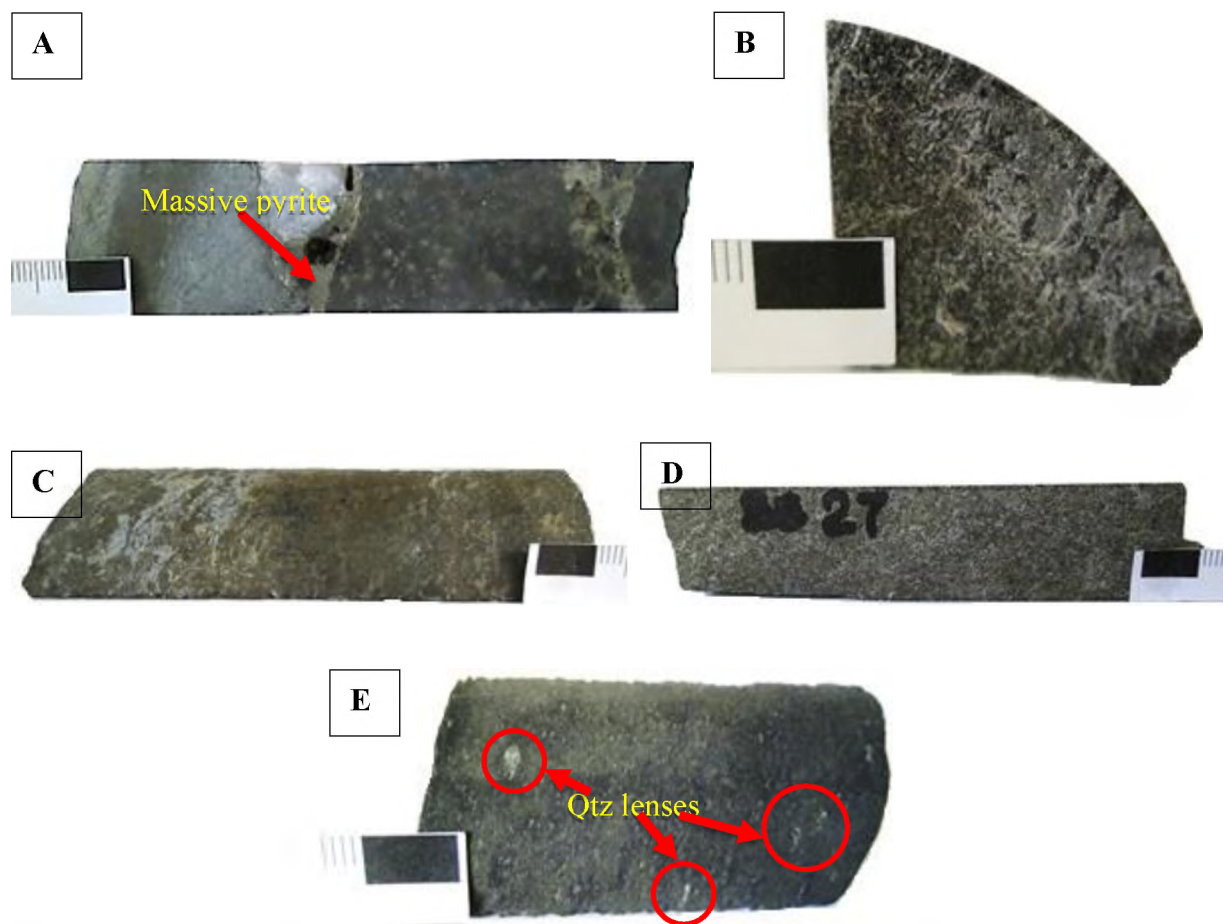
Figure 4.3: Hand specimen photographs of host rock samples from Kamituga. **A**) Sample KG-SIS-2 displaying massive pyrite along the margin of a quartz vein. Some pyrite has been disseminated into the host rock. **B**) Foliation visible in sample KG-SIS-4. **C**) Brown weathering on metadiorite sample KG-SIS-5. **D**) Metadiorite sample KG-SIS-6 displaying smaller quartz grains than sample KG-SIS-5. **E**) KG-SIS-7 displaying quartz (Qtz) lenses in dark metapelite rock. Scale is segmented in 1 cm units.

Figure 4.4: Hand specimen photographs of vein samples from Kamituga. A) Sample K17 displaying a quartz vein with biotite-rich marginal zone. B) Sample KG-SIS-1 is a massive quartz vein with arsenopyrite and pyrrhotite grains 1 mm or less in size. Scale is segmented in 1 cm units.

4.3. Lugushwa deposit

Sample material from the Lugushwa deposit includes six metapelitic host rocks and one hydrothermal vein sample. The metapelite rocks are mesoscopically light grey to dark grey in colour and range from fine- to very fine-grained. Some samples display a weak foliation. Metamorphism in the Lugushwa area is up to lower greenschist facies (O'Donovan et al., 2005). Individual mineral grains cannot be identified macroscopically and are therefore discussed in microscopic observation (see Chapter 5.3). In the host rocks, sulphide crystals are typically randomly distributed.

Samples LG-FS-1 and LG-FS-4 are mesoscopically similar and are both light grey in colour. They have a slight slaty cleavage with LG-FS-4 displaying foliation of mica minerals. These samples do not contain mesoscopically visible sulphides.

Host rock sample LG-SI-01 displays light grey weathering on the surface and a slight slaty cleavage. It contains randomly distributed pyrrhotite grains that are 1 mm or less and pyrrhotite lenses that measure up to 12 mm in size (Figure 4.5A). Some of the lenses appear to be stretched and lineated. Sample LG-SI-02 is medium grey to light grey in colour and contains euhedral pyrite grains which measure up to 5 mm (Figure 4.5B). Quartz veinlets that are up to 1 mm thick also occur in the rock. LG-SI-03, which is similar to LG-SI-01, is fine grained and displays a slight slaty cleavage. The sample contains randomly distributed pyrrhotite grains that are 1 mm or less and pyrrhotite lenses that measure up to 13 mm in size (Figure 4.5C). Some of the lenses appear to be stretched and lineated. Sample LG-SI-04 is fine grained and grey in colour with a slight slaty cleavage. Pyrrhotite grains are randomly distributed and are 1 mm or smaller. Some pyrrhotite is found in quartz-sulphide nodules that are up to 11 mm long (Figure 4.5D). Sample LG-SI-05 displays slight slaty cleavage and has quartz veinlets that are up to 1 mm wide. The sample contains randomly distributed pyrrhotite grains that are 1 mm or less in size, and pyrrhotite lenses that measure up to 9 mm in length (Figure 4.5E). These lenses appear to be stretched and are well aligned with one another. LG-SI-06 is light grey in colour on the surface and displays a slight slaty cleavage. Pyrite lenses up to 13 mm long appear to be stretched and well-aligned. The sample has quartz-pyrite nodules that are up to 19 mm long and 8 mm wide (Figure 4.5F). These nodules typically have a mica-rich margin.

Vein sample L4 is found in a mesoscopically fine-grained, medium grey, metapelitic host rock. The vein contains a network of several 2 mm thick quartz-sulphide veins that are connected to 1 mm thick veins at a high angle (Figure 4.6).
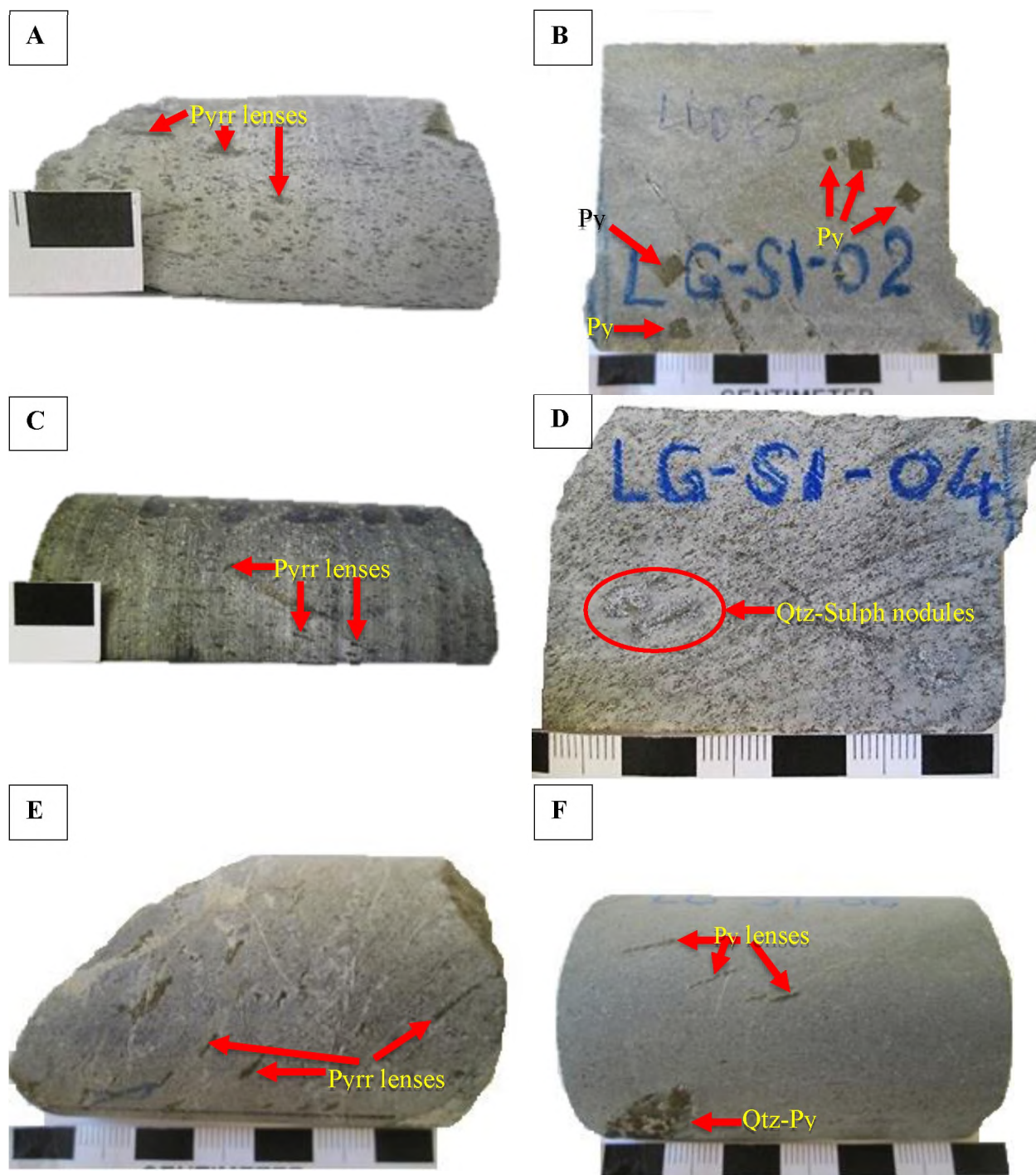
Figure 4.5: Hand specimen photographs of host rock samples from Lugushwa. **A)** Sample LG-SI-01 displaying stretched pyrrhotite (Pyrr) lenses. **B)** Cubic pyrite (Py) grains in sample LG-SI-02. **C)** Sample LG-SI-03 displaying stretched pyrrhotite (Pyrr) lenses. **D)** Quartz-sulphide (Qtz-Sulph) nodules in sample LG-SI-04. **E)** Sample LG-SI-05 displaying stretched pyrrhotite (Pyrr) lenses and quartz veinlets. **F)** Stretched pyrite (Py) lenses and quartz-pyrite (Qtz-Py) nodule in LG-SI-06. Scale is segmented in 1 cm units.
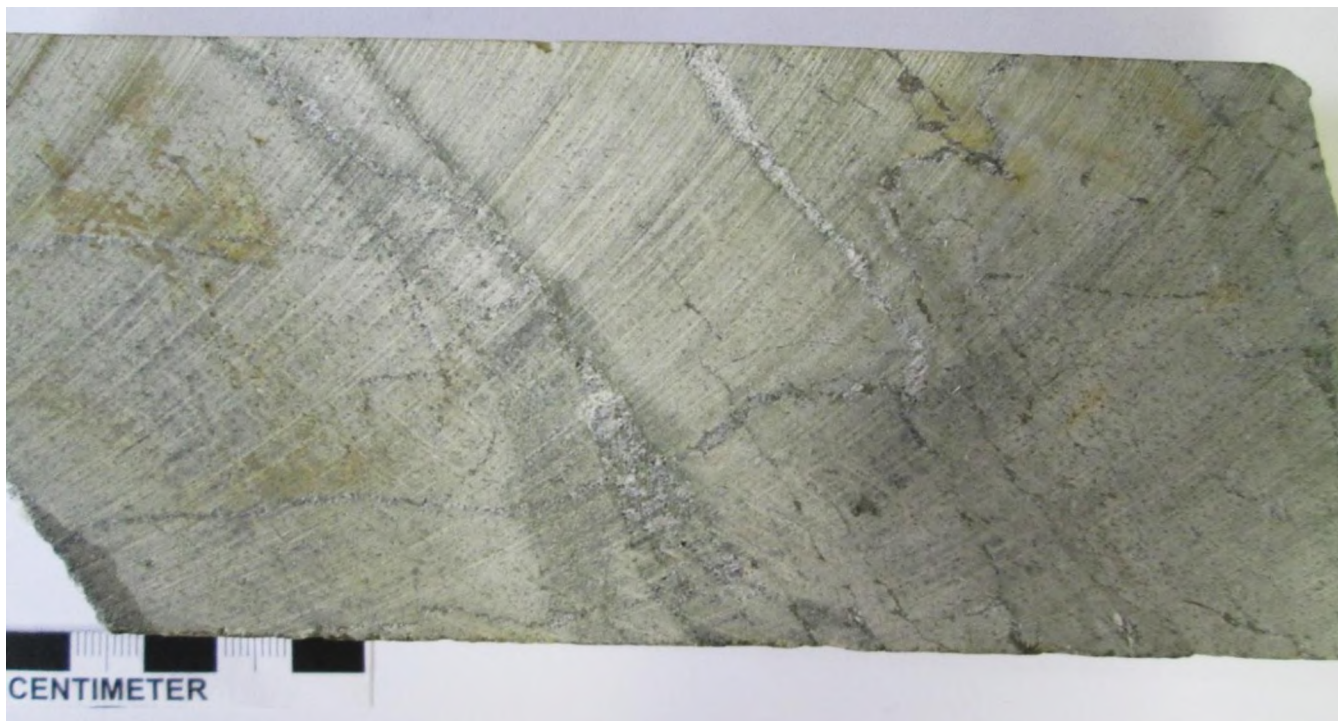
Figure 4.6: Hand specimen photograph of vein sample from Lugushwa. Sample L4 displaying a network of quartz-sulphide veins. Scale is segmented in 1 cm units.

4.4. Namoya deposit

All sample material from the Namoya deposit are schists or dolerite. Seven samples are sericite schists and three samples are dolerites. The sericite schists are mesoscopically medium-grained to fine-grained and have a greenish-grey to light grey colour. The dolerites are dark grey with a greenish grey weathered surface. All the samples display some foliation which may be due to the lower to mid greenschist metamorphism that the area has undergone (Fall, 2008). Individual mineral grains cannot be identified macroscopically and/or mesoscopically and are therefore discussed in microscopic observations (see Chapter 5.4). Sulphide crystals typically are randomly distributed.

Sample NM-FS-1 is a schist that is mesoscopically light greenish-grey and has a narrowly spaced slaty cleavage. The sample contains a single, euhedral pyrite grain measures up to 4 mm in size (Figure 4.7A). Sample NM-FS-2 is also mesoscopically light greenish-grey and has a s narrowly spaced slaty cleavage. The sample has randomly distributed euhedral pyrites that measure up to 9 mm (Figure 4.7B).

Sample NM-SI-1 is a dolerite that displays a schistose texture and is mesoscopically grey. The sample has quartz veins that are up to 1 mm thick. Up to 1 mm sized euhedral pyrites are randomly distributed (Figure 4.7C). NM-SI-2 is a slightly foliated dolerite that is composed of euhedral arsenopyrite and pyrite grains that are 1 mm or smaller in size. An up to ~2.5 cm thick quartz vein cuts through the rock (Figure 4.7D). The vein contains arsenopyrite and pyrite in its fractures. Sample NM-SI-3 is slightly foliated dolerite with randomly distributed pyrite grains that are 1 mm or smaller. A disrupted quartz vein that is up to 3 mm wide (Figure 4.7E) contains pyrite grains along its margins to the host rock. Sample NM-SI-4 is greenish-grey and has a thin slaty cleavage. Quartz veins are up to 1 mm thick and euhedral arsenopyrite grains are 1 mm or less (Figure 4.7F). NM-SI-5 is a fine-grained greenish sericite schist with a slight schistose texture. An up to 1 mm thick pyrite vein cuts through the rock (Figure 4.8A).

NM-SI-6 is also greenish sericite schist with a slight schistose texture (Figure 4.8B). The sample has quartz-pyrite nodules that are up to 3 cm long and 1 cm wide. Pyrite and pyrrhotite is randomly distributed and do not exceed 1 mm. Sample NM-SI-7 is also a greenish-grey graphitic schist with a slight schistose texture. Euhedral pyrite grains are randomly distributed and are 1 mm or less. An up to 1 cm thick quartz vein cuts through the rock (Figure 4.8C) and does not contain any visible sulphides. NM-SI-8 is a greenish-grey sericite schist with a slight schistose texture. The sample contains quartz-pyrite nodules that are up to 11 mm long and 7 mm wide. Euhedral pyrite grains are randomly distributed and are 1 mm or less. In addition, the sample also contains quartz veins that are up to 2 mm wide (Figure 4.8D).
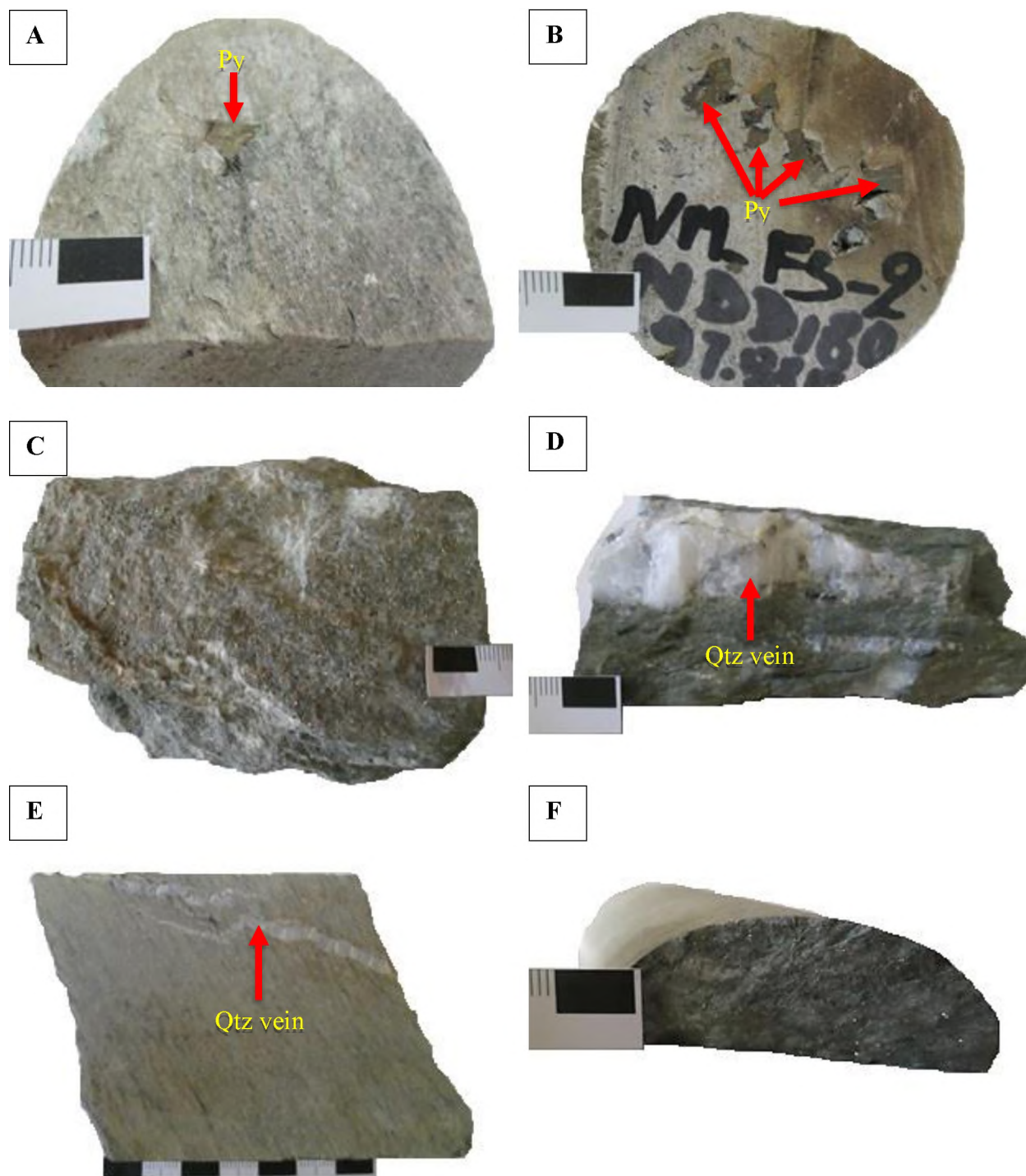
Figure 4.7: Hand specimen photographs of host rock samples from Namoya. **A)** Euhedral pyrite (Py) grain in sample NM-FS-1. **B)** Randomly distributed euhedral pyrite (Py) grains in sample NM-FS-2. **C)** Sample NM-SI-1 displaying up to 1mm thick quartz veins and pyrites (< 1mm). **D)** An up to 2.5 cm thick disrupted quartz (Qtz) vein cross-cutting sample NM-SI-2. **E)** Sample NM-SI-3 displaying a disrupted quartz (Qtz) vein that measures up to 3 mm wide. **F)** Randomly distributed pyrite grains in sample NM-SI-4. Scale is segmented in 1 cm units.
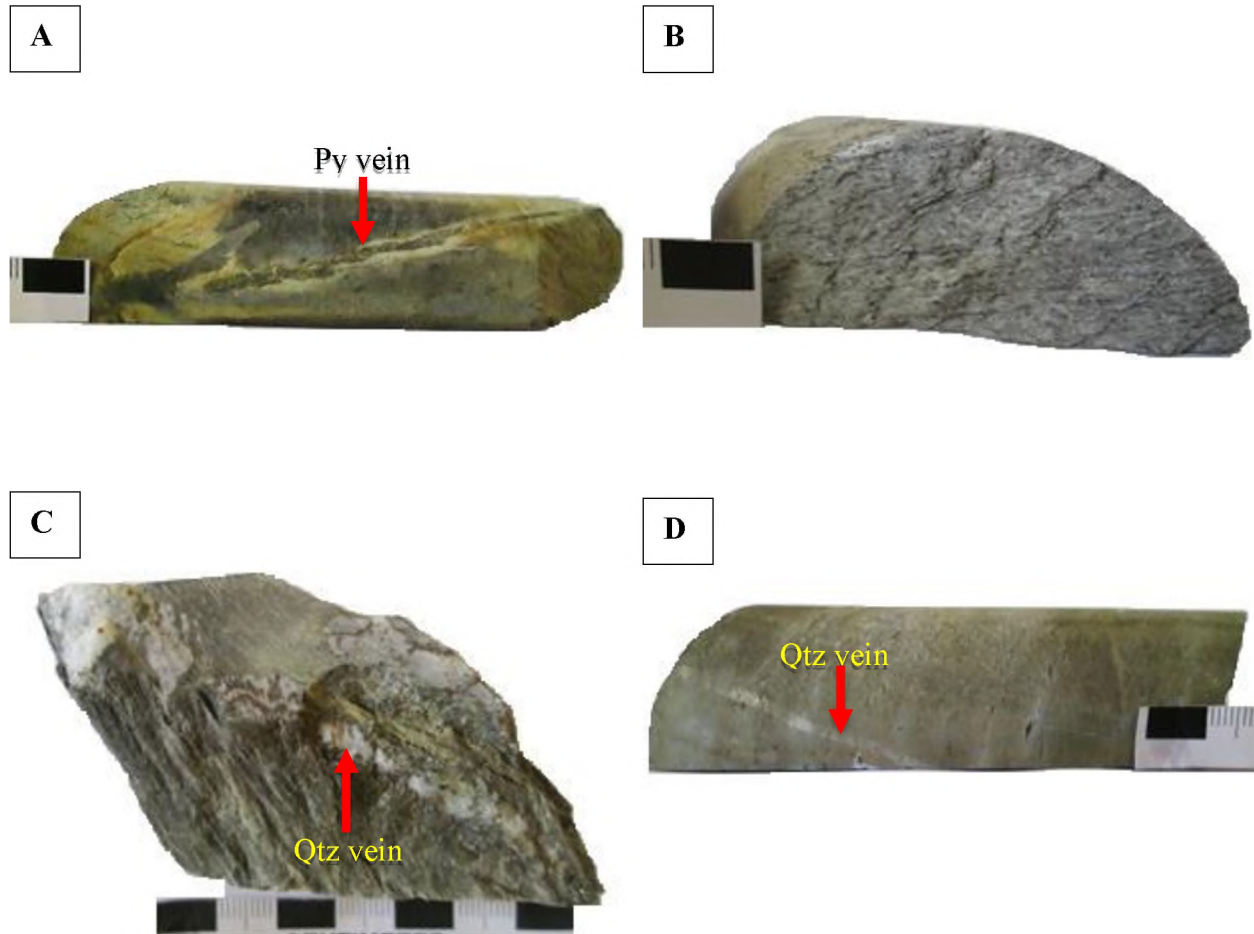
Figure 4.8: Hand specimen photographs of host rock samples from Namoya. **A)** An up to 1 mm thick pyrite (Py) vein cuts through sample NM-SI-5. **B)** Sample NM-SI-6 displaying a schistose texture. **C)** An up to 1 cm thick quartz (Qtz) vein cuts through sample NM-SI-7. **D)** Sample NM-SI-8 showing a 1 mm thick quartz (Qtz) vein. Scale is segmented in 1 cm units.

5. Microscopic Observations

5.1. Twangiza deposit

Sample TW-FS-03 is a mudstone that contains abundant, fine-grained quartz and plagioclase grains up to 300 μm in size. Minor apatite and rutile were identified using EDS. A quartz veinlet up to ~600 μm wide cross-cuts the mudstone. The vein and the host rock matrix are overgrown by euhedral pyrite and minor arsenopyrite (Figure 5.1A) of 300-800 μm. Arsenopyrite contains inclusions of pyrite and rutile. Furthermore, some pyrite, which is the most abundant sulphide in this thin section, contains inclusions of rutile.

There is no specific distribution pattern of pyrite in the host, and some crystals are present along the vein boundary, protruding into the vein. These crystals show some corrosion (white rings in Figure 5.1A) that appear to be more significant than similar textures in pyrite away from the vein. This suggests that sulphide in sample TW-FS-03 is unrelated to, and predates the vein formation. The hydrous fluid along the veinlets may well have been generated or mobilised locally and caused minor sulphide dissolution during fluid extraction. Hence the pyrite in this sample is considered authigenic/metamorphic (HR-type pyrite), formed from local sulphur sources.

Sample TW-FS-05 is a mudstone that contains a fine-grained matrix that is mostly composed of plagioclase with minor quartz, phlogopite and apatite. A small quartz veinlet (~10 μm wide) cross-cuts the host rock and seems to have pre-dated mineral growth. The veinlet is overgrown by plagioclase and minor quartz. Sulphides in the matrix are fine-grained and occur as anhedral grains. Larger pyrite grains (up to ~500 μm wide) have a plagioclase corona and inclusions of arsenopyrite, phlogopite, plagioclase (Figure 5.1B). The phlogopite in this pyrite is, however, considered to be detrital. One of these larger pyrite grains has a small native gold inclusion (<10 μm; Figure 5.1C). These large pyrites and their coronas are isolated agglomerates in the metapelite matrix, and hence interpreted as HR type pyrites. They are not interconnected by veins. This suggests that gold particles in the mudstone matrix was overgrown by pyrite that formed authigenically, which in turn suggests that gold particles were present in the sediment prior to pyrite growth.

Carbonaceous mudstone sample TW-FS-07 contains a fine-grained matrix made up mostly of plagioclase, quartz, phlogopite and siderite. A quartz veinlet (~1 mm wide) cross-cuts the host rock. Pyrite occurs as anhedral to subhedral grains and is confined to the quartz veinlet. Pyrite is typically associated with phlogopite, which forms a corona around some pyrite grains (Figure 5.1D). Plagioclase inclusions are common in pyrite. These textures suggest precipitation from a fluid phase but due to the smallness of the vein the fluid source may be nearby. The sulphur isotope signature for this pyrite is similar to that in TW-FS-05, which shows authigenic pyrite growth (see Chapter 7.5.1). Therefore, the pyrite that may have formed in the veinlet in TW-FS-07 is interpreted to have formed from proximally sourced sulphur, and hence is classified as AM-HR

type pyrite. SIMS analyses was however, performed on HR pyrite. The isotopic signature of HR and AM HR type pyrite should reflect the local sulphur source which is most likely from the host rock.

Sample T3 mostly consists of fine-grained dark material with a quartz-pyrite vein intersecting it. Minerals that were identified in the host rock using EDS are plagioclase, muscovite, phlogopite with minor quartz, apatite and presumably periclase (MgO). According to Deer et al. (1992), periclase may form in contact aureoles due to the metamorphism of dolomite. However, the borehole from which sample T3 (TDD023) was collected is not close to any plutonic rock. On the other hand, the metasedimentary sequence of the Twangiza deposit is interspersed with feldspathic porphyry sills (Chuwa, 2011). The heat from these sills may have caused the replacement of dolomite with periclase.

Sample T9 consists of fine-grained carbonaceous material. The thin section shows quartz and carbonates (calcite and ankerite) with minor chlorite and apatite in the carbonaceous mudstone host rock. A primary quartz-carbonate vein (2.4 mm) is crosscut by a younger and thinner pyrite vein (~500 µm; Figure 5.2A). The younger vein contains anhedral pyrites that vary in grain size (≤ 350 µm). Pyrite in this sample only occurs within and around veins and is thus considered as vein (V) pyrite.

Sample T12 consists of carbonaceous host rock material. Fine-grained, wavy carbonate laminae occur between the coarser grained matrix of the host rock. The most abundant minerals in the host rock are quartz, ankerite and calcite with minor apatite and chlorite. Pyrite, which can be larger than 2 mm in size, is mostly anhedral and has inclusions of quartz, ankerite and calcite (Figure 5.2B). Pyrite only occurs within a quartz-pyrite vein (i.e. V-type pyrite).

Sample T25 (Figure 5.2C) is a thick coarse-grained quartz-sulphide vein with abundant micro-fractures. Quartz is the most abundant mineral in this thin section. Siderite was identified as the main carbonate using EDS and is usually associated with pyrite, occurring along its boundaries or in close proximity. Pyrite and arsenopyrite are mostly subhedral to anhedral. Some up to 3 mm large pyrite in the quartz-sulphide vein contains quartz inclusions. Pyrite in this sample only occurs within veins and is classified as V pyrite.
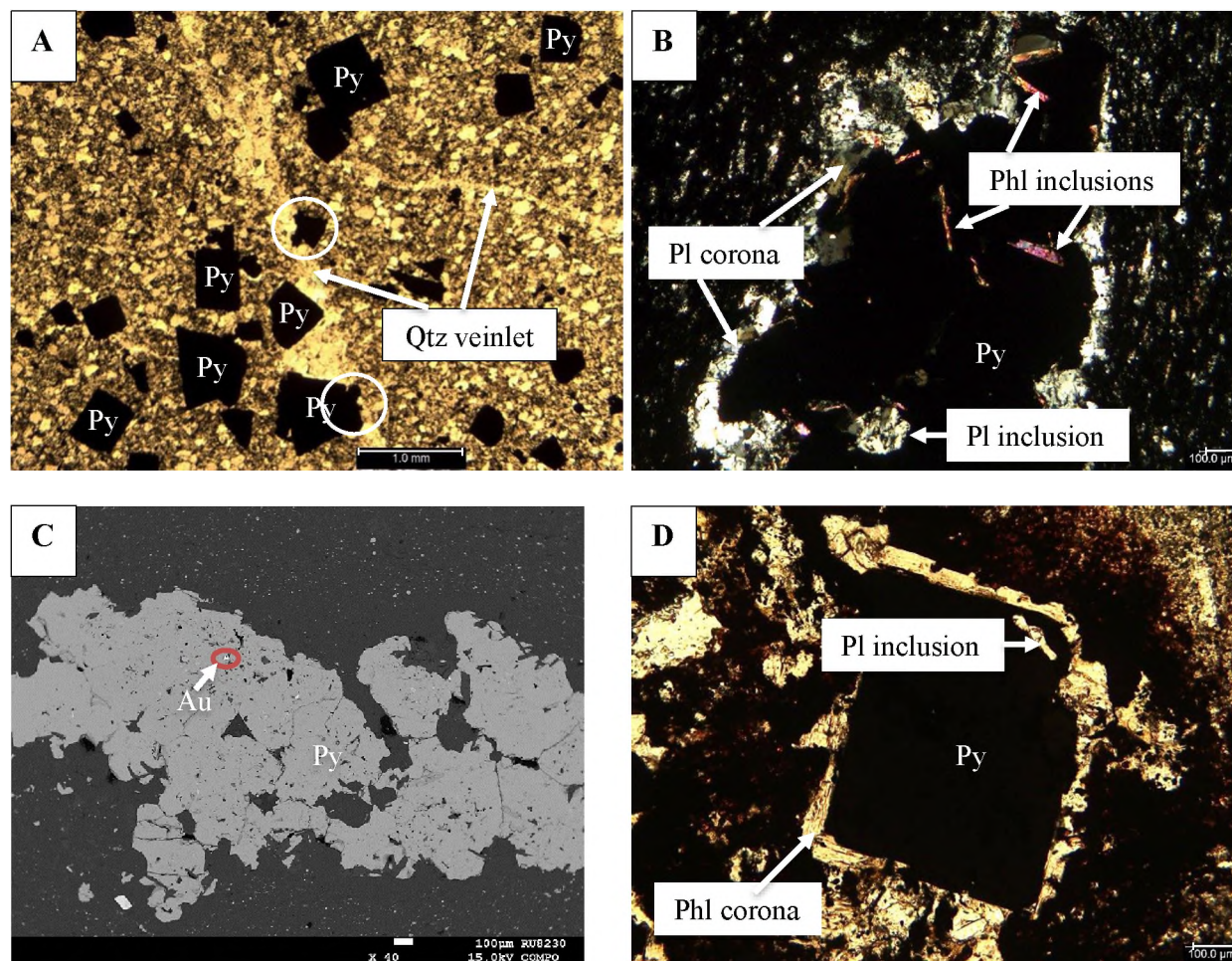
Figure 5.1: Photomicrographs of host samples from Twangiza. **A**) PPL photomicrograph of euhedral to subhedral HR pyrite (Py) grains in sample TW-FS-03. Pyrite is randomly distributed in the matrix. Some crystals are present along the boundary of thin quartz veins and here they appear partly resorbed (white circles), suggesting growth prior to vein formation and minor dissolution of pyrite in the incoming fluid phase. **B**) XPL photomicrograph of HR pyrite (Py) with phlogopite (Phl), plagioclase inclusions and plagioclase (Pl) corona in sample TW-FS-05. **C**) BSE image of native gold (Au) grain in HR-type pyrite (Py) in sample TW-FS-05. **D**) PPL photomicrograph of a euhedral AM HR pyrite (Py) with a plagioclase (Pl) inclusion and phlogopite (Phl) corona in sample TW-FS-07.
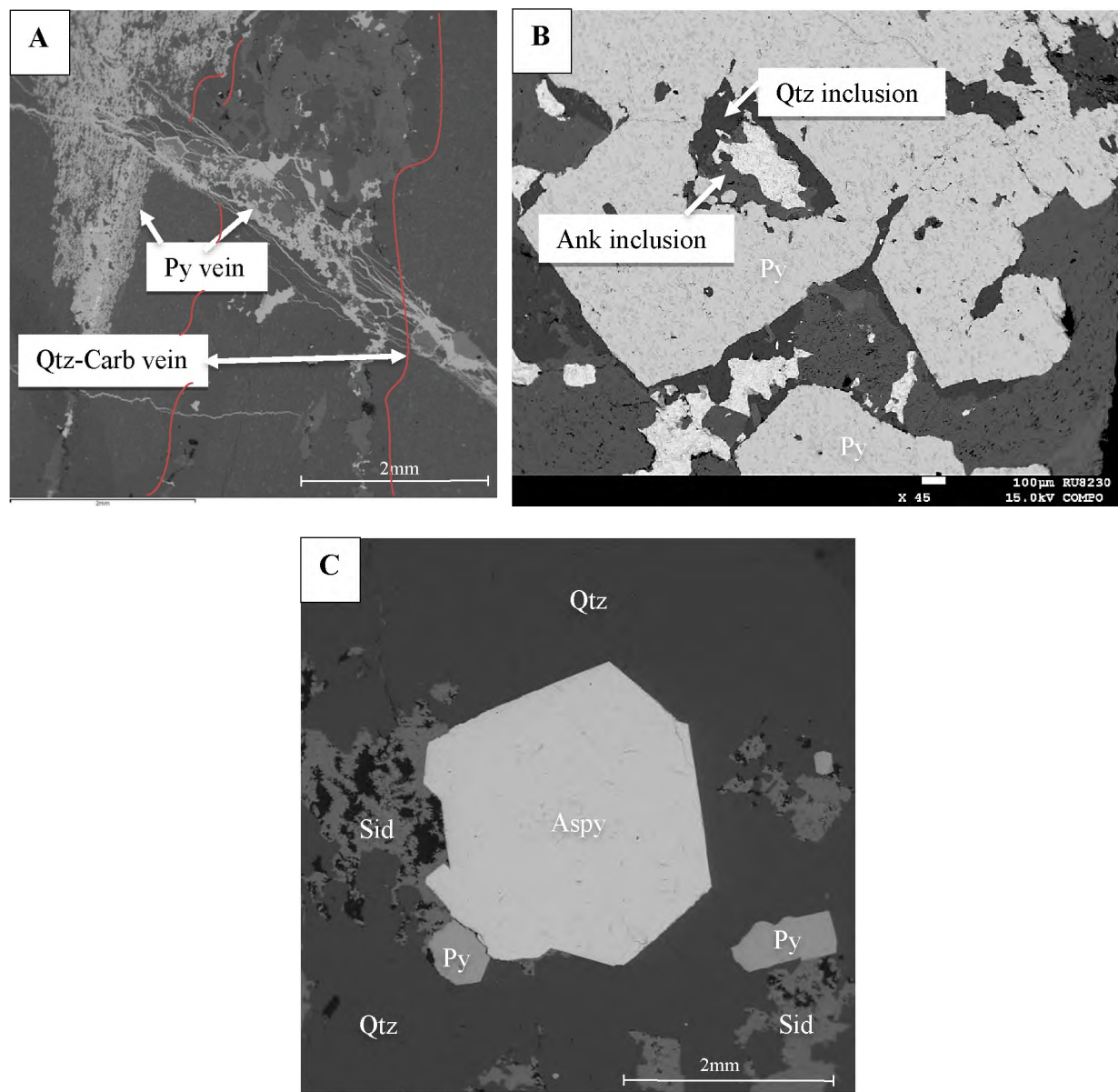
Figure 5.2: Photomicrographs of samples from Twangiza. **A)** BSE photomicrograph of a pyrite (Py) vein cross-cutting a quartz-carbonate (Qtz-Carb) vein in sample T9. **B)** BSE photomicrograph of vein pyrite (Py) with inclusions of quartz (Qtz) and ankerite (Ank) in sample T12. **C)** BSE photomicrograph of V-type pyrite in association with euhedral arsenopyrite (Aspy) in sample T25.

5.2. Kamituga deposit

Sample KG-FS-1 is a metapelite that contains a fine-grained matrix that is mostly composed of quartz, chlorite, plagioclase and lath shaped biotite. Biotite and chlorite seem to be aligned in a preferred orientation (Figure 5.3A). Sulphides in the matrix are fine-grained and occur as anhedral grains. Pyrrhotite contains inclusions of arsenopyrite. Some pyrite, which is the least abundant sulphide in this thin section, contains inclusions of quartz and biotite. There is no evidence of fluid infiltration in this sample and therefore pyrite is interpreted as authigenic/metamorphic (HR pyrite).

Sample KG-FS-2, a mica-schist, contains a disjunctive cleavage defined by biotite-chlorite rich layers and quartz-biotite rich layers (Figure 5.3B). Garnet porphyroblasts, which are up to 2 mm wide, show deflection of the foliation formed by chlorite, indicating pre-tectonic garnet growth. Garnet shows poikilititc quartz and mica inclusions. In places, biotite enrichment along garnet boundaries coincides with low abundance or absence of quartz (Figure 5.3B). This pattern is most likely a result of dissolution creep that removed quartz from such sites (Vernon, 2004). The garnet is interpreted to be of metamorphic origin and is most likely prograde. Chuwa (2011) described the Kamituga deposit as generally weakly metamorphosed to lower greenschist facies. The presence of metamorphic biotite, chlorite and garnet may suggest a somewhat higher grade of metamorphism, perhaps upper greenschist to lower amphibolite facies conditions (Spear and Cheney, 1989). Pyrite and arsenopyrite are fine-grained and mostly anhedral in shape. Some pyrite, which is the most abundant sulphide in this thin section, contain inclusions of quartz. Sample KG-FS-2 shows no evidence of fluid infiltration and therefore pyrite is interpreted as authigenic/metamorphic HR pyrite.

Sample KG-SIS-2 contains three domains: a coarser grained altered domain, a quartz-pyrite vein, and as the host rock a fine-grained chlorite schist domain. Pyrite is typically associated with siderite in the vein and the host rock. The contact between the domains is irregular. Within the 15mm thick quartz vein, a massive pyrite cluster that has formed along the vein contact to the host rock. Here, pyrite is several millimetre in size (Figure 5.3C). Pyrite in the chlorite schist domain is fine-grained. Some larger hydrothermal pyrites contain inclusions of quartz and siderite (Figure 5.3C). The association of pyrite in the host rock with siderite, which is rarely seen in host rock away from veins, is likely to be the product of fluid infiltration. Therefore the pyrite in the chlorite schist is seen as dissemination of sulphur from the intruding hydrothermal fluid. Pyrite in this sample is therefore classified as VD HR and V pyrite.

KG-SIS-3 is a metapelite that that is mostly made up of fine-grained quartz, biotite and muscovite. Chlorite, ilmenite and plagioclase were identified using EDS. A pyrite vein that measures up to 1.34 mm wide cuts through the rock (Figure 5.3D). The vein contains inclusions of quartz and biotite. Pyrites in the matrix are mostly anhedral in shape and display no spatial relationship with the vein. These pyrites are much smaller in size (up to 390 μm) when compared to pyrite in the vein which can measure up to 1mm. Pyrite in the matrix is not associated with the vein and displays

no evidence of fluid infiltration. The pyrite is therefore interpreted as authigenic/metamorphic HR type.

Sample KG-SIS-5 is a metadiorite that mostly consists of coarse grained quartz. Apatite and siderite were identified using EDS. Pyrite and pyrrhotite are mostly anhedral and vary in grain size ($\leq$ 2.2 mm long). Pyrite is the most abundant sulphide and is typically associated with siderite which mostly occurs along its boundaries. Some pyrite contain siderite and quartz inclusions (Figure 5.4B). The sample shows no sign of fluid infiltration and therefore pyrite is considered to be authigenic/metamorphic (HR type).

Sample KG-SIS-6 is also a metadiorite but contains less quartz than KG-SIS-5. Quartz, siderite and phlogopite are the most abundant minerals in this rock. Pyrite, chalcopyrite and pyrrhotite are mostly anhedral and vary in grain size ($\leq$ 2.9 mm). Pyrite is more abundant than chalcopyrite and pyrrhotite and seems to be associated with siderite, which either occurs along pyrite boundaries or as inclusions. Some pyrite also contain, chalcopyrite and quartz inclusions (Figure 5.4C). Although the occurrence of both pyrite and siderite in the host rock might be a sign of an incoming fluids, the sample does not show any evidence of external fluid infiltration and the pyrite is therefore considered to be authigenic/metamorphic.

Sample KG-SIS-7 contains a fine-grained quartz with minor siderite and rutile. A small quartz veinlet that measures up to 90 mm cross-cuts the rock. Pyrite and arsenopyrite are mostly anhedral and vary in grain size ($\leq$ 350 μm). Some pyrites in the matrix contain inclusions of arsenopyrite and quartz. The sulphur isotope signature for this pyrite is significantly different from vein pyrites in Kamituga and therefore the matrix pyrite is interpreted to be authigenic/metamorphic (see Chapter 7.5.2). An up to 1.9 mm wide pyrite vein cuts through the rock. The vein contains inclusions of arsenopyrite, quartz, and rutile (Figure 5.4D). This sample contains pyrite that is HR, VD HR and V. However, SIMS was only performed on HR pyrite.
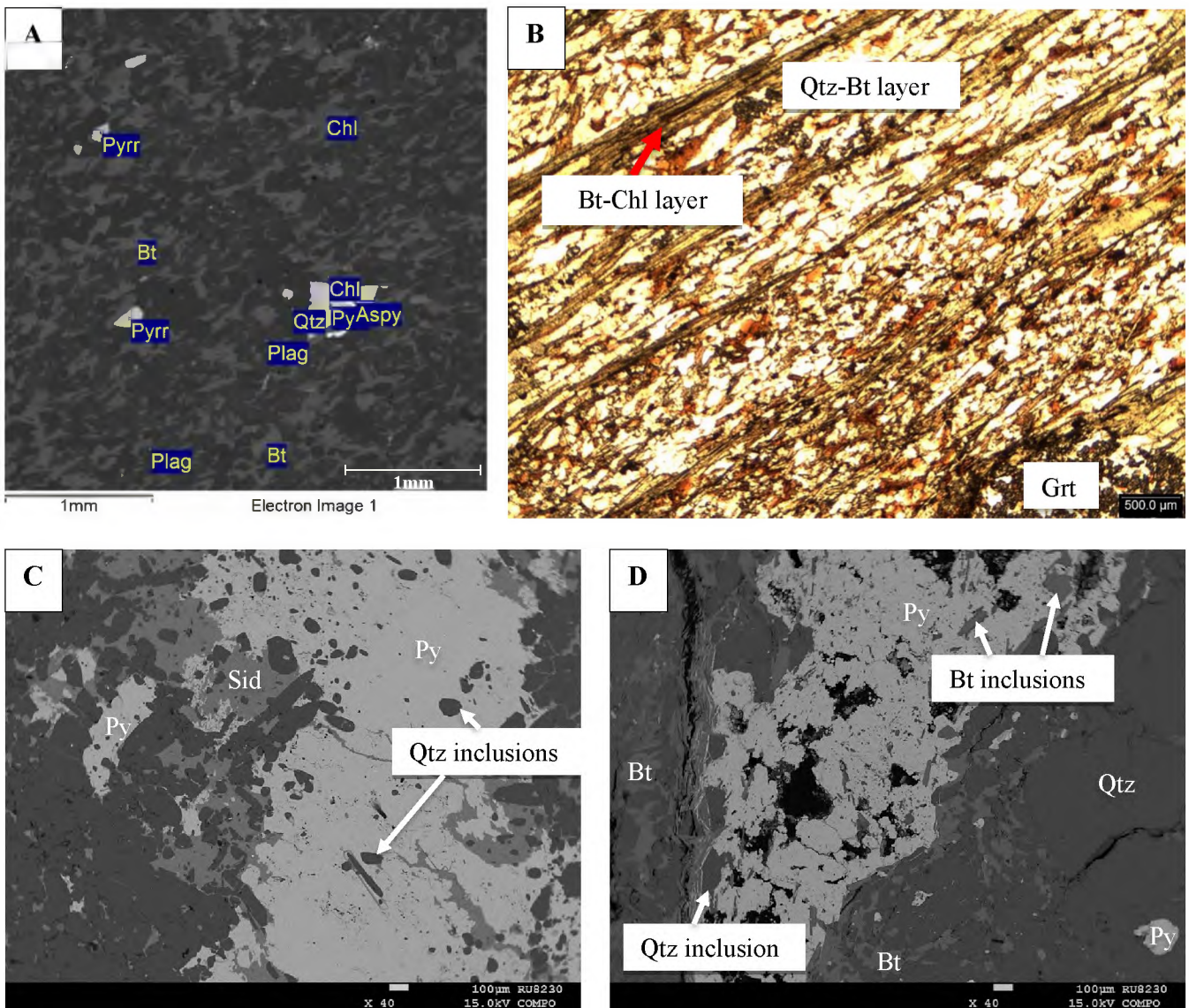
Figure 5.3: Photomicrographs of samples from Kamituga. **A**) BSE image of aligned biotite (Bt) and chlorite (Chl) grains in sample KG-FS-1. **B**) PPL photomicrograph of disjunctive cleavage in sample KG-FS-2. Note the garnet (Grt) poikiloblast with biotite concentrations along the margin, suggesting removal of quartz by dissolution creep. **C**) BSE image of V-type pyrite (Py) grain with quartz (Qtz) inclusions in sample KG-SIS-2. **D**) BSE image of a pyrite (Py) vein with inclusions of biotite (Bt) and quartz (Qtz) in sample KG-SIS-3. Sid = siderite; Pyrr = pyrrhotite; Aspy = arsenopyrite; Plag = plagioclase.
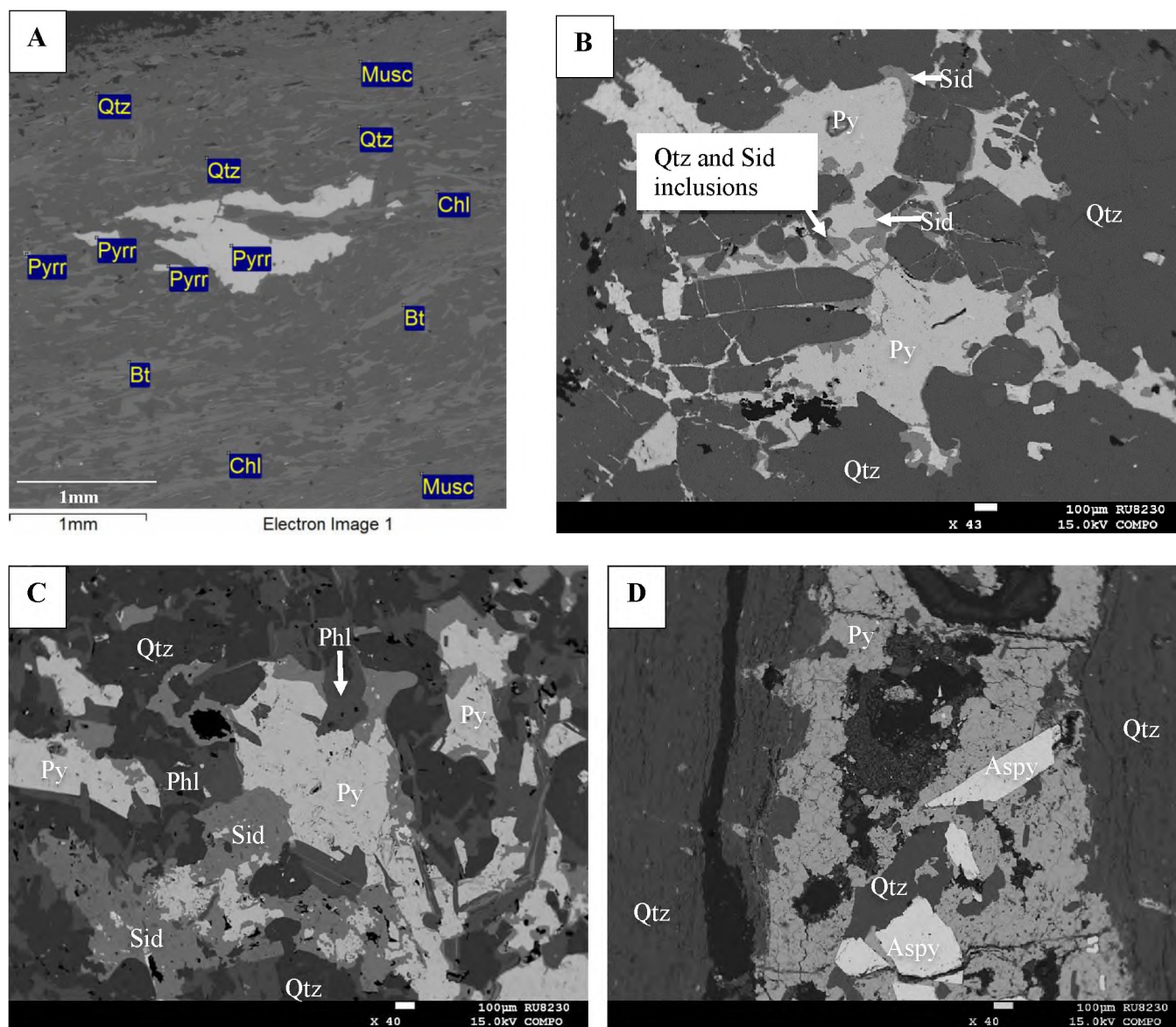
Figure 5.4: Photomicrographs of samples from Kamituga. **A**) BSE photomicrograph depicting continuous cleavage defined by quartz (Qtz)-biotite (Bt) rich layers and biotite-chlorite(Chl) rich layers in sample KG-SIS-4. **B**) BSE photomicrograph of HR pyrite with quartz (Qtz) and siderite (Sid) inclusions in sample KG-SIS-5. **C**) BSE photomicrograph of sample KG-SIS-6 showing the association of HR pyrite (Py) with siderite (Sid). **D**) BSE photomicrograph of a pyrite (Py) vein with inclusions of arsenopyrite (Aspy) and quartz (Qtz) in sample KG-SIS-7. Pyrr = pyrrhotite; Chl = chlorite; Musc = muscovite; Phl = phlogopite.

5.3. Lugushwa deposit

The metapelitic sample LG-SI-02 contains a fine-grained matrix that is mostly composed of biotite, quartz. Calcite, chlorite and muscovite were identified using EDS. An up to 710 μm wide calcite vein cuts through the rock. Pyrite is the main sulphide in this rock and is mostly fine-grained and anhedral in shape. A single, 4 mm wide euhedral pyrite shows quartz and some calcite precipitates in its strain shadow, suggesting local fluid mobility (Figure 5.5A). Pyrite in this sample is considered to be authigenic/metamorphic (HR-type), but considering its size, sulphur must have migrated over some distance towards the nucleation point. On the other hand there is no connection with any veins that might have supplied sulphur from distal sources. Accordingly, this pyrite crystal is classified as AM-HR-type.

Sample LG-SI-05 is a carbonaceous metapelite that consists of a fine-grained matrix that is mostly composed of quartz, biotite and minor calcite. The rock contains quartz lenses that measure up to 600 μm and some of these lenses contain pyrite. Furthermore, a network of quartz veins occurs in the rock. Some veins are disrupted into separate segments, suggesting deformation/boudinage after vein formation. One quartz-pyrite veinlet of up to ~570 μm thickness is cross-cut by an up to ~160 μm wide calcite vein (Figure 5.5B), indicating the mobility of a CO_2-rich fluid after the emplacement of the Si-S-rich hydrous fluid that formed the quartz vein. Pyrite occurs as anhedral grains and measure up to 1.4 mm. The largest pyrite grains occur in the quartz and calcite veins. This sample most likely shows pyrite that has formed from an external, distal or proximal hydrothermal fluid source. Pyrite in this sample is considered to be V-type pyrite (V) and VD HR pyrite as it is located/found within a quartz vein or along the vein boundary (Figure 5.5B). SIMS was, however, only performed on VD HR pyrite.

The carbonaceous metapelite sample LG-SI-06 consists of a fine-grained matrix that is mostly composed of quartz, chlorite, biotite and calcite. The rock contains a network of quartz lenses that are up to 1.6 mm thick. Some larger lenses contain pyrite grains. Quartz veinlets of up to ~250 μm thick also occur in the rock. The formation of these quartz lenses and veinlets may have been due to segregation or influx of fluids at different stages of the rock's evolution, in the course of hydrothermal/autometasomatic processes. Pyrite and chalcopyrite in the matrix are fine-grained and occur as anhedral grains. Some pyrites in a large quartz vein (> 4mm) are bigger (≤ 2.8 mm) and occur as subhedral to anhedral grains (Figure 5.5C). Pyrite analysed for SIMS in this sample is classified as AM HR due to the presence of quartz lenses indicating auto-metasomatic growth of pyrite in the host rock.
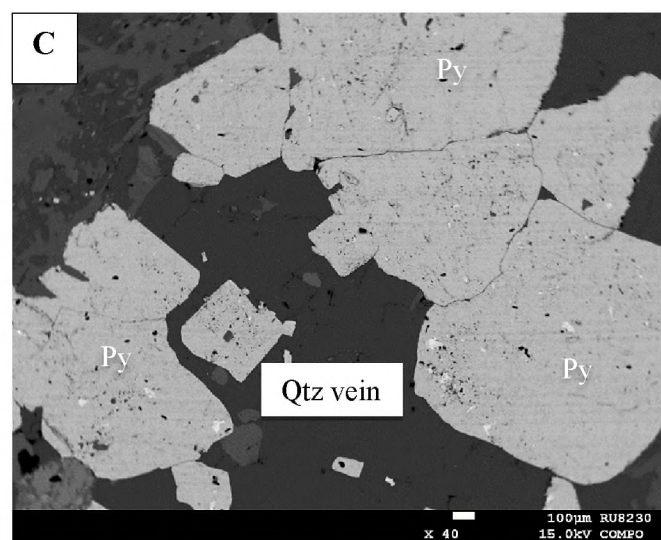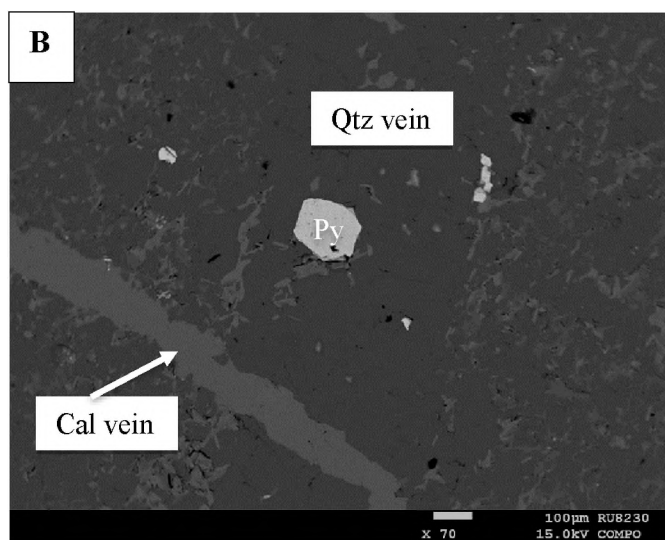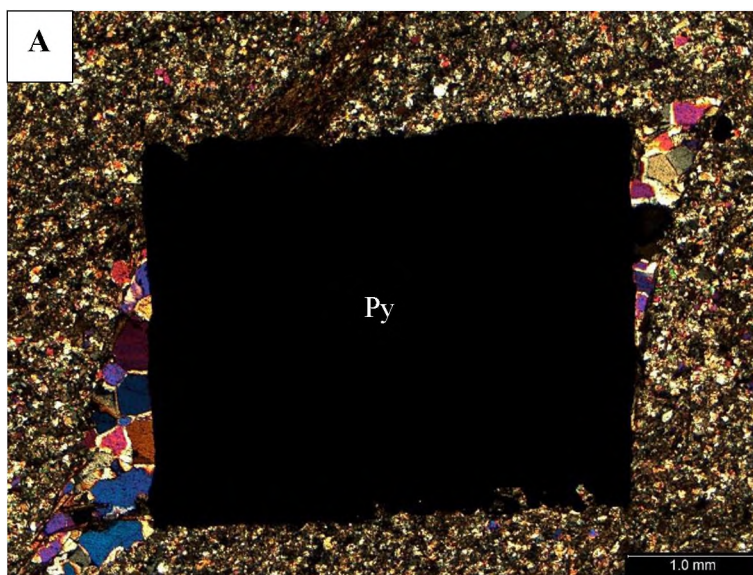
Figure 5.5: Photomicrographs of samples from Lugushwa. **A**) PPL photomicrograph of euhedral AM-HR pyrite (Py) with a quartz-calcite fringe structure adjacent to it in sample LG-SI-02. Quartz appeared to have grown from hydrous fluid in the strain shadow of pyrite. **B**) BSE image of a V-type pyrite (Py) grain in a quartz (Qtz) vein that is cross-cut by a calcite (Cal) vein in LG-SI-05. **C**) BSE image of LG-SI-06 showing AM HR pyrite (Py) grains in a quartz (Qtz) vein.

5.4. Namoya deposit

Sample NM-FS-1 is a schist that contains a continuous cleavage made up of quartz, biotite and chlorite. Their grain size is less than 100 μm. Minor muscovite and sphalerite were identified using EDS. Biotite, muscovite and chlorite seem to be aligned in a preferred orientation. An approximately 4 mm sigmoidal quartz lens with slightly inclined tips occurs in the matrix of the rock. A 3.5 mm euhedral pyrite formed in the pelitic matrix nearby but not within a fibrous quartz veinlet (Figure 5.6A). This pyrite crystal shows quartz and apatite inclusions. Smaller pyrites are randomly distributed in the metapelite matrix and occurs as anhedral grains of up to 100 μm in size. The sample shows no evidence of fluid infiltration and pyrite is considered to be authigenic/metamorphic (HR).

Sample NM-FS-2 is a schist that contains abundant, fine grained quartz and mica. Apatite, sphalerite and siderite were identified using EDS. Quartz lenses of up to 1.5 mm occur in the matrix. Pyrite grains are anhedral and do not exceed 50 μm. They are randomly distributed and occur as matrix phases without textural relationship to any phases that could be interpreted as hydrothermal precipitates. Quartz lenses are spatially separated from matrix pyrite. Accordingly the pyrite is interpreted as authigenic (HR-type pyrite) phase that formed from local sulphur. Chalcopyrite was also identified and occurs as randomly distributed anhedral grains within the metapelite matrix.

Sample NM-SI-1 is an altered dolerite that contains a fine-grained matrix that is mostly composed of quartz and chlorite. Minor calcite, rutile and apatite were identified using EDS. Two quartz veinlets, up to 1 mm wide, cross-cut the host rock. A cluster of pyrite occurs within the host rock but nearby the boundary to one of the quartz veins (Figure 5.6B). This pyrite is anhedral and up to 180 μm in size. This cluster of pyrite is interpreted to come into existence as a result of dissemination from the vein into the host rock during fluid infiltration. However, V pyrite in quartz vein was analysed for SIMS.

Sample NM-SI-2 is a dolerite that is mostly composed of a fine-grained quartz and carbonate matrix. Calcite was identified as the main carbonate. Rutile, chlorite and apatite were identified using EDS. A network of quartz veins up to 3.9 mm wide cross-cut the host rock. Adjacent to a 2.4 mm quartz vein is a 1.9 mm wide subhedral arsenopyrite grain with apatite, rutile and gold inclusions up to 379 μm in size (Figure 5.6C). There is no spatial relationship between this arsenopyrite and pyrite in the matrix. Pyrite is mostly anhedral and measure up to 80 μm in size. The largest grains occur within a 3 mm wide quartz vein. The appearance of pyrite and arsenopyrite in the quartz veins suggests that the dolerite was infiltrated by Si-S rich fluids which formed the quartz veins and the sulphides. This further suggests that the gold in this sample was introduced by either an external, distal or proximal hydrothermal fluid source

Sample NM-SI-3 is also a dolerite that contains a fine-grained matrix that is mostly composed of carbonate, quartz, and chlorite. Rutile, apatite and calcite were identified using EDS. A quartz vein

of up to 3.5 mm cross-cuts the host rock. The vein quartz show a fibrous texture (Figure 5.6D). Some up to 157 μm pyrite either occur along the boundary of the quartz vein or within the vein. Pyrite in the matrix is randomly distributed and occurs as anhedral grains that measure up to 200 μm in size. These pyrites are not spatially related to the quartz vein and are interpreted to be authigenic/metamorphic (HR pyrite). However, SIMS analyses was performed on V pyrite

Sample NM-SI-4 is a schist that contains a fine-grained matrix that is mostly composed of carbonates, muscovite and chlorite. Calcite was identified as the main carbonate using EDS. Other minerals that were also identified using EDS are: ankerite, plagioclase, and apatite. An up to 280 μm wide quartz veinlet cross-cuts the host rock. Arsenopyrite and pyrite are randomly distributed in the metapelite matrix. They are mostly anhedral in shape and measure up to 100 μm in size. Pyrite is not spatially separated from the quartz veinlet and is thus interpreted to be authigenic/metamorphic (HR-type).

Sample NM-SI-5 is a schist that consists of a fine-grained matrix that is mostly made up of quartz, chlorite, and muscovite. Apatite, siderite and zircon were identified using EDS. An up to ~2.3 mm wide pyrite vein cross-cuts the host rock (Figure 5.7A). Sphalerite, quartz and chlorite grains are included in the vein. An 890 μm long quartz fibrous vein occurs adjacent to the pyrite vein. Pyrites in the matrix are randomly distributed and occur as anhedral grains measuring up to ~250 μm in size. Only V pyrite was analysed for SIMS.

Sample NM-SI-6 is a schist that consists of a fine-grained matrix that is mostly made up of quartz and muscovite. Minor siderite and apatite were identified using EDS. Siderite occurs as globules that measure up to 420 μm. Pyrites in the pelitic matrix occur as randomly distributed subhedral to anhedral grains that are up to 1.4 mm in size. A ~1.3 mm long pyrite stringer occurs in the matrix of the host rock (Figure 5.7B). The sample shows no evidence of fluid infiltration and pyrite is therefore interpreted to be authigenic/metamorphic.

Sample NM-SI-7 is a schist that consists of a fine-grained matrix that is mostly composed of quartz and muscovite. Minor apatite and siderite were identified using EDS. A quartz vein, up to 4 mm wide, cross-cuts the host rock. Pyrite generally occur as anhedral to subhedral grains along the vein margin (Figure 5.7C). Larger grains are mostly euhedral and measure up to 730 μm in size. This pyrite is texturally part of the vein assemblage and hence of hydrothermal origin. Siderite forms irregularly shaped aggregates within the quartz vein. Pyrite in this sample is therefore considered as VD HR pyrite.

Sample NM-SI-8 is a schist that consists of a fine-grained quartz-muscovite matrix. Minor siderite is present but was only identified by using EDS. Pyrite generally occur as anhedral to subhedral grains and measure up to 330 μm in size (Figure 5.7D). Some pyrites have muscovite, quartz and siderite inclusions. Pyrite forms part of the pelitic matrix and there is no textural evidence of hydrothermal activity contributing to pyrite formation. Accordingly, this pyrite is interpreted as an authigenic phase/HR pyrite that formed from the host rock material.
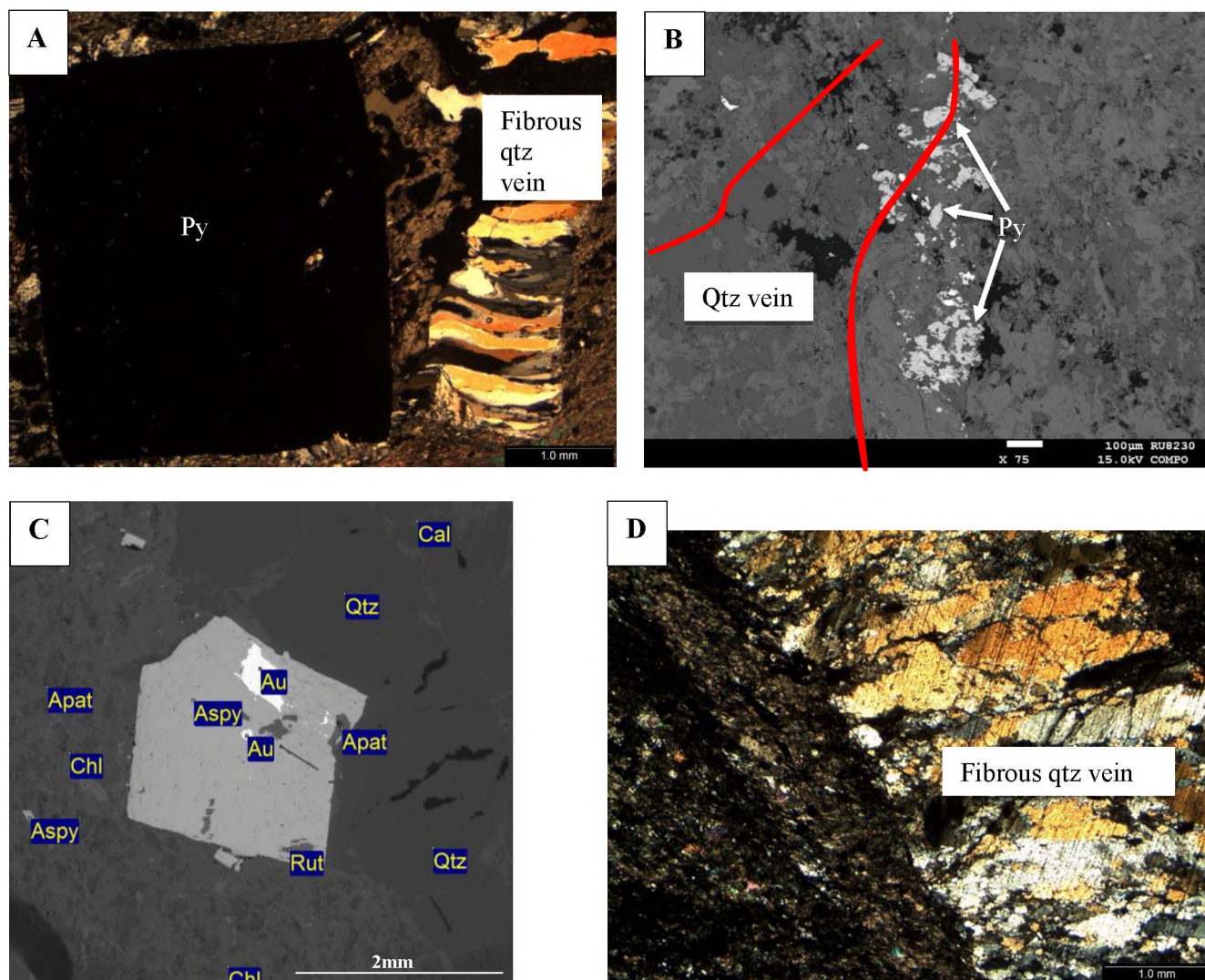
Figure 5.6: Photomicrographs of samples from Namoya. **A)** XPL photomicrograph showing a euhedral HR pyrite (Py) grain adjacent to a quartz (Qtz) fibrous vein in NM-FS-1. **B)** BSE image of a cluster of VD HR and V-type pyrite (Py) adjacent to a quartz vein in NM-SI-1. **C)** BSE image showing arsenopyrite (Aspy) with inclusions of rutile (Rut), fluorapatite (Apat) and gold (Au) in NM-SI-2. **D)** XPL photomicrograph of a fibrous quartz (qtz) vein in NM-SI-3. Cal = calcite; Chl = chlorite.
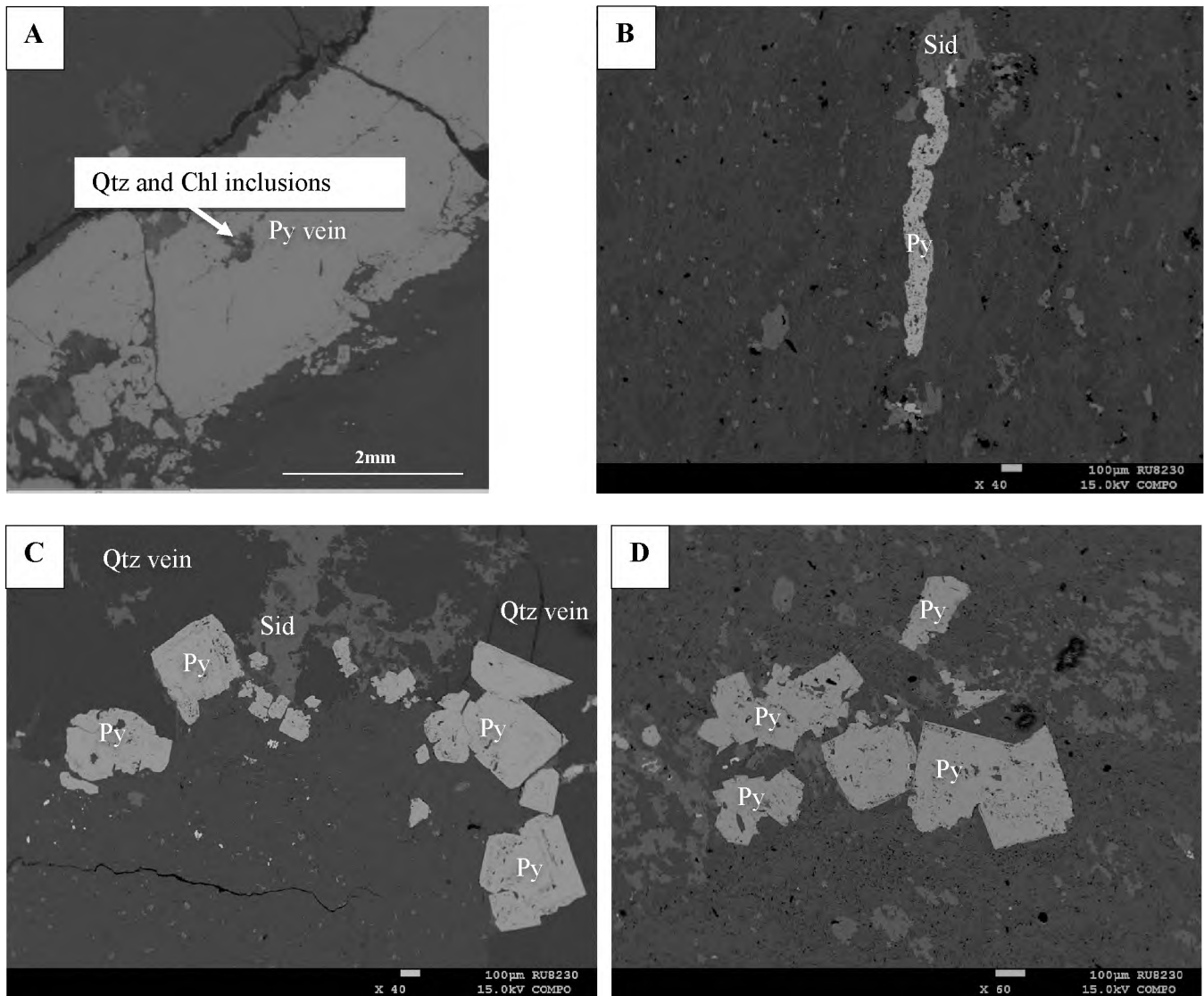
Figure 5.7: Photomicrographs of samples from Namoya. **A)** BSE image of a pyrite (Py) vein with inclusions of quartz (Qtz) and chlorite (Chl) in NM-SI-5. **B)** BSE image of a pyrite stringer (Py) in host rock NM-SI-6. **C)** BSE image showing subhedral VD HR pyrite (Py) along a margin of a quartz-siderite vein in sample NM-SI-7. Sid = siderite. **D)** BSE image of sample NM-SI-8 showing a cluster of HR pyrite in a pelitic matrix.

6. Pyrite and associated mineral chemistry

Pyrite has the structural formula FeS_2 which corresponds to approximately 53.3 wt. % S and 46.7 wt. % Fe. Pyrite has a cubic crystal structure in which each Fe atom is octahedrally coordinated with six S atoms. The substitution of other elements for Fe is limited at greenschist facies temperatures, but Cu, As, Pb, Mn, and Co may be present as trace or minor elements. Deer et al. (1992) associate larger amounts of these elements with small impurities containing other sulphides, such as chalcopyrite, arsenopyrite or galena. At temperatures exceeding ~600 °C more extensive substitutions of Fe and other elements appears to be possible (Deer et al., 1992) but such temperatures were not reached in the host rocks of the hydrothermal system of the TNGB. Pyrite is reported as stable up to granulite facies conditions where it melts to pyrrhotite and liquid (Deer et al., 1992).

Pyrrhotite, a common sulphide in the host rocks of the TNGB, is a phase that may be variable in its Fe-S ratio, ranging from Fe_7S_8 to FeS. The latter is referred to as troilite. Arsenopyrite (FeAsS) is abundant in both the host rocks and in the vein system. Chalcopyrite ($CuFeS_2$) is less commonly, present in host rocks and hydrothermal veins. Pyrite typically contains traces or minor contents (>0.1 wt%) of As. The pyrite from the TNGB contains variable amounts of As and other trace elements which will be described in section 6.2.2.

The main purpose of this study is the analysis of S isotopes in pyrite, and therefore other sulphides have been analysed only using EDS, mainly in order to identify them. In this chapter these results are reported in the form of spectra and as selected analyses, but fully quantitative analysis of major and trace elements (EPMA) is only reported for pyrite.

Polished thin sections from the TNGB were analysed by EDS and EPMA for their mineral composition and pyrite chemistry to provide detailed context to the pyrite variation, distribution and association of pyrite with the matrix minerals. The analytical methods have been described in Chapter 3.3. This chapter presents the results of EDS analysis in section 6.1, and EPMA results in section 6.2. EDS data are documented in form of BSE imagery, semi-quantitative spectra, and in table format where selected representative analyses are shown (Table 6.1.1 to 6.1.10). Section 6.2 contains quantitative major, minor and trace elemental compositions of pyrite (Table 6.2.1 to 6.2.7), and element maps.

6.1. EDS Data

6.1.1. Twangiza deposit

Two types of sulphides were identified in host rock samples from Twangiza: pyrite and arsenopyrite. Pyrite is either randomly distributed in the matrix or occurs in clusters of several grains. Pyrite often contains inclusions of matrix phases such as plagioclase and phlogopite. Some pyrite grains were found to be included in arsenopyrite (Figure 6.1A). An approximately 39 μm native gold grain is included in HR pyrite in sample TW-FS-05 (Figure 6.1B). The gold is pure without any other elements detectable with

EDS (Figure 6.2). Pyrite appears to be homogenous with compositions of close to FeS_2 (Table 6.1.1). Minor elements were not identified via EDS.

Table 6.1.1: Representative EDS pyrite compositions from host rock samples in Twangiza. Data is presented in wt. %. TW-FS-07 analyses are normalised to 100 wt. %. Ions are normalised to 3 ions.

Sample Name	TW-FS-03	TW-FS-03	TW-FS-05	TW-FS-05	TW-FS-07	TW-FS-07
S (wt. %)	56.28	56.12	56.38	56.79	56.34	55.90
Fe (wt. %)	45.38	44.19	45.56	44.63	43.66	44.10
As (wt. %)	0.00	0.00	0.00	0.00	0.00	0.00
Cu (wt. %)	0.00	0.00	0.00	0.00	0.00	0.00
Total (wt. %)	101.66	100.31	101.94	101.42	100.00	100.00
S	2.05	2.07	2.05	2.07	2.07	2.08
Fe	0.95	0.93	0.95	0.93	0.93	0.92
As	0.00	0.00	0.00	0.00	0.00	0.00
Cu	0.00	0.00	0.00	0.00	0.00	0.00
Total ions	3.00	3.00	3.00	3.00	3.00	3.00

Minerals that were identified in the matrix are: mainly rutile, fluorapatite, plagioclase, quartz, phlogopite and minor zircon, siderite and muscovite (Table 6.1.2). Phlogopite and plagioclase form inclusions in some pyrite grains. Plagioclase is albite-rich with anorthite contents less than 4 mol%.

Table 6.1.2: Representative EDS analyses of matrix phases in host rock samples from Twangiza. Zircon and muscovite analyses are normalised to 100 wt. %. and 96 wt. %, respectively Data is represented in wt. %.

Sample Name	TW-FS-03	TW-FS-03	TW-FS-03	TW-FS-03	TW-FS-05	TW-FS-05	TW-FS-07	TW-FS-07
Mineral type	Rutile	Quartz	Zircon	Fluorapatite	Plagioclase	Muscovite	Phlogopite	Siderite
SiO_2	0.00	101.31	30.82	0.00	71.24	51.30	45.07	0.00
Na_2O	0.00	0.00	0.00	0.00	10.74	0.00	0.00	0.00
MgO	0.00	0.00	0.00	0.00	0.00	1.17	26.87	1.65
Al_2O_3	0.00	0.00	0.00	0.00	20.28	34.86	10.56	0.00
K_2O	0.00	0.00	0.00	0.00	0.61	8.67	9.05	0.00
CaO	0.00	0.00	0.00	53.71	0.00	0.00	0.00	1.35
TiO_2	98.16	0.00	0.00	0.00	0.00	0.00	0.00	0.00
ZrO_2	0.00	0.00	69.18	0.00	0.00	0.00	0.00	0.00
FeO	0.00	0.00	0.00	0.00	0.00	0.00	2.49	47.47
MnO	0.00	0.00	0.00	0.00	0.00	0.00	0.00	3.43
P_2O_5	0.00	0.00	0.00	43.74	0.00	0.00	0.00	0.00
Total (wt. %)	98.16	101.31	100.00	97.45	103.29	96.00	94.04	53.90

Three types of sulphides were identified in hydrothermal vein samples from Twangiza: pyrite, arsenopyrite, and minor chalcopyrite. Pyrite in these samples either occurs along vein boundaries or within the veins. Minor elements were not identified in vein pyrite and it appears to be homogenous with compositions close to FeS_2.

Table 6.1.3: Representative EDS pyrite compositions from hydrothermal vein samples in Twangiza. Data is presented in wt. %. Analyses are normalised to 100 wt. %. Ions are normalised to 3 ions.

Sample Name	T3	T3	T9	T9	T12	T12	T25	T25
S (wt. %)	54.85	54.63	55.18	55.54	55.20	55.64	54.74	54.32
Fe (wt. %)	45.15	45.37	44.82	44.46	44.80	44.36	45.25	45.68
As (wt. %)	0.00	0.00	0.00	0.00	0.00	0.00	0.00	0.00
Cu (wt. %)	0.00	0.00	0.00	0.00	0.00	0.00	0.00	0.00
Total (wt. %)	100.00	100.00	100.00	100.00	100.00	100.00	100.00	100.00
S	2.04	2.03	2.05	2.06	2.05	2.06	2.04	2.02
Fe	0.96	0.97	0.95	0.94	0.95	0.94	0.96	0.98
As	0.00	0.00	0.00	0.00	0.00	0.00	0.00	0.00
Cu	0.00	0.00	0.00	0.00	0.00	0.00	0.00	0.00
Total ions	3.00	3.00	3.00	3.00	3.00	3.00	3.00	3.00

Minerals that were identified in the matrix are: siderite, fluorapatite, quartz, muscovite, chlorite, calcite, ankerite and minor plagioclase and periclase (Table 6.1.4). Calcite and periclase are included in some pyrite grains (Figure 6.1C and D). Periclase is likely to have formed as a result of the replacement of dolomite. Chamosite is the main chlorite mineral in the samples. According to Deer et al. (1992), most siderite forms from the carbonation of chamosite. Since both siderite and chamosite are present in the Twangiza vein samples, a genetic relationship is possible, implying secondary influx of CO_2-rich fluids.

Table 6.1.4: Representative EDS analyses of matrix phases in hydrothermal vein samples from Twangiza. Plagioclase and muscovite analyses are normalised to 100 wt. % and 96 wt. %, respectively. Data is represented in wt. %.

Sample Name	T3	T3	T3	T9	T9	T9	T12	T12	T25
Mineral type	Periclase	Fluorapatite	Plagioclase	Ankerite	Calcite	Quartz	Chlorite	Muscovite	Siderite
SiO_2	0.00	0.00	70.75	0.00	0.00	100.98	26.01	49.92	0.00
Na_2O	0.00	0.00	10.92	0.00	0.00	0.00	0.00	0.63	0.00
MgO	92.69	0.00	0.00	13.42	0.00	0.00	13.03	0.58	1.23
Al_2O_3	0.00	0.00	18.33	0.00	0.00	0.00	20.48	35.42	0.00
K_2O	0.00	0.00	0.00	0.00	0.00	0.00	0.00	8.45	0.00
CaO	0.00	54.10	0.00	29.89	51.99	0.00	0.00	0.00	1.06
FeO	6.66	0.00	0.00	10.85	0.00	0.00	25.00	1.00	58.46
MnO	0.00	0.00	0.00	1.76	0.00	0.00	0.00	0.00	1.02
P_2O_5	0.00	47.46	0.00	0.00.	0.00	0.00	0.00	0.00	0.00
Total (wt. %)	99.35	101.56	100.00	55.92	51.99	100.98	82.01	96.00	53.90
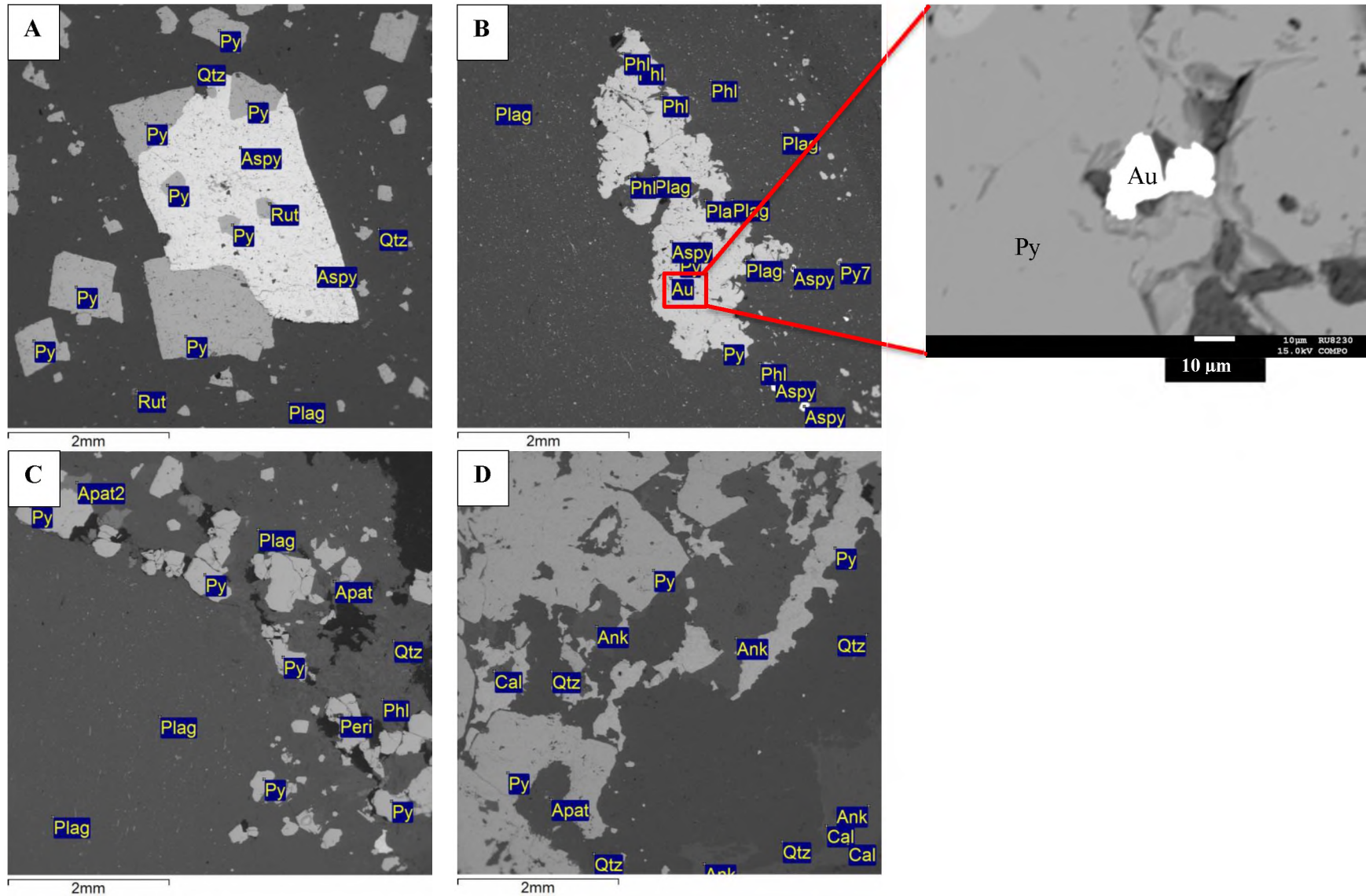
Figure 6.1: BSE photomicrographs of samples from Twangiza. **A)** Pyrite (Py) inclusions in a subhedral arsenopyrite (Aspy) grain in sample TW-FS-03. **B)** Sample TW-FS-05 showing native gold (Au) grain included in HR pyrite (Py). Phlogopite (Phl), arsenopyrite (Aspy), and plagioclase (Plag) are also included in the pyrite (Py). **C)** Sample T3 showing periclase (Peri) included in V-type pyrite (Py) **D)** Sample T12 showing calcite (Cal) included in V-type pyrite (Py). Qtz = quartz; Plag = plagioclase; Rut = rutile; Apat = fluorapatite; Ank = ankerite.
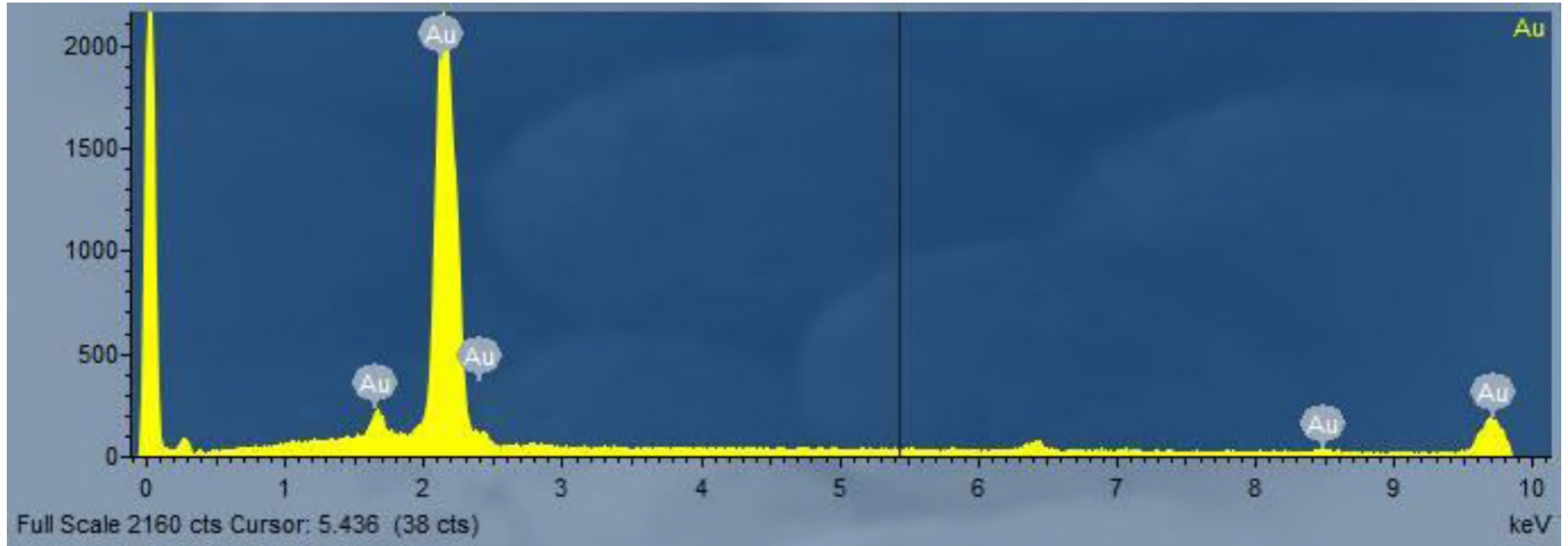
Figure 6.2: EDS spectrum of a gold (Au) crystal in HR pyrite from sample TW-FS-05. Gold is practically pure. The small peak at 6.4 keV is at the position of the main Fe peak, suggesting the presence of iron traces in the excitation volume.

6.1.2. Kamituga deposit

Six types of sulphides were identified in samples from Kamituga: pyrite, arsenopyrite, pyrrhotite, sphalerite, chalcopyrite, and galena (Figure 6.3). The sample in which galena was identified, however, did not contain any pyrite and will therefore not be discussed further. Pyrite occurs as either HR pyrite in samples KG-FS-1, KG-FS-2, KG-SIS-3, KG-SIS-5, KG-SIS-6 and KG-SIS-7 or as VD HR and V-type pyrite in samples KG-SIS-2 and KG-SIS7 (Table 3.3.1). Also in the Kamituga samples, pyrite is nearly pure FeS_2 with little or no minor elements that could be detected using EDS (Table 6.1.5).

Table 6.1.5: Representative EDS pyrite compositions from hydrothermal vein samples in Kamituga. Data is presented in wt. %. Analyses are normalised to 100 wt. %. Ions are normalised to 3 ions.

Sample Name	KG-FS-1	KG-FS-2	KG-SIS-3	KG-SIS-5	KG-SIS-6	KG-SIS-2	KG-SIS-7
Pyrite type	HR	HR	HR	HR	HR	VD HR and V	VD HR and V
S (wt. %)	56.69	56.82	53.33	52.90	54.56	54.34	54.24
Fe (wt. %)	43.31	43.18	46.67	47.10	45.44	45.66	45.76
As (wt. %)	0.00	0.00	0.00	0.00	0.00	0.00	0.00
Cu (wt. %)	0.00	0.00	0.00	0.00	0.00	0.00	0.00
Total (wt. %)	100.00	100.00	100.00	100.00	100.00	100.00	100.00
S	2.09	2.09	2.00	1.99	2.03	2.02	2.02
Fe	0.91	0.91	1.00	1.01	0.97	0.98	0.98
As	0.00	0.00	0.00	0.00	0.00	0.00	0.00
Cu	0.00	0.00	0.00	0.00	0.00	0.00	0.00
Total ions	3.00	3.00	3.00	3.00	3.00	3.00	3.00

Minerals that were identified in the matrix are: quartz, chlorite, biotite, garnet, fluorapatite, muscovite, plagioclase, siderite, and minor phlogopite, ilmenite, and rutile (Table 6.1.6). Plagioclase is albite-rich with anorthite contents less than 32 mol%. The chlorite is close to the Fe-endmember chamosite . Like in the Twangiza samples siderite may have formed from the carbonation of chamosite (Deer et al., 1992). The presence of chamosite and siderite implies secondary influx of CO_2-rich fluids in Kamituga. Siderite, quartz, biotite, rutile, arsenopyrite and chalcopyrite also occur in pyrite-rich veins (Figure 6.4).

Table 6.1.6: Representative EDS analyses of matrix phases in samples from Kamituga. Rutile and muscovite analyses are normalised to 100 wt. % and 96 wt. % respectively. Data is represented in wt. %.

Sample Name	KG-FS-2	KG-FS-2	KG-FS-2	KG-SIS-3	KG-SIS-5	KG-SIS-5	KG-SIS-6	KG-SIS-2	KG-SIS-7
Mineral type	Chlorite	Biotite	Garnet	Muscovite	Quartz	Siderite	Phlogopite	Ilmenite	Rutile
SiO_2	26.10	38.69	39.58	47.52	100.35	0.00	45.39	0.00	0.00
Na_2O	0.00	0.00	0.00	0.70	0.00	0.00	0.00	0.00	0.00
MgO	15.57	10.37	2.31	1.38	0.00	0.82	18.89	0.00	0.00
Al_2O_3	21.78	18.38	21.10	32.69	0.00	0.00	13.11	0.00	0.00
K_2O	0.00	9.96	0.00	10.24	0.00	0.00	9.21	0.00	0.00
CaO	0.00	0.00	4.61	0.00	0.00	1.73	0.00	0.00	0.00
TiO_2	0.00	1.64	0.00	0.50	0.00	0.00	0.85	54.27	100.00
FeO	21.77	17.96	27.06	2.98	0.00	60.44	9.29	44.16	0.00
MnO	0.00	0.00	6.82	0.00	0.00	1.32	0.00	2.88	0.00
Total wt. %)	85.22	97.00	101.48	96.00	100.35	64.31	96.74	101.31	100.00
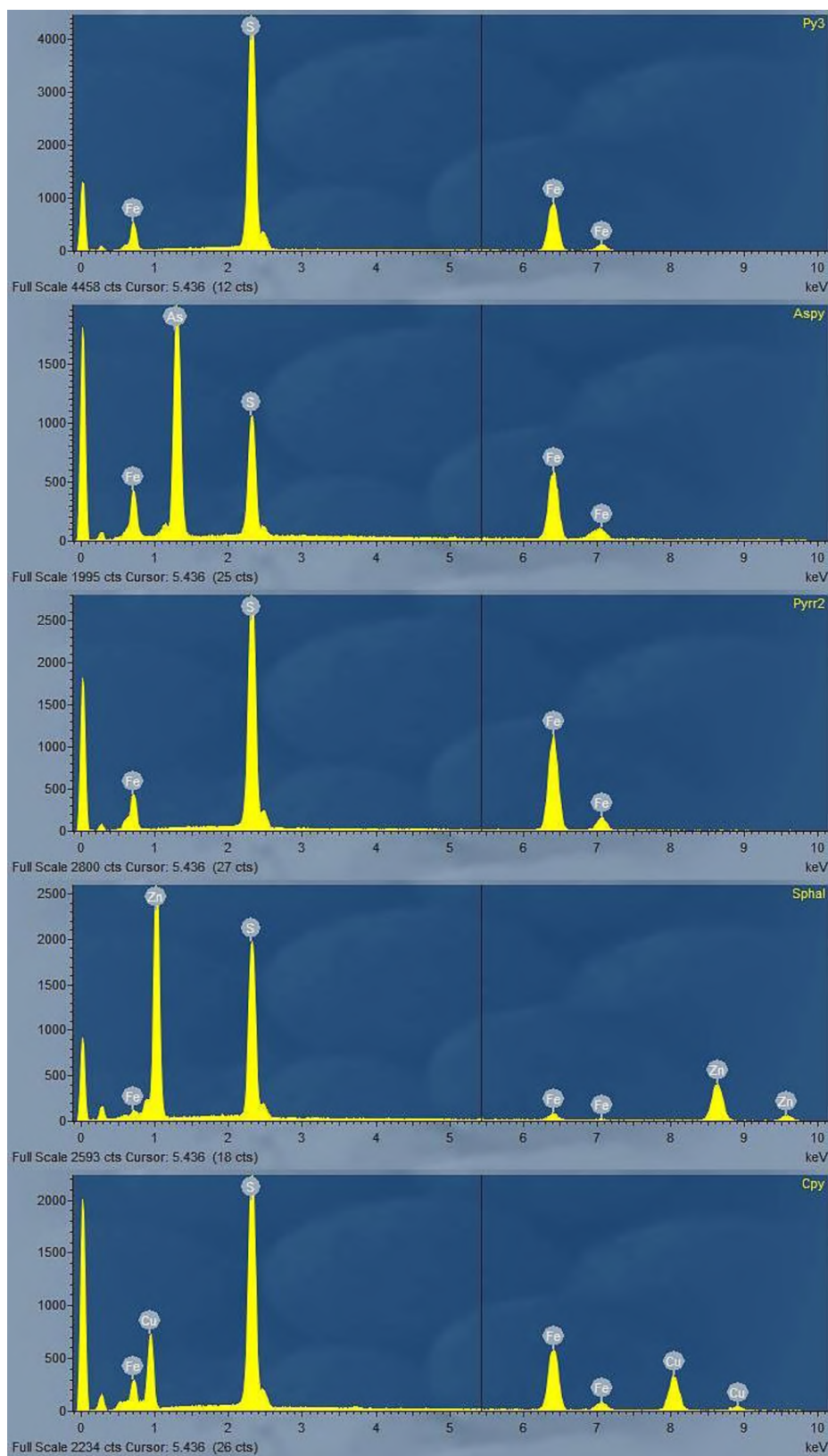
Figure 6.3: EDS spectra of selected sulphides from Kamituga. Py = Pyrite; Aspy = Arsenopyrite; Pyrr = Pyrrhotite; Sphal = Sphalerite; Cpy = Chalcopyrite.
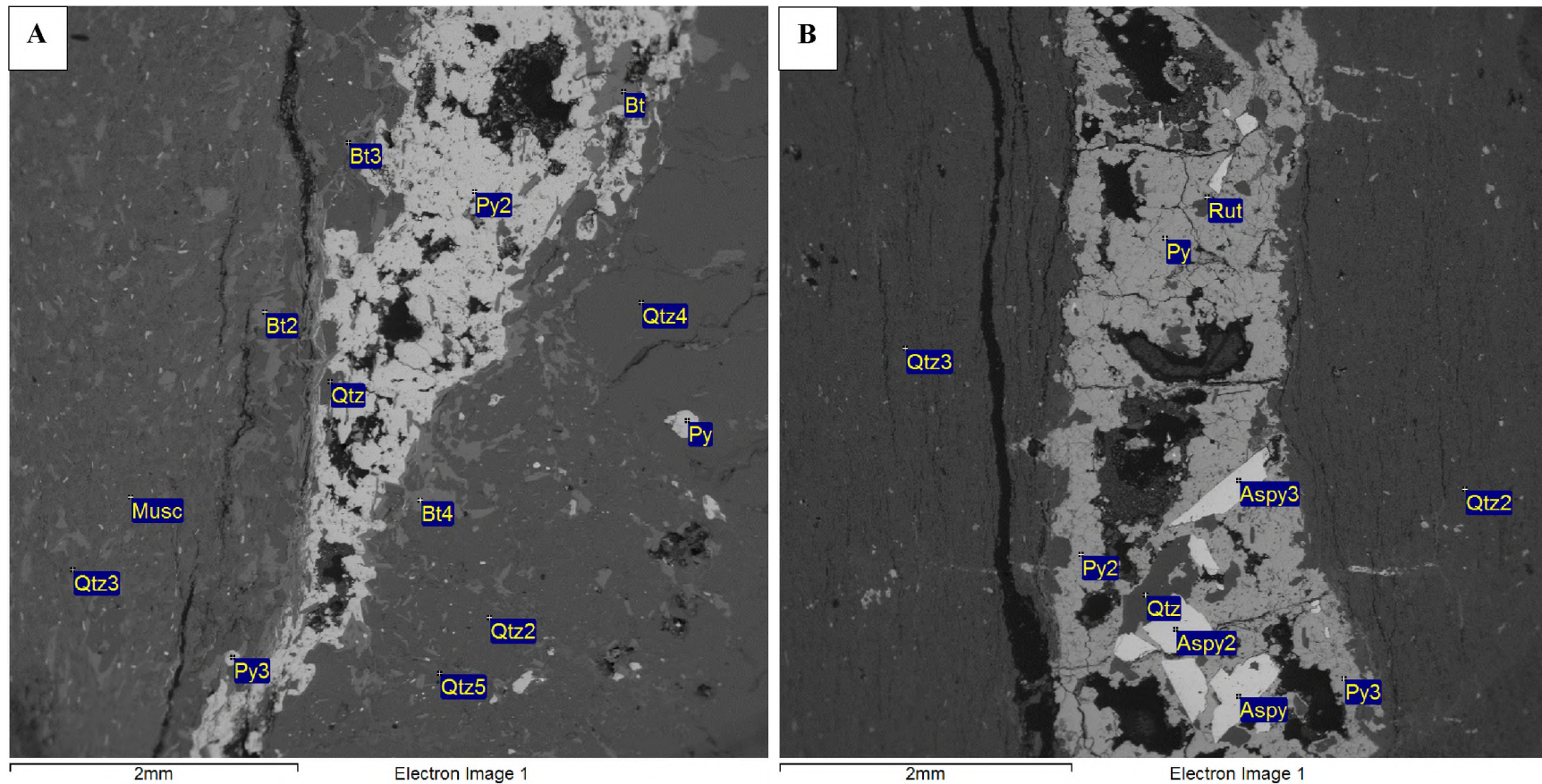
Figure 6.4: BSE images of samples from Kamituga. **A)** Sample KG-SIS-3 showing biotite (Bt) and quartz (Qtz) grains included in a pyrite vein (Py). **B)** Sample KG-SIS-7 showing rutile (Rut), quartz (Qtz) and arsenopyrite (Aspy) in a pyrite vein. Musc = muscovite.

6.1.3. Lugushwa deposit

Three types of sulphides were identified in samples from Lugushwa: pyrite, pyrrhotite, and chalcopyrite. Samples that contained pyrrhotite did not have any pyrite and will not be discussed any further. Pyrite occurs as either HR pyrite in sample LG-SI-02, AM HR pyrite in samples and LG-SI-02 LG-SI-06, or as V and VD HR pyrite in sample LG-SI-05 (Table 2 and Table 6.1.7). Sample LG-SI-02 single, 4 mm wide euhedral pyrite crystal has two quartz fringe structures adjacent to it (Figure 6.5A). Most pyrite grains appear to be homogenous and pure FeS_2 without minor elements above the detection limit of EDS. Sample LG-SI-06 is an exception with three pyrite grains that contain minor arsenic at 0.83, 0.65 and 0.80 wt. %, respectively. These values are from normalised results. These samples were also analysed using EPMA and will be discussed further in chapter 6.2.

Table 6.1.7: Representative EDS pyrite compositions from hydrothermal vein samples in Lugushwa. Data is presented in wt. %. LG-SI-05 V pyrite and LG-SI-06 analyses are normalised to 100 wt. %. Ions are normalised to 3 ions.

Sample Name	LG-SI-02	LG-SI-05	LG-SI-05	LG-SI-06
Pyrite type	HR	VD HR	V	AM HR
S (wt. %)	54.12	55.19	54.78	54.28
Fe (wt. %)	48.06	46.23	45.22	44.90
As (wt. %)	0.00	0.00	0.00	0.83
Cu (wt. %)	0.00	0.00	0.00	0.00
Total (wt. %)	102.18	101.42	100.00	100.00
S	1.99	2.03	2.04	2.03
Fe	1.01	0.97	0.96	0.96
As	0.00	0.00	0.00	0.01
Cu	0.00	0.00	0.00	0.00
Total ions	3.00	3.00	3.00	3.00

Minerals that were identified in the matrix are: mainly quartz, sericite/muscovite, chlorite, calcite, biotite, rutile, fluorapatite, with minor zircon and plagioclase (Table 6.1.8). Chlorite is chamositic (Fe-rich) plagioclase albitic (less than 2 mol% anorthite), as seen in Twangiza and Kamituga. Quartz and chalcopyrite form inclusions in some pyrite grains (Figure 6.5B).

Table 6.1.8: Representative EDS analyses of matrix phases in samples from Lugushwa. Data is represented in wt. %. Muscovite, rutile and fluorapatite analyses are normalised to 96,100 and 91 wt. %, respectively.

Sample Name	LG-SI-02	LG-SI-02	LG-SI-02	LG-SI-05	LG-SI-05	LG-SI-06	LG-SI-06	LG-SI-06
Mineral type	Calcite	Chlorite	Muscovite	Rutile	Zircon	Fluorapatite	Biotite	Quartz
SiO_2	0.00	28.40	49.40	0.00	31.69	0.00	37.70	102.73
Na_2O	0.00	0.00	0.00	0.00	0.00	0.00	0.00	0.00
MgO	0.00	21.55	1.72	0.00	0.00	0.00	13.67	0.00
Al_2O_3	0.00	21.30	31.02	0.00	0.00	0.00	16.92	0.00
K_2O	0.00	0.00	10.99	0.00	0.00	0.00	8.70	0.00
CaO	55.37	0.00	0.00	0.00	0.00	53.11	0.00	0.00
TiO_2	0.00	0.00	0.71	99.09	0.00	0.00	1.62	0.00
FeO	0.00	14.81	2.15	0.91	0.00	0.00	16.41	0.00
MnO	0.69	0.00	0.00	0.00	0.00	0.00	0.00	0.00
ZrO_2	0.00	0.00	0.00	0.00	65.84	0.00	0.00	0.00
P_2O_5	0.00	0.00	0.00	0.00	0.00	45.89	0.00	0.00
Total (wt. %)	56.06	86.06	96.00	100.00	64.31	99.00	95.02	102.73
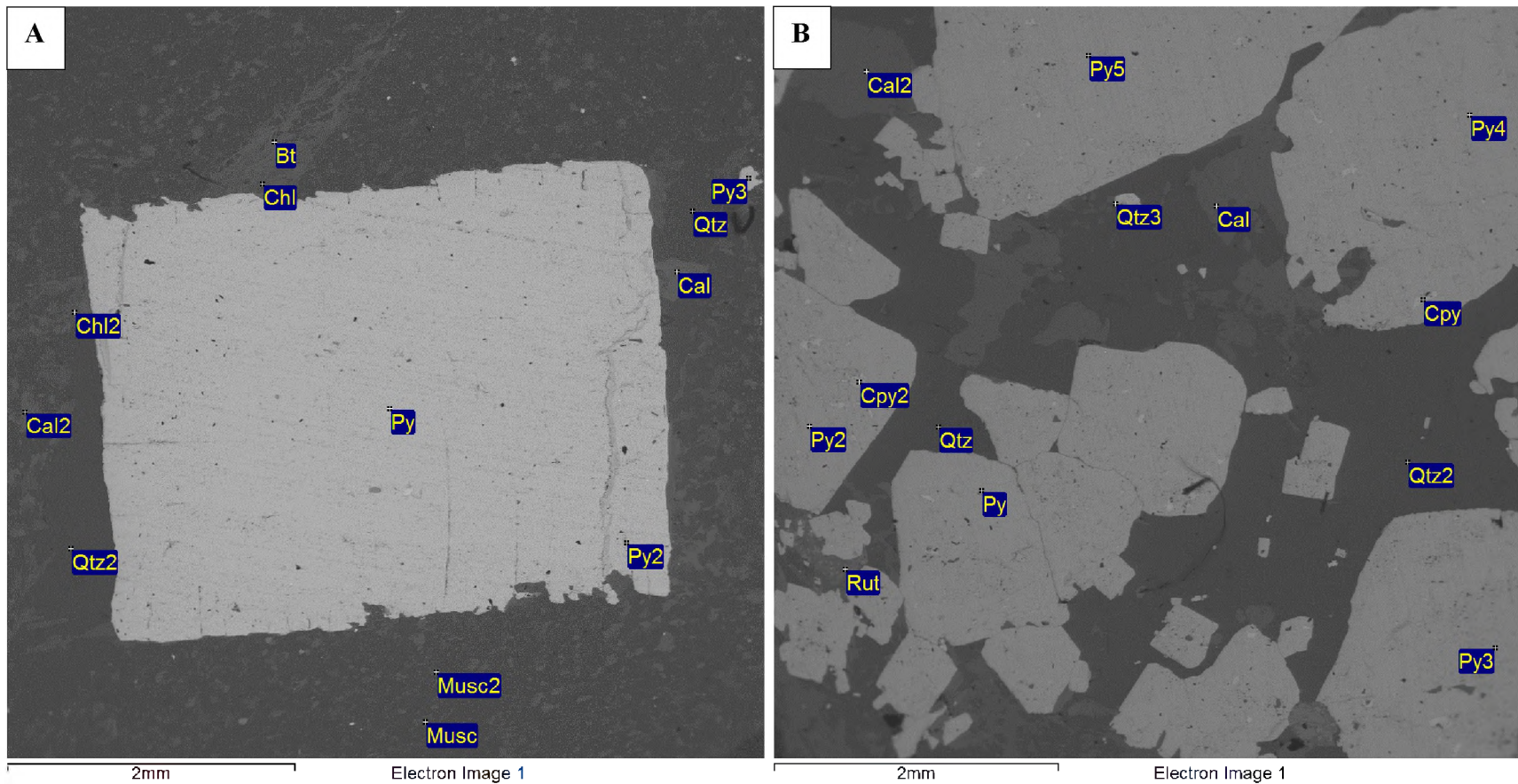
Figure 6.5: BSE images of samples from Lugushwa. **A)** Cube-shaped AM HR pyrite (Py) grain with two quartz fringe structures adjacent to it in host rock sample LG-SI-02. **B)** Sample LG-SI-06 showing Quartz (Qtz) and chalcopyrite (Cpy) grains included in some AM HR pyrite (Py). Musc = muscovite; Cal = calcite; Bt = biotite; Rut = rutile.

6.1.4. Namoya deposit

Five types of sulphides were identified in samples from Namoya: pyrite, sphalerite, chalcopyrite, arsenopyrite, and pyrrhotite (Figure 6.6; selected spectra). Pyrite occurs as HR pyrite in samples NM-FS-1, NM-FS-2, NM-SI-4 NM-SI-6 and NM-SI-8; VD HR pyrite in sample NM-SI-7; and V pyrite in samples NM-SI-1,-2,-3 and NM-SI-5 (Table 2 and Table 6.1.9). Some pyrite grains form inclusions in siderite (Figure 6.7A) in sample NM-SI-5. Native gold of up to 379 μm in size are form inclusions in a 1.9 mm wide subhedral arsenopyrite grain in sample NM-SI-2 (Figure 6.7B). The gold contains up to 2.89 at. % silver (Figure 6.8). Also pyrite does not show minor elements. Sample NM-SI-1, however, has a pyrite grain that contains 1.38 wt. % arsenic (from normalised results).

Table 6.1.9: Representative EDS pyrite compositions from hydrothermal vein samples in Namoya. Data is presented in wt. %. Analyses are normalised to 100 wt. %. Ions are normalised to 3 ions.

Sample Name	NM-FS-1	NM-FS-2	NM-SI-1	NM-SI-2	NM-SI-3	NM-SI-4	NM-SI-5	NM-SI-6	NM-SI-7	NM-SI-8
Pyrite type	HR	HR	V	V	V	V	V	HR	VD HR	HR
S (wt. %)	56.78	56.79	54.55	54.35	56.11	55.42	54.99	54.08	53.90	53.91
Fe (wt. %)	43.22	43.21	44.07	45.65	43.89	44.58	45.01	45.92	46.10	46.09
As (wt. %)	0.00	0.00	1.38	0.00	0.00	0.00	0.00	0.00	0.00	0.00
Cu (wt. %)	0.00	0.00	0.00	0.00	0.00	0.00	0.00	0.00	0.00	0.00
Total (wt. %)	100.00	100.00	100.00	100.00	100.00	100.00	100.00	100.00	100.00	100.00
S	2.10	2.08	2.034	2.03	2.07	2.05	2.04	2.02	2.01	2.01
Fe	0.90	0.92	0.943	0.97	0.93	0.95	0.96	0.98	0.99	0.99
As	0.00	0.00	0.022	0.00	0.00	0.00	0.00	0.00	0.00	0.00
Cu	0.00	0.00	0.00	0.00	0.00	0.00	0.00	0.00	0.00	0.00
Total ions	3.00	3.00	3.00	3.00	3.00	3.00	3.00	3.00	3.00	3.00

Minerals that were identified in the matrix are: mainly quartz, chlorite, sericite/muscovite, fluorapatite, rutile, siderite, calcite with minor, plagioclase, ankerite, and zircon (Table 6.1.10). Chlorite is chamositic (Fe-rich) and plagioclase is albitic (less than 4 mol% anorthite), as seen in the other TNGB deposits. Like in the Twangiza and Kamituga samples, siderite may have formed from the from the carbonation of chamosite (Deer et al., 1992). Furthermore, quartz, chlorite, sphalerite, apatite and sericite/muscovite form inclusions in some pyrite (Figure 6.7C and D).

Table 6.1.10: Representative EDS analyses of matrix phases in samples from Namoya. Data is represented in wt. %. Rutile, zircon and plagioclase analysis are normalised to 100 wt. %.

Sample Name	NM-FS-1	NM-FS-2	NM-SI-1	NM-SI-2	NM-SI-3	NM-SI-4	NM-SI-4	NM-SI-5	NM-SI-7	NM-SI-7
Mineral type	Quartz	Muscovite	Calcite	Chlorite	Rutile	Ankerite	Plagioclase	Zircon	Fluorapatite	Siderite
SiO_2	100.22	46.43	0.00	26.09	0.00	0.00	69.75	30.38	0.00	0.00
Na_2O	0.00	0.86	0.00	0.00	0.00	0.00	10.67	0.00	0.00	0.00
MgO	0.00	0.00	0.67	12.65	0.00	15.35	0.00	0.00	0.00	9.63
Al_2O_3	0.00	33.63	0.00	19.99	0.00	0.00	19.04	0.00	0.00	0.00
K_2O	0.00	9.12	0.00	0.00	0.00	0.00	0.00	0.00	0.00	0.00
CaO	0.00	0.00	51.71	0.00	0.00	33.16	0.55	0.00	53.69	0.60
TiO_2	0.00	0.00	0.00	1.10	100.00	0.00	0.00	0.00	0.00	0.00
FeO	0.00	1.97	1.73	24.39	0.00	13.92	0.00	0.00	0.00	51.56
MnO	0.00	0.00	0.00	0.00	0.00	0.00	0.00	0.00	0.00	0.51
ZrO_2	0.00	0.00	0.00	0.00	0.00	0.00	0.00	69.62	0.00	0.00
P_2O_5	0.00	0.00	0.00	0.00	0.00	0.00	0.00	0.00	46.78	0.00
BaO	0.00	2.57	0.00	0.00	0.00	0.00	0.00	0.00	0.00	0.00
Total (wt. %)	100.22	94.58	54.11	84.22	100.00	62.43	100.00	100.00	101.47	62.30
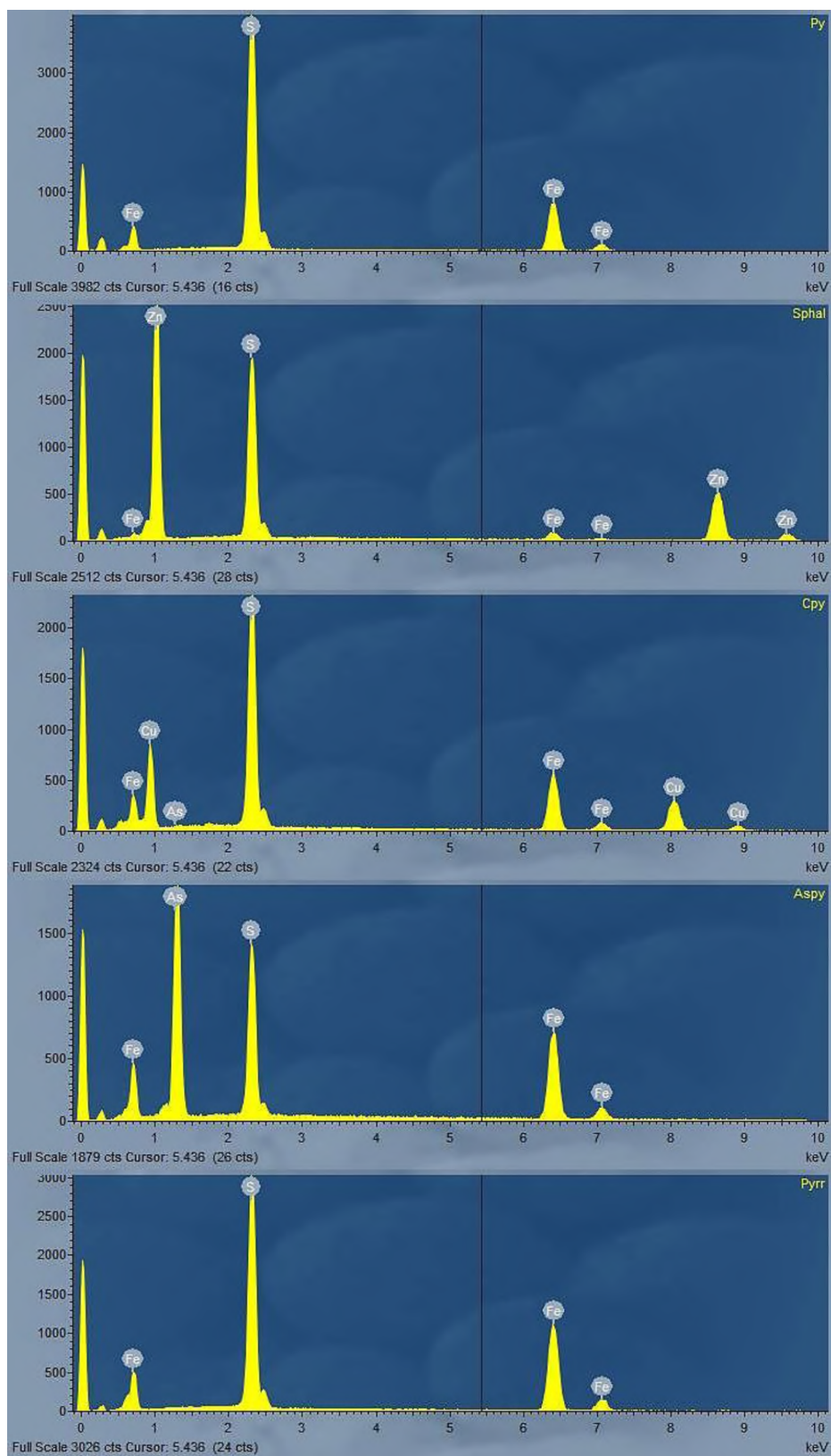
Figure 6.6: EDS spectra of selected sulphides from Namoya. Py = Pyrite; Sphal = Sphalerite; Cpy = Chalcopyrite; Aspy = Arsenopyrite; Pyrr = Pyrrhotite;
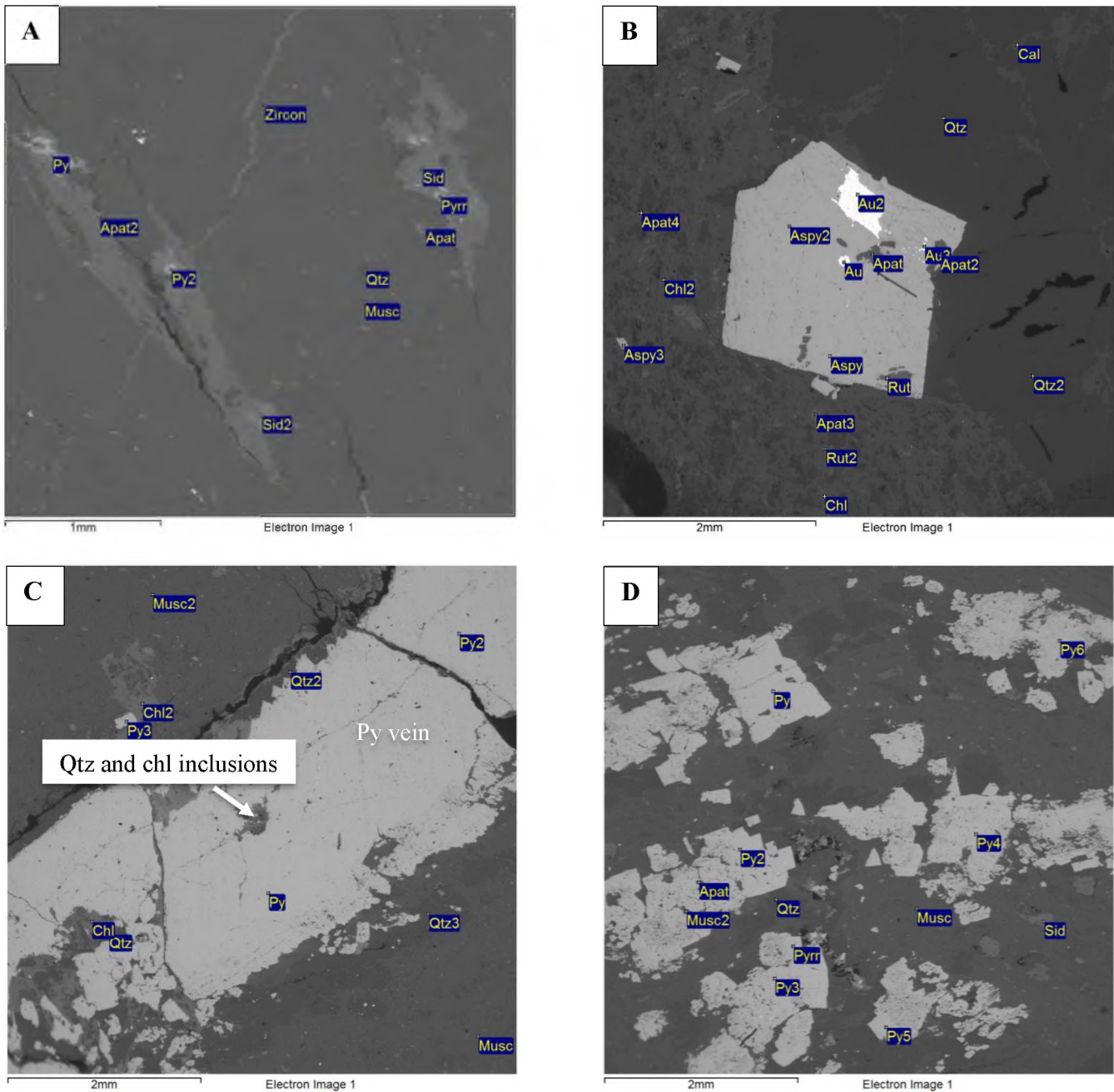
Figure 6.7: BSE images of samples from Namoya. **A)** Vein pyrite (Py) included in siderite (Sid) grains in sample NM-SI-5. **B)** Native gold (Au) inclusions in a subhedral arsenopyrite (Aspy) grain in sample NM-SI-2. **C)** Quartz (Qtz) and chlorite (Chl) inclusions in a pyrite (Py) vein in sample NM-SI-5. **D)** Fluorapatite (Apat) and muscovite (Musc)/sericite inclusions in some pyrite (Py) grains in sample NM-SI-6. Apat = fluorapatite; Qtz = quartz; Musc = muscovite/sericite; Pyr = pyrrhotite; Chl = chlorite; Rut = rutile; Cal = calcite.; Sid = siderite.
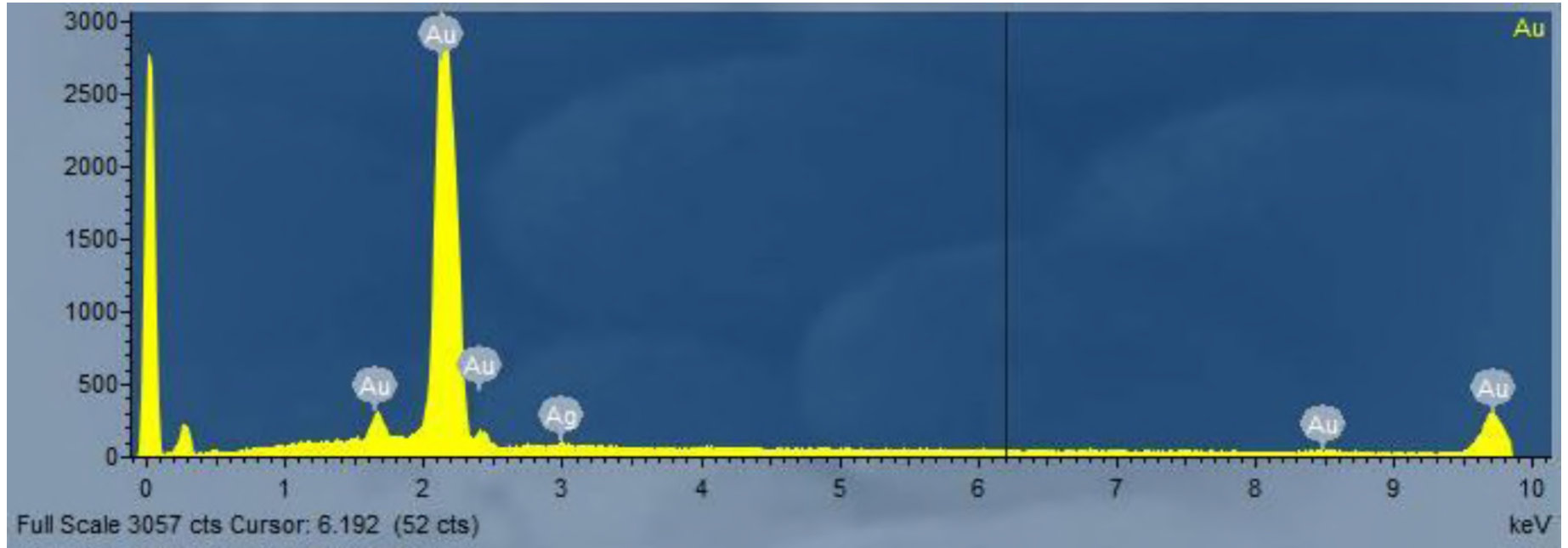
Figure 6.8: EDS spectrum of a gold (Au) grain included in arsenopyrite from sample NM-SI-2. The Ag concentration is < 2.89 at. %.

6.2. EMPA analysis of pyrite

Analytical methods for the quantitative mineral analyses of pyrite from the TNGB are detailed in Chapter 3.3.3. Trace element abundance in a few pyrite crystals is large enough to be reliably quantified using the major element EPMA calibration, and in these instances they are described together with the major elements in section 6.2.1. The trace element variations are described thereafter in section 6.2.2.

Back-scattered electron images were produced to highlight characteristic mineral assemblages. Furthermore, 29 elemental maps, show possible compositional variations in the pyrite, but these maps may not resolve trace elemental variations accurately.

6.2.1. Major and minor element composition of pyrite

Major element analyses of pyrites (from a total of 389 analyses) in the TNGB suggests that there is no significant variation between pyrites from the four deposits. S contents range from 51.36 wt. % to 55.10 wt. % with an average value of 53.45 wt. % ± 0.71 wt. % (1-sigma stdv). Fe values range from 42.63 wt. % to 48.22 wt. % with an average value of 46.17 wt. % ± 0.82. Gold contents in the pyrite structure are always below the detection limit of 268 ppm (refer to Appendix 1).

Authigenic/metamorphic pyrite from Twangiza have on average, more As (0.007 to 0.581 wt. %), Ni (0.00 to 0.177 wt. %) and Cu (0.003 to 1.641 wt. %) when compared to pyrite from hydrothermal veins (Table 6.2.1). Average values for As, Ni and Cu are 0.219, 0.031 and 0.168 wt. % respectively. In hydrothermal veins, pyrite is richer in Co (0 to 0.533 wt. %) but does not contain significant Ni (Table 6.2.2). Major element analysis of pyrite (from 115 analyses) in host rocks and veins are quite similar to each other and have little variation in S and Fe ranging from 52.02 to 54.47 wt. % (average 53.433 wt. %) and 44.22 to 48.07 wt. % (average 45.75 wt. %), respectively.

Table 6.2.1: Representative EPMA pyrite compositions from authigenic/metamorphic pyrite in Twangiza. Data is presented in wt. %. Ions are normalised to 3 ions.

Sample Name	TW-FS-03 _SI1_py3_ 1	TW-FS-03 _SI1_py5_	TW-FS-03 _S2_py3_ 2	TW-FS-05 _S1_py5	TW-FS-05 _S2_py1_ 2	TW-FS-05 _S3_py_5	TW-FS-07 _S1_py_2	TW-FS-07 _S2_py1_ 1	TW-FS-07 _S2_py5
S (wt. %)	53.54	53.57	54.16	54.28	53.34	53.79	53.39	53.87	53.32
Fe (wt. %)	45.35	45.38	45.55	46.11	46.73	45.31	46.22	45.42	45.55
As (wt. %)	0.47	0.44	0.31	0.11	0.12	0.16	0.07	0.19	0.19
Cu (wt. %)	0.23	0.17	0.19	0.13	0.10	0.17	1.64	0.18	0.14
Ni (wt. %)	0.08	0.14	0.00	0.04	0.07	0.05	0.18	0.00	0.00
Zn (wt. %)	0.00	0.00	0.00	0.00	0.02	0.04	0.00	0.00	0.00
Co (wt. %)	0.00	0.01	0.00	0.00	0.05	0.04	0.09	0.00	0.00
Au (wt. %)	0.00	0.00	0.12	0.00	0.07	0.00	0.00	0.12	0.00
Total (wt. %)	99.67	99.71	100.33	100.67	100.50	99.56	101.59	99.78	99.20
S	2.01	2.01	2.02	2.01	1.99	2.02	1.98	2.02	2.01
Fe	0.98	0.98	0.97	0.98	1.00	0.98	0.99	0.98	0.99
As	0.01	0.01	0.01	0.00	0.00	0.00	0.00	0.00	0.00
Cu	0.00	0.00	0.00	0.00	0.00	0.00	0.03	0.00	0.00
Ni	0.00	0.00	0.00	0.00	0.00	0.00	0.00	0.00	0.00
Zn	0.00	0.00	0.00	0.00	0.00	0.00	0.00	0.00	0.00
Co	0.00	0.00	0.00	0.00	0.00	0.00	0.00	0.00	0.00
Au	0.00	0.00	0.00	0.00	0.00	0.00	0.00	0.00	0.00
Total ions	3.00	3.00	3.00	2.99	2.99	3.00	3.00	3.00	3.00

Table 6.2.2: Representative EPMA pyrite compositions from vein pyrite in Twangiza. Data is presented in wt. %. Ions are normalised to 3 ions.

Sample Name	T3_S1_py1_2	T3_S2_py2_1	T3_S2_py4_2	T9_S2_py3_1	T9_py4_4	T9_S2_py4_5	T12_S1_py3_2	T12_S2_py1_2	T12_S2_py1_4	T25_S1_py1_2	T25_S2_py1_1	T25_S3_py1_2
Pyrite type	VD HR	V	V	V	VD HR	V	V	V	V	V	V	V
S (wt. %)	52.96	52.56	52.75	53.44	53.50	53.97	53.09	53.52	53.26	53.09	53.41	53.50
Fe (wt. %)	46.51	46.56	46.73	45.46	45.15	46.28	46.30	45.31	45.75	46.00	45.88	45.52
As (wt. %)	0.48	0.07	0.47	0.05	0.06	0.05	0.24	0.11	0.04	0.31	0.13	0.12
Cu (wt. %)	0.03	0.20	0.19	0.17	0.26	0.17	0.25	0.19	0.20	0.08	0.04	0.30
Ni (wt. %)	0.09	0.00	0.07	0.00	0.00	0.00	0.07	0.00	0.00	0.00	0.03	0.00
Zn (wt. %)	0.08	0.00	0.00	0.06	0.00	0.00	0.00	0.00	0.03	0.00	0.00	0.00
Co (wt. %)	0.10	0.00	0.14	0.00	0.53	0.00	0.09	0.02	0.00	0.01	0.00	0.00
Au (wt. %)	0.12	0.00	0.00	0.14	0.00	0.00	0.02	0.13	0.00	0.00	0.05	0.00
Total (wt. %)	100.37	99.39	100.35	99.32	99.50	100.47	100.06	99.28	99.28	99.49	99.54	99.44
S	1.98	1.99	1.98	2.01	2.01	2.01	1.99	2.01	2.01	2.00	2.01	2.01
Fe	1.00	1.01	1.01	0.98	0.97	0.99	0.99	0.98	0.99	0.99	0.99	0.98
As	0.01	0.00	0.01	0.00	0.00	0.00	0.00	0.00	0.00	0.01	0.00	0.00
Cu	0.00	0.00	0.00	0.00	0.01	0.00	0.01	0.00	0.00	0.00	0.00	0.01
Ni	0.00	0.00	0.00	0.00	0.00	0.00	0.00	0.00	0.00	0.00	0.00	0.00
Zn	0.00	0.00	0.00	0.00	0.00	0.00	0.00	0.00	0.00	0.00	0.00	0.00
Co	0.00	0.00	0.00	0.00	0.01	0.00	0.00	0.00	0.00	0.00	0.00	0.00
Au	0.00	0.00	0.00	0.00	0.00	0.00	0.00	0.00	0.00	0.00	0.00	0.00
Total ions	2.99	3.00	3.00	2.99	2.99	3.00	2.99	2.99	2.99	3.00	3.00	3.00

Elemental map analyses indicate largely uniform Fe and S contents in pyrite. Some domains where the elemental map shows apparent variations correlate with insufficiently polished patches on the surface and inclusion clusters that are evident on the BSE image (Figure 6.10; Sample TW-FS-03). Hence these apparent variations are artefacts or related to clusters of higher trace element concentrations of small mineral inclusions.

Gold was detected in elemental maps from pyrite in both the host rock samples TW-FS-03 and TW-FS-05 and VD HR pyrite in sample T9. Gold in these pyrites is usually too small to analyse (< 10 μm), however one gold analysis from TW-FS-05 shows that the 39 μm gold is mostly pure (Table 6.2.3). Although S, Fe, As, Co and Cu occur as minor elements, these may be due to overlaps in the EPMA analyses. Figure 6.11 shows a gold speck (< 10 μm) in sample T9 contained in pyrite within the foliated host rock that protrudes into the vein. This pyrite is classified as disseminated (VD HR) type pyrite. It is unclear whether the gold was present in the host at the time of vein formation or whether gold crystallised from the vein fluid.

Table 6.2.3: EPMA analysis of a 39 μm gold grain in HR pyrite from sample TW-FS-05. Data is represented in wt. %.

Sample	TW-FS-05_S2_au2
S	0.155
Zn	0.000
Fe	0.477
As	0.033
Ni	0.000
Co	0.046
Cu	0.364
Au	101.772
Total (wt. %)	102.847
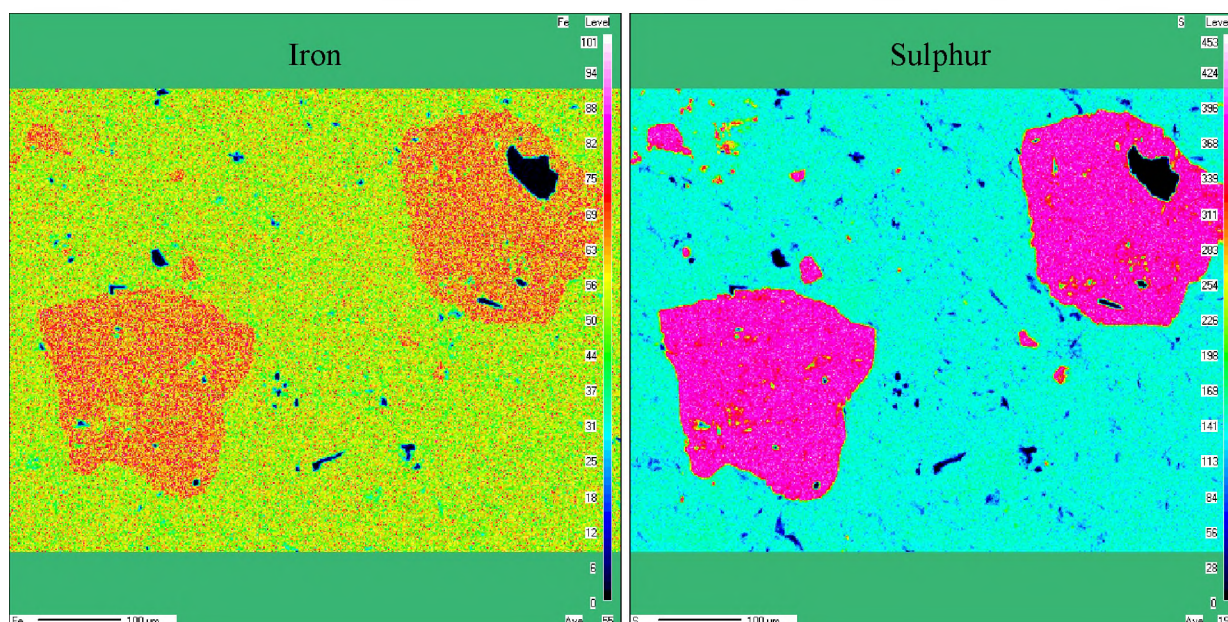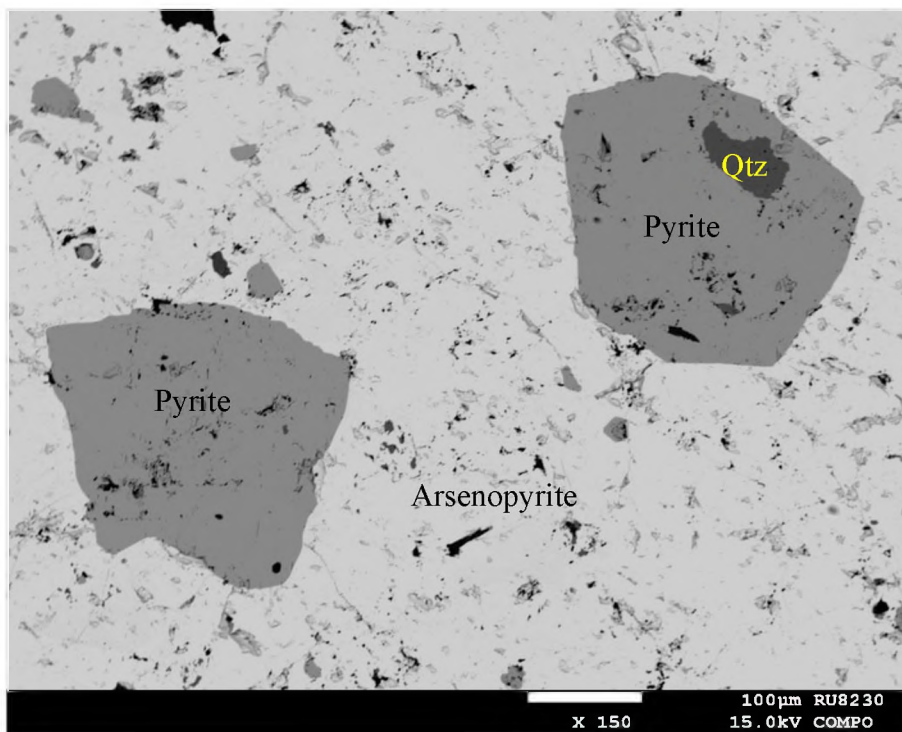
Figure 6.9: BSE photomicrograph and corresponding EPMA element maps of host rock sample TW-FS-03 showing chemical variation in Fe content in two pyrite grains that are included in arsenopyrite. Pyrite is pure FeS_2 as minor elements were not detected in the elemental maps.
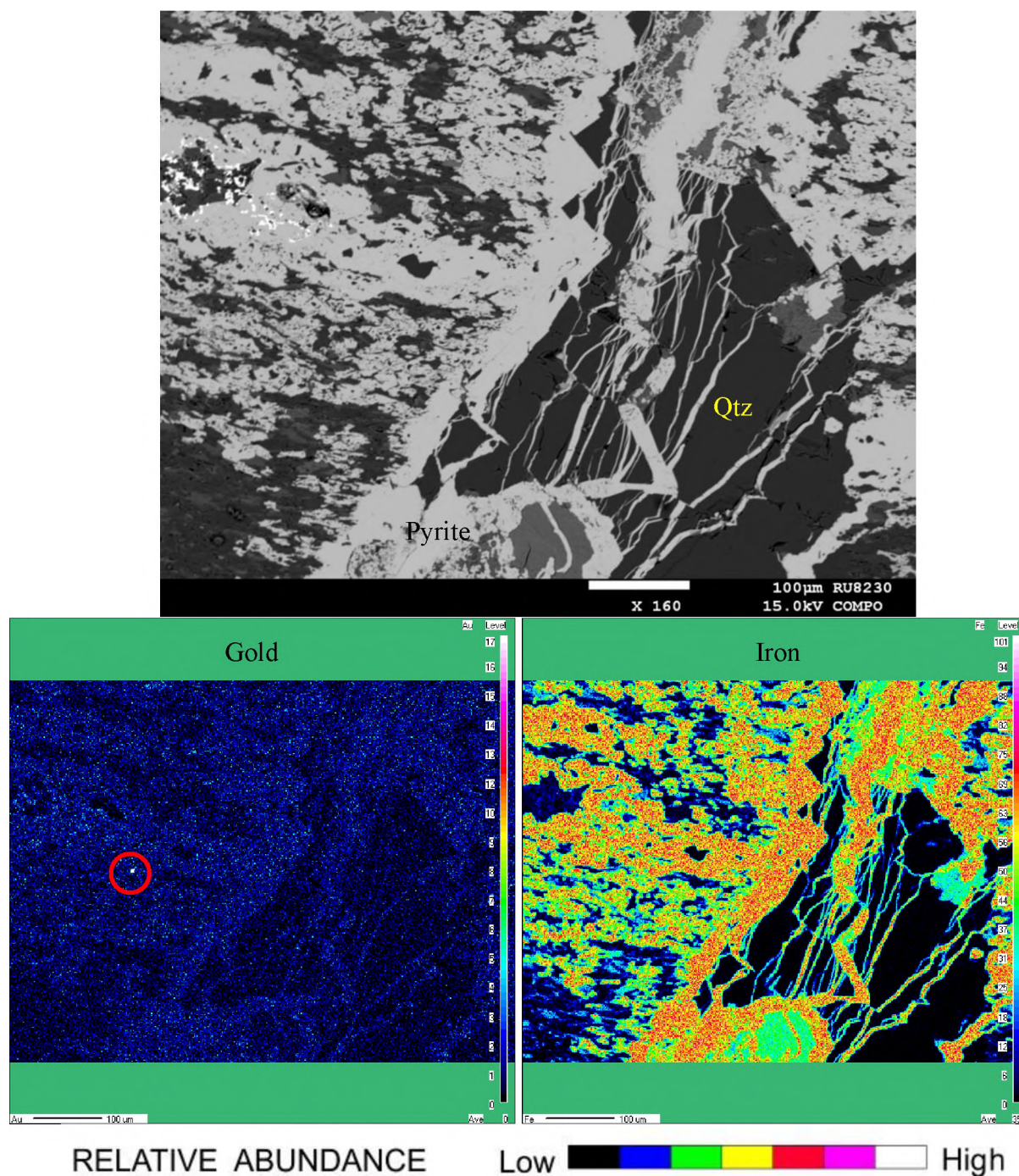
Figure 6.10: BSE photomicrograph and corresponding EPMA element maps of vein sample T9 showing chemical variation in Fe content in a pyrite vein. Pyrite is pure FeS_2 as minor elements were not detected in the maps. A larger (<10 μm) gold speck (white spot inside the red circle) and is located in pyrite within the host rock that most likely is disseminated pyrite from the vein. The mid-blue Au signal that is seen in most of the map outside quartz represents concentrations that are not quantifiable using EPMA in trace element analysis configuration Brecciation of the vein quartz (black) may suggest re-mobilisation or auto-metasomatism of fluids post-dating the formation of the vein. The orange is pyrite, the green is matrix silicates and the black is quartz.

Pyrite from the host rock from Kamituga generally have more Ni (0 to 0.702 wt. %) and Co (0 to 0.588 wt. %) when compared to pyrite in hydrothermal veins (Table 6.2.4). There is no particular difference in As and Cu content in the vein and host rock pyrite. Major element analysis of pyrite (from 101 analyses) in host rocks and veins are quite similar and have little variation in S and Fe ranging from 51.36 to 54.65 wt. % (average 52.88 wt. %) and 45.01 to 48.22 wt. % (average 46.64 wt. %), respectively.

On elemental maps, hydrothermal pyrite from sample KG-SIS-7 shows apparent variations in Fe which, however are minor and probably associated with surface roughness (Figure 6.11). Two arsenopyrite crystals show lower Fe contents due to As substitution. Gold specks (< 10 μm) were detected in elemental maps of pyrite in samples KG-FS-1, KG-SIS-2 and KG-SIS-3. The gold specks occur on the margins of pyrite that is disseminated from a pyrite vein (Figure 6.12). These gold specks are too small for EPM analysis.
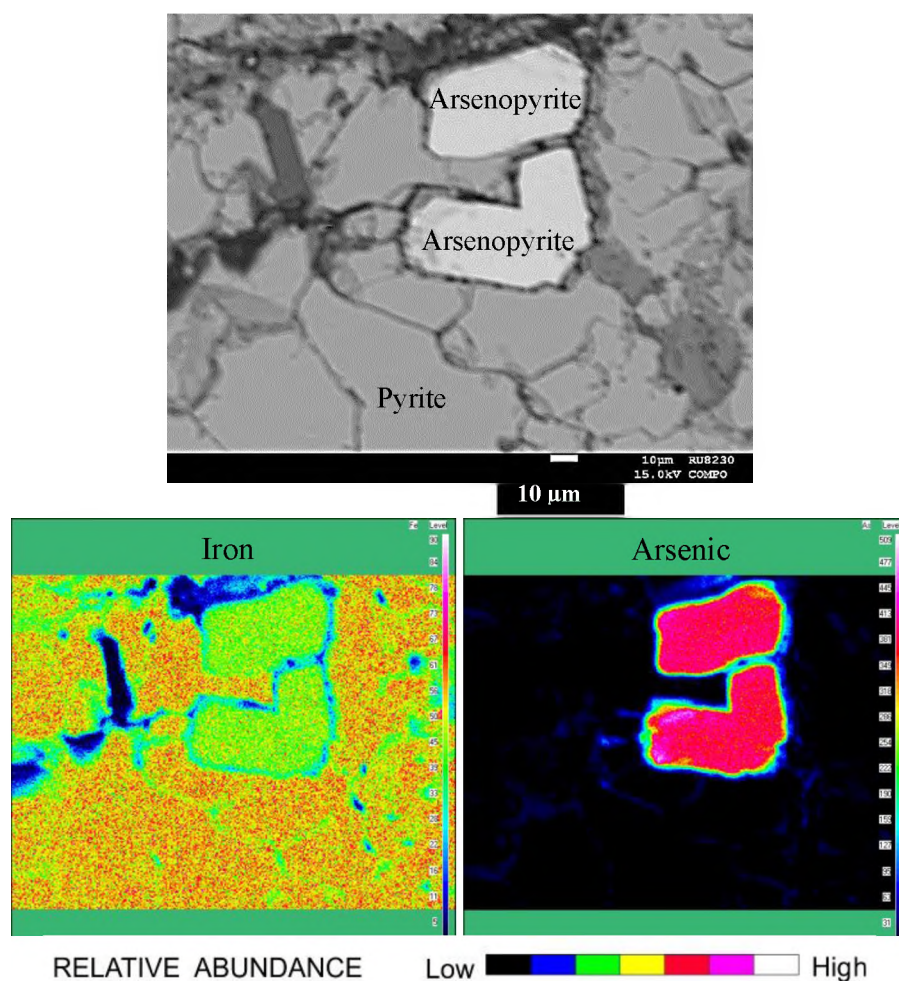
Figure 6.11: BSE photomicrograph and corresponding EPMA element maps of sample KG-SIS-7 showing minor apparent variation in Fe content in pyrite which is attributed to uneven polishing. Two arsenopyrite crystals show the Fe-As substitution.
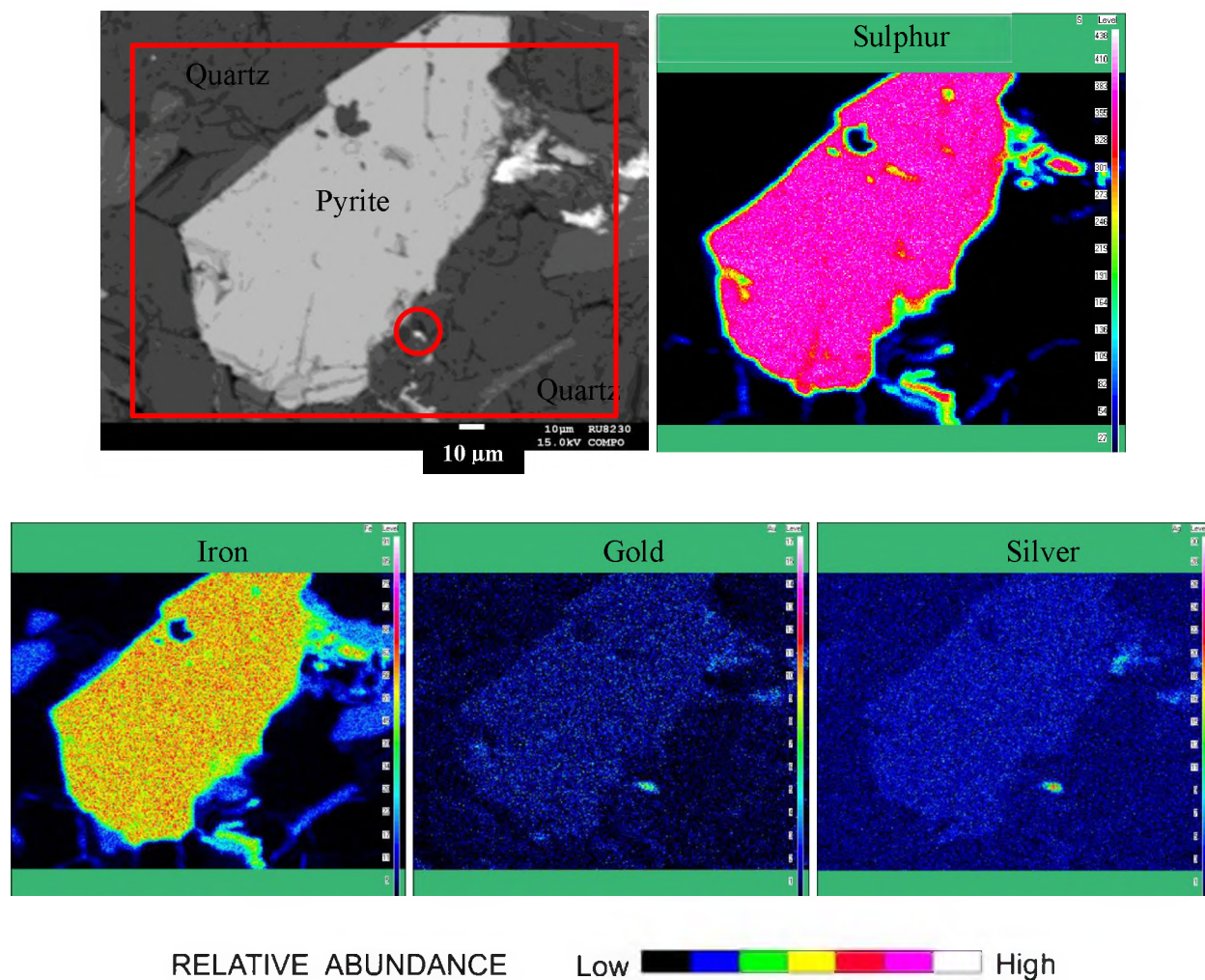
Figure 6.12: BSE photomicrograph and corresponding EPMA element maps of sample KG-SIS-3 showing a gold speck (white spot inside the red circle) close to a VD HR pyrite. Silver (Ag), Fe, and S were also detected in the maps. These may be due to peak overlaps. Mapped area is marked by red square.

Table 6.2.4: Representative pyrite compositions from Kamituga. Data is presented in wt. %. Ions are normalised to 3 ions.

Sample Name	KG-FS-1 _SI2_py3 _1	KG-FS-2 _SI2_py1 _2	KG-SIS-3 _S1_py2_ 1	KG-SIS-5 _S2_py3_ 1	KG-SIS-6 _S2_py1_ 2	KG-SIS-2 _S1_py1_ 1	KG-SIS-2 _S2_py3_ 2	KG-SIS-7 _S1_py1_ 4	KG-SIS-7 _S2_py2_ 2
Pyrite type	HR	HR	HR	HR	HR	V	VD HR	V	HR
S	52.83	53.64	53.39	52.49	52.14	53.09	52.67	53.89	53.55
Fe	46.46	46.83	45.75	46.92	47.00	47.29	47.09	46.03	46.27
As	0.00	0.02	0.00	0.00	0.00	0.00	0.00	0.11	0.00
Cu	0.07	0.14	0.26	0.18	0.06	0.14	0.12	0.00	0.11
Ni	0.00	0.00	0.25	0.05	0.08	0.00	0.00	0.06	0.03
Zn	0.00	0.04	0.12	0.00	0.10	0.00	0.02	0.00	0.02
Co	0.02	0.01	0.10	0.00	0.08	0.00	0.00	0.00	0.00
Au	0.00	0.00	0.03	0.00	0.00	0.00	0.01	0.00	0.07
Total (wt. %)	99.38	100.68	99.90	99.64	99.46	100.52	100.00	100.09	100.05
S	1.99	2.00	1.99	1.98	1.97	1.98	1.98	2.01	2.00
Fe	1.01	1.00	1.00	1.02	1.02	1.01	1.02	0.99	0.99
As	0.01	0.00	0.00	0.00	0.00	0.00	0.00	0.00	0.00
Cu	0.00	0.00	0.00	0.00	0.00	0.00	0.00	0.00	0.00
Ni	0.00	0.00	0.01	0.00	0.00	0.00	0.00	0.00	0.00
Zn	0.00	0.00	0.00	0.00	0.00	0.00	0.00	0.00	0.00
Co	0.00	0.00	0.00	0.00	0.00	0.00	0.00	0.00	0.00
Au	0.00	0.00	0.00	0.00	0.00	0.00	0.00	0.00	0.00
Total ions	2.99	3.00	3.00	3.00	2.99	2.99	3.00	3.00	2.99

In the Lugushwa deposit, pyrite that has grown in the host rock and from host rock sources show generally lower Co contents (0 to 0.149 wt. %) when compared to pyrite from vein samples (0 to 0.501 wt. %; Table 6.2.5). Ni and Cu contents in host rock and hydrothermal vein pyrite are the lowest in the TNGB. Zn is either absent or occurs as a trace element. Major element analysis from pyrite (from 31 analyses) follow a similar trend to the rest of the samples in the TNGB. Like the Twangiza and Kamituga pyrites, S and Fe in pyrite show little variation ranging from 53.17 to 55.10 wt. % (average 54.09 wt. %) and 45.16 to 47.37 wt. % (average 46.24 wt. %), respectively.

Elemental map analyses indicate that Fe is evenly distributed within a single pyrite grain. However, slight differences in Fe composition may be due to the uneven surface of the polished thin section. Sample LG-SI-02 shows the variable distribution of Fe in pyrite. An approximately 20 μm small gold grain is found in HR pyrite (Figure 6.13). A tiny gold speck (< 10 μm was also detected in of a pyrite in hydrothermal vein sample LG-SI-05. The gold grains are either too small (< 10 μm) or have a poor surface and could not be analysed with the EPMA.
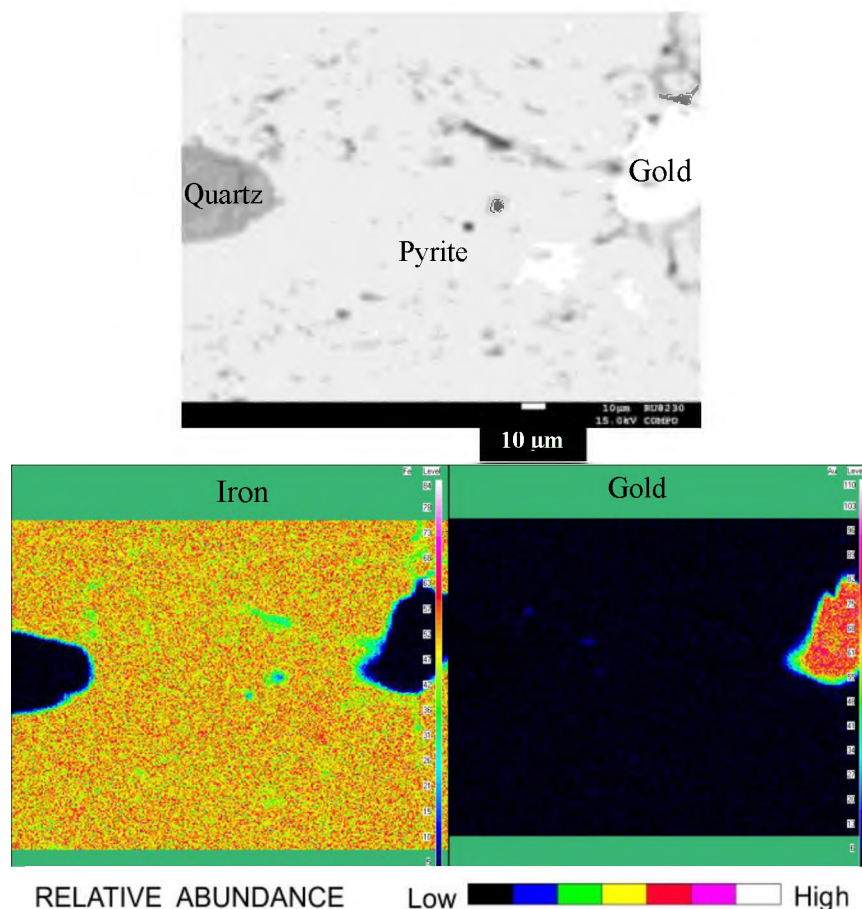
Figure 6.13: BSE photomicrograph and corresponding EPMA element maps of sample LG-SI-02 showing apparent variation in Fe content which is attributed to poor polishing. A ~20 μm gold grain in the HR pyrite other elements detected in the elemental map. $\delta^{34}S$ of HR pyrite in sample LG SI-02 ranges from -18.4‰ to -14.8‰.

Table 6.2.5: Representative pyrite compositions from Lugushwa. Data is presented in wt. % and pyrite type is given. Ions are normalised to 3 ions.

Sample Name	LG-SI-02 _S2_py_1	LG-SI-02 _S2_py_4	LG-SI-05 _S2_py2_1	LG-SI-05_ S1_py1_2	LG-SI-05 _S1_py2_1	LG-SI-06 _S1_py2_2	LG-SI-06 _S3_py3_1
Pyrite type	HR	HR	VD HR	V	V	AM HR	AM HR
S	54.31	53.91	53.52	54.23	54.22	54.17	53.75
Fe	45.55	45.9	46.83	46.11	45.30	45.88	45.69
As	0.05	0.03	0.55	0.08	0.03	0.00	0.62
Cu	0.15	0.06	0.00	0.00	0.11	0.01	0.00
Ni	0.00	0.00	0.01	0.00	0.00	0.00	0.00
Zn	0.00	0.00	0.00	0.00	0.00	0.03	0.00
Co	0.00	0.00	0.00	0.00	0.02	0.00	0.00
Au	0.00	0.00	0.00	0.00	0.04	0.00	0.01
Total (wt. %)	100.06	99.9	100.91	100.42	99.72	100.09	100.07
S	2.02	2.01	1.99	2.02	2.03	2.02	2.01
Fe	0.97	0.98	1.00	0.98	0.97	0.98	0.98
As	0.00	0.00	0.01	0.00	0.00	0.00	0.01
Cu	0.00	0.00	0.00	0.00	0.00	0.00	0.00
Ni	0.00	0.00	0.00	0.00	0.00	0.00	0.00
Zn	0.00	0.00	0.00	0.00	0.00	0.00	0.00
Co	0.00	0.00	0.00	0.00	0.00	0.00	0.00
Au	0.00	0.00	0.00	0.00	0.00	0.00	0.00
Total ions	2.99	2.99	3.00	3.00	3.00	3.00	3.00

In Namoya, minor element levels are generally higher with 0 to 4.75 wt. % Cu and 0 to 3.04 wt. % Co, with the highest values in the veins. Pyrite that has grown in the host rocks have higher As (0 to 1.16 wt. %) and Ni (0 to 2.45 wt. %). Zn occurs as either a trace element or is absent. Unlike pyrite from Twangiza, Lugushwa and Kamituga, major element analysis of pyrite (from 142 analyses) in host rocks and veins show significant variation in S and Fe ranging from 51.57 to 54.82 wt. % (average 53.72 wt. %) and 42.63 to 47.89 wt. % (average 46.15 wt. %), respectively. These variations may be due to minor elements such as Cu, Co, As and Ni substituting for Fe (Table 6.2.6).

Elemental map analyses indicate that Fe is not evenly distributed within a single pyrite grain. This slight variation in Fe composition may be due the substitution of Fe with As, Ni, Cu, and Co. Sample NM-SI-03 shows the variable distribution of Fe in pyrites where Ni decreases from the centre to the rim of one pyrite (Figure 6.14). Conversely, As increases from the centre to the rim of the pyrites. Gold was not detected in any of the elemental maps of pyrites from Namoya.
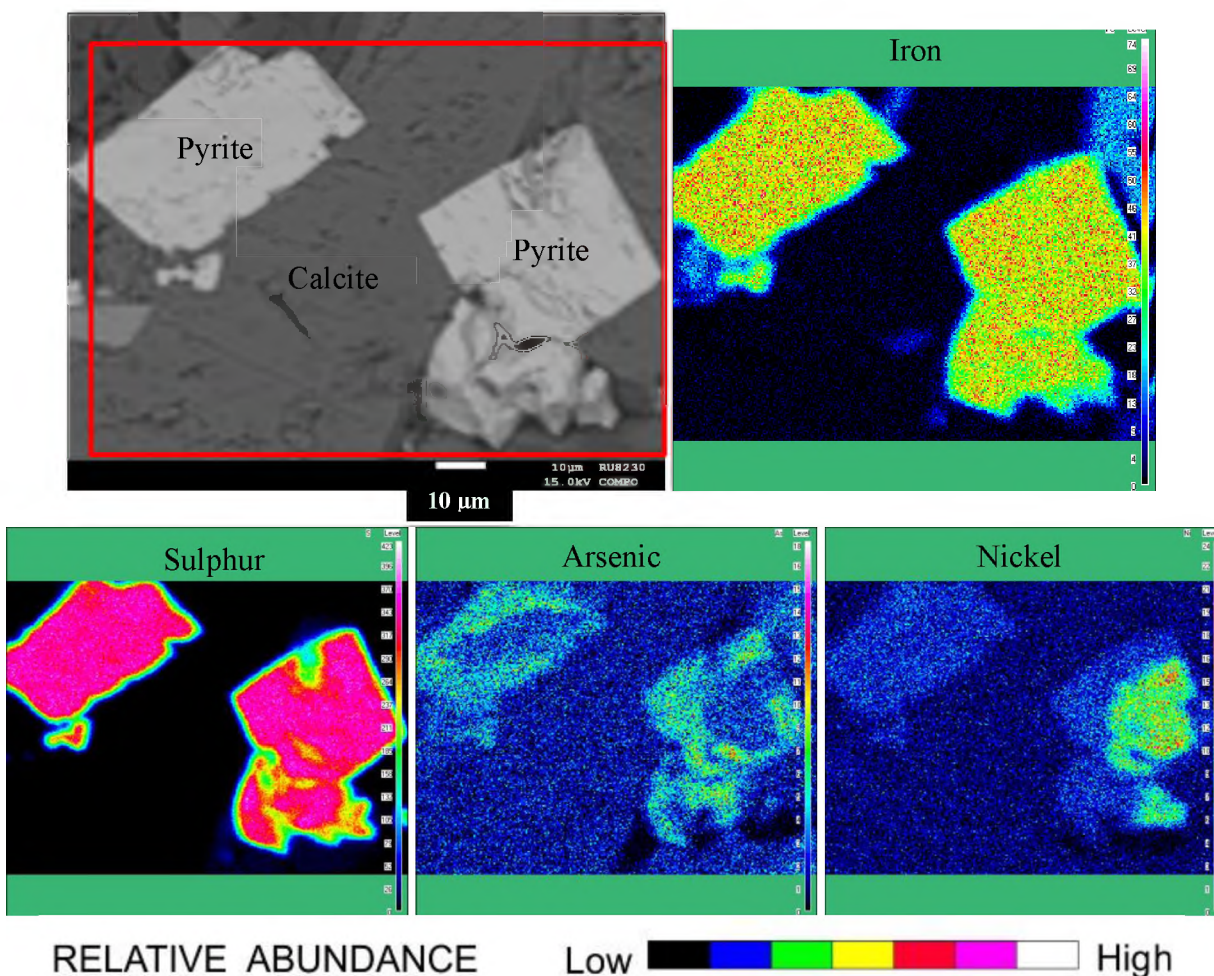
Figure 6.14: BSE photomicrograph and corresponding EPMA element maps of sample NM-SI-03 showing chemical variation in Fe content in HR pyrite where As and Ni substitute for Fe. Mapped area is marked by red square..

Table 6.2.6: Representative pyrite compositions from Namoya. Data is presented in wt. %. Ions are normalised to 3 ions.

Sample Name	NM-FS-1 _py2_2	NM-FS-2 _SI1_py3 _1	NM-SI-1 _S2_py3_ 2	NM-SI-2 _S2_py2_ 22	NM-SI-3 _S2_py1_ 1	NM-SI-4 _S1_py1_ 2	NM-SI-5 _S2_py2_ 2	NM-SI-6 _S2_py3_ 1	NM-SI-7 _S1_py2_ 2	NM-SI-8 _S2_py1_ 2
Pyrite type	HR	HR	HR	V	HR	HR	V	HR	VD HR	HR
S	52.98	53.04	53.33	53.47	53.17	52.23	53.89	54.13	54.09	53.37
Fe	45.36	47.11	45.39	46.06	46.44	47.01	45.24	46.24	46.64	45.64
As	0.10	0.10	0.29	0.00	0.19	0.11	0.00	0.11	0.48	0.34
Cu	0.21	0.12	0.65	0.00	0.00	0.00	0.01	0.05	0.01	0.00
Ni	0.14	0.00	0.91	0.01	0.29	0.34	0.00	0.00	0.00	0.14
Zn	0.03	0.00	0.00	0.08	0.00	0.00	0.03	0.00	0.03	0.00
Co	0.54	0.49	0.18	0.00	0.10	0.08	0.00	0.00	0.00	0.00
Au	0.00	0.00	0.00	0.03	0.00	0.00	0.06	0.00	0.00	0.01
Total (wt. %)	99.36	100.56	100.75	99.65	100.19	99.77	99.23	100.53	101.25	99.50
S	2.00	1.99	1.99	2.01	1.99	1.97	2.02	2.01	2.00	2.01
Fe	0.98	1.00	0.97	0.99	1.00	1.02	0.98	0.99	0.99	0.99
As	0.00	0.00	0.00	0.00	0.00	0.00	0.00	0.00	0.01	0.01
Cu	0.00	0.00	0.01	0.00	0.00	0.00	0.00	0.00	0.00	0.00
Ni	0.00	0.00	0.02	0.00	0.01	0.01	0.00	0.00	0.00	0.00
Zn	0.00	0.00	0.00	0.00	0.00	0.00	0.00	0.00	0.00	0.00
Co	0.01	0.01	0.00	0.00	0.00	0.00	0.00	0.00	0.00	0.00
Au	0.00	0.00	0.00	0.00	0.00	0.00	0.00	0.00	0.00	0.00
Total ions	2.99	3.00	3.00	3.00	3.00	3.00	3.00	3.00	2.99	3.00

6.2.2. Trace element composition of pyrite

Table 6.2.7 shows average trace element contents of pyrite from the four different TNGB deposits, distinguishing also pyrite forming in veins or in the host rock. The full trace element data set of pyrites from the TNGB is presented in Appendix 3. Trace element concentrations in host rock pyrite tend to be higher than in veins from the same deposits. This particularly applies to As in Twangiza, Kamituga and Namoya, where authigenic/metamorphic pyrite from the host rock contains more than 2-4 times as much As than vein-hosted pyrite >2000-4000 ppm vs. <1000 ppm). A similar pattern is seen for Ni, with lower abundances and usually smaller differences between vein and host rock pyrite. Ni varies between 40 and 66400 ppm across the TNGB. It appears to be most abundant in Namoya and least abundant in Lugushwa.

Cobalt is generally below the detection limit of 30 ppm. In nine analyses, one from Twangiza (> 4000 ppm) and eight from Namoya (>9000 ppm), significant amounts probably reflect Co-rich inclusions hidden below, but close to the surface of the thin section (Appendix 3). Cobalt reaches a maximum composition of 41 860 ppm across the TNGB with the highest values detected in hydrothermal vein pyrite from Namoya. It appears to be most abundant in authigenic/metamorphic pyrite from Twangiza, Kamituga and Lugushwa.

Despite of its high detection limit of 104 ppm, copper could be quantified in Twangiza host rock pyrite (~210, 5190 ppm), in Kamituga vein pyrite (260 ppm) and in Namoya authigenic/metamorphic and vein pyrite (160, 2790 ppm; Table 6.2.7). Individual analyses from all deposits may show several thousand ppm Cu, which may relate to micro-inclusions of chalcopyrite in the excitation volume of the EPM analysis. Copper concentrations range from below detection limit (bdl) to 13 860 ppm in the TNGB deposits. Host rock pyrite tends to have higher Cu concentrations when compared to vein pyrite from the same deposit.

Silver, tellurium and bismuth show relatively lower concentrations when compared to other analysed elements. Ag ranges from bdl to 460 ppm and appears to be most abundant in vein pyrite from Namoya. Lower abundances and smaller differences occur between authigenic/metamorphic and vein pyrite from Twangiza, Kamituga and Lugushwa. Similarly, Te ranges from bdl to 450 ppm and is most abundant in vein pyrite from Namoya with smaller differences occurring between host rock and vein pyrite in Twangiza, Kamituga and Lugushwa. Bi reaches maximum concentrations of 1290 ppm. It has higher concentrations in authigenic/metamorphic pyrite than in vein pyrite from the same deposits. Host rock pyrite in Kamituga and Lugushwa contains up to 2.7 times as much Bi than in vein pyrite (650-1290 ppm vs. 290-480ppm).

Gold was detected in three of the 394 trace element analyses. Twangiza has one analysis with Au concentrations of 70 ppm in vein-hosted pyrite Kamituga has a single analysis that has 340 ppm Au in a host rock pyrite. Namoya also has a single analysis that detected Au with a concentration of 100 ppm, which also comes from a pyrite from the host rock. Au was not detected in samples

from Lugushwa. However, the gold detected in the Kamituga and Namoya pyrite suggest that primary gold is present in the sedimentary sequence. This is in agreement with gold particles found in similar settings in the Belt Supergroup (USA; Strauss and Schieber, 1989), the Juneau gold belt (USA; Goldfarb et al., 1991), and the Sukhoi Log in Russia (Chang et al., 2008).

Overall, EPM analyses has indicated that pyrite composition throughout the TNGB is fairly homogenous. Some grains contain traces of As, Ni, Cu, and Co which may sometimes substitute for Fe. This data was instrumental in: confirming that pyrite is close to or equal to FeS_2 structural formula, that concentrations of Cu, As, Ni, Co and other traces are minimal, and in identifying gold and its association with pyrite. However, this data has no implications for sulphur isotopes and sulphur provenance.

Table 6.2.7: Representative trace element analysis of pyrite from the TNGB. All data is presented in ppm and where no value is given represents data below the detection limit (bdl). The detection limit is written in brackets after the element symbol.

Sample name	TW-FS-05 _S1_py5	TW-FS-07 _S1_py_2	T9_S1_py2_1	T25_S1_py1_ 1	KG-FS-1 _SI2_py3_4	KG-SIS-7 _S1_py1_4	KG-SIS-2 _S2_py2_1	KG-SIS-7 _S1_py1_1
Deposit	Twangiza	Twangiza	Twangiza	Twangiza	Kamituga	Kamituga	Kamituga	Kamituga
Pyrite type	HR	AM HR	V	V	HR	HR	V	V
Co (30)	bdl	4200	bdl	bdl	bdl	bdl	bdl	bdl
As (29)	2350	80	940	3950	800	920	680	690
Ni (7)	170	660	140	50	10	650	190	840
Ag (7)	bdl	bdl	bdl	30	bdl	20	bdl	bdl
Te (8)	bdl	bdl	bdl	10	30	200	20	210
Cu (104)	210	5190	bdl	bdl	bdl	bdl	260	bdl
Au (43)	bdl	bdl	bdl	bdl	bdl	bdl	bdl	bdl
Bi (54)	bdl	60	bdl	bdl	130	70	bdl	250

Table 6.2.7: (continued)

Sample name	LG-SI-02 _S2_py2_1	LG-SI-06 _S1_py3_2	LG-SI-05 _S1_py1_2	LG-SI-05 _S2_py5_2	NM-FS-2 _SI2_py1_1	NM-SI-03 _S1_py2_2	NM-SI-02 _S2_py2_2	NM-SI-05 _S2_py2_1
Deposit	Lugushwa	Lugushwa	Lugushwa	Lugushwa	Namoya	Namoya	Namoya	Namoya
Pyrite type	HR	AM HR	V	VD HR	HR	HR	V	V
Co (30)	bdl	bdl	bdl	bdl	10770	bdl	bdl	bdl
As (29)	730	850	1730	3080	4330	4120	1230	980
Ni (7)	170	30	310	290	410	1130	390	250
Ag (7)	bdl	40	10	10	10	20	20	bdl
Te (8)	240	190	180	50	bdl	110	220	210
Cu (104)	bdl	bdl	bdl	bdl	2790	bdl	bdl	160
Au (43)	bdl	bdl	bdl	bdl	bdl	bdl	bdl	bdl
Bi (54)	90	650	bdl	bdl	240	220	bdl	310

7. Sulphur Isotope Analysis

7.1. Introduction

Sulphur has five naturally occurring isotopes, of which four are stable (^{32}S, ^{33}S, ^{34}S and ^{36}S). The stable isotopes have proportional abundances of approximately ^{32}S: 95.02%, ^{33}S 0.75%, ^{34}S 4.21% and ^{36}S 0.02%, respectively (Macnamara and Thode, 1950). ^{35}S is unstable with a half-life of 87 days (Seal, 2006) and is formed radiogenically in the atmosphere from cosmic ray spallation of ^{40}Ar (Peters, 1959).

Sulphur isotope ratios vary and show characteristic signatures that allow to identify specific geological environments in which sulphur containing minerals may have formed (Seal, 2006). This may include diagenetic, hydrothermal, biogenic, magmatic or metasomatic environments (Seal, 2006). Sulphur isotope data is especially useful in ore exploration and research. They can be used to constrain: the temperature of mineralisation, the sulphur chemistry of ore forming minerals, and the source of sulphur in ore deposits (Ohmoto, 1986; Ohmoto and Goldhaber, 1997). They can also be used to constrain depositional environment parameters such as sulphate concentration, carbon or electron donor availability, and temperature (Habicht et al. 2002; Canfield et al. 2006).

Sulphide provenance in mineral deposits is especially useful as the sulphur source can be used to infer the source of ore that might be genetically associated with the sulphide mineral. Key studies that laid the groundwork for sulphur isotope geochemistry in mineral deposits were done by Jensen (1967), Ohmoto and Rye (1979) and Ohmoto and Goldhaber (1997). In the current study, sulphur isotopes from pyrite will be used to infer the provenance of gold in the TNGB.

Previous studies that have used sulphur isotopes to infer pyrite genesis were done by Strauss and Schieber (1989). Their study used sulphur isotopic compositions in sedimentary pyrite from the Mid-Proterozoic Newland Formation in order to infer the paleoenvironmental conditions of pyrite. From their $\delta^{34}S$ data (-14‰ to +18‰), Strauss and Schieber (1989) proposed that early diagenetic pyrite from the Mid-Proterozoic Newland Formation was formed during bacterial reduction of seawater sulphate. Recent successful studies using pyrite isotope geochemistry in gold deposits were performed by Chang et al. (2008), Abdollahi et al. (2009), and Yan et al. (2014). These studies used sulphur isotopes in pyrite to infer the source of sulphur and/or gold, and to determine the number of geological events.

Chang et al. (2008) reported sulphur isotopic compositions of -6.5‰ to +24.0‰ in pyrites from the Sukhoi Log sediment-hosted orogenic gold deposit in Russia. They compared their $\delta^{34}S$ analyses of pyrite from different generations with that of other major orogenic gold deposits hosted in sedimentary rocks (e.g. Olimpiada, Bendigo, Nezhdaninskoye and Spanish Mountain). Chang et al. (2008) concluded from their study that most sediment-hosted gold orogenic deposits originate from the reduction of seawater sulphate.

In their study, Abdollahi et al. (2009) used sulphur isotope data measured from pyrite in quartz veins and schists from the Muteh gold district (Iran) in order to determine the primary source or sources of sulphur in the rocks. According to Abdollahi et al. (2009), isotope data from their study ranged from +2.2‰ to +16.9‰ and indicated three generations of pyrite within the quartz veins and host rocks of the Muteh gold district. Abdollahi et al. (2009) thus inferred, from their δ^{34}S data, a metamorphic source for sulphur in the Muteh gold district. Finally, Yan et al. (2014) sought to determine the mineral chemistry as well as the S, Pb and H-O isotope geochemistry of pyrite from the Heilangou gold deposit in the Jiaodong Peninsula, eastern China. The main orebody formed within the granite, unlike the aforementioned Newland Formation, Sukhoi log, and Muteh gold deposits which are all hosted in sediments. Their pyrite chemistry indicated that the Heilangou deposit is a magmatic hydrothermal deposit. Their sulphur isotope data (+5.5‰ to +7.8‰) from pyrite indicated a single source for granite and the different sulphides in the deposit. Yan et al. (2014) then concluded that sulphur in the Heilangou gold deposit originated from magmatic systems.

Walemba (2001) previously analysed stable isotopes (sulphur, carbon and oxygen) from the Kadubu area in the Kivu Province, DRC. The Twangiza, Kamituga and Lugushwa deposits all lie in the South Kivu Province (cf. section 1.1), however Walemba (2001) only studied the Twangiza deposit. Walemba (2001) analysed sulphide veins, quartz-carbonate veins and host rocks adjacent to these veins from the Twangiza deposit in order to identify the source of gold and associated base-metals and to understand the geological process responsible for gold mineralization. δ^{34}S data from 20 pyrites ranged from +1.03‰ to +8.48‰, with 95% of the data falling in the range of +2.62‰ to +3.37‰.From this data, Walemba (2001) proposed a magmatic source for sulphur and ore-forming hydrothermal fluids.

7.2. Sulphur isotope analysis

The principal and most commonly used ratio used in sulphur isotope studies is the ratio of the most abundant isotopes: ^{34}S/^{32}S. The isotope ratio of any sample is compared to that of a reference material and is expressed in delta notation (δ) where:

$$\delta^{34}S = \left(\frac{\left(^{34}S/^{32}S \right)_{sample} - \left(^{34}S/^{32}S \right)_{reference}}{\left(^{34}S/^{32}S \right)_{reference}} \right) \times 1000$$

This equation delivers the δ^{34}S value in permil (‰). The accepted reference standard for sulphur isotopes is the Vienna Canyon Diablo Troilite (VCDT) as the previous Canyon Diablo Troilite (CDT) meteorite reference material has been exhausted (Krouse and Coplen, 1997). The VCDT is

based on an artificially prepared silver sulphide (Ag$_2$S) material (IAEA-S-1) enriched in sulphur isotopes (Ding et al., 1999) The true value of the VCDT was calculated by Ding et al. (2001) to be ^{34}S/^{32}S = 0.044162. This value will be used to calculate the δ^{34}S value of the samples from the TNGB. The VCDT reference is considered to represent the primordial terrestrial sulphur isotopic composition (Nielsen et al., 1991). Therefore, any variations in sulphur isotope compositions relative to VCDT implies differentiation since the Earth was formed. The investigation of sulphur isotope concentrations and ratios allows us to study and unravel such isotope differentiation or fractionation processes in the geological past.

7.3. Geological reservoirs

Sulphur commonly occurs as sulphates and sulphides on Earth. Oxidation and reduction processes fractionate sulphur isotopes which changes their ratios from primordial ratios. Oxidation processes form sulphates which are generally more enriched in ^{34}S. Conversely, reduction processes produce sulphides which are depleted in ^{34}S (Seal, 2006). The isotope exchange equation between sulphate and sulphide is written as follows:

$$H_2{}^{34}S + {}^{32}SO_2 \leftrightarrows H_2{}^{32}S + {}^{34}SO_2$$
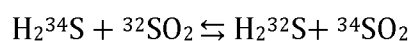
The theoretical value of the exchange constant is 1.075 at 25 °C (Tudge and Thode, 1950). The above equation shows that ^{34}S preferentially fractionates into oxidized sulphur. Thus sulphates will be more enriched in ^{34}S in nature when compared to sulphides.

However, in the TNGB the process of interest is:(i) hydrothermal dissolution of authigenic or metamorphic host rock pyrite, transport of the dissolved sulphur into the hydrothermal system, and subsequent pyrite precipitation in hydrothermal veins, or (ii) influx of external sulphur dissolved in fluids from a distal source, from which pyrite with a potentially different isotopic signature may have precipitated. The first process, dissolution and re-precipitation of pyrite is considered to result in hydrothermal pyrite with an isotopic signature similar to that in authigenic pyrite in the sedimentary source rock nearby. Pyrite crystallising from fluids generated elsewhere may have isotopic signatures different from host rock pyrite. In either case, fractionation related to oxidation or reduction processes is unlikely to be a significant factor changing the S isotopic signature in pyrite. This is also supported by Goldhaber (2003), who referring to results of experimental work by Price and Shieh (1979) and Böttcher et al. (1998), states that inorganic reactions during pyrite formation does not cause isotopic fractionation larger than 1.5‰ δ^{34}S. The variations discussed in this study are significantly larger.

More important may be the combination of both processes, the mixing of locally generated fluids from the sedimentary host containing sulphur characteristic for that reservoir with external fluids with sulphur of different isotopic signature. This would lead to a resulting isotopic signature in

hydrothermal sulphide proportional to the abundance and signature in the different sulphur sources (Seal, 2006). Possible fluid mixing will be considered in the discussion section.

Since the VCDT reference standard is regarded as representing the bulk Earth composition, it is used to illustrate the fractionation of sulphur isotopes in nature. For this reason sulphur isotope variations on Earth can be considered relative to geological reservoirs.

Figure 7.1 (Seal, 2006) and Figure 7.2 (Thode, 1991) show $\delta^{34}S$ values for various geological reservoirs. Sulphur in meteorites, basic sills, and igneous rocks of primary origin plot close to zero and display a narrow range of $\delta^{34}S$ values. Granites, which are abundant in the TNGB, have $\delta^{34}S$ values that typically range between -10 and +10, but less commonly may show larger values up to +40‰ and down to -50‰. Modern sea water also has a narrow range of $\delta^{34}S$ values around +20. However, the sulphur mostly occurs as sulphates, and the oxidation process increases $\delta^{34}S$. Evaporites, which may contain large proportions of sulphates, range in $\delta^{34}S$ from +5 to >40. Modern and ancient sedimentary pyrite may show any value from $\delta^{34}S$= -50 to ~+18‰, depending on the specific S isotope signature in the sediment. However, most non-evaporitic sediments appear to show pyrite with $\delta^{34}S$ between -15 to +10. Seal (2006) reports $\delta^{34}S$ for coal and petroleum predominantly between 0 and +10; Thode (1991) provides a significantly larger range. Thode (1970) described this spread as being secondary in nature as the sulphides may have been involved in the sedimentary cycle aided by biological activity. This also may explain the large spread reported for sedimentary rocks.
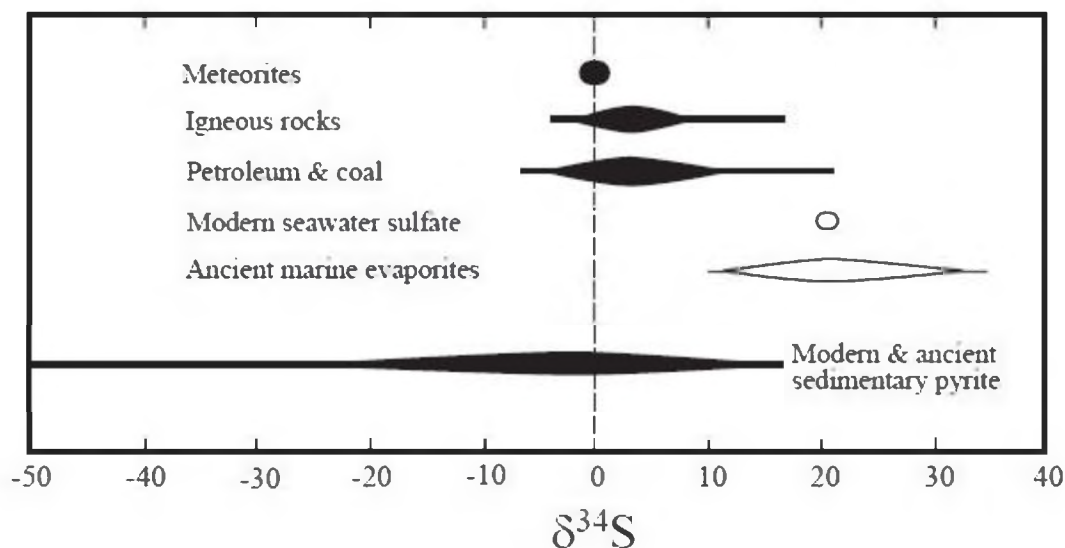
Figure 7.1: $\delta^{34}S$ values of sulphur isotope distribution in various geological reservoirs. All isotopic values in permil (VCDT) (Seal, 2006).
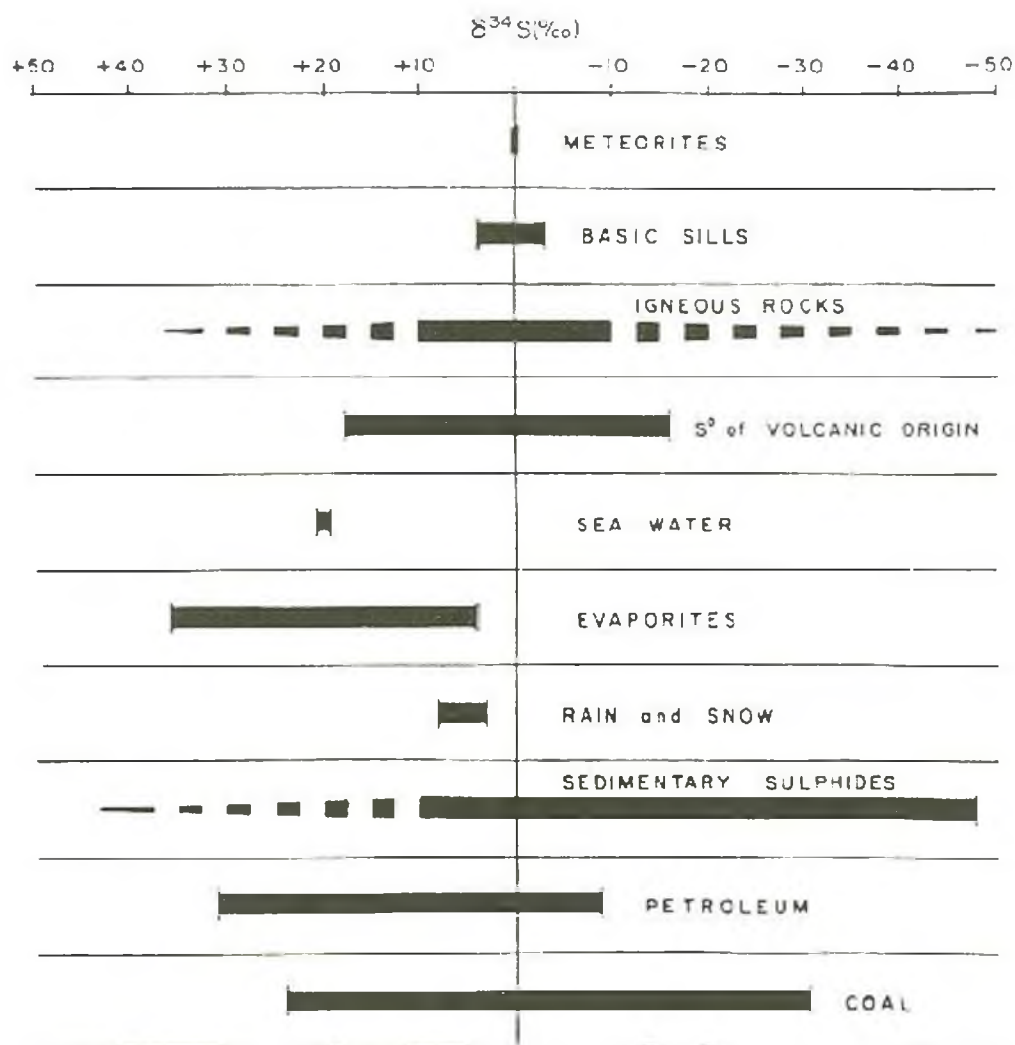
Figure 7.2: $\delta^{34}S$ values of sulphur isotope distribution in various geological reservoirs. All isotopic values in permil (VCDT) (Thode, 1991). Note that compared to Seal (2006) this diagram shows a reversed $\delta^{34}S$ scale.

7.4. Analytical Methods

There are three ways to analyse sulphur isotopes: Conventional, in-situ and continuous flow techniques. Conventional methods involve the physical separation of sulphur-containing phases either by handpicking or gravimetric techniques, or using wet chemical techniques, converting them to gases such as SO_2 or SF_6. In solution, the sulphur will be analyses using a mass spectrometer and compared to reference material (Rees and Holt, 1991). This technique has some limitations as it requires a large quantity of sample material and the separation of pure mineral phases, which can may be quite difficult or impossible, depending upon the nature of the sample.

The most recent method is the continuous flow technique that can measure samples in the microgram range. Continuous flow isotope ratio mass spectrometry (CF-IRMS) uses He carrier gas to carry SO_2, CO_2 and H_2O into the IRMS where isotope ratios are obtained from SO_2 gas peaks (Grassineau et al., 2001). This method reduces sample quantity and has rapid analytical cycle of less than 8 min (Grassineau et al., 2001).

Most studies use in-situ techniques, which do not need large sample quantities and allow the analysis of individual crystals with spatial resolutions from approximately 20 μm to approximately 200 μm in diameter (Ohmoto and Goldhaber, 1997). Instruments of choice are LA-ICP-MS or, with higher analytical precision, secondary ion mass spectrometers (SIMS) (Ohmoto and Goldhaber, 1997).

Samples in this study have been analysed at the Geological Research Centre Potsdam, Germany. A CAMECA 1280 HR SIMS instrument has been used to determine the $\delta^{34}S$ values on pyrite from the host rocks and from hydrothermal veins. Analytical methods are detailed in chapter 3.3.4. This data has been used to determine the possible provenance of sulphur.

7.5. Results

The sulphur isotope values from 143 analyses show a broad range from -18.4 to +22.6‰ versus VCDT. This distribution of $\delta^{34}S$ values for the TNGB spans a large part of the naturally occurring range of geological reservoirs (Figures 7.1 and 7.2). Considering that significant isotope fractionation is not likely in the TNGB (see section 7.3) this wide range indicated isotopically different sulphur sources. The S isotope data are reported graphically and in data tables (e.g., Figure 7.3, 7.4; Table 7.5.1 to 7.5.4). Appendix 4 lists the complete pyrite sulphur isotope composition datasheet.

As a general trend in the TNGB, and without distinguishing pyrite from hydrothermal veins or from the host rock, sulphur isotopes appear to get somewhat lighter from Twangiza in the north to Lugushwa in the centre of the TNGB. Then there is a significant step up to heavy $\delta^{34}S$ in the Namoya deposit, at the southern end of the TNGB. In Twangiza, the spread in $\delta^{34}S$ ranges from -5.2 to +3‰ with an average around -0.3‰ (Figure 7.3). Kamituga shows a $\delta^{34}S$ range from -0.6 to -9.1‰, averaging at -5.0‰. This average is 5‰ heavier than that from Lugushwa (-10‰), but at Lugushwa the spread in $\delta^{34}S$, ranging from +3.0 to -18.4‰, is much larger than in Twangiza or Kamituga. A similarly large spread of over 20‰, but with much heavier isotope compositions, is seen in Namoya at the southern end of the TNGB. Here the $\delta^{34}S$ in pyrite ranges from +1.3 to +22.6‰ with an average of +12.2‰. Hence, overall the large variety of isotopic signatures amongst the four deposits indicates isotopically different sulphur sources. However, in all deposits at least a few analyses show near-neutral $\delta^{34}S$ values (Figure 7.4).
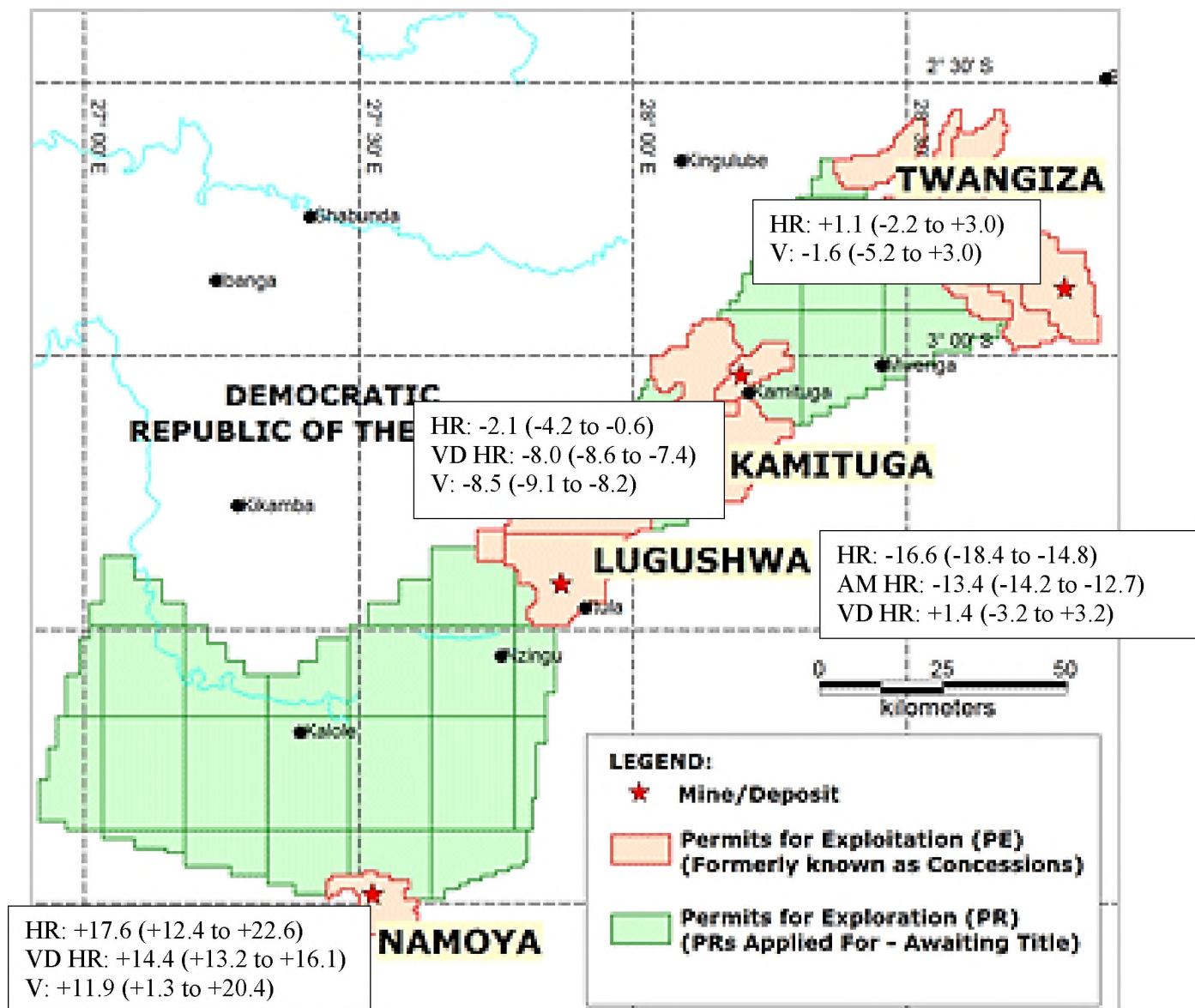
Figure 7.3: Sulphur isotope compositions of pyrite samples from the TNGB deposits. $\delta^{34}S$ values are in permil (VCDT). HR=Host rock pyrite; AM HR =pyrite in HR displaying auto-metasomatic growth; VD HR = pyrite disseminated from hydrothermal vein into HR; V = vein pyrite (modified from source: www. BANRO.com).
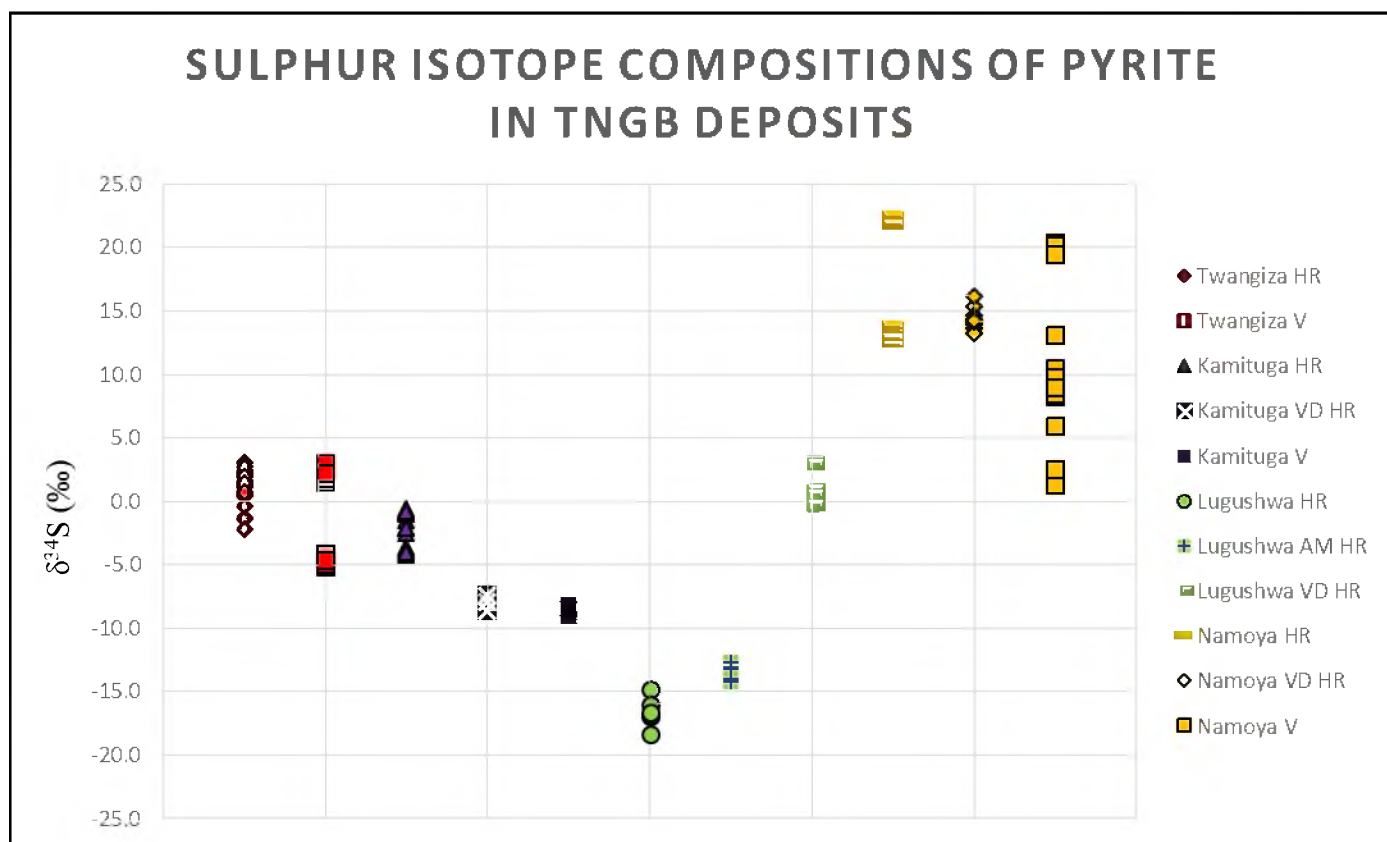
Figure 7.4: δ^{34}S compositions (VCDT) of pyrite in samples from the TNGB. HR=Host rock pyrite; AM HR = pyrite in HR displaying auto-metasomatic growth; VD HR = pyrite disseminated from hydrothermal vein into HR; V = vein pyrite.

7.5.1. Twangiza deposit

SIMS data from host rock pyrite (a total of 24 analyses) show moderate variation in sulphur isotopic composition obtained from 11 different pyrite crystals, covering a range of -2.2‰ to +3.0‰ (average +1.1‰; Figure 7.3). There is little variation in $\delta^{34}S$ within and among different crystals from the same sample. All three samples show an average standard deviation of 1.4‰. Samples TW-FS-03 and TW-FS-07 display slightly heavier ^{34}S compared to sample TW-FS-05, with average $\delta^{34}S$ values of 1.2‰, 1.9‰ and 0.6‰, respectively. However, this variation in $\delta^{34}S$ is approximately within the analytical uncertainty. Therefore the sulphur source from which pyrite in host rock samples from Twangiza most likely has formed is from a homogeneous, isotopically near-neutral geological reservoir. In addition, TW-FS-03 and -05 contain 9.85 and 7.12 g/t gold, and the S isotopes in associated pyrite are around neutral ($\delta^{34}S$ -2.2‰ to +3‰; Table 7.5.1). TW-FS-07 also contains gold, but at a lower grade (0.57 g/t), and its isotopic signature is similar to TW-FS-03 and -05. This shows that there is a good correlation between sulphur isotopic signature and gold grade in Twangiza HR pyrite.

Similar to the host rocks, pyrite from four veins (a total of 27 analyses, 12 pyrite crystals) show moderate variation in sulphur isotopic composition in pyrites, covering a range of -5.2‰ to +3.0‰ (average -1.6‰; Figure 7.3). There is little variation in $\delta^{34}S$ within and among grains from the same sample, with an average standard deviation of -1.6‰ of all four samples. Samples T3 and T25 display slightly heavier ^{34}S average values of 2.3‰. On the other hand, samples T9 and T12 are isotopically lighter, with average $\delta^{34}S$ values of -4.6‰ and -4.8‰, respectively.

The variations in $\delta^{34}S$ signatures imply that pyrite from samples T9 and T12 originate from an isotopically lighter fluid than pyrite in samples T3 and T25 (Figure 7.4). Furthermore, samples T3 and T25 have a similar isotopic signature to pyrite from the host rock, which suggests that the fluid forming T3 and T25 either originated in from the host rocks or from an isotopically similar source. T9 and T12 may have formed from another source further away. The $\delta^{34}S$ value of ~-5‰ is not specific to any source, which could be sedimentary, igneous (Figures 7.1, 7.2), or a mixture between different isotopically lighter and heavier sources. However, according to Seal (2006) igneous sources more commonly show positive $\delta^{34}S$ signature.

T3 and T9 have contain 9.19 and 63 g/t, gold respectively (Table 7.5.1). On the other hand, samples T9 and T12 are not mineralised and have similar isotopic values to HR pyrite. This suggests that local fluids mobilised and concentrated gold in the Twangiza veins. The isotopically lighter fluid that precipitated pyrite with $\delta^{34}S$ of ~-4 to -5‰ seems not to be associated with high gold grade. This however does not mean that no gold at all is associated with the low-grade veins. In sample T9 small gold particles (section 6.2.1) occur in VD HR pyrite, but the provenance of that gold, whether it was present or not before fluid influx and vein formation or whether this particle already was present in the host rock, is unclear.
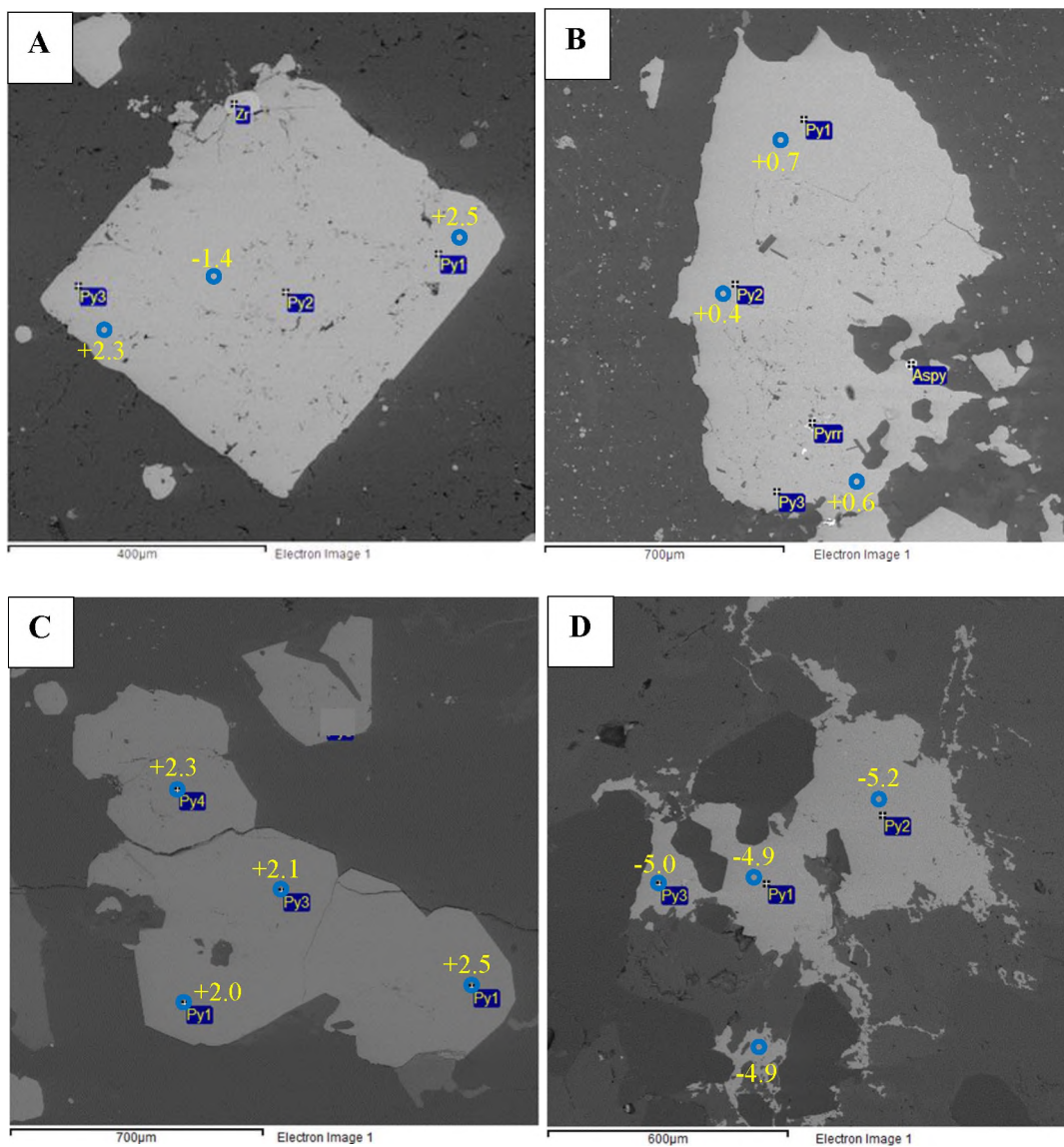
Figure 7.5: Sulphur isotopic compositions (in yellow) of HR pyrite (**A**:TW-FS-03; **B**: TW-FS-05), and V pyrite (**C**: T3; **D**: T9) from Twangiza. Blue circles indicate the locations of SIMS δ^{34}S analyses. Small blue squares indicate positions of EDS analysis.

Table 7.5.1: Sulphur isotope compositions of pyrite in Twangiza. All $\delta^{34}S$ are relative to VCDT. Pyrite type: V = Vein pyrite; HR = Host rock pyrite; AM HR = Pyrite in host rock displaying auto-metasomatic growth; VD HR = Pyrite disseminated from hydrothermal vein into host rock.

Analysis name	Sample	Pyrite type	Au grade and association	$\delta^{34}S$
Tm1-SI1@1	TW-FS-03	HR	9.85 g/t; Au flake in Py	1.5
Tm1-SI1@2	TW-FS-03	HR	9.85 g/t; Au flake in Py	-1.3
Tm1-SI3@1	TW-FS-03	HR	9.85 g/t; Au flake in Py	1.6
Tm1-SI3@2	TW-FS-03	HR	9.85 g/t; Au flake in Py	3.0
Tm1-SI2@1	TW-FS-03	HR	9.85 g/t; Au flake in Py	2.5
Tm1-SI2@2	TW-FS-03	HR	9.85 g/t; Au flake in Py	-1.4
Tm1-SI2@3	TW-FS-03	HR	9.85 g/t; Au flake in Py	2.3
Tm6-SI2@1	TW-FS-05	HR	7.12 g/t; Au flake in Py	0.6
Tm6-SI2@2	TW-FS-05	HR	7.12 g/t; Au flake in Py	0.4
Tm6-SI2@3	TW-FS-05	HR	7.12 g/t; Au flake in Py	0.7
Tm6-SI1@1	TW-FS-05	HR	7.12 g/t; Au flake in Py	1.1
Tm6-SI1@2	TW-FS-05	HR	7.12 g/t; Au flake in Py	0.5
Tm6-SI1@3	TW-FS-05	HR	7.12 g/t; Au flake in Py	-2.2
Tm6-SI1@4	TW-FS-05	HR	7.12 g/t; Au flake in Py	0.6
Tm6-SI3@1	TW-FS-05	HR	7.12 g/t; Au flake in Py	2.1
Tm6-SI3@2	TW-FS-05	HR	7.12 g/t; Au flake in Py	-0.4
Tm6-SI3@3	TW-FS-05	HR	7.12 g/t; Au flake in Py	1.4
Tm6-SI3@4	TW-FS-05	HR	7.12 g/t; Au flake in Py	2.2
Tm3-SI1@1	TW-FS-07	HR	0.57 g/t	2.2
Tm3-SI1@2	TW-FS-07	HR	0.57 g/t	2.1
Tm3-SI1@3	TW-FS-07	HR	0.57 g/t	2.8
Tm3-SI3@1	TW-FS-07	HR	0.57 g/t	1.9
Tm3-SI3@2	TW-FS-07	HR	0.57 g/t	1.5
Tm3-SI3@3	TW-FS-07	HR	0.57 g/t	0.7
Tm15SI1@1	T12	V	<0.1 g/t	-4.8
Tm15SI1@2	T12	V	<0.1 g/t	-5.0
Tm15SI1@3	T12	V	<0.1 g/t	-4.6
Tm2-SI2@1	T25	V	63 g/t	2.1
Tm2-SI2@2	T25	V	63 g/t	1.5
Tm2-SI2@3	T25	V	63 g/t	2.9
Tm2-SI1@1	T25	V	63 g/t	1.8
Tm2-SI1@2	T25	V	63 g/t	3.0

Table 7.5.1: (continued)

Tm2-SI1@3	T25	V	63 g/t	2.2
Tm12-SI1@2	T3	V	9.19 g/t	2.6
Tm12-SI1@3	T3	V	9.19 g/t	2.3
Tm12-SI2@1	T3	V	9.19 g/t	2.5
Tm12-SI2@2	T3	V	9.19 g/t	2.0
Tm12-SI2@3	T3	V	9.19 g/t	2.1
Tm12-SI2@4	T3	V	9.19 g/t	2.3
Tm9-SI1@1	T9	V	<0.1 g/t; Au flake in Py	-4.2
Tm9-SI1@2	T9	V	<0.1 g/t; Au flake in Py	-4.2
Tm9-SI1@3	T9	V	<0.1 g/t; Au flake in Py	-4.8
Tm9-SI1@4	T9	V	<0.1 g/t; Au flake in Py	-4.6
Tm9-SI1@5	T9	V	<0.1 g/t; Au flake in Py	-4.2
Tm9-SI3@1	T9	V	<0.1 g/t; Au flake in Py	-4.7
Tm9-SI3@2	T9	V	<0.1 g/t; Au flake in Py	-4.7
Tm9-SI3@3	T9	V	<0.1 g/t; Au flake in Py	-4.1
Tm9-SI2@1	T9	V	<0.1 g/t; Au flake in Py	-4.9
Tm9-SI2@2	T9	V	<0.1 g/t; Au flake in Py	-5.2
Tm9-SI2@3	T9	V	<0.1 g/t; Au flake in Py	-5.0
Tm9-SI2@4	T9	V	<0.1 g/t; Au flake in Py	-4.9

7.5.2. Kamituga deposit

SIMS data from host rock pyrite (a total of 14 analyses, six pyrite crystals) show moderate variations in sulphur isotopic composition in pyrites, covering a range of -4.2‰ to -0.6‰ (average -2.1‰; Figure 7.3). The authigenic/metamorphic pyrite in samples KG-SIS-5, KG-SIS-6 and KG-SIS-7 show averages in $\delta^{34}S$ values of -2.2‰, -1.1‰ and -3.9‰, respectively. The standard deviation amongst all pyrites in the three host rock samples is relatively small at 1.3‰. Sulphur in the Kamituga HR pyrite is most likely sourced from a homogeneous geological reservoir.

Sample KG-SIS-2 is texturally and isotopically different. This sample contains a quartz-pyrite vein, and the pyrite in the hosting chlorite schist is likely to be the product of fluid influx from the vein (VD HR type; cf. section 4.2, 5.2). The isotopic signatures confirm that. Sulphur isotopic composition obtained from two VD HR pyrite crystals (3 analyses) show moderate variation, covering a range of -8.6‰ to -7.4‰ (average -8.0‰; Figure 7.3). The standard deviation is 0.6‰. VD HR pyrite in this sample displays an isotopically lighter ^{34}S values than HR Pyrite (Figure 7.4). The variations in $\delta^{34}S$ signatures imply that sulphur from VD HR pyrite originates from an isotopically lighter fluid. Similarly, sulphur isotope composition in V pyrite (a total of 8 analyses in four pyrite crystals also shows isotopically lighter with $\delta^{34}S$ values of -9.1‰ to -8.2‰ (average -8.5‰; Figure 7.3) and a standard deviation of 0.3‰.

Hence, the three samples from Kamituga suggest isotopically heavier sulphur in the sedimentary host ($\delta^{34}S$ ~-2.1‰), and a different sulphur source in an external fluid phase forming vein pyrite that is about 6‰ lighter. According to Seal (2006) the hydrothermal fluid composition of $\delta^{34}S$ ~-8‰ to -8.5‰ is out of the range of common granitic fluids (Figure 7.1), but Thode (1991) sees it within the igneous range (Figure 7.2). Hence, the hydrothermal fluid, while being well in the range of sedimentary sulphur reservoirs, could be granitic, or a mix between heavier granitic and much lighter sedimentary fluids.

The association of Kamituga pyrite with gold is less clear than in Twangiza. The highest grade is seen for sample KG-SIS-5 with 1.9 g/t. Pyrite in this sample shows $\delta^{34}S$ around -2.2‰. Other host rocks showing similar isotopic signature in pyrite are not mineralised (Table 7.5.2).

KG-SIS-2 containing the isotopically lighter V- and VD HR-type pyrite is associated with a low gold grade (0.41 g/t) but shows small gold inclusions in pyrite. This suggests that Au and light sulphur were mobile and precipitated together.
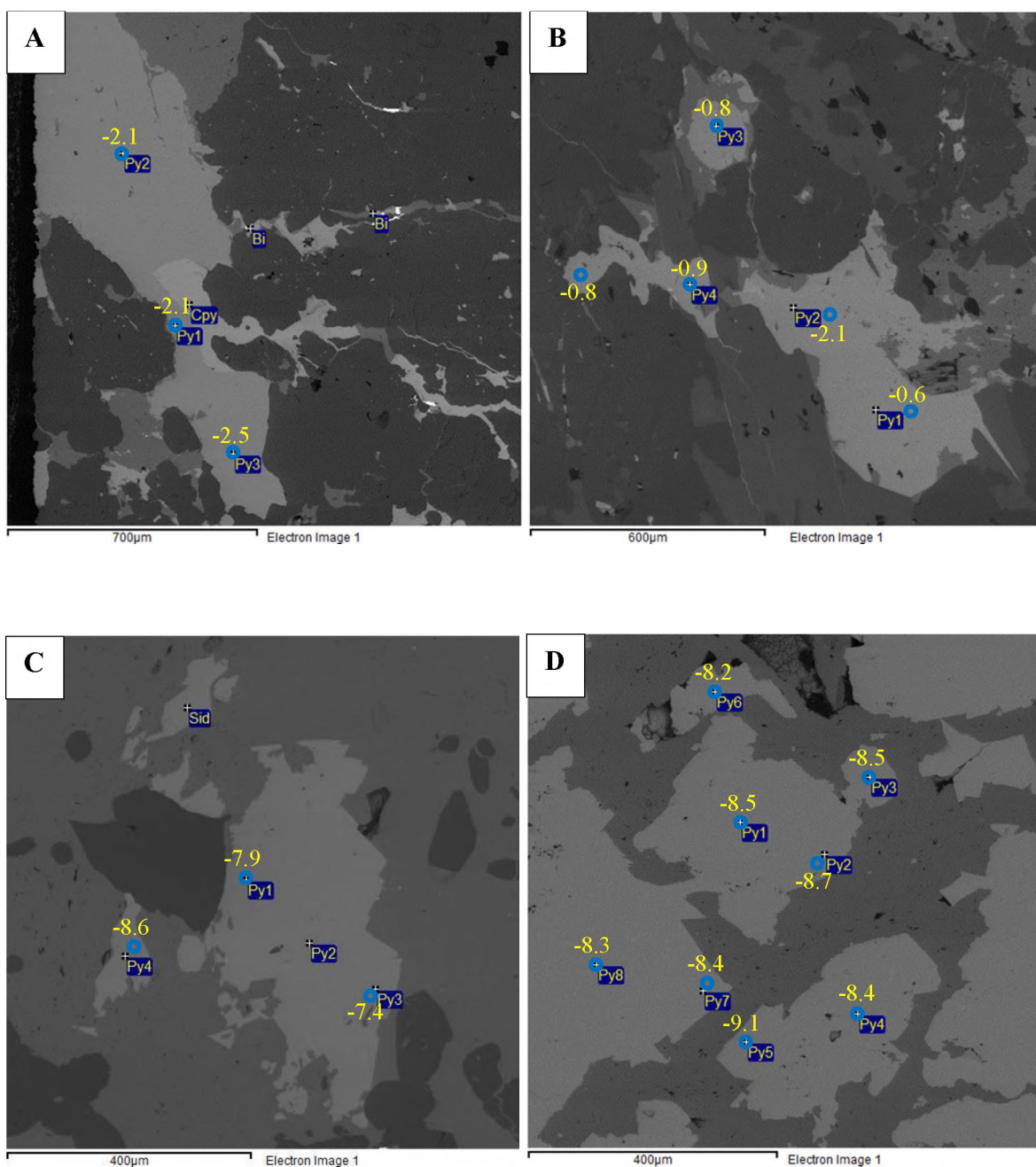
Figure 7.6: Sulphur isotopic compositions (in yellow) of HR pyrite (**A**: KG-SIS-5; **B**: KG-SIS-6), VD HR pyrite (**C**: KG-SIS-2) and V pyrite (**D**: KG-SIS-2) from Kamituga. Blue circles indicate the locations of SIMS δ^{34}S analyses. Small blue squares indicate positions of EDS analysis.

Table 7.5.2: Sulphur isotope compositions of pyrite in Kamituga. All $\delta^{34}S$ are relative to VCDT. Pyrite type: V = Vein pyrite; HR = Host rock pyrite; AM HR = Pyrite in host rock displaying auto-metasomatic growth; VD HR = Pyrite disseminated from hydrothermal vein into host rock.

Analysis name	Sample	Pyrite type	Au grade and association	$\delta^{34}S$
Tm20-SI2@1	KG-SIS-5	HR	1.9 g/t	-2.1
Tm20-SI2@2	KG-SIS-5	HR	1.9 g/t	-2.1
Tm20-SI2@3	KG-SIS-5	HR	1.9 g/t	-2.5
Tm22-SI1@1	KG-SIS-6	HR	0.2 g/t	-1.0
Tm22-SI1@2	KG-SIS-6	HR	0.2 g/t	-1.5
Tm22-SI2@1	KG-SIS-6	HR	0.2 g/t	-0.6
Tm22-SI2@3	KG-SIS-6	HR	0.2 g/t	-0.8
Tm22-SI2@4	KG-SIS-6	HR	0.2 g/t	-0.9
Tm22-SI2@5	KG-SIS-6	HR	0.2 g/t	-0.8
Tm25-SI1@1	KG-SIS-7	HR	0.07 g/t	-3.8
Tm25-SI1@2	KG-SIS-7	HR	0.07 g/t	-3.6
Tm25-SI2@2	KG-SIS-7	HR	0.07 g/t	-4.2
Tm25-SI2@3	KG-SIS-7	HR	0.07 g/t	-4.0
Tm17-SI2@1	KG-SIS-2	VD HR	0.41g/t, Au flake in Py	-8.5
Tm17-SI2@2	KG-SIS-2	VD HR	0.41g/t, Au flake in Py	-8.7
Tm17-SI2@3	KG-SIS-2	VD HR	0.41g/t, Au flake in Py	-8.5
Tm17-SI2@4	KG-SIS-2	VD HR	0.41g/t, Au flake in Py	-8.4
Tm17-SI2@5	KG-SIS-2	VD HR	0.41g/t, Au flake in Py	-9.1
Tm17-SI2@6	KG-SIS-2	VD HR	0.41g/t, Au flake in Py	-8.2
Tm17-SI2@7	KG-SIS-2	VD HR	0.41g/t, Au flake in Py	-8.4
Tm17-SI2@8	KG-SIS-2	VD HR	0.41g/t, Au flake in Py	-8.3
Tm17-SI1@1	KG-SIS-2	V	0.41g/t, Au flake in Py	-7.9
Tm17-SI1@3	KG-SIS-2	V	0.41g/t, Au flake in Py	-7.4
Tm17-SI1@4	KG-SIS-2	V	0.41g/t, Au flake in Py	-8.6

7.5.3. Lugushwa deposit

Data from three samples (a total of 16 analyses) reveal significant variation in sulphur isotopic composition in pyrites, covering a range of -18.4‰ to +3.2‰ (Figure 7.3). Overall, sulphur in pyrite from Lugushwa is the most depleted in ^{34}S amongst the four deposits (Figure 7.4). Pyrite in the three Lugushwa samples formed by either precipitation from fluids in veins (LG-SI-05; V-type), authigenic or metamorphic in the sedimentary host rock (LG-SI-02 (HR-type), or autometasomatically by minor fluid mobility (LG-SI-06, AM HR type pyrite). Samples LG-SI-02 and LG-SI-06, in which pyrite most likely formed from sulphur from the sedimentary host, are more depleted in ^{34}S with sulphur isotopic compositions ranging from -18.4‰ to -14.8‰ (average 16.6‰) and -14.2‰ to -12.7‰ (average -13.4‰), respectively. These values are well in the range of the sedimentary sources, which is in agreement with the petrographic evidence. In contrast, hydrothermal pyrite in the vein from sample LG-SI-05 is more enriched in ^{34}S with δ^{34}S values ranging from -0.3‰ to +3.2‰ (average +1.4‰). Such signatures have been seen in Twangiza in both host rocks and in highly mineralised veins. In Namoya (see section 7.5.4 below) such signatures occur in dolerite-hosted veins. Hence the vein pyrite in sample LG-SIS-05 may be related to either magmatic sulphur sources or to much heavier sedimentary sources than likely for LG-SI-02 and -06 (Figures 7.1, 7.2). The current data base does not allow to identify whether the fluid forming LG-SI-05 may have originated from local or distal sources.

The HR and AM HR pyrites in samples LG-SI-02 and -06 are not associated with significant gold mineralisation. Grades are <0.1 g/t in both sample sections. However, the gold flake in LG-SI-02 (Figure 6.13) allows to associate the host rock and the light S isotopic signature in pyrite of δ^{34}S (~-16‰) with the presence of gold. In the vein pyrite of LG-SI-05 gold was seen in BSE imagery but here the gold grade of 0.63 g/t (see section 6.2.1), suggesting that the vein is associated with mineralisation. However, the assay result was obtained from a 1 m long core section that has included vein and host rock material. Hence the grade may not be related to the vein formation.
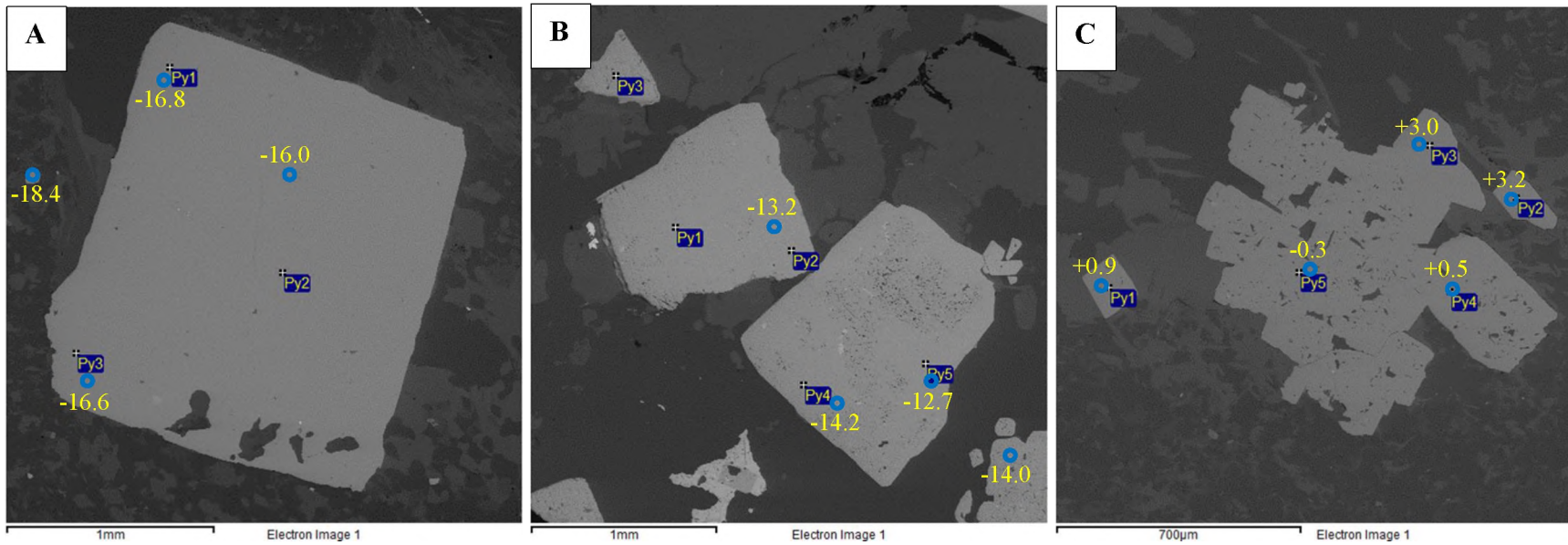
Figure 7.7: Lugushwa sulphur isotopic compositions (in yellow) of: **A**) HR pyrite in sample LG-SI-02; **B**) AM HR pyrite in sample LG-SI-06; **C**) VD HR pyrite in sample LG-SI-05. Blue circles indicate the locations of SIMS δ^{34}S analyses. Small blue squares indicate positions of EDS analysis.

Table 7.5.3: Sulphur isotope compositions of pyrite in Lugushwa. All $\delta^{34}S$ are relative to VCDT. Pyrite type: V = Vein pyrite; HR = Host rock pyrite; AM HR = Pyrite in host rock displaying auto-metasomatic growth; VD HR = Pyrite disseminated from hydrothermal vein into host rock.

Analysis name	Sample	Pyrite type	Au grade and association	$\delta^{34}S$
Tm19-SI1@1	LG-SI-02	HR	<0.01 g/t, Au flake in Py	-17.0
Tm19-SI1@2	LG-SI-02	HR	<0.01 g/t, Au flake in Py	-14.8
Tm19-SI2@1	LG-SI-02	HR	<0.01 g/t, Au flake in Py	-16.8
Tm19-SI2@2	LG-SI-02	HR	<0.01 g/t, Au flake in Py	-16.0
Tm19-SI2@3	LG-SI-02	HR	<0.01 g/t, Au flake in Py	-16.6
Tm19-SI2@4	LG-SI-02	HR	<0.01 g/t, Au flake in Py	-18.4
Tm24-SI1@1	LG-SI-06	AM HR	<0.1 g/t	-6.6
Tm24-SI1@2	LG-SI-06	AM HR	<0.1 g/t	-13.1
Tm24-SI2@1	LG-SI-06	AM HR	<0.1 g/t	-13.2
Tm24-SI2@2	LG-SI-06	AM HR	<0.1 g/t	-14.2
Tm24-SI2@3	LG-SI-06	AM HR	<0.1 g/t	-12.7
Tm24-SI2@4	LG-SI-06	AM HR	<0.1 g/t	-14.0
Tm21-SI2@1	LG-SI-05	V	0.63 g/t	0.9
Tm21-SI2@2	LG-SI-05	V	0.63 g/t	3.2
Tm21-SI2@3	LG-SI-05	V	0.63 g/t	3.0
Tm21-SI2@4	LG-SI-05	V	0.63 g/t	0.5
Tm21-SI2@5	LG-SI-05	V	0.63 g/t	-0.3

7.5.4. Namoya deposit

The samples from the Namoya deposit show a large variation in $\delta^{34}S$, commonly between about +8‰ and +22‰ (Table 7.5.4), a range that overlaps with the heavier sulphur commonly seen in igneous sources (up to ~+10‰; e.g. Seal, 2006; Figures 7.1, 7.2), but most data suggest sedimentary and evaporitic sulphur sources. Only three analyses in NM-SI-3 show lighter $\delta^{34}S$ of +1.3‰ to +5.9‰. Pyrite in the host rock samples NM-SI-6 and -8 shows variably heavy S-isotopic signatures (Figures 7.3,7.4). In sample NM-SI-6, $\delta^{34}S$ ranges between +21.8‰ and +22.6‰, a range that indicates sedimentary/evaporitic sulphur sources. Pyrite in NM-SI-8 is isotopically lighter with $\delta^{34}S$ ranging from +12.5‰ to +13.9‰ (Table 7.5.4). These values are also consistent with evaporitic sedimentary sources, which is in agreement with the meso- and microscopic petrographic observation that indicate authigenic/metamorphic pyrite growth.

Veins in Namoya show isotopically heavy pyrite with a range that includes that seen in the host rock pyrites (up to $\delta^{34}S$ of +20.4‰; sample NM-SI-5; Table 7.5.4). Also the lighter isotopic signature of around +14.4‰ is seen in VD HR pyrite from sample NM-SI-7. However, veins from the Seketi pit (NM-SI-1, -2, and -3), are lighter and range between $\delta^{34}S$ of +1.3‰ to +13.1‰, with an average of +8.5‰ (standard deviation: 2.6‰). Sample NM-SI-3 shows the largest range that includes the minimum and maximum value seen in the Seketi pit veins (+1.3‰, +13.1‰; Table 7.5.4). All Seketi pit veins (NM-SI-1, -2 and -3) are hosted in sheared and altered dolerite. This may suggest that these veins formed from mixing the heavy host rock sulphur source with a significantly lighter sulphur, probably sourced from the local dolerite.

Seketi pit is a mineralised zone but only NM-SI-3 has been assayed, yielding 1.32 g/t gold. There is a likelihood of a mixed sedimentary and doleritic sulphur source that is expressed in the variable sulphur isotopic compositions. It is unclear whether the gold found at Seketi pit also comes from these different sources or is associated with only one of them.

Very high-grade gold mineralisation of 173 g/t is associated with heavy sulphur ($\delta^{34}S$ +19.5 to +20.4) in V pyrite from sample NM-SI-5. Such sulphur, and very likely the gold in that section, is derived from sedimentary/evaporitic sources. Arias et al. (1997) reported similar S-isotopic values in pyrite from the Navia gold belt in Spain, and associate the sulphur with a sedimentary source. The second vein outside Seketi shows low-grade gold mineralisation (0.44 g/t; VD HR pyrite in sample NM-SI-7; Table 7.5.4) associated with somewhat lighter sulphur in pyrite ($\delta^{34}S$ ~14‰). The sedimentary host rock samples show S-signatures identical to the veins (~+14 and +21‰ in samples NM-SI-8 and SI-6) but these host rocks are not mineralised. However, the similarity between sulphur in mineralised vein pyrite and in barren host rock pyrite suggests that sulphur in the veins, and probably also the gold, was derived from more or less evaporitic host rock sediments.
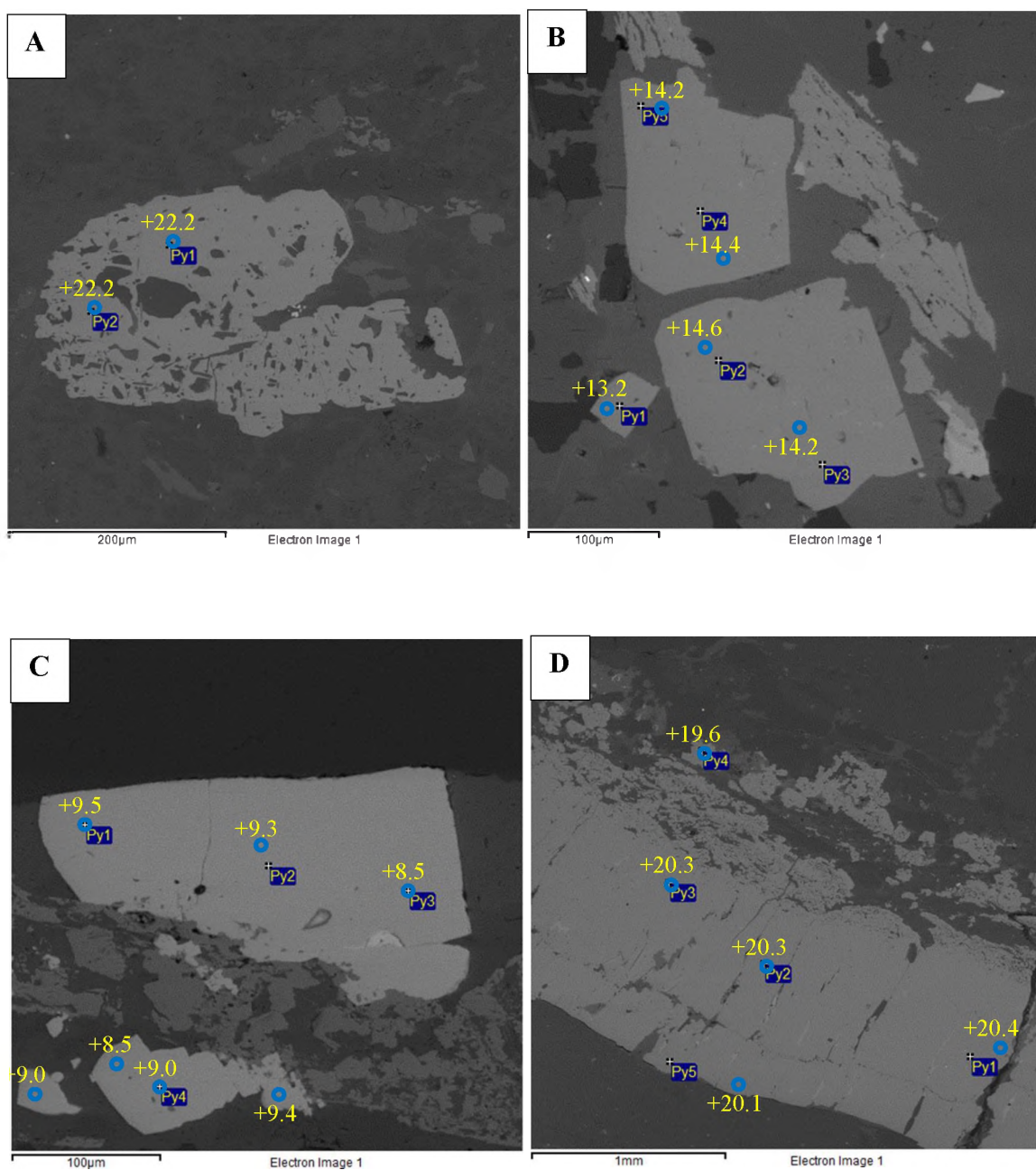
Figure 7.8: Sulphur isotopic compositions (in yellow) of HR pyrite (**A**: NM-SI-6), VD HR pyrite (**B**: NM-SI-7) and V pyrite (**C**: NM-SI-2; **D**: NM-SI-5) from Namoya. Blue circles indicate the locations of SIMS δ^{34}S analyses. Small blue squares indicate positions of EDS analysis.

Table 7.5.4: Sulphur isotope compositions of pyrite in Namoya. All $\delta^{34}S$ are relative to VCDT. Pyrite type: V = Vein pyrite; HR = Host rock pyrite; AM HR = Pyrite in host rock displaying auto-metasomatic growth; VD HR = Pyrite disseminated from hydrothermal vein into host rock.

Analysis name	Sample	Pyrite type	Au grade and association	$\delta^{34}S$
Tm27-SI2@1	NM-SI-6	HR	0.01 g/t	22.2
Tm27-SI2@2	NM-SI-6	HR	0.01 g/t	22.2
Tm27-SI1@1	NM-SI-6	HR	0.01 g/t	21.8
Tm27-SI1@2	NM-SI-6	HR	0.01 g/t	21.9
Tm27-SI3@1	NM-SI-6	HR	0.01 g/t	22.0
Tm27-SI3@2	NM-SI-6	HR	0.01 g/t	22.6
Tm18-SI1@1	NM-SI-8	HR	0.09 g/t	12.5
Tm18-SI1@2	NM-SI-8	HR	0.09 g/t	13.3
Tm18-SI1@3	NM-SI-8	HR	0.09 g/t	12.4
Tm18-SI2@1	NM-SI-8	HR	0.09 g/t	13.0
Tm18-SI2@2	NM-SI-8	HR	0.09 g/t	13.6
Tm18-SI2@3	NM-SI-8	HR	0.09 g/t	13.9
Tm23-SI1@1	NM-SI-7	VD HR	0.44 g/t	13.6
Tm23-SI1@2	NM-SI-7	VD HR	0.44 g/t	15.4
Tm23-SI1@3	NM-SI-7	VD HR	0.44 g/t	16.1
Tm23-SI1@4	NM-SI-7	VD HR	0.44 g/t	14.2
Tm23-SI1@5	NM-SI-7	VD HR	0.44 g/t	14.3
Tm23-SI1@6	NM-SI-7	VD HR	0.44 g/t	13.9
Tm23-SI2@1	NM-SI-7	VD HR	0.44 g/t	13.2
Tm23-SI2@2	NM-SI-7	VD HR	0.44 g/t	14.6
Tm23-SI2@3	NM-SI-7	VD HR	0.44 g/t	14.2
Tm23-SI2@4	NM-SI-7	VD HR	0.44 g/t	14.4
Tm23-SI2@5	NM-SI-7	VD HR	0.44 g/t	14.2
Tm4-SI2@1	NM-SI-1	V	N.A.; mineral. zone	8.3
Tm4-SI2@2	NM-SI-1	V	N.A.; mineral. zone	9.3
Tm4-SI2@3	NM-SI-1	V	N.A.; mineral. zone	9.4
Tm4-SI1@1	NM-SI-1	V	N.A.; mineral. zone	10.0
Tm4-SI1@2	NM-SI-1	V	N.A.; mineral. zone	8.6
Tm4-SI1@3	NM-SI-1	V	N.A.; mineral. zone	10.0
Tm7-SI1@1	NM-SI-2	V	N.A.; mineral. zone	9.5
Tm7-SI1@2	NM-SI-2	V	N.A.; mineral. zone	9.3
Tm7-SI1@3	NM-SI-2	V	N.A.; mineral. zone	8.9
Tm7-SI1@4	NM-SI-2	V	N.A.; mineral. zone	9.0
Tm7-SI1@5	NM-SI-2	V	N.A.; mineral. zone	8.5
Tm7-SI1@6	NM-SI-2	V	N.A.; mineral. zone	9.4

Table 7.5.4: (continued)

Tm7-SI1@7	NM-SI-2	V	N.A.; mineral. zone	9.0
Tm7-SI2@1	NM-SI-2	V	N.A.; mineral. zone	10.5
Tm7-SI2@2	NM-SI-2	V	N.A.; mineral. zone	9.8
Tm7-SI2@3	NM-SI-2	V	N.A.; mineral. zone	8.9
Tm10-SI1@1	NM-SI-3	V	1.32 g/t	1.3
Tm10-SI1@2	NM-SI-3	V	1.32 g/t	5.9
Tm10-SI1@3	NM-SI-3	V	1.32 g/t	2.5
Tm10-SI1@4	NM-SI-3	V	1.32 g/t	13.1
Tm26-SI2@1	NM-SI-5	V	173 g/t	20.4
Tm26-SI2@2	NM-SI-5	V	173 g/t	20.3
Tm26-SI2@3	NM-SI-5	V	173 g/t	20.3
Tm26-SI2@4	NM-SI-5	V	173 g/t	19.6
Tm26-SI2@5	NM-SI-5	V	173 g/t	20.1
Tm26-SI1@1	NM-SI-5	V	173 g/t	20.4
Tm26-SI1@2	NM-SI-5	V	173 g/t	20.2
Tm26-SI1@3	NM-SI-5	V	173 g/t	19.5

8. Discussion

In this study, S isotopes from pyrite have been used in order to investigate the possible gold provenance of the host rocks and hydrothermal vein system in the TNGB. A higher gold grade is usually associated with sulphide enrichment (Chuwa, 2011), therefore the source of pyrite has implications for the source of gold. Pyrite formed in the metasedimentary sequence of the TNGB which includes: mudstones and carbonaceous mudstones in Twangiza, metapelites in Kamituga and Lugushwa, and schists in Namoya. It is also found in and around quartz veins, quartz-pyrite and quartz-carbonate-pyrite veins that have precipitated in the metasedimentary host rocks. Native gold, however, precipitated from hydrothermal fluids in quartz-sulphide veins in all four deposits (Figure 8.1). Identifying the primary source of these fluids would also provide clues to the primary source of gold. Potential candidates are the host rock sedimentary sequence whereby elevated temperature and deformation could have mobilised gold bearing fluids, and concentrated this gold in the hydrothermal vein system. Another possibility are granites which are common in the TNGB. These granites may have released gold-bearing fluids during crystallization and cooling.

8.1. Sulphur sources

Figure 8.1 shows the results of sulphur isotope analysis of pyrite in the TNGB in relation with the S-isotope signatures of potential source rocks, such as igneous rocks, evaporites, and sedimentary rocks. Gold grade and sightings are also included in this figure. The overall observed range in the sulphur isotopic signature of pyrites from the TNGB is from -18.4‰ to +22.6‰ versus VCDT. This broad distribution of $\delta^{34}S$ values spans a large part of sulphur isotopic compositions typically seen on Earth (Figure 7.1 and 7.2). Broad distributions of $\delta^{34}S$ values were also seen in Strauss and Schieber (1989), Chang et al., 2008), and Ushikubo (2014), who report sulphur isotopic ratios in sedimentary pyrite as -14‰ to +18‰, -6.5‰ to +24‰, and -32.7‰ to +13.5‰, respectively. Pyrite in igneous rocks from other studies show narrow $\delta^{34}S$ ranges of +5.5‰ to +7.8‰ (Yan et.al., 2014) and -1‰ to +0.6‰ (Noku et al., 2015), whereas pyrite in metamorphic rocks may be more variable with $\delta^{34}S$ values of -17.8‰ to +1.2‰ (Goldfarb et al., 1991) and +2.2‰ to +16.9‰ (Abdollahi et al., 2009). From these previous studies, it can be inferred that pyrite in sedimentary and metamorphic rocks may have a wide range of $\delta^{34}S$ values. In contrast, pyrite in igneous rocks tends to have a narrow range in $\delta^{34}S$ values. This is due to the fact that sulphur in magmas will be homogenised whereas sedimentary or metamorphic sequences may preserve their primary heterogeneity.

In the TNGB deposits, sulphur isotopes (Figures 7.4; 8.1) display broad variations in Lugushwa ($\delta^{34}S$ -18.4‰ to +3.2‰) and in Namoya (+1.3‰ to 22.6‰). Conversely, the Twangiza and Kamituga deposits display narrower isotopic ranges of -5.2‰ to +3.0‰ and -9.1‰ to -0.6‰.
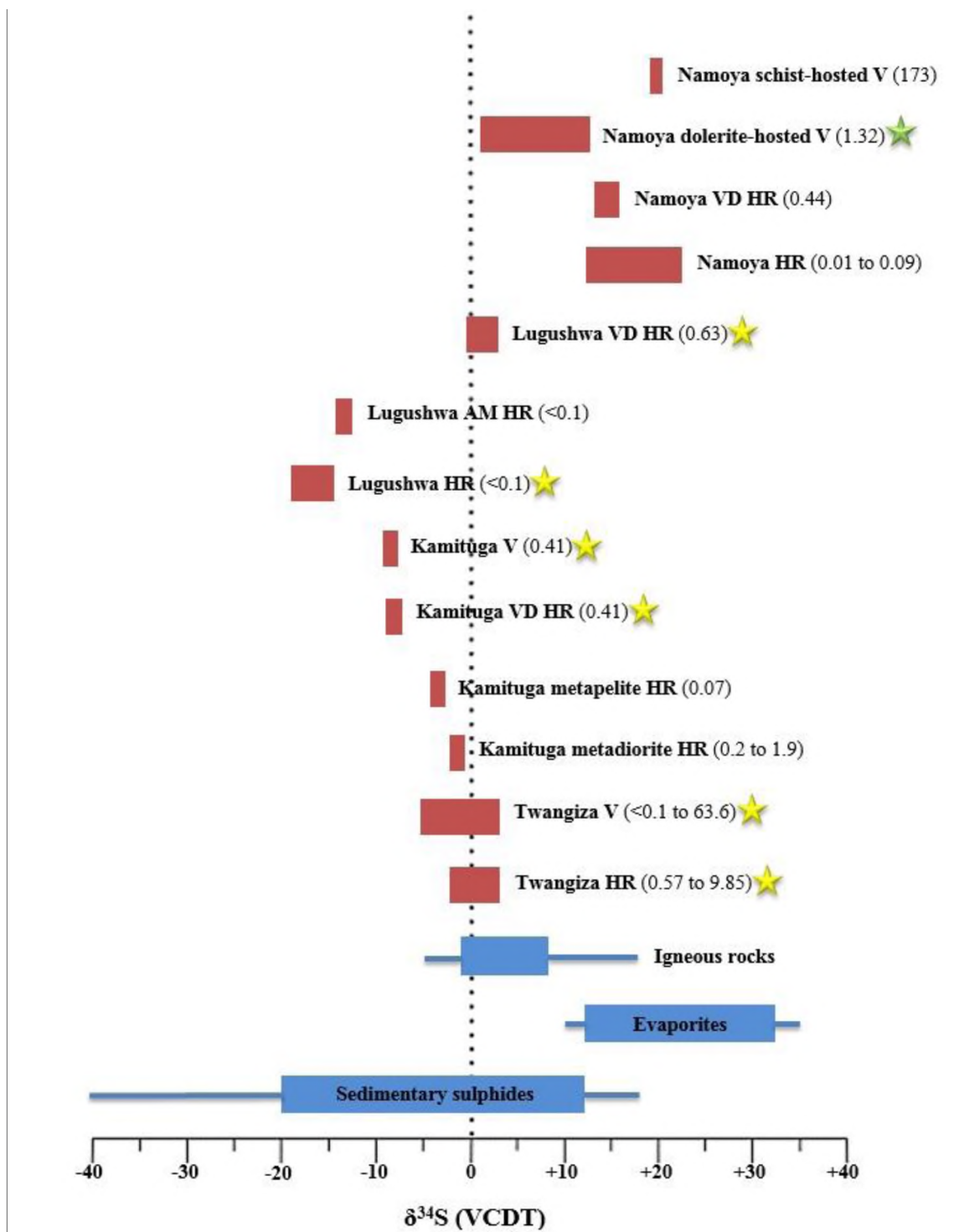
Figure 8.1: δ^{34}S of the TNGB deposits compared with δ^{34}S in granites, evaporites and sedimentary sulphides. HR=Host rock pyrite; AM HR =pyrite in HR displaying auto-metasomatic growth; VD HR = pyrite disseminated from hydrothermal vein into HR; V= vein pyrite. Blue bars are from Seal (2006). Gold grades are given in the brackets. Yellow stars indicate native gold sightings in pyrite. The green star indicates native gold sightings in arsenopyrite.

Sulphur isotopic signatures of HR pyrite in the Twangiza deposit display moderate variation of $\delta^{34}S$ values from -2.2‰ to +3.0‰ (average +1.1‰). The isotopic signature is near-neutral and falls well into the range typically seen in sedimentary rocks. However, also igneous rocks typically show such isotope compositions (Figure 8.1). Since textural evidence indicates authigenic pyrite growth in sedimentary rocks, the isotope range of -2.2‰ to +3.0‰ indicates the isotopic signature of the pelitic to carbonaceous host rocks in Twangiza deposit.

Vein-type pyrite in Twangiza also shows moderate variation in $\delta^{34}S$ values, ranging from -5.2‰ to +3.0‰ (average -1.6‰; Table 7.5.1), which includes the range seen in the sedimentary host. These isotopic values are in agreement with a sedimentary or, at least in part, an igneous source (Figure 8.1). Samples T3 and T25 have V-type pyrite that is isotopically similar to HR –pyrite, and the fluid in these veins might well have originated from carbonaceous mudstones nearby. Samples T9 and T12 display an isotopically lighter signature that is not seen in the HR pyrites, implying a different source. This source might be either sedimentary (isotopically lighter than the investigated HR pyrites), or a rather light igneous source. The $\delta^{34}S$ values in the range of -5.2‰, are rather light for igneous sources, at least according to Seal (2006) (Figure 8.1). Thode (1991) expands the field of typical igneous S-isotopic signatures further to negative values (~-10‰; Figure 7.2). Since igneous rocks are abundant in Twangiza, a light granitic fluid cannot be ruled out as a sulphur source for the vein samples T3 and T9, but a lighter sedimentary source, that is not identified, appears equally or even more likely. In addition, Walemba (2001) proposed a magmatic source for sulphur and hydrothermal fluids in Twangiza after finding sulphur compositions of +1.03‰ to +8.48‰ (cf. section 7.1), therefore providing further argument for an igneous source of hydrothermal fluids. However, this igneous source is not clear from the current data set in this study.

In Kamituga, all analysed pyrite shows negative $\delta^{34}S$ values between -9.1‰ and -0.6‰. Sulphur isotopic signatures from HR-type pyrite in two metadiorite samples (-2.5‰ to -0.6‰) and one metapelite (-4.2‰ to -3.6‰) display narrow ranges (Figure 8.1). The metadiorites have a slightly heavier isotopic signature that is in agreement with isotopically light igneous rocks (Figure 8.1). The narrow range in $\delta^{34}S$ from the one metapelitic HR pyrite (sample KG-SIS-7) may not be representative for the sedimentary sequence in the Kamituga deposit, is well compatible with a sedimentary sulphur source.

Sulphur isotopic compositions of VD HR- and V-type pyrite in Kamituga, both samples from metapelite-hosted veins, display isotopically lighter sulphur signatures (-9.1‰ to -7.4‰) than HR-type pyrite. These signatures fall well within the range of sedimentary sulphide sources, but these sources are not identical with the analysed host rock pyrites (Figure 8.1). This suggests that sulphur in the hydrothermal fluids formed from an unidentified sedimentary sulphur source that is approximately 6‰ lighter than the sulphur in the analysed HR pyrite.

Sulphur isotopic signatures of pyrite from the Lugushwa host rocks display significant variation of $\delta^{34}S$ values from -18.4‰ to +3.2‰ (Figure 7.3, 8.1). Sulphur in metapelitic host rock pyrite,

both AM HR- and HR-type (-18.4‰ to -12.7‰), fall well within the sedimentary sulphide range (Figure 8.1). In pyrite veins (Figure 7.7C), VD HR pyrite is more enriched in ^{34}S (-0.3‰ to +3.2‰) and falls within the range of either igneous rocks and sedimentary sulphides (Figure 8.1). These signatures have been seen in pyrite from Twangiza and in diorite-hosted veins from Namoya. (see section 7.5.1 and 7.5.4). Hence, the source of sulphur in the analysed hydrothermal vein from Lugushwa may have formed from either a sedimentary source that is significantly heavier than that in the analysed host rocks, or from an igneous fluid. Chuwa (2011) pointed out the association of metadiorites and granites with the metapelitic sequence, which might make these igneous rocks a possible sulphur source of these veins. However, Büttner et al. (2016) dated a hydrothermal vein from Lugushwa as Pan-African, and no igneous activity has been reported for that time period. Accordingly, metamorphic leaching of sulphur from any of the available rock types in Lugushwa, or an older, late-Kibaran granitic fluid, are potential sources for the pyrite in the analysed Lugushwa vein.

In Namoya, the very heavy δ^{34}S of HR, VD-HR and schist-hosted V-pyrite (+12.4‰ to +22.6‰) falls within the range of evaporitic sulphur sources or, for some samples, heavy sedimentary and igneous sources (Figure 8.1). Evaporites have not been described as a common constituent of the sedimentary protoliths in the Namoya region (Chuwa, 2011). It appears possible that such evaporites have been largely or entirely dissolved during fluid-present regional metamorphism and deformation. Typical evaporite minerals such as salt minerals or gypsum are easily dissolved in hydrous fluids at greenschist facies pressure-temperature (P-T) conditions. Alternatively, such evaporites simply may not have been recorded during mineral exploration. However, no other than evaporitic sources are likely explanations for most S-isotope analyses from Namoya.

Sulphur isotopic signatures in hydrothermal veins show large variation in δ^{34}S from +1.3‰ to +20.4‰, but there is a clear distinction between pyrite in dolerite hosted veins and pyrite in schist hosted veins. The latter is isotopically heavier and coincide isotopically with host rock pyrite signatures (+13.2 to +20.4‰; Figure 8.1). Accordingly, these veins likely to have originated from sedimentary host rock sources. Pyrite in dolerite hosted veins, which are all from the Seketi pit, shows signature between +1.3 to +13.1 ‰. These values indicate an igneous source contribution, mostly likely sulphur leached from the hosting diorite during regional metamorphism, possibly mixed with some heavier sulphur from the Namoya metasedimentary sequence that hosts the metadiorites.

8.2. Regional trends in the TNGB

δ^{34}S values from the approximately 210 km long TNGB are near neutral in HR-type pyrite from Twangiza, becoming isotopically lighter towards the central part of the TNGB in Kamituga and Lugushwa. The Namoya deposit at the southern end of the TNGB shows significantly heavier

sulphur than all other deposits (Figure 7.3). In broad terms, Figure 8.1 shows more overlaps and similarities amongst the Twangiza, Lugushwa and Kamituga data, but a large distinction in the Namoya sedimentary sulphur.

The most likely reason for these trends and differences may be the geological association of the sedimentary rocks in the different deposits with different geological episodes of deposition. Lugushwa and Kamituga, in the central part of the TNGB, are likely to be part of the Mesoproterozoic Kibaran basin. Twangiza in the north belongs to the younger Neoproterozoic Itombwe Supergroup, that was deposited in extensional basins overlying the Kibaran basement. The rocks in Namoya in the south is likely to be part of the Ubendian/Rusizian, and hence are Palaeoproterozoic. These differences in depositional age and sediment provenance, and likely also depositional environment, may explain the S-isotopic difference amongst the deposits, and the overall large variety in isotopic signatures within the TNGB.

8.3. Possible gold sources

The association of gold grades with individual samples is somewhat problematic because assaying delivers average grades for 1 m long core sections. This may dilute the grade of highly mineralised thin veins in such sections that are otherwise barren. On the other hand, mineralisation in the host rock might lead to the assumption that veins in such a core section that are actually barren might have contained mineralising fluids. Therefore, only tentative interpretations can be made from comparing sulphur isotopes and gold grades.

In the Twangiza deposit there is a fairly good correlation between sulphur isotopic signature and the assaying grade of gold. The host rocks TW-FS-03 and -05 contain 9.85 and 7.12 g/t gold, and the S isotopes in associated pyrite are around neutral (δ^{34}S -2.2‰ to +3.0‰; Table 7.5.1). These samples also show native gold (cf. section 6.2.1). TW-FS-07 also contains gold, but at a lower grade (0.57 g/t), and its isotopic signature is similar to TW-FS-03 and -05. Also the veins T3 and T25, both with similar low positive δ^{34}S values in pyrite (~+2 ‰) are highly mineralised (9.19 and 63 g/t, respectively). In contrast, two veins T9 and T12, in which pyrite has negative δ^{34}S around -4.5 ‰, are not mineralised (Table 7.5.1). However, V-type pyrite from T9 does contain some gold which is identified in microchemical analysis (Figure 6.10).

Accordingly, the current data set suggests that in Twangiza substantial gold is contained in the host rock sedimentary sequence, and some of it may have been extracted into veins. On the other hand, some veins with lighter isotopic signature than the host sediments contain little or no gold. This means that part of the hydrothermal system may have formed from barren fluids from more distal and S-isotopically different places. However, the available data set is too small for more solid interpretations.

Kamituga shows a less clear correlation of gold and sulphur isotopic signature. Only the metadioritic host rock sample KG-SIS-5, with δ^{34}S values around -2.2‰, is mineralised with 1.9 g/t gold (Table 7.5.2), suggesting that the metadiorites are a potential source of gold. However, the diorites are not the source of the analysed less mineralised veins in Kamituga, which show much lighter S-isotope signature (Figure 8.1). VD HR- and V-type pyrite (-9.1‰ to -7.4‰) in these veins (sample KG-SIS-2) is associated with a low gold grade of 0.41 g/t (Figure 8.1). Hence, these mobile fluids from distal sources cannot be associated with high gold grades based on the available data. However, native gold has been seen in these vein samples during microchemical analysis (cf. section 6.2.1), which indicates that gold was carried in these fluids. The source of these fluids was likely a sedimentary rock that is isotopically lighter than the analysed metapelite sample KG-SIS-7 (cf. section 8.1). Analyses of more HR-type pyrite from Kamituga are necessary to test whether this source could be proximal or distal to the Kamituga deposit.

The association of Lugushwa pyrite and gold is less clear than in Twangiza and Kamituga host rocks, because gold grades in samples where HR and AM HR pyrite was analysed are less than 0.1 g/t. A gold flake was however identified in HR pyrite from sample LG-SI-02 (Figure 6.13, 8.1), indicates that primary gold is present in the metapelitic sedimentary sequence. Also in isotopically heavier V-type pyrite native gold was seen (sample LG-SI-05; cf. section 6.2.1). This suggests that Au and sulphur were mobile and precipitated together after influx from a source that is isotopically different to the analysed host samples.

At Namoya, very high gold grade (173 g/t) in schist-hosted V-type pyrite is associated with heavy sulphur (+19.5‰ to +20.4‰; Figure 8.1), and evidently this fluid must have been sourced from an evaporitic sedimentary rock similar to those that have been analysed (Figure 8.1). Pyrite in dolerite-hosted veins shows a lower grade of mineralisation (1.32 g/t) and a lighter sulphur isotopic signature. Gold was spotted in arsenopyrite in such a vein (sample NM-SI-2; Figure 5.6). This gold may have been leached together with the lighter sulphur from the doleritic host.

VD HR pyrite in schistose metapelite shows δ^{34}S values between +13.2‰ and +16.1‰ associated with a low gold grade (0.44 g/t). The samples with HR pyrite are not mineralised and gold was not spotted in them. However, their sulphur isotopic signature range covers the isotopic signature of VD HR pyrite (Figure 8.1). This suggests that gold and sulphur were mobilised from the sedimentary host rocks and precipitated together in the dissemination halo of the vein.

9. Conclusions

The findings of the discussion sections lead to the following conclusions:

1. Pyrite in the TNGB displays a large variety of sulphur isotopic signature. The current data set indicates highly variable sedimentary to evaporitic sources of sulphur in the TNGB. Magmatic sulphur isotope signatures are restricted to metadiorite bodies, where sulphur may have been leached and re-precipitated in nearby veins. Only in Lugushwa one vein, with a significantly heavier S isotope signature than the host rocks, may have formed from a granitic fluid. Only granitic pyrite from Lugushwa and from the other deposits may provide evidence for granites as a main sulphur and possibly gold source in the TNGB.

2. Overall isotopic trends and differences between deposits may be related to different protoliths in the approximately 210 km long TNGB. Namoya lies in the Palaeoproterozoic Ubendian/Rusizian basin. Lugushwa and Kamituga Mesoproterozoic Kibara belt, and Twangiza falls in the Neoproterozoic, post-Kibaran Itombwe Supergoup.

3. Native gold was seen in host rocks from Twangiza and Lugushwa. This clearly indicates that sediments are a primary source of gold. In addition, assayed gold grades from metadiorites in Kamituga suggests that there is a possibility of some gold being contained in these host rocks.

4. Native gold was only spotted in vein pyrite from the Kamituga deposit. These veins have a sulphur isotopic signature that is different from the metapelitic and metadioritic host rocks suggesting that sulphur and gold were brought in to the Kamituga deposit by fluids from an isotopically different, possibly distal sedimentary source.

5. High gold grade is reported in Twangiza veins and host rocks. $\delta^{34}S$ values in the Twangiza deposit shows a sedimentary host rock signature that is similar to the vein signatures. These signatures are in the granitic range (near neutral) suggesting a possible, but not likely, granitic fluid source for sulphur and gold.

6. The highest gold grade is seen in Namoya schist-hosted vein associated with sulphur from a sedimentary-evaporitic source. Although native gold was not spotted in this vein, it does not rule out an evaporitic sedimentary gold source.

7. Overall, it is not always clear whether the hydrothermal fluids with isotopic signatures that are different from nearby host rocks originated from distal or local sources. However the presence of these fluids may suggest that gold and sulphur were highly mobile in the TNGB. In places such mobile gold is present in proximity to gold leached and mobilised from the sedimentary host rocks nearby.

Recommendations

There is a prospect for additional geochemical, petrographic and sulphur isotope work to be conducted on the metasediments from the TNGB. The following recommendations are proposed based on the existing knowledge gap in understanding gold provenance inferred from sulphur isotopes:

1. Better identification of suitable pyrite samples in the TNGB drill core collections. More well-defined pyrite (HR-, V-type) is scarce particularly from Lugushwa and Kamituga. The data set needs to be broadened, possibly in separate studies for each deposit.

2. Granites and other igneous rocks from the four TNGB deposits must be added in future studies in order to determine whether granitic pyrite has a different source compared to the metasedimentary sequence.

3. The sampling for further S isotope analysis should particularly target highly mineralised zones.

References

Abdollahi, M.J., Karimpour, M.H., & Kheradmand, A., 2009. Petrography and sulphur isotope studies of pyrites in the Muteh gold deposit. *American Journal of Applied Sciences* 6(6), 1086-1092.

Arias, D., Corretgi, L.G., Villa, L., Gallastegui, G., Suárez, O., & Cuesta, A., 1997. A sulphur isotopic study of the Navia gold belt (Spain). *Journal of Geochemical Exploration* 59 (1997), 1-10.

Banro, 2017. Banro Corporation: http://www.banro.com/: *QuickReport*. Accessed 31/03/2017.

Bawah, C., Hannam, M., & Daud, D., 2008. Geological overview of the Twangiza project, South Kivu, Democratic Republic of the Congo. *Company report*. Banro Corporation.

Böttcher, M.E., Smock, A.M., & Cypionka, H., 1998. Sulfur isotope fractionation during experimental precipitation of iron (II) and manganese (II) sulfide at room temperature *Chemical Geology*, 146 (3-4), 127-134.

Brinckmann, J., Lehmann, B., Timm, F., 1994. Proterozoic gold mineralization in NW Burundi. *Ore Geology Reviews* 9, 85–103.

Brinckmann, J., Lehmann, B., Hein, U., Höhndorf, A., Mussallam, K., Weiser, T, & Timm, F., 2001. La géologie et la minéralisation primaire de l'or de la chaîne Kibarienne, Nord-Ouest du Burundi, Afrique orientale. *Geologisches Jahrbuch Reihe D*. 101, 195.

Büttner, S.H., Reid, W., Glodny, J., Wiedenbeck,M., Chuwa, G., Moloto, T., & Gucsik, A., 2016. Fluid sources in the Twangiza-Namoya Gold Belt (Democratic Republic of Congo): evidence from tourmaline and fluid compositions, and from Rb-Sr isotope systematics. *Precambrian Research* 280, 161-178.

Cahen, L., Snelling, N.J., Delhal, J., & Vail, J.R., 1984. The geochronology and evolution of Africa. *Oxford Science Publication, Clarendon Press*, Oxford, pp. 512.

Canfield, D.E., Oleson, C.A., & Cox, R.P., 2006. Temperature and its control of isotopic fractionation by sulfate-reducing bacterium. *Geochimica et Cosmochimica Acta* 70, 548–561.

Chang, Z., Large, R.R., & Maslennikov, V., 2008. Sulfur isotopes in sediment-hosted orogenic gold deposits: Evidence for an early timing and a seawater sulfur source: *Geology* 36, 971–974.

Chuwa, M.G., 2011. A review of gold deposits in the Twangiza-Namoya Gold Belt, eastern Democratic Republic of Congo, with emphasis on grass-root exploration models. *MSc thesis*, Rhodes University, Grahamstown, South Africa, 184 p.

Crowe, D.E., & Vaughan, R.G., 1996. Characterization and use of isotopically homogeneous standards for in situ laser microprobe analysis of $^{34}S/^{32}S$ ratios. *American Mineralogist* 81, 187-193.

De Bruyne, D., Hulsbosch, N., van Wilderode, J., Balcaen, L., Vanhaecke, F., & Muchez, P., 2015. Regional geodynamic context for the Mesoproterozoic Kibara Belt (KIB) and the Karagowe-Ankole Belt: Evidennce from the geochemistry and isotopes in the KIB. *Precambrian Research* 264, 82-97.

Deer, W.A., Howie, R.A., & Zussman, J., 1992.An Introduction to the Rock-Forming Minerals. 2nd ed. *Prentice Hall*. 696 pp.

Ding, T., Bai, R., Li, Y., Wan, D., Zou, X., & Zhang, Q., 1999. Determination of the absolute $^{32}S/^{34}S$ ratio of IAEA-S-1 reference material and V-CDT sulfur isotope standard. *Science in China Series D* 42, 45-51.

Ding, T., Valkiers, S., Kipphardt, H., De Bièvre, P., Taylor, P.D.P., Gonfiantini, R., & Krouse, R., 2001. Calibrated sulfur isotope abundance ratios of three IAEA sulfur isotope reference materials and V-CDT with a reassessment of the atomic weight of sulfur. *Geochimica et Cosmochimica Acta* 65/15, 2433-2437.

Fall, H.G., 2006b. Lugushwa project; assessment of rock-types intersected by diamond drilling. *Company report*. Banro Corporation.

Fall, H.G., 2007b. Petrographic study of gold mineralisation. Lugushwa project. *Company report*. Banro Corporation.

Fall, H.G., 2007c. Petrographic study of gold mineralisation. Namoya project. *Company report*. Banro Corporation.

Fall, H.G., 2008. Overview of the geology, gold mineralisation and resource potential of the Twangiza-Namoya Gold Belt, eastern Democratic Republic of the Congo. *Technical report*. Banro Congo Mining SARL.

Fall, H.G., & Chuwa, G., 2007. Lugushwa concession: Summary of prospects geology, mineralisation and resource potential. *Company report*. Banro Congo Mining SARL. 38p.

Fernandez-Alonso, M., Cutten, H., De Waele, B., Tack, L., Tahon, A., Baudet, D., & Barritt, S.D., 2012. The Mesoproterozoic Karagwe-Ankole Belt (formerly the NE Kibara Belt): the result of prolonged extensional intracratonic basin development punctuated by two shortlived far-field compressional events. *Precambrian Research* 216–219, 63–86.

Goldfarb, R.J., Newberry, R.J., Pickthorn, W.J., & Gent, C.A., 1991. Oxygen, Hydrogen, and Sulfur Isotope Studies in the Juneau Gold Belt, Southeastern Alaska: Constraints on the Origin of Hydrothermal Fluids. *Economic Geology* 86, 66-80.

Goldhaber, M.B., 2003. Sulfur-rich sediments. *In*: Treatise on Geochemistry. Holland, H.D., Turekian, K.K. (eds) *Elsevier*, p 257-288.

Grassineau, N.V., Mattey, D.P., & Lowry, D., 2001. Sulfur isotope analysis of sulfide and sulfate minerals by continuous flow-isotope ratio mass spectrometry. *Analytical Chemistry* 73, 220-225.

Habicht, K.S., Gade, M., Thamdrup, B., Berg, P., & Canfield, D.E., 2002. Calibration of sulfate levels in the Archean Ocean. *Science* 298, 2372–2374.

Jensen, M.L., 1967. Sulfur isotopes and mineral genesis. *In:* Geochemistry of Hydrothermal Ore Deposits. Barnes H.L., (ed) *Holt, Rinehart, and Winston*, p 143-165.

Kokonyangi, J.W., Armstrong, R., Kampunzu, A.B., Yoshida, M., & Okudaira, T., 2004. U-Pb zircon geochronology of granitoids from Mitwaba (Katanga, Congo): implications for the evolution of the Mesoproterozoic Kibaran belt. *Precambrian Research* 132, 79-106.

Kokonyangi, J.W., Kampunzu, A.B., Armstrong, R., Arima, M., Yoshida, M., & Okudaira, T., 2007. U-Pb SHRIMP dating of detrital zircons from the Nzilo Group (Kibaran Belt): Implications for the source of sediments and Mesoproterozoic evolution of Central Africa. *The Journal of Geology* 115, 99-113.

Krouse, H.R., & Coplen, T.B., 1997. Reporting of relative sulfur isotope-ratio data. *Pure and Applied Chemistry* 69, 293-295.

Macnamara, J., & Thode, H.G., 1950. Comparison of the isotopic constitution of terrestrial and meteoritic sulphur. *Physical Review* 78, 307-308.

Mbuya, P.W., Machano, R., & Murhula, P., 2008. Geological overview of the Namoya Project, Maniema Province, Democratic Republic of the Congo. *Company report*, Banro Corporation.

Melcher, F., Graupner, T., Gäbler, H.-E., Sitnikova, M., Henjes-Kunst, F., Oberthür, T., Gerdes, A., & Dewaele, S., 2015. Tantalum–(niobium–tin) mineralisation in African pegmatites and rare metal granites: constraints from Ta–Nb oxide mineralogy, geochemistry and U–Pb geochronology. *Ore Geology Reviews* 64, 667–719.

Naas, C.O., 1998. Technical report on phase-1 geological, geochemical and diamond drilling exploration of the Twangiza Project, Democratic Republic of the Congo for Banro Resource Corporation. *CME and company*, Volume I of XII. pp. 98.

Nielsen, H., Pilot, J., Grinenko, L.N., Grinenko, V.A., Lein, A.Y., Smith, J.W., & Pankina, R.G., 1991. Lithospheric sources of sulphur. *In:* Stable Isotopes in the Assessment of Natural and Anthropogenic Sulphur in the Environment. Krouse H.R., Grinenko V.A. (eds) *SCOPE 43, J Wiley and Sons*, p 65-132.

Noku, S.K., Espi, J.O., & Matsueda, H., 2015. Involvement of magmatic fluids at the Laloki and Federal Flag massive sulfide Cu–Zn–Au–Ag deposits, Astrolabe mineral district, Papua New Guinea: sulfur isotope evidence. *Mineralium Deposita* 50, 55–64.

O'Donovan, G., Kentwell, D., Brodie-Good, B., McRobbie, S., & Clayton, R., 1999. Kamituga mineral concession, South Kivu Province, Democratic Republic of Congo. Report on the compilation and geological interpretation of historical data by SRK for Banro Resource Corporation. pp.51.

O'Donovan, G., Kentwell, D., Brodie-Good, B., McRobbie, S., & Pittuck, M., 2005. Resource estimation and exploration potential at the Kamituga, Lugushwa, and Namoya concessions, Democratic Republic of Congo. *NI 43-101 Technical Report*. SRK, pp111.

Ohmoto, H., 1986. Stable isotope geochemistry of ore deposits. *Reviews in Mineralogy & Geochemistry* 16, 185-225.

Ohmoto, H., & Goldhaber, M.B., 1997. Sulfur and carbon isotopes. *In:* Geochemistry of Hydrothermal Ore Deposits, 3rd edition. Barnes H.L. (ed) *J Wiley and Sons*, p 517-611.

Ohmoto, H., & Rye, R.O., 1979. Isotopes of sulfur and carbon. *In:* Geochemistry of Hydrothermal Ore Deposits. Barnes H.L. (ed) *J Wiley and Sons*, p 509-567.

Peters, B., 1959. Cosmic-ray produced radioactive isotopes as tracers for studying large-scale atmospheric circulation. *Journal of Atmospheric and Terrestrial Physics* 13, 351-370.

Pohl, W., 1994. Metallogeny of the northeastern Kibara Belt, Central Africa- Recent perspectives. *Ore Geology Reviews* 9, 105-130.

Pohl, W.L., Biryabarema, M., & Lehmann, B., 2013. Early Neoproterozoic rare metal (Sn, Ta, W) and gold metallogeny of the Central Africa Region: a review. *Applied Earth Science* 122, 66–82.

Price, F.T., & Shieh, Y.N., 1979. Fractionation of sulfur isotopes during laboratory synthesis of pyrite at low temperatures. *Chemical Geology* 27, 245-253.

Rees, C.E., & Holt, B.D., 1991. The isotopic analysis of sulphur and oxygen. *In:* Stable Isotopes in the Assessment of Natural and Anthropogenic Sulphur in the Environment. Krouse H.R., Grinenko V.A., (eds) *SCOPE 43, J Wiley and Sons*, p 43-64.

Rusill, J., Williams, B., & Holwell, D.A., 2009. Geophysical interpretation and target generation for the Twangiza-Namoya Gold Belt, DRC. *Report prepared for Banro Corporation.* SRK Exploration services. pp. 34.

Seal, R.R. II, 2006. Sulfur Isotope Geochemistry of Sulfide Minerals. *Reviews in Mineralogy & Geochemistry* 6, 633-677.

Strauss, H. & Schieber, J., 1989. A sulfur isotope study of pyrite genesis: The Mid-Proterozoic Newland Formation, Belt Supergroup, Montana. *Geochemica et Cosmochimica Acta* 54, 197-204.

Skead, M.B., 2007. Third NI 43-101 Technical report, Lugushwa project, South Kivu Province, Democratic Republic of Congo. *Company report.* Banro Corporation.

Spear, F.S. & Cheney, J.T., 1989. A petrogenetic grid for pelitic schists in the system SiO_2-Al_2O_3-FeO-MgO-K_2O-H_2O. *Contributions to Mineralogy and Petrology* 101 (2), 149-164.

Tack, L., Wingate, M.T.D., De Waele, B., Meert, J., Belousova, E., Griffin, B., Tahon, A. & Fernandez-Alonso, M., 2010. The 1375 Ma "Kibaran event" in Central Africa: Prominent

emplacement of bimodial magmatism under extensional regime. *Precambrian Research* 180, 63-84

Thode, H.G., 1970. Sulfur isotope geochemistry and fractionation between coexisting sulphide minerals. *Mineralogical Society of America Spec. Paper* 3, 133-144

Thode, H.G., 1991. Sulfur isotopes in nature and the environment: An overview. *In*: Stable Isotopes: Natural and Anthropogenic Sulphur in the Environment. H.R Krouse & V.A. Grinenko (eds) *J Wiley and Sons*, p 1-26.

Tudge, A. P., & Thode, H.G, 1950. Thermodynamic properties of isotopic compounds of sulphur. *Canadian Journal of Research B*28, 567-578.

Ushikubo, T., Williford, K.H., Farquhar, J., Johnston, D.T., van Kranendonk, M.L, & Valley, J.W., 2014. Development of in situ sulfur four-isotope analysis with multiple Faraday cup detectors by SIMS and application to pyrite grains in a Paleoproterozoic glaciogenic sandstone. *Chemical Geology* 383, 86-99.

Vernon, R.H., 2004. A Practical Guide to Rock Microstructure. *Cambridge University Press*, Cambridge, pp 606.

Walemba, K.M.A., 2001. Geology, geochemistry, and tectono-metallogenic evolution of Neoproterozoic gold deposits in the Kadubu area, Kivu, Democratic Republic of Congo. *Ph.D. thesis (unpubl.)*, University of the Witwatersrand, Johannesburg, South Africa, 491 p.

Walemba, K.M.A., & Master, S., 2005. Neoproterozoic diamictites from the Itombwe Synclinorium, Kivu Province, Democratic Republic of Congo: Palaeoclimatic significance and regional correlations. *Journal of African Earth Sciences* 42, 200-210.

Whitehouse, M.J., 2013. Multiple sulfur isotope determination by SIMS: Evaluation of reference sulfides for $\Delta^{33}S$ with observations and a case study on the determination of $\Delta^{36}S$. *Geostandards and Geoanalytical Research* 37(1), 19-33.

Yan, Y., Zhang, N., Shengrong, L., & Yongsheng, L., 2014. Mineral chemistry and isotope geochemistry of pyrite from the Heilangou gold deposit, Jiaodong Peninsula, Eastern China. *Geoscience Frontiers* 5, 205-213.

APPENDIX 1: EPMA analytical conditions.
Major element analyses:

Element	X-ray	Crystal	Standard	Detection limit (ppm)
S	Ka	PETJ	Pyrite	82
Zn	La	TAP	Sphalerite	134
Fe	Ka	LIF	Pyrite	433
As	La	TAP	Arsenopyrite	144
Ni	Ka	LIFL	Pentlandite	153
Co	Ka	LIFL	Cobalt	122
Cu	La	TAPL	Chalcopyrite	257
Au	Ma	PETL	Gold	268

Overlap correction: 0.33 (Co cps) = 10.4 (Co Net) - 0.00200 x 5049.9 (S Net)

Trace element analyses:

Element	X-ray	Crystal	Standard	Detection limit (ppm)
S	Ka	PETJ	Pyrite	42
Fe	Ka	LIF	Pyrite	130
Co	Ka	LIF	Cobalt	30
As	La	TAP	Arsenopyrite	29
Ni	Ka	LIFL	Pentlandite	7
Ag	La	PETL	Silver	7
Te	La	PETL	Antimony telluride	8
Cu	La	TAPL	Chalcopyrite	104
Au	Ma	PETL	Gold	43
Bi	Ma	PETL	Bismuth	54

Overlap correction:-137.55 (Co cps) = -4.3 (Co Net) - 0.00200 x 66639.8 (S Net)

APPENDIX 2: Mesoscopic descriptions of samples from the TNGB.

Matrix grain size: Fine grained < 1 mm, medium grained > 1 mm – 5 mm, coarse grained > 5 mm.

Sample no.	Sample type	Colour	Matrix grain size	Structural features/textures	Mesoscopically visible sulphides	Host rock type
1. TW-FS-03 TDD040 161.00m	Host rock	Dark grey (light grey and brown weathering)	Medium grained	None	Euhedral pyrite and arsenopyrite (up to 2mm in size).	Mudstone
2. TW-FS-05 TDD300 190.17m	Host Rock	Dark grey	Fine grained	Stretched quartz lenses	Pyrite (up to 2mm in size)	Mudstone
3. TW-FS-06 TDD023 142.20-142.30m	Host Rock	Grey	Fine grained	Quartz veinlets (~1mm thick and smaller)	None	Metapelite
4. TW-FS-07 TDD023 189.20-189.29m	Host Rock	Dark grey	Fine grained	Vein (~28mm thick, consists of sulphides, brownish weathering)	Pyrite (~1mm)	Carbonaceous mudstone
5. KG-FS-1 KDD015 46.40m	Host Rock	Light grey (surface) Dark grey (inside)	Fine grained	Slight slaty cleavage	None	Metapelite

APPENDIX 2: Mesoscopic descriptions of samples from the TNGB

Matrix grain size: Fine grained < 1 mm, medium grained > 1 mm – 5 mm, coarse grained > 5 mm.

Sample no.	Sample type	Colour	Matrix grain size	Structural features/textures	Mesoscopically visible sulphides	Host rock type
6. KG-FS-2 KDD001 82.50m	Host Rock	Light grey to dark grey	Fine grained	Slaty cleavage (biotite sheets)	None	Metapelite
7. LG-FS-1 LDD162 88.10m	Host Rock	Light grey	Fine grained	Slight slaty cleavage (not prominent)	None	Metapelite
8. LG-FS-4 LDD088 126.10m	Host Rock	Light grey	Fine grained	Slight slaty cleavage. Foliation of mica minerals	None	Metapelite
9. NM-FS-1 NDD180 97.62-97.70m	Host Rock	Light grey	Fine grained	Narrowly spaced slaty cleavage	Single, euhedral pyrite grain (~4mm)	Sericite schist
10. NM-FS-2 NDD180 97.98m	Host Rock	Light grey	Fine grained	Narrowly spaced slaty cleavage	Euhedral pyrite (<9mm)	Sericite schist
11. L4 (Borehole: LDD 162) 84.5m	Vein	Medium grey/light grey (host rock)	Fine grained	Slight slaty cleavage. Network of quartz-sulphide veinlets (~1mm thick)	Pyrrhotite (~1mm)	Metapelite

APPENDIX 2: Mesoscopic descriptions of samples from the TNGB

Matrix grain size: Fine grained < 1 mm, medium grained > 1 mm – 5 mm, coarse grained > 5 mm.

Sample no.	Sample type	Colour	Matrix grain size	Structural features/textures	Mesoscopically visible sulphides	Host rock type
12. T3 (Borehole: TDD023) 123m	Vein	Dark grey (host rock)	Fine grained	Quartz vein and veinlets	Pyrite (~1mm)	Carbonaceous mudstone
13. T9 (Borehole: TDD023) 176.7m	Vein	Dark grey (host rock)	Fine grained	Quartz-pyrite vein (up to ~1cm thick, zig-zagging) Off-shoots seem to be lineated	Pyrite (up to ~4mm in vein)	Carbonaceous mudstone.
14. T12 (Borehole: TDD023) 206.3m	Vein	Dark grey (host rock)	Fine grained	Narrowly spaced slaty cleavage Quartz-pyrite vein (~1mm to 19mm thick)	Pyrite (up to ~5mm in vein)	Carbonaceous mudstone. Brownish weathering on the surface of vein
15. T25 (Borehole: TDD040) 152m	Vein	Dark grey, white, and yellow. (Quartz-sulphide vein)	Coarse grained	None	Pyrite and Arsenopyrite (up to 2mm in size)	Carbonaceous mudstone
16. K17 (Borehole: KDD015) 51.8m	Vein	Grey	Fine grained	Quartz vein with biotite margin and sulphides	Fine grained pyrrhotite and arsenopyrite (<1mm)	Dark metapelite

APPENDIX 2: Mesoscopic descriptions of samples from the TNGB

Matrix grain size: Fine grained < 1 mm, medium grained > 1 mm – 5 mm, coarse grained > 5 mm.

Sample no.	Sample type	Colour	Matrix grain size	Structural features/textures	Mesoscopically visible sulphides	Host rock type
17. KG-SIS-1 KDD01 116.65-116.75m	Host rock and quartz vein	Dark grey (light grey and brown weathering)	Fine grained	Slightly foliated (schistose) with mica minerals Quartz vein in host rock (~6mm long)	Fine grained pyrrhotite and arsenopyrite (<1mm)	Metapelite
18. KG-SIS-2 KDD09 141.30-141.40m	Host Rock	Grey (weathered surface, some minerals look brown)	Fine grained	Weathered quartz vein	Pyrite (up to 3mm wide)	Metapelite
19. KG-SIS-3 KDD09 142.25-142.35m	Host rock	Light grey (brownish weathering on the surface)	Fine grained	Slight schistose texture (slaty cleavage)	None	Metapelite
20. KG-SIS-4 KDD014 96.40-96.50m	Host Rock	Grey	Fine grained	Slight biotite foliation	Fine grained pyrrhotite and arsenopyrite (<1mm)	Metapelite
21. KG-SIS-5 KDD038 109.20-109.30m	Host Rock	Grey to dark grey (weathered surface)	Medium grained	~1mm quartz veinlets	Pyrites (up to 2mm wide)	Metadiorite

APPENDIX 2: Mesoscopic descriptions of samples from the TNGB

Matrix grain size: Fine grained < 1 mm, medium grained > 1 mm – 5 mm, coarse grained > 5 mm.

Sample no.	Sample type	Colour	Matrix grain size	Structural features/textures	Mesoscopically visible sulphides	Host rock type
22. KG-SIS-6 KDD038 148.50-148.60m	Host Rock	Grey to dark grey (weathered surface)	Medium grained	No structural features	Pyrites (up to 2mm wide)	Metadiorite
23. KG-SIS-7 KDD041 85.05-85.15m	Host Rock	Dark grey	Fine grained	Very slight slaty texture Fine grained pyrite stringers	Fine grained pyrite (<1mm)	Metapelite
24. LG-SI-01 LDD063 182.65-182.70m	Host Rock	Light grey (outside) Grey (inside)	Fine grained	Slight slaty cleavage	Pyrrhotite (up to 4mm wide)	Metapelite
25. LG-SI-02 LDD063 334.25-334.30m	Host Rock	Light Grey	Fine grained	Quartz veinlets (up to 1mm thick)	Euhedral pyrite grains (up to 4mm wide)	Metapelite
26. LG-SI-03 LDD057 197.98-198.03m	Host Rock	Grey	Fine grained	Slight slaty cleavage	Fine grained pyrrhotite (<1mm)	Metapelite

APPENDIX 2: Mesoscopic descriptions of samples from the TNGB

Matrix grain size: Fine grained < 1 mm, medium grained > 1 mm – 5 mm, coarse grained > 5 mm.

Sample no.	Sample type	Colour	Matrix grain size	Structural features/textures	Mesoscopically visible sulphides	Host rock type
27. LG-SI-04 LDD057 350.14-350.20m	Host Rock	Grey	Fine grained	Slight slaty cleavage	Fine grained pyrrhotite (<1mm)	Metapelite
28. LG-SI-05 LDD083 123.55-123.60m	Host Rock	Grey	Fine grained	Slight schistosity Small veinlets (stringers, quartz)	Pyrite (disseminated some as euhedral pyrite stringers up to 5mm wide)	Metapelite
29. LG-SI-06 LDD073 200.64-200.70m	Host Rock	Grey	Fine grained	Slight schistosity	Euhedral pyrite stringers (up to 4mm wide)	Metapelite
30. NM-SI-1 Seketi pit Grab sample	Host Rock	Light grey	Fine to medium grained	Foliated (schistose texture) ~1mm thick quartz veins	Euhedral pyrites (~1mm wide)	Dolerite
31. NM-SI-2 Seketi pit Grab sample	Host Rock	Grey	Fine grained	Zone of quartz stringer (has sulphides in fractures) Slight foliation	Fine grained pyrite (< 1mm). Euhedral arsenopyrite (~1mm)	Dolerite

APPENDIX 2: Mesoscopic descriptions of samples from the TNGB.
Matrix grain size: Fine grained < 1 mm, medium grained > 1 mm – 5 mm, coarse grained > 5 mm.

Sample no.	Sample type	Colour	Matrix grain size	Structural features/textures	Mesoscopically visible sulphides	Host rock type
32. NM-SI-3 NDD077 36.30-37.03m	Host Rock	Grey	Fine to medium grained	Vein (quartz or , up to 3mm wide. Slight foliation on one side	Few fine grained pyrite (<1mm)	Dolerite
33. NM-SI-4 NDD018 144.05-144.15m	Host Rock	Greenish Grey	Mostly fine grained	Narrowly spaced slaty cleavage Quartz veinlet (~1mm thick)	Fine grained euhedral arsenopyrite (<1mm)	Sericite schist
34. NM-SI-5 NDD018 145.00-145.10m	Host Rock	Greenish grey (brownish weathered surface)	Fine grained	Slight schistose texture (due to foliation of white mica) Pyrite vein (~1mm thick)	Only in pyrite vein	Sericite schist
35. NM-SI-6 NDD018 142.00-142.10m	Host Rock	Greenish grey (weathered surface)	Fine grained	Slight schistose texture	Pyrite (dark greenish, ~3mm wide). Pyrrhotite	Sericite schist
36. NM-SI-7 NDD223 146.70-146.80m	Host Rock	Greenish grey (weathered surface)	Fine grained	Slight schistose texture Quartz stringer	Fine grained euhedral pyrite (<1mm)	Sericite schist
37. NM-SI-8 NDD223 144.24-144.40m	Host Rock	Greenish grey	Fine grained	Slight schistose texture Quartz veinlet (stringer, ~1mm thick)	Euhedral pyrites (~1mm wide)	Sericite schist

APPENDIX 3: Trace element analysis of pyrite from the TNGB. All data is presented in ppm and where no value is given represents data below the detection limit (bdl). The detection limit is written in brackets below the element symbol.

Point	Pyrite type	Comment	Co (30)	As (29)	Ni (7)	Ag (7)	Te (8)	Cu (104)	Au (43)	Bi (54)
101	HR	TW-FS-07_S2_py8	bdl	1630	bdl	bdl	bdl	110	bdl	80
100	HR	TW-FS-07_S2_py7	bdl	1210	bdl	bdl	bdl	200	bdl	bdl
99	HR	TW-FS-07_S2_py6	bdl	1490	40	bdl	bdl	bdl	bdl	120
98	HR	TW-FS-07_S2_py5	bdl	3310	60	bdl	bdl	bdl	bdl	bdl
97	HR	TW-FS-07_S2_py4_2	bdl	1870	20	bdl	bdl	bdl	bdl	bdl
96	HR	TW-FS-07_S2_py4_1	bdl	2350	10	20	bdl	bdl	bdl	bdl
95	HR	TW-FS-07_S2_py3_2	bdl	1860	30	bdl	10	bdl	bdl	bdl
94	HR	TW-FS-07_S2_py3_1	bdl	1180	60	bdl	10	200	bdl	bdl
93	HR	TW-FS-07_S2_py2_3	bdl	3680	630	20	10	bdl	bdl	140
92	HR	TW-FS-07_S2_py2_2	bdl	2630	140	bdl	bdl	bdl	bdl	bdl
91	HR	TW-FS-07_S2_py2_1	bdl	1640	240	10	bdl	bdl	bdl	bdl
90	HR	TW-FS-07_S2_py1_2	bdl	1470	110	bdl	20	bdl	bdl	bdl
89	HR	TW-FS-07_S2_py1_1	bdl	2030	bdl	bdl	bdl	bdl	bdl	100
88	HR	TW-FS-07_S1_py_4	bdl	40	bdl	bdl	bdl	bdl	bdl	bdl
87	HR	TW-FS-07_S1_py_3	bdl	40	60	bdl	10	bdl	bdl	110
86	HR	TW-FS-07_S1_py_2	4200	80	660	bdl	bdl	5190	bdl	60
85	HR	TW-FS-07_S1_py_1	bdl	2460	330	40	10	bdl	bdl	bdl
84	HR	TW-FS-05_S3_py_5	bdl	1780	230	bdl	bdl	bdl	bdl	260
83	HR	TW-FS-05_S3_py_4	bdl	2980	650	bdl	bdl	bdl	bdl	80
82	HR	TW-FS-05_S3_py_3	bdl	1760	290	bdl	bdl	bdl	bdl	110
81	HR	TW-FS-05_S3_py_2	bdl	2990	580	bdl	bdl	bdl	bdl	bdl
80	HR	TW-FS-05_S3_py_1	bdl	2450	840	bdl	bdl	bdl	bdl	110
79	HR	TW-FS-05_S2_py1_5	bdl	4470	900	bdl	bdl	bdl	bdl	bdl
78	HR	TW-FS-05_S2_py1_4	bdl	5270	950	bdl	bdl	bdl	bdl	bdl
77	HR	TW-FS-05_S2_py1_3	bdl	3140	700	20	40	430	bdl	120

APPENDIX 3: Trace element analysis of pyrite from the TNGB. All data is presented in ppm and where no value is given represents data below the detection limit (bdl). The detection limit is written in brackets below the element symbol.

Point	Pyrite type	Comment	Co (30)	As (29)	Ni (7)	Ag (7)	Te (8)	Cu (104)	Au (43)	Bi (54)
76	HR	TW-FS-05_S2_py1_2	bdl	1450	480	30	bdl	140	bdl	bdl
75	HR	TW-FS-05_S2_py1_1	bdl	2150	320	20	20	130	bdl	180
74	HR	TW-FS-05_S1_py6	bdl	4560	340	bdl	10	bdl	bdl	100
73	HR	TW-FS-05_S1_py5	bdl	2350	170	bdl	bdl	210	bdl	bdl
72	HR	TW-FS-05_S1_py4	bdl	3880	250	bdl	bdl	bdl	bdl	bdl
71	HR	TW-FS-05_S1_py3	bdl	1730	120	bdl	bdl	bdl	bdl	90
70	HR	TW-FS-05_S1_py2	bdl	1020	80	bdl	bdl	bdl	bdl	180
69	HR	TW-FS-05_S1_py1	bdl	4310	100	10	bdl	bdl	bdl	bdl
58	HR	TW-FS-03_SI1_py5_2	bdl	3070	20	bdl	10	bdl	bdl	bdl
57	HR	TW-FS-03_SI1_py5_1	bdl	5780	1220	30	20	bdl	bdl	bdl
56	HR	TW-FS-03_SI1_py4_2	bdl	4100	190	bdl	bdl	bdl	bdl	bdl
55	HR	TW-FS-03_SI1_py4_1	bdl	3420	bdl	bdl	10	bdl	bdl	bdl
54	HR	TW-FS-03_SI1_py3_2	bdl	4580	20	bdl	20	bdl	bdl	bdl
53	HR	TW-FS-03_SI1_py3_1	bdl	4880	300	10	20	bdl	bdl	bdl
52	HR	TW-FS-03_SI1_py2_3	bdl	2200	120	20	bdl	bdl	bdl	bdl
51	HR	TW-FS-03_SI1_py2_2	bdl	2180	10	bdl	40	110	bdl	bdl
50	HR	TW-FS-03_SI1_py2_1	bdl	1570	30	30	30	bdl	bdl	360
49	HR	TW-FS-03_SI1_py1_3	bdl	3130	530	bdl	10	bdl	bdl	bdl
48	HR	TW-FS-03_SI1_py1_2	bdl	1790	210	20	bdl	bdl	bdl	90
47	HR	TW-FS-03_SI1_py1_1	bdl	3620	40	40	bdl	bdl	bdl	bdl
68	HR	TW-FS-03_S2_py5_2	bdl	1950	210	bdl	bdl	bdl	bdl	80
67	HR	TW-FS-03_S2_py5_1	bdl	2320	180	bdl	30	bdl	bdl	bdl
66	HR	TW-FS-03_S2_py4_2	bdl	1910	bdl	10	bdl	420	bdl	bdl
65	HR	TW-FS-03_S2_py4_1	bdl	3160	bdl	10	30	bdl	bdl	80
64	HR	TW-FS-03_S2_py3_2	bdl	3260	10	bdl	10	240	bdl	bdl
63	HR	TW-FS-03_S2_py3_1	bdl	2470	10	bdl	bdl	bdl	bdl	100

APPENDIX 3: Trace element analysis of pyrite from the TNGB. All data is presented in ppm and where no value is given represents data below the detection limit (bdl). The detection limit is written in brackets below the element symbol.

Point	Pyrite type	Comment	Co (30)	As (29)	Ni (7)	Ag (7)	Te (8)	Cu (104)	Au (43)	Bi (54)
62	HR	TW-FS-03_S2_py2_2	bdl	2290	350	10	10	bdl	bdl	150
61	HR	TW-FS-03_S2_py2_1	bdl	7530	bdl	bdl	20	bdl	bdl	bdl
60	HR	TW-FS-03_S2_py1_2	bdl	5720	60	10	bdl	200	bdl	120
59	HR	TW-FS-03_S2_py1_1	bdl	4300	10	20	bdl	bdl	bdl	bdl
119	V	T9_S2_py4_3	bdl	80	20	20	10	bdl	bdl	bdl
118	V	T9_S2_py4_2	bdl	480	bdl	bdl	bdl	bdl	bdl	70
117	V	T9_S2_py4_1	bdl	390	10	bdl	bdl	bdl	bdl	120
116	V	T9_S2_py3_3	bdl	830	30	10	10	bdl	bdl	bdl
115	V	T9_S2_py3_2	bdl	620	30	20	10	bdl	bdl	170
114	V	T9_S2_py3_1	bdl	40	10	bdl	bdl	430	bdl	bdl
113	V	T9_S2_py2_2	bdl	1020	730	bdl	bdl	bdl	bdl	bdl
112	V	T9_S2_py2_1	bdl	470	320	bdl	bdl	bdl	bdl	bdl
111	V	T9_S2_py1_2	bdl	540	1150	20	bdl	bdl	bdl	260
110	V	T9_S2_py1_1	bdl	410	240	bdl	bdl	bdl	bdl	bdl
109	V	T9_S1_py2_4	bdl	880	20	10	bdl	bdl	bdl	bdl
108	V	T9_S1_py2_3	bdl	480	70	10	10	bdl	bdl	bdl
107	V	T9_S1_py2_2	bdl	800	70	bdl	bdl	bdl	bdl	120
106	V	T9_S1_py2_1	bdl	940	140	bdl	bdl	bdl	bdl	bdl
105	V	T9_S1_py1_4	bdl	580	240	bdl	10	bdl	bdl	120
104	V	T9_S1_py1_3	bdl	580	280	20	20	bdl	bdl	100
103	V	T9_S1_py1_2	bdl	1000	10	10	bdl	bdl	bdl	80
102	V	T9_S1_py1_1	bdl	600	320	bdl	bdl	bdl	bdl	180
20	V	T-3_S2_py6	bdl	2480	230	bdl	bdl	130	bdl	80
19	V	T-3_S2_py5	bdl	2130	190	bdl	bdl	bdl	bdl	110
18	V	T-3_S2_py4_2	bdl	3450	420	10	bdl	bdl	bdl	bdl
17	V	T-3_S2_py4_1	bdl	4580	600	10	bdl	bdl	bdl	bdl

APPENDIX 3: Trace element analysis of pyrite from the TNGB. All data is presented in ppm and where no value is given represents data below the detection limit (bdl). The detection limit is written in brackets below the element symbol.

Point	Pyrite type	Comment	Co (30)	As (29)	Ni (7)	Ag (7)	Te (8)	Cu (104)	Au (43)	Bi (54)
16	V	T-3_S2_py3_2	bdl	1950	280	bdl	bdl	bdl	bdl	bdl
15	V	T-3_S2_py3_1	bdl	2300	280	bdl	bdl	bdl	bdl	bdl
14	V	T-3_S2_py2_2	bdl	2620	130	10	bdl	bdl	bdl	bdl
13	V	T-3_S2_py2_1	bdl	1340	40	20	bdl	200	bdl	bdl
12	V	T-3_S2_py1_2	bdl	3820	680	10	bdl	560	bdl	bdl
11	V	T-3_S2_py1_1	bdl	2730	360	20	bdl	200	bdl	bdl
10	V	T-3_S1_py5_2	bdl	3320	bdl	bdl	10	bdl	bdl	bdl
9	V	T-3_S1_py5_1	bdl	1790	170	bdl	bdl	bdl	bdl	bdl
8	V	T-3_S1_py4_2	bdl	4730	710	bdl	bdl	bdl	bdl	60
7	V	T-3_S1_py4_1	bdl	3770	10	bdl	20	bdl	bdl	bdl
6	V	T-3_S1_py3_2	bdl	3040	450	bdl	bdl	110	bdl	bdl
5	V	T-3_S1_py3_1	bdl	3280	460	bdl	bdl	280	bdl	bdl
4	V	T-3_S1_py2_2	bdl	1410	bdl	10	bdl	bdl	bdl	bdl
3	V	T-3_S1_py2_1	bdl	3830	460	bdl	bdl	bdl	bdl	bdl
2	V	T-3_S1_py1_2	bdl	3290	520	10	bdl	bdl	bdl	bdl
1	V	T-3_S1_py1_1	bdl	850	20	bdl	bdl	190	bdl	bdl
141	V	T25_S3_py1_3	bdl	2170	70	bdl	bdl	150	bdl	bdl
140	V	T25_S3_py1_2	bdl	1700	bdl	10	10	480	bdl	130
139	V	T25_S3_py1_1	bdl	2710	430	bdl	bdl	390	bdl	bdl
138	V	T25_S2_py1_2	bdl	1810	50	40	10	bdl	bdl	130
137	V	T25_S2_py1_1	bdl	2210	170	bdl	bdl	bdl	bdl	bdl
136	V	T25_S1_py3_2	bdl	3340	180	bdl	bdl	200	bdl	bdl
135	V	T25_S1_py3_1	bdl	4260	810	bdl	20	bdl	bdl	bdl
134	V	T25_S1_py2_2	bdl	3250	460	20	10	bdl	bdl	bdl

APPENDIX 3: Trace element analysis of pyrite from the TNGB. All data is presented in ppm and where no value is given represents data below the detection limit (bdl). The detection limit is written in brackets below the element symbol.

Point	Pyrite type	Comment	Co (30)	As (29)	Ni (7)	Ag (7)	Te (8)	Cu (104)	Au (43)	Bi (54)
133	V	T25_S1_py2_1	bdl	1870	120	10	bdl	280	bdl	130
132	V	T25_S1_py1_2	bdl	2310	30	bdl	bdl	bdl	bdl	bdl
131	V	T25_S1_py1_1	bdl	3950	50	30	10	bdl	bdl	bdl
130	V	T12_S2_py1_3	bdl	1050	bdl	bdl	40	bdl	bdl	90
129	V	T12_S2_py1_2	bdl	1030	bdl	20	10	460	bdl	bdl
128	V	T12_S2_py1_1	bdl	960	60	bdl	bdl	bdl	bdl	bdl
127	V	T12_S1_py3_2	bdl	3240	170	30	bdl	bdl	bdl	120
126	V	T12_S1_py3_1	bdl	1170	bdl	bdl	bdl	bdl	bdl	bdl
125	V	T12_S1_py2_2	bdl	3570	20	bdl	bdl	bdl	bdl	bdl
124	V	T12_S1_py2_1	bdl	1540	bdl	bdl	30	bdl	bdl	bdl
123	V	T12_S1_py1_2	bdl	3140	bdl	bdl	30	bdl	bdl	bdl
122	V	T12_S1_py1_1	bdl	1610	bdl	bdl	30	210	70	260
286	HR	NM-SI-08_S2_py5_2	bdl	7790	1460	30	190	bdl	bdl	80
285	HR	NM-SI-08_S2_py5_1	bdl	5000	1010	bdl	bdl	bdl	bdl	bdl
284	HR	NM-SI-08_S2_py4_2	bdl	3210	1090	bdl	bdl	bdl	bdl	bdl
283	HR	NM-SI-08_S2_py4_1	bdl	3050	530	30	bdl	bdl	bdl	270
282	HR	NM-SI-08_S2_py3_2	bdl	5050	1520	50	220	200	bdl	190
281	HR	NM-SI-08_S2_py3_1	bdl	2200	250	bdl	170	bdl	bdl	120
280	HR	NM-SI-08_S2_py2_2	bdl	1360	120	bdl	bdl	270	bdl	110
279	HR	NM-SI-08_S2_py2_1	bdl	4120	1960	bdl	140	bdl	bdl	bdl
278	HR	NM-SI-08_S2_py1_2	bdl	5100	3020	50	300	bdl	bdl	170
277	HR	NM-SI-08_S2_py1_1	bdl	180	770	10	bdl	bdl	bdl	110
276	HR	NM-SI-08_S1_py4	bdl	4700	1720	bdl	bdl	440	bdl	200
274	HR	NM-SI-08_S1_py2	bdl	1150	6640	40	210	bdl	bdl	70
273	HR	NM-SI-08_S1_py1	bdl	4040	440	40	bdl	530	bdl	260

APPENDIX 3: Trace element analysis of pyrite from the TNGB. All data is presented in ppm and where no value is given represents data below the detection limit (bdl). The detection limit is written in brackets below the element symbol.

Point	Pyrite type	Comment	Co (30)	As (29)	Ni (7)	Ag (7)	Te (8)	Cu (104)	Au (43)	Bi (54)
272	VD HR	NM-SI-07_S3_py5	bdl	810	1900	50	380	bdl	bdl	180
271	VD HR	NM-SI-07_S3_py4	bdl	520	1070	bdl	320	bdl	bdl	130
270	VD HR	NM-SI-07_S3_py3	9130	910	600	bdl	190	780	bdl	bdl
269	VD HR	NM-SI-07_S3_py2	bdl	180	850	10	370	bdl	bdl	260
268	VD HR	NM-SI-07_S3_py1	bdl	860	2480	bdl	280	bdl	bdl	160
267	VD HR	NM-SI-07_S2_py5_2	bdl	2850	750	bdl	160	bdl	bdl	230
266	VD HR	NM-SI-07_S2_py5_1	bdl	2100	400	bdl	340	bdl	bdl	380
265	VD HR	NM-SI-07_S2_py4_2	bdl	2540	70	460	190	bdl	bdl	360
264	VD HR	NM-SI-07_S2_py4_1	bdl	1080	40	bdl	bdl	6750	bdl	160
263	VD HR	NM-SI-07_S2_py3_2	bdl	1520	100	30	160	bdl	bdl	240
262	VD HR	NM-SI-07_S2_py3_1	bdl	1880	70	20	160	bdl	bdl	bdl
261	VD HR	NM-SI-07_S2_py2_2	bdl	6330	720	bdl	420	bdl	bdl	130
260	VD HR	NM-SI-07_S2_py2_1	bdl	2220	350	40	450	900	bdl	bdl
259	VD HR	NM-SI-07_S2_py1_2	bdl	1730	200	20	bdl	bdl	bdl	300
258	VD HR	NM-SI-07_S2_py1_1	bdl	2210	30	bdl	bdl	1390	bdl	190
257	VD HR	NM-SI-07_S1_py5_2	bdl	3710	60	40	220	bdl	bdl	180
256	VD HR	NM-SI-07_S1_py5_1	bdl	1680	40	bdl	bdl	bdl	bdl	240
255	VD HR	NM-SI-07_S1_py4_2	bdl	1520	1550	50	260	bdl	bdl	bdl
254	VD HR	NM-SI-07_S1_py4_1	bdl	2410	130	bdl	410	bdl	bdl	270
253	VD HR	NM-SI-07_S1_py3_2	bdl	2600	40	bdl	bdl	bdl	bdl	bdl
251	VD HR	NM-SI-07_S1_py2_2	bdl	6450	50	10	bdl	bdl	bdl	bdl
250	VD HR	NM-SI-07_S1_py2_1	bdl	5200	50	bdl	bdl	540	bdl	130
249	VD HR	NM-SI-07_S1_py1_2	bdl	7920	50	bdl	440	460	bdl	bdl
248	VD HR	NM-SI-07_S1_py1_1	bdl	3960	50	bdl	320	190	bdl	80
247	HR	NM-SI-06_S3_py5	bdl	750	1530	10	230	bdl	bdl	230

APPENDIX 3: Trace element analysis of pyrite from the TNGB. All data is presented in ppm and where no value is given represents data below the detection limit (bdl). The detection limit is written in brackets below the element symbol.

Point	Pyrite type	Comment	Co (30)	As (29)	Ni (7)	Ag (7)	Te (8)	Cu (104)	Au (43)	Bi (54)
246	HR	NM-SI-06_S3_py4	bdl	920	2150	30	160	bdl	bdl	180
245	HR	NM-SI-06_S3_py3	bdl	610	5320	10	200	bdl	bdl	60
244	HR	NM-SI-06_S3_py2_2	bdl	bdl	130	10	40	bdl	bdl	270
243	HR	NM-SI-06_S3_py2_1	6760	12150	150	50	150	bdl	bdl	200
242	HR	NM-SI-06_S3_py1_2	bdl	560	bdl	30	330	bdl	bdl	bdl
241	HR	NM-SI-06_S3_py1_1	bdl	250	90	10	bdl	bdl	bdl	bdl
240	HR	NM-SI-06_S2_py5	bdl	150	840	bdl	30	110	bdl	140
239	HR	NM-SI-06_S2_py4	bdl	720	60	60	bdl	bdl	bdl	110
238	HR	NM-SI-06_S2_py3_2	bdl	940	30	10	370	bdl	bdl	330
237	HR	NM-SI-06_S2_py3_1	bdl	750	30	bdl	250	bdl	bdl	470
236	HR	NM-SI-06_S2_py2_2	bdl	920	80	10	bdl	bdl	bdl	140
235	HR	NM-SI-06_S2_py2_1	bdl	1120	50	20	340	230	bdl	410
234	HR	NM-SI-06_S2_py1_2	bdl	80	bdl	10	bdl	bdl	bdl	160
233	HR	NM-SI-06_S2_py1_1	bdl	1700	bdl	bdl	bdl	bdl	bdl	230
232	HR	NM-SI-06_S1_py5_2	bdl	1620	180	30	240	bdl	bdl	100
231	HR	NM-SI-06_S1_py5_1	bdl	1750	330	40	200	350	bdl	80
230	HR	NM-SI-06_S1_py4_2	1730	3220	20	30	210	bdl	bdl	230
229	HR	NM-SI-06_S1_py4_1	bdl	920	40	20	100	bdl	bdl	350
228	HR	NM-SI-06_S1_py3_2	bdl	70	80	40	130	bdl	bdl	bdl
227	HR	NM-SI-06_S1_py3_1	bdl	1160	210	bdl	bdl	bdl	bdl	360
226	HR	NM-SI-06_S1_py2_2	bdl	320	240	bdl	bdl	bdl	bdl	210
225	HR	NM-SI-06_S1_py2_1	bdl	2620	120	20	210	bdl	bdl	bdl
224	HR	NM-SI-06_S1_py1_2	bdl	1630	100	bdl	170	bdl	bdl	60
223	HR	NM-SI-06_S1_py1_1	bdl	1350	210	bdl	110	bdl	bdl	170
222	V	NM-SI-05_S2_py4	bdl	640	670	10	bdl	bdl	bdl	130

APPENDIX 3: Trace element analysis of pyrite from the TNGB. All data is presented in ppm and where no value is given represents data below the detection limit (bdl). The detection limit is written in brackets below the element symbol.

Point	Pyrite type	Comment	Co (30)	As (29)	Ni (7)	Ag (7)	Te (8)	Cu (104)	Au (43)	Bi (54)
221	V	NM-SI-05_S2_py3_2	bdl	250	1260	10	180	bdl	bdl	310
220	V	NM-SI-05_S2_py3_1	bdl	840	650	bdl	bdl	bdl	bdl	bdl
219	V	NM-SI-05_S2_py2_3	bdl	700	80	bdl	20	bdl	bdl	bdl
218	V	NM-SI-05_S2_py2_2	bdl	bdl	60	60	150	bdl	bdl	200
217	V	NM-SI-05_S2_py2_1	bdl	980	250	bdl	210	160	bdl	310
216	V	NM-SI-05_S2_py1_2	bdl	840	10	70	50	bdl	bdl	bdl
215	V	NM-SI-05_S2_py1_1	bdl	830	bdl	bdl	bdl	bdl	bdl	bdl
214	V	NM-SI-05_S1_py3_2	41860	470	210	30	220	bdl	bdl	120
213	V	NM-SI-05_S1_py3_1	bdl	700	2970	bdl	bdl	9510	bdl	bdl
212	V	NM-SI-05_S1_py2_2	bdl	210	1940	bdl	bdl	5740	bdl	bdl
211	V	NM-SI-05_S1_py2_1	bdl	270	4480	20	bdl	bdl	bdl	190
210	V	NM-SI-05_S1_py1_2	18750	510	70	bdl	bdl	bdl	bdl	310
209	V	NM-SI-05_S1_py1_1	15110	530	bdl	10	bdl	bdl	bdl	110
208	HR	NM-SI-04_S1_py1_2	bdl	1060	1730	bdl	160	bdl	bdl	250
207	HR	NM-SI-04_S1_py1_1	bdl	1400	4820	50	bdl	bdl	bdl	170
206	V	NM-SI-03_S2_py5	bdl	970	2640	bdl	bdl	bdl	bdl	150
205	V	NM-SI-03_S2_py4_2	bdl	480	6480	40	bdl	bdl	bdl	120
204	V	NM-SI-03_S2_py4_1	bdl	690	1930	50	190	bdl	bdl	bdl
203	V	NM-SI-03_S2_py3	bdl	2320	2240	bdl	180	bdl	bdl	bdl
202	V	NM-SI-03_S2_py2_2	bdl	740	2470	30	bdl	bdl	bdl	210
201	V	NM-SI-03_S2_py2_1	bdl	1520	490	bdl	bdl	bdl	bdl	290
200	V	NM-SI-03_S2_py1_2	bdl	3390	1340	bdl	140	bdl	bdl	bdl
199	V	NM-SI-03_S2_py1_1	bdl	1320	2840	20	70	bdl	bdl	bdl
197	HR	NM-SI-03_S1_py5_1	bdl	3600	2500	bdl	bdl	bdl	bdl	250
195	HR	NM-SI-03_S1_py4_1	bdl	660	1770	40	bdl	160	bdl	230

APPENDIX 3: Trace element analysis of pyrite from the TNGB. All data is presented in ppm and where no value is given represents data below the detection limit (bdl). The detection limit is written in brackets below the element symbol.

Point	Pyrite type	Comment	Co (30)	As (29)	Ni (7)	Ag (7)	Te (8)	Cu (104)	Au (43)	Bi (54)
194	HR	NM-SI-03_S1_py3_2	bdl	720	670	10	80	bdl	bdl	60
193	HR	NM-SI-03_S1_py3_1	bdl	630	1630	40	bdl	bdl	bdl	260
192	HR	NM-SI-03_S1_py2_2	bdl	4120	1130	20	110	bdl	bdl	220
191	HR	NM-SI-03_S1_py2_1	bdl	7790	2010	bdl	190	bdl	bdl	430
190	HR	NM-SI-03_S1_py1_2	bdl	1610	150	bdl	80	bdl	bdl	140
189	HR	NM-SI-03_S1_py1_1	bdl	1320	180	30	80	220	bdl	bdl
188	V	NM-SI-02_S3_py5	bdl	330	160	bdl	100	bdl	bdl	80
187	V	NM-SI-02_S3_py4	bdl	650	2240	bdl	210	bdl	bdl	320
186	V	NM-SI-02_S3_py3	bdl	860	4150	40	200	bdl	bdl	250
185	V	NM-SI-02_S3_py2	bdl	7020	1530	bdl	220	bdl	bdl	bdl
184	V	NM-SI-02_S3_py1_2	9130	25690	1600	bdl	bdl	bdl	bdl	210
183	V	NM-SI-02_S3_py1_1	bdl	650	90	10	120	bdl	bdl	140
181	V	NM-SI-02_S2_py4	bdl	110	20	bdl	320	bdl	bdl	bdl
180	V	NM-SI-02_S2_py3	bdl	1260	10	bdl	270	bdl	bdl	240
179	V	NM-SI-02_S2_py2_2	bdl	1230	390	20	220	bdl	bdl	bdl
178	V	NM-SI-02_S2_py2_1	bdl	1000	110	bdl	170	bdl	bdl	bdl
177	V	NM-SI-02_S2_py1	bdl	990	190	30	220	bdl	bdl	140
176	HR	NM-SI-01_S2_py5	bdl	1400	2350	bdl	100	bdl	bdl	360
175	HR	NM-SI-01_S2_py4_2	bdl	130	170	20	290	bdl	bdl	200
174	HR	NM-SI-01_S2_py4_1	bdl	80	150	40	270	bdl	bdl	120
173	HR	NM-SI-01_S2_py3_2	bdl	3090	5570	40	bdl	13860	bdl	bdl
172	HR	NM-SI-01_S2_py3_1	bdl	3100	6050	40	150	7640	bdl	140
171	HR	NM-SI-01_S2_py2_2	bdl	90	20	30	bdl	bdl	bdl	70
170	HR	NM-SI-01_S2_py2_1	bdl	50	bdl	30	230	bdl	bdl	bdl
169	HR	NM-SI-01_S2_py1_2	bdl	11040	2410	bdl	220	bdl	bdl	bdl
168	HR	NM-SI-01_S2_py1_1	bdl	660	1250	bdl	230	bdl	bdl	bdl

APPENDIX 3: Trace element analysis of pyrite from the TNGB. All data is presented in ppm and where no value is given represents data below the detection limit (bdl). The detection limit is written in brackets below the element symbol.

Point	Pyrite type	Comment	Co (30)	As (29)	Ni (7)	Ag (7)	Te (8)	Cu (104)	Au (43)	Bi (54))
167	HR	NM-SI-01_S1_py5_2	bdl	2970	1820	50	bdl	bdl	bdl	220
166	HR	NM-SI-01_S1_py5_1	bdl	170	680	20	250	bdl	bdl	160
164	HR	NM-SI-01_S1_py4_1	bdl	840	550	bdl	170	bdl	bdl	80
163	HR	NM-SI-01_S1_py3_2	bdl	1060	3390	bdl	bdl	bdl	bdl	300
162	HR	NM-SI-01_S1_py3_1	bdl	720	640	70	bdl	bdl	bdl	100
161	HR	NM-SI-01_S1_py2_2	bdl	500	80	40	bdl	bdl	bdl	bdl
160	HR	NM-SI-01_S1_py2_1	bdl	100	1010	40	140	bdl	bdl	260
158	HR	NM-SI-01_S1_py1_1	bdl	90	150	40	20	bdl	bdl	160
36	HR	NM-FS-2_SI2_py5_2	bdl	500	bdl	20	bdl	bdl	bdl	bdl
35	HR	NM-FS-2_SI2_py5_1	bdl	110	10	bdl	bdl	180	bdl	bdl
34	HR	NM-FS-2_SI2_py4_2	1090	1580	280	10	bdl	bdl	bdl	bdl
33	HR	NM-FS-2_SI2_py4_1	1360	1350	300	20	bdl	bdl	bdl	250
32	HR	NM-FS-2_SI2_py3_2	bdl	1030	bdl	bdl	20	bdl	bdl	100
30	HR	NM-FS-2_SI2_py2_2	bdl	1110	30	bdl	bdl	bdl	bdl	bdl
29	HR	NM-FS-2_SI2_py2_1	bdl	1060	40	20	bdl	190	bdl	90
28	HR	NM-FS-2_SI2_py1_2	10490	5340	320	bdl	bdl	330	bdl	bdl
27	HR	NM-FS-2_SI2_py1_1	10770	4330	410	10	bdl	2790	bdl	240
46	HR	NM-FS-2_SI1_py4_2	bdl	670	90	20	10	240	bdl	bdl
45	HR	NM-FS-2_SI1_py4_1	bdl	540	500	bdl	bdl	bdl	100	200
44	HR	NM-FS-2_SI1_py3_2	bdl	1140	bdl	bdl	30	bdl	bdl	bdl
43	HR	NM-FS-2_SI1_py3_1	bdl	1070	bdl	10	bdl	bdl	bdl	170
42	HR	NM-FS-2_SI1_py2_2	bdl	240	80	60	bdl	bdl	bdl	180
41	HR	NM-FS-2_SI1_py2_1	bdl	940	350	bdl	40	150	bdl	bdl
40	HR	NM-FS-2_SI1_py1_2	bdl	1140	20	bdl	100	bdl	bdl	bdl

APPENDIX 3: Trace element analysis of pyrite from the TNGB. All data is presented in ppm and where no value is given represents data below the detection limit (bdl). The detection limit is written in brackets below the element symbol.

Point	Pyrite type	Comment	Co (30)	As (29)	Ni (7)	Ag (7)	Te (8)	Cu (104)	Au (43)	Bi (54)
39	HR	NM-FS-2_SI1_py1_1	bdl	800	40	bdl	bdl	bdl	bdl	160
22	HR	NM-FS-1_SI1_py1_4	13150	10300	320	bdl	bdl	bdl	bdl	110
21	HR	NM-FS-1_SI1_py1_3	bdl	760	630	10	bdl	bdl	bdl	bdl
20	HR	NM-FS-1_SI1_py1_2	bdl	770	470	20	bdl	bdl	bdl	bdl
19	HR	NM-FS-1_SI1_py1_1	bdl	640	540	bdl	bdl	bdl	bdl	bdl
26	HR	NM-FS-1_py3_2	bdl	510	10	bdl	bdl	170	bdl	bdl
25	HR	NM-FS-1_py3_1	bdl	60	bdl	10	20	bdl	bdl	bdl
24	HR	NM-FS-1_py2_2	3970	3250	810	bdl	bdl	bdl	bdl	bdl
23	HR	NM-FS-1_py2_1	9950	4740	210	bdl	bdl	bdl	bdl	bdl
157	AM HR	LG-SI-06_S3_py3_2	bdl	2190	60	30	130	bdl	bdl	180
156	AM HR	LG-SI-06_S3_py3_1	bdl	7180	70	40	50	bdl	bdl	190
155	AM HR	LG-SI-06_S3_py2_2	bdl	3170	70	20	230	bdl	bdl	bdl
154	AM HR	LG-SI-06_S3_py2_1	bdl	4570	10	20	230	bdl	bdl	150
153	AM HR	LG-SI-06_S3_py1_2	bdl	710	bdl	40	bdl	1360	bdl	120
152	AM HR	LG-SI-06_S3_py1_1	bdl	7690	10	50	bdl	3170	bdl	240
150	AM HR	LG-SI-06_S2_py1_1	bdl	950	60	20	170	bdl	bdl	bdl
149	AM HR	LG-SI-06_S1_py3_2	bdl	850	30	40	190	bdl	bdl	650
148	AM HR	LG-SI-06_S1_py3_1	bdl	480	60	20	220	bdl	bdl	130
147	AM HR	LG-SI-06_S1_py2_2	bdl	820	60	30	bdl	bdl	bdl	bdl
146	AM HR	LG-SI-06_S1_py2_1	1190	1180	bdl	30	110	bdl	bdl	100
145	AM HR	LG-SI-06_S1_py1_2	490	1410	290	40	bdl	bdl	bdl	bdl
144	AM HR	LG-SI-06_S1_py1_1	bdl	1110	80	bdl	10	bdl	bdl	120
143	AM HR	LG-SI-05_S3_py5	bdl	1200	130	100	140	320	bdl	270
142	AM HR	LG-SI-05_S3_py4	bdl	870	10	bdl	150	bdl	bdl	220
141	HR	LG-SI-05_S3_py3_2	bdl	980	bdl	bdl	bdl	bdl	bdl	290

APPENDIX 3: Trace element analysis of pyrite from the TNGB. All data is presented in ppm and where no value is given represents data below the detection limit (bdl). The detection limit is written in brackets below the element symbol.

Point	Pyrite type	Comment	Co (30)	As (29)	Ni (7)	Ag (7)	Te (8)	Cu (104)	Au (43)	Bi (54)
140	V	LG-SI-05_S3_py3_1	bdl	1090	110	50	180	bdl	bdl	170
139	V	LG-SI-05_S3_py2_2	bdl	820	590	20	170	bdl	bdl	120
138	V	LG-SI-05_S3_py2_1	bdl	1600	150	bdl	100	2710	bdl	160
137	V	LG-SI-05_S3_py1_2	bdl	5380	130	30	200	410	bdl	bdl
135	V	LG-SI-05_S2_py5_2	bdl	3080	290	10	50	bdl	bdl	bdl
134	V	LG-SI-05_S2_py5_1	bdl	1310	80	bdl	190	bdl	bdl	100
133	V	LG-SI-05_S2_py4_2	bdl	1130	120	bdl	170	bdl	bdl	bdl
132	V	LG-SI-05_S2_py4_1	bdl	920	70	bdl	200	bdl	bdl	100
131	V	LG-SI-05_S2_py3_2	bdl	5590	240	20	200	bdl	bdl	200
130	V	LG-SI-05_S2_py3_1	bdl	2550	130	bdl	bdl	bdl	bdl	120
129	V	LG-SI-05_S2_py2_2	bdl	11600	620	30	bdl	bdl	bdl	200
128	V	LG-SI-05_S2_py2_1	bdl	3760	80	bdl	260	bdl	bdl	bdl
127	V	LG-SI-05_S2_py1_2	500	4640	580	70	160	450	bdl	200
126	V	LG-SI-05_S2_py1_1	bdl	1250	190	bdl	130	bdl	bdl	90
125	V	LG-SI-05_S1_py2_2	bdl	850	1100	bdl	bdl	bdl	bdl	bdl
124	V	LG-SI-05_S1_py2_1	bdl	810	60	bdl	190	bdl	bdl	120
123	V	LG-SI-05_S1_py1_2	bdl	1730	310	10	180	bdl	bdl	bdl
122	V	LG-SI-05_S1_py1_1	bdl	1140	240	bdl	140	bdl	bdl	bdl
121	HR	LG-SI-02_S2_py2_2	bdl	590	60	90	140	bdl	bdl	bdl
120	HR	LG-SI-02_S2_py2_1	bdl	730	170	bdl	240	bdl	bdl	90
119	HR	LG-SI-02_S2_py_4	bdl	390	bdl	bdl	230	bdl	bdl	100
118	HR	LG-SI-02_S2_py_3	bdl	1180	50	40	280	bdl	bdl	bdl
117	HR	LG-SI-02_S2_py_2	bdl	1300	40	10	220	bdl	bdl	bdl
116	HR	LG-SI-02_S2_py_1	bdl	1230	60	bdl	140	bdl	bdl	260

APPENDIX 3: Trace element analysis of pyrite from the TNGB. All data is presented in ppm and where no value is given represents data below the detection limit (bdl). The detection limit is written in brackets below the element symbol.

Point	Pyrite type	Comment	Co (30)	As (29)	Ni (7)	Ag (7)	Te (8)	Cu (104)	Au (43)	Bi (54)
115	HR	KG-SIS-7_S2_py5_2	bdl	840	950	bdl	bdl	bdl	bdl	130
114	HR	KG-SIS-7_S2_py5_1	bdl	1010	580	bdl	bdl	bdl	bdl	120
113	HR	KG-SIS-7_S2_py4_2	bdl	980	390	40	250	bdl	bdl	bdl
112	HR	KG-SIS-7_S2_py4_1	bdl	910	340	30	50	230	bdl	120
111	HR	KG-SIS-7_S2_py3_2	bdl	340	700	10	50	bdl	bdl	bdl
110	HR	KG-SIS-7_S2_py3_1	bdl	1090	520	20	290	130	bdl	280
109	HR	KG-SIS-7_S2_py2_2	bdl	810	690	bdl	140	bdl	bdl	150
108	HR	KG-SIS-7_S2_py2_1	bdl	130	910	50	190	bdl	bdl	240
107	HR	KG-SIS-7_S2_py1_2	bdl	530	1090	70	240	bdl	bdl	bdl
106	HR	KG-SIS-7_S2_py1_1	bdl	180	680	20	70	bdl	bdl	60
105	V	KG-SIS-7_S1_py2_2	bdl	50	1870	30	150	bdl	bdl	250
104	V	KG-SIS-7_S1_py2_1	bdl	530	710	60	bdl	bdl	bdl	370
103	V	KG-SIS-7_S1_py1_5	bdl	580	1600	bdl	bdl	bdl	bdl	60
102	V	KG-SIS-7_S1_py1_4	bdl	920	650	20	200	bdl	bdl	70
101	V	KG-SIS-7_S1_py1_3	bdl	930	570	50	100	bdl	bdl	150
100	V	KG-SIS-7_S1_py1_2	bdl	1010	730	20	270	bdl	bdl	480
99	V	KG-SIS-7_S1_py1_1	bdl	690	840	bdl	210	bdl	bdl	250
97	HR	KG-SIS-6_S2_py4_2	bdl	1100	380	10	150	bdl	bdl	180
94	HR	KG-SIS-6_S2_py3_1	bdl	220	880	30	150	190	bdl	bdl
92	HR	KG-SIS-6_S2_py2_1	bdl	1310	480	bdl	320	bdl	bdl	1290
87	HR	KG-SIS-6_S1_py4_2	bdl	520	320	60	210	bdl	bdl	200
86	HR	KG-SIS-6_S1_py4_1	bdl	920	230	10	310	bdl	bdl	320
85	HR	KG-SIS-6_S1_py3_2	bdl	930	120	90	210	bdl	bdl	bdl
84	HR	KG-SIS-6_S1_py3_1	bdl	610	340	80	60	bdl	bdl	120
83	HR	KG-SIS-6_S1_py2_2	bdl	240	400	10	230	bdl	bdl	240

APPENDIX 3: Trace element analysis of pyrite from the TNGB. All data is presented in ppm and where no value is given represents data below the detection limit (bdl). The detection limit is written in brackets below the element symbol.

Point	Pyrite type	Comment	Co (30)	As (29)	Ni (7)	Ag (7)	Te (8)	Cu (104)	Au (43)	Bi (54)
82	HR	KG-SIS-6_S1_py2_1	bdl	490	120	bdl	180	420	bdl	bdl
81	HR	KG-SIS-6_S1_py1_2	bdl	580	410	50	170	560	bdl	190
80	HR	KG-SIS-6_S1_py1_1	bdl	900	170	70	bdl	bdl	bdl	180
79	HR	KG-SIS-5_S2_py4_2	bdl	840	480	bdl	200	bdl	bdl	460
78	HR	KG-SIS-5_S2_py4_1	bdl	930	470	80	240	bdl	bdl	360
77	HR	KG-SIS-5_S2_py3_2	bdl	1030	190	20	150	bdl	bdl	240
76	HR	KG-SIS-5_S2_py3_1	bdl	1000	420	10	140	bdl	bdl	bdl
75	HR	KG-SIS-5_S2_py2_2	bdl	610	250	bdl	160	bdl	bdl	290
74	HR	KG-SIS-5_S2_py2_1	bdl	660	470	40	160	bdl	bdl	bdl
73	HR	KG-SIS-5_S2_py1_2	bdl	600	410	20	120	bdl	bdl	bdl
72	HR	KG-SIS-5_S2_py1_1	bdl	240	510	40	bdl	bdl	bdl	bdl
71	HR	KG-SIS-5_S1_py5	bdl	690	100	bdl	bdl	bdl	bdl	bdl
70	HR	KG-SIS-5_S1_py4	bdl	80	20	10	bdl	bdl	bdl	90
69	HR	KG-SIS-5_S1_py3_2	bdl	910	1520	30	290	bdl	bdl	110
68	HR	KG-SIS-5_S1_py3_1	bdl	50	380	bdl	180	bdl	bdl	360
67	HR	KG-SIS-5_S1_py2_2	bdl	260	140	30	210	140	bdl	290
66	HR	KG-SIS-5_S1_py2_1	bdl	1010	360	bdl	140	bdl	bdl	120
65	HR	KG-SIS-5_S1_py1_2	bdl	1110	100	bdl	100	150	bdl	bdl
64	HR	KG-SIS-5_S1_py1_1	bdl	1060	330	bdl	190	bdl	bdl	330
62	HR	KG-SIS-3B_S1_py4_2	bdl	1420	470	90	290	870	340	1040
61	HR	KG-SIS-3B_S1_py4_1	bdl	1080	450	20	240	150	bdl	270
60	HR	KG-SIS-3B_S1_py3_2	bdl	860	2260	10	190	bdl	bdl	240
59	HR	KG-SIS-3B_S1_py3_1	bdl	820	970	10	250	bdl	bdl	140
58	HR	KG-SIS-3B_S1_py2_2	bdl	740	1500	30	200	bdl	bdl	80
57	HR	KG-SIS-3B_S1_py2_1	bdl	840	620	bdl	150	bdl	bdl	70

APPENDIX 3: Trace element analysis of pyrite from the TNGB. All data is presented in ppm and where no value is given represents data below the detection limit (bdl). The detection limit is written in brackets below the element symbol.

Point	Pyrite type	Comment	Co (30)	As (29)	Ni (7)	Ag (7)	Te (8)	Cu (104)	Au (43)	Bi (54)
56	HR	KG-SIS-3B_S1_py1_2	bdl	950	970	30	240	bdl	bdl	bdl
55	HR	KG-SIS-3B_S1_py1_1	bdl	620	840	60	150	bdl	bdl	bdl
54	V	KG-SIS-3A_S2_py4	bdl	600	550	bdl	190	bdl	bdl	290
53	V	KG-SIS-3A_S2_py2_3	bdl	930	550	30	40	bdl	bdl	bdl
52	V	KG-SIS-3A_S2_py2_2	bdl	580	410	bdl	170	bdl	bdl	120
51	V	KG-SIS-3A_S2_py2_1	bdl	420	360	50	60	bdl	bdl	110
50	V	KG-SIS-3A_S2_py1_2	bdl	210	2760	40	250	bdl	bdl	160
49	V	KG-SIS-3A_S2_py1_1	1510	840	4940	20	280	300	bdl	130
48	HR	KG-SIS-3A_S1_py3_2	bdl	660	640	10	210	bdl	bdl	60
47	HR	KG-SIS-3A_S1_py3_1	bdl	700	540	bdl	190	bdl	bdl	270
46	HR	KG-SIS-3A_S1_py2_2	bdl	920	1490	40	230	bdl	bdl	bdl
45	HR	KG-SIS-3A_S1_py2_1	bdl	550	2010	10	70	bdl	bdl	bdl
44	HR	KG-SIS-3A_S1_py1_2	bdl	120	1830	20	30	bdl	bdl	160
43	HR	KG-SIS-3A_S1_py1_1	bdl	670	960	bdl	200	bdl	bdl	210
42	VD HR	KG-SIS-2_S3_py6	bdl	890	240	bdl	10	bdl	bdl	bdl
41	VD HR	KG-SIS-2_S3_py5	bdl	640	100	20	bdl	bdl	bdl	bdl
40	VD HR	KG-SIS-2_S3_py4	bdl	720	320	bdl	bdl	bdl	bdl	110
39	VD HR	KG-SIS-2_S3_py3	bdl	1090	70	10	bdl	bdl	bdl	200
38	VD HR	KG-SIS-2_S3_py2	bdl	780	20	20	10	560	bdl	bdl
37	VD HR	KG-SIS-2_S3_py1	bdl	370	60	30	10	140	bdl	90
36	V	KG-SIS-2_S2_py6	bdl	640	bdl	20	bdl	350	bdl	bdl
35	V	KG-SIS-2_S2_py5	bdl	570	70	10	10	bdl	bdl	bdl
34	V	KG-SIS-2_S2_py4	bdl	290	60	10	30	170	bdl	bdl
33	V	KG-SIS-2_S2_py3_2	bdl	950	20	bdl	bdl	bdl	bdl	bdl
32	V	KG-SIS-2_S2_py3_1	bdl	1020	20	10	bdl	bdl	bdl	170

APPENDIX 3: Trace element analysis of pyrite from the TNGB. All data is presented in ppm and where no value is given represents data below the detection limit (bdl). The detection limit is written in brackets below the element symbol.

Point	Pyrite type	Comment	Co (30)	As (29)	Ni (7)	Ag (7)	Te (8)	Cu (104)	Au (43)	Bi (54)
31	V	KG-SIS-2_S2_py2_2	bdl	940	170	bdl	bdl	bdl	bdl	bdl
30	V	KG-SIS-2_S2_py2_1	bdl	680	190	bdl	20	260	bdl	bdl
29	V	KG-SIS-2_S2_py1_2	bdl	200	bdl	bdl	40	150	bdl	90
28	V	KG-SIS-2_S2_py1_1	bdl	970	570	40	bdl	90	bdl	bdl
27	V	KG-SIS-2_S1_py4	bdl	560	bdl	10	bdl	100	bdl	bdl
26	V	KG-SIS-2_S1_py3	bdl	200	bdl	bdl	bdl	bdl	bdl	130
25	V	KG-SIS-2_S1_py2_2	bdl	170	170	20	10	bdl	bdl	bdl
24	V	KG-SIS-2_S1_py2_1	bdl	770	60	bdl	bdl	bdl	bdl	bdl
23	V	KG-SIS-2_S1_py1_3	bdl	430	90	bdl	10	bdl	bdl	bdl
22	V	KG-SIS-2_S1_py1_2	bdl	660	140	10	bdl	bdl	bdl	bdl
21	V	KG-SIS-2_S1_py1_1	bdl	250	bdl	bdl	10	bdl	bdl	bdl
10	HR	KG-FS-1_SI2_py5_2	bdl	830	bdl	bdl	bdl	bdl	bdl	120
9	HR	KG-FS-1_SI2_py5_1	bdl	830	bdl	bdl	bdl	bdl	bdl	bdl
8	HR	KG-FS-1_SI2_py4_2	bdl	650	bdl	50	20	bdl	bdl	bdl
7	HR	KG-FS-1_SI2_py4_1	bdl	430	bdl	bdl	bdl	280	bdl	bdl
6	HR	KG-FS-1_SI2_py3_4	bdl	800	10	bdl	30	bdl	bdl	130
5	HR	KG-FS-1_SI2_py3_3	bdl	990	bdl	bdl	bdl	bdl	bdl	bdl
4	HR	KG-FS-1_SI2_py3_2	bdl	920	bdl	bdl	bdl	bdl	bdl	bdl
3	HR	KG-FS-1_SI2_py3_1	bdl	1000	bdl	10	50	bdl	bdl	210
2	HR	KG-FS-1_SI2_py2_2	bdl	1360	20	60	20	230	bdl	310
1	HR	KG-FS-1_SI2_py2_1	bdl	760	20	bdl	30	bdl	bdl	bdl

APPENDIX 4: Sulphur isotope compositions of pyrite. All δ^{34}S are relative to VCDT. Pyrite growth: V: hydrothermal in vein; HR: authigenic/metamorphic in host rock; AM HR: autometasomatic segregation in host rock; VD HR: disseminated from vein into host rock.

Analysis name	Sample	Pyrite type	Au grade and association	δ^{34}S
Tm17-SI1@1	KG-SIS-2	V	0.41g/t, Au flake in Py	-7.9
Tm17-SI1@3	KG-SIS-2	V	0.41g/t, Au flake in Py	-7.4
Tm17-SI1@4	KG-SIS-2	V	0.41g/t, Au flake in Py	-8.6
Tm17-SI2@1	KG-SIS-2	VD HR	0.41g/t, Au flake in Py	-8.5
Tm17-SI2@2	KG-SIS-2	VD HR	0.41g/t, Au flake in Py	-8.7
Tm17-SI2@3	KG-SIS-2	VD HR	0.41g/t, Au flake in Py	-8.5
Tm17-SI2@4	KG-SIS-2	VD HR	0.41g/t, Au flake in Py	-8.4
Tm17-SI2@5	KG-SIS-2	VD HR	0.41g/t, Au flake in Py	-9.1
Tm17-SI2@6	KG-SIS-2	VD HR	0.41g/t, Au flake in Py	-8.2
Tm17-SI2@7	KG-SIS-2	VD HR	0.41g/t, Au flake in Py	-8.4
Tm17-SI2@8	KG-SIS-2	VD HR	0.41g/t, Au flake in Py	-8.3
Tm20-SI2@1	KG-SIS-5	HR	1.9 g/t	-2.1
Tm20-SI2@2	KG-SIS-5	HR	1.9 g/t	-2.1
Tm20-SI2@3	KG-SIS-5	HR	1.9 g/t	-2.5
Tm22-SI1@1	KG-SIS-6	HR	0.2 g/t	-1.0
Tm22-SI1@2	KG-SIS-6	HR	0.2 g/t	-1.5
Tm22-SI2@1	KG-SIS-6	HR	0.2 g/t	-0.6
Tm22-SI2@3	KG-SIS-6	HR	0.2 g/t	-0.8
Tm22-SI2@4	KG-SIS-6	HR	0.2 g/t	-0.9
Tm22-SI2@5	KG-SIS-6	HR	0.2 g/t	-0.8
Tm25-SI1@1	KG-SIS-7	HR	0.07 g/t	-3.8
Tm25-SI1@2	KG-SIS-7	HR	0.07 g/t	-3.6
Tm25-SI2@2	KG-SIS-7	HR	0.07 g/t	-4.2
Tm25-SI2@3	KG-SIS-7	HR	0.07 g/t	-4.0
Tm19-SI1@1	LG-SI-02	HR	<0.01 g/t, Au flake in Py	-17.0
Tm19-SI1@2	LG-SI-02	HR	<0.01 g/t, Au flake in Py	-14.8
Tm19-SI2@1	LG-SI-02	HR	<0.01 g/t, Au flake in Py	-16.8
Tm19-SI2@2	LG-SI-02	HR	<0.01 g/t, Au flake in Py	-16.0
Tm19-SI2@3	LG-SI-02	HR	<0.01 g/t, Au flake in Py	-16.6
Tm19-SI2@4	LG-SI-02	HR	<0.01 g/t, Au flake in Py	-18.4
Tm21-SI2@1	LG-SI-05	V	0.63 g/t	0.9
Tm21-SI2@2	LG-SI-05	V	0.63 g/t	3.2
Tm21-SI2@3	LG-SI-05	V	0.63 g/t	3.0
Tm21-SI2@4	LG-SI-05	V	0.63 g/t	0.5
Tm21-SI2@5	LG-SI-05	V	0.63 g/t	-0.3

APPENDIX 4: Sulphur isotope compositions of pyrite. All $\delta^{34}S$ are relative to VCDT. Pyrite growth: V: hydrothermal in vein; HR: authigenic/metamorphic in host rock; AM HR: autometasomatic segregation in host rock; VD HR: disseminated from vein into host rock.

Analysis name	Sample	Pyrite type	Au grade and association	$\delta^{34}S$
Tm24-SI1@1	LG-SI-06	AM HR	<0.1 g/t	-6.6
Tm24-SI1@2	LG-SI-06	AM HR	<0.1 g/t	-13.1
Tm24-SI2@1	LG-SI-06	AM HR	<0.1 g/t	-13.2
Tm24-SI2@2	LG-SI-06	AM HR	<0.1 g/t	-14.2
Tm24-SI2@3	LG-SI-06	AM HR	<0.1 g/t	-12.7
Tm24-SI2@4	LG-SI-06	AM HR	<0.1 g/t	-14.0
Tm4-SI2@1	NM-SI-1	V	N.A.; mineral. zone	8.3
Tm4-SI2@2	NM-SI-1	V	N.A.; mineral. zone	9.3
Tm4-SI2@3	NM-SI-1	V	N.A.; mineral. zone	9.4
Tm4-SI1@1	NM-SI-1	V	N.A.; mineral. zone	10.0
Tm4-SI1@2	NM-SI-1	V	N.A.; mineral. zone	8.6
Tm4-SI1@3	NM-SI-1	V	N.A.; mineral. zone	10.0
Tm7-SI1@1	NM-SI-2	V	N.A.; mineral. zone	9.5
Tm7-SI1@2	NM-SI-2	V	N.A.; mineral. zone	9.3
Tm7-SI1@3	NM-SI-2	V	N.A.; mineral. zone	8.9
Tm7-SI1@4	NM-SI-2	V	N.A.; mineral. zone	9.0
Tm7-SI1@5	NM-SI-2	V	N.A.; mineral. zone	8.5
Tm7-SI1@6	NM-SI-2	V	N.A.; mineral. zone	9.4
Tm7-SI1@7	NM-SI-2	V	N.A.; mineral. zone	9.0
Tm7-SI2@1	NM-SI-2	V	N.A.; mineral. zone	10.5
Tm7-SI2@2	NM-SI-2	V	N.A.; mineral. zone	9.8
Tm7-SI2@3	NM-SI-2	V	N.A.; mineral. zone	8.9
Tm10-SI1@1	NM-SI-3	V	1.32 g/t	1.3
Tm10-SI1@2	NM-SI-3	V	1.32 g/t	5.9
Tm10-SI1@3	NM-SI-3	V	1.32 g/t	2.5
Tm10-SI1@4	NM-SI-3	V	1.32 g/t	13.1
Tm26-SI2@1	NM-SI-5	V	173 g/t	20.4
Tm26-SI2@2	NM-SI-5	V	173 g/t	20.3
Tm26-SI2@3	NM-SI-5	V	173 g/t	20.3
Tm26-SI2@4	NM-SI-5	V	173 g/t	19.6
Tm26-SI2@5	NM-SI-5	V	173 g/t	20.1
Tm26-SI1@1	NM-SI-5	V	173 g/t	20.4
Tm26-SI1@2	NM-SI-5	V	173 g/t	20.2
Tm26-SI1@3	NM-SI-5	V	173 g/t	19.5
Tm27-SI2@1	NM-SI-6	HR	0.01 g/t	22.2
Tm27-SI2@2	NM-SI-6	HR	0.01 g/t	22.2
Tm27-SI1@1	NM-SI-6	HR	0.01 g/t	21.8

APPENDIX 4: Sulphur isotope compositions of pyrite. All $\delta^{34}S$ are relative to VCDT. Pyrite growth: V: hydrothermal in vein; HR: authigenic/metamorphic in host rock; AM HR: autometasomatic segregation in host rock; VD HR: disseminated from vein into host rock.

Analysis name	Sample	Host rock or vein	Au grade and association	$\delta^{34}S$
Tm27-SI1@2	NM-SI-6	HR	0.01 g/t	21.9
Tm27-SI3@1	NM-SI-6	HR	0.01 g/t	22.0
Tm27-SI3@2	NM-SI-6	HR	0.01 g/t	22.6
Tm23-SI1@1	NM-SI-7	VD HR	0.44 g/t	13.6
Tm23-SI1@2	NM-SI-7	VD HR	0.44 g/t	15.4
Tm23-SI1@3	NM-SI-7	VD HR	0.44 g/t	16.1
Tm23-SI1@4	NM-SI-7	VD HR	0.44 g/t	14.2
Tm23-SI1@5	NM-SI-7	VD HR	0.44 g/t	14.3
Tm23-SI1@6	NM-SI-7	VD HR	0.44 g/t	13.9
Tm23-SI2@1	NM-SI-7	VD HR	0.44 g/t	13.2
Tm23-SI2@2	NM-SI-7	VD HR	0.44 g/t	14.6
Tm23-SI2@3	NM-SI-7	VD HR	0.44 g/t	14.2
Tm23-SI2@4	NM-SI-7	VD HR	0.44 g/t	14.4
Tm23-SI2@5	NM-SI-7	VD HR	0.44 g/t	14.2
Tm18-SI1@1	NM-SI-8	HR	0.09 g/t	12.5
Tm18-SI1@2	NM-SI-8	HR	0.09 g/t	13.3
Tm18-SI1@3	NM-SI-8	HR	0.09 g/t	12.4
Tm18-SI2@1	NM-SI-8	HR	0.09 g/t	13.0
Tm18-SI2@2	NM-SI-8	HR	0.09 g/t	13.6
Tm18-SI2@3	NM-SI-8	HR	0.09 g/t	13.9
Tm15SI1@1	T12	V	<0.1 g/t	-4.8
Tm15SI1@2	T12	V	<0.1 g/t	-5.0
Tm15SI1@3	T12	V	<0.1 g/t	-4.6
Tm2-SI2@1	T25	V	63 g/t	2.1
Tm2-SI2@2	T25	V	63 g/t	1.5
Tm2-SI2@3	T25	V	63 g/t	2.9
Tm2-SI1@1	T25	V	63 g/t	1.8
Tm2-SI1@2	T25	V	63 g/t	3.0
Tm2-SI1@3	T25	V	63 g/t	2.2
Tm12-SI1@2	T3	V	9.19 g/t	2.6
Tm12-SI1@3	T3	V	9.19 g/t	2.3
Tm12-SI2@1	T3	V	9.19 g/t	2.5
Tm12-SI2@2	T3	V	9.19 g/t	2.0
Tm12-SI2@3	T3	V	9.19 g/t	2.1
Tm12-SI2@4	T3	V	9.19 g/t	2.3
Tm9-SI1@1	T9	V	<0.1 g/t; Au flake in Py	-4.2
Tm9-SI1@2	T9	V	<0.1 g/t; Au flake in Py	-4.2

APPENDIX 4: Sulphur isotope compositions of pyrite. All $\delta^{34}S$ are relative to VCDT. Pyrite growth: V: hydrothermal in vein; HR: authigenic/metamorphic in host rock; AM HR: autometasomatic segregation in host rock; VD HR: disseminated from vein into host rock.

Analysis name	Sample	Host rock or vein	Au grade and association	$\delta^{34}S$
Tm9-SI1@3	T9	V	<0.1 g/t; Au flake in Py	-4.8
Tm9-SI1@4	T9	V	<0.1 g/t; Au flake in Py	-4.6
Tm9-SI1@5	T9	V	<0.1 g/t; Au flake in Py	-4.2
Tm9-SI3@1	T9	V	<0.1 g/t; Au flake in Py	-4.7
Tm9-SI3@2	T9	V	<0.1 g/t; Au flake in Py	-4.7
Tm9-SI3@3	T9	V	<0.1 g/t; Au flake in Py	-4.1
Tm9-SI2@1	T9	V	<0.1 g/t; Au flake in Py	-4.9
Tm9-SI2@2	T9	V	<0.1 g/t; Au flake in Py	-5.2
Tm9-SI2@3	T9	V	<0.1 g/t; Au flake in Py	-5.0
Tm9-SI2@4	T9	V	<0.1 g/t; Au flake in Py	-4.9
Tm1-SI1@1	TW-FS-03	HR	9.85 g/t; Au flake in Py	1.5
Tm1-SI1@2	TW-FS-03	HR	9.85 g/t; Au flake in Py	-1.3
Tm1-SI3@1	TW-FS-03	HR	9.85 g/t; Au flake in Py	1.6
Tm1-SI3@2	TW-FS-03	HR	9.85 g/t; Au flake in Py	3.0
Tm1-SI2@1	TW-FS-03	HR	9.85 g/t; Au flake in Py	2.5
Tm1-SI2@2	TW-FS-03	HR	9.85 g/t; Au flake in Py	-1.4
Tm1-SI2@3	TW-FS-03	HR	9.85 g/t; Au flake in Py	2.3
Tm6-SI2@1	TW-FS-05	HR	7.12 g/t; Au flake in Py	0.6
Tm6-SI2@2	TW-FS-05	HR	7.12 g/t; Au flake in Py	0.4
Tm6-SI2@3	TW-FS-05	HR	7.12 g/t; Au flake in Py	0.7
Tm6-SI1@1	TW-FS-05	HR	7.12 g/t; Au flake in Py	1.1
Tm6-SI1@2	TW-FS-05	HR	7.12 g/t; Au flake in Py	0.5
Tm6-SI1@3	TW-FS-05	HR	7.12 g/t; Au flake in Py	-2.2
Tm6-SI1@4	TW-FS-05	HR	7.12 g/t; Au flake in Py	0.6
Tm6-SI3@1	TW-FS-05	HR	7.12 g/t; Au flake in Py	2.1
Tm6-SI3@2	TW-FS-05	HR	7.12 g/t; Au flake in Py	-0.4
Tm6-SI3@3	TW-FS-05	HR	7.12 g/t; Au flake in Py	1.4
Tm6-SI3@4	TW-FS-05	HR	7.12 g/t; Au flake in Py	2.2
Tm3-SI1@1	TW-FS-07	HR	0.57 g/t	2.2
Tm3-SI1@2	TW-FS-07	HR	0.57 g/t	2.1
Tm3-SI1@3	TW-FS-07	HR	0.57 g/t	2.8
Tm3-SI3@1	TW-FS-07	HR	0.57 g/t	1.9
Tm3-SI3@2	TW-FS-07	HR	0.57 g/t	1.5
Tm3-SI3@3	TW-FS-07	HR	0.57 g/t	0.7